INTERFACE ENGINEERING AND CHARACTERIZATION IN DYE- AND QUANTUM DOT-SENSITIZED SOLAR CELLS

A DISSERTATION

SUBMITTED TO THE DEPARTMENT OF CHEMICAL ENGINEERING

AND THE COMMITTEE ON GRADUATE STUDIES

OF STANFORD UNIVERSITY

IN PARTIAL FULFILLMENT OF THE REQUIREMENTS

FOR THE DEGREE OF

DOCTOR OF PHILOSOPHY

Thomas P. Brennan

June 2013

© 2013 by Thomas Patrick Brennan. All Rights Reserved.

Re-distributed by Stanford University under license with the author.



This work is licensed under a Creative Commons Attribution-Noncommercial 3.0 United States License.
http://creativecommons.org/licenses/by-nc/3.0/us/

This dissertation is online at: http://purl.stanford.edu/gz567jy2979

Includes supplemental files:

1. Video of a molecular dynamics simulation to complement Chapter 6. *(Chapter 6 - DFT-MD Simulation_300K_15ps.avi)*

I certify that I have read this dissertation and that, in my opinion, it is fully adequate in scope and quality as a dissertation for the degree of Doctor of Philosophy.

Stacey Bent, Primary Adviser

I certify that I have read this dissertation and that, in my opinion, it is fully adequate in scope and quality as a dissertation for the degree of Doctor of Philosophy.

Zhenan Bao

I certify that I have read this dissertation and that, in my opinion, it is fully adequate in scope and quality as a dissertation for the degree of Doctor of Philosophy.

Michael McGehee

Approved for the Stanford University Committee on Graduate Studies.

Patricia J. Gumport, Vice Provost Graduate Education

This signature page was generated electronically upon submission of this dissertation in electronic format. An original signed hard copy of the signature page is on file in University Archives.

Abstract

The increasing demand for energy as standards of living and population sizes rise across the globe motivates the development of scalable resources to meet the forecasted doubling of energy consumption. This challenge is further compounded by the need to reduce the CO_2 emissions associated with our current level of energy consumption in order to stave off costly changes in the global climate. Solar energy promises renewable, carbon-free energy and a resource that is orders of magnitude larger than alternative sources. Capturing this solar energy with photovoltaic devices has become an increasingly economical means of energy production, but further development is needed to make solar energy conversion inexpensive and ubiquitous. One particular class of photovoltaics—the dye-sensitized solar cell (DSSC)—is especially appealing because it can be constructed with abundant, inexpensive materials and be engineered in a modular fashion for a wide array of product applications.

Challenges remain, however, in order to make DSSCs more efficient, more economical, and more practical. The DSSC architecture is quite different than traditional—*i.e.* silicon and thin film inorganic—photovoltaics in that light harvesting and charge collection are decoupled. This is achieved by depositing a thin nanometer-scale layer of light-absorbing dye molecules atop a high surface area nanostructured TiO_2 anode. The consequence of this architecture, however, is an abundance of interfacial area at which deleterious charge recombination processes can occur. Further improvements in DSSC performance therefore require a thorough understanding of and high control over the dual-interface that exists between the dye layer and the electron-conducting anode and the dye layer and the hole-transporting material (HTM).

In the first part of this work we describe the application of thin, sub-nanometer insulating metal oxide layers grown by atomic layer deposition (ALD) to the TiO_2 anode for the purpose of slowing down the undesirable back-recombination of electrons injected into TiO_2 by the light-absorbing dye molecules. We use the well-characterized insulator Al_2O_3 as a recombination barrier material and perform a comprehensive study of different

parameters that impact how such barriers change device performance. In a solid-state DSSC we demonstrate the importance of the dye chemical structure and the anode fabrication process in dictating whether or not improvements achieved through the recombination suppression outweigh device current losses that result from the insertion of an insulating layer. We apply these lessons to a new barrier layer material, In_2O_3, that unlike Al_2O_3 has not been previously well-characterized but is less-insulating and can be grown at an extremely low growth rate, providing excellent control over the competing consequences of barrier layers. With In_2O_3 we are able to demonstrate some of the highest ever reported open-circuit voltages for this class of DSSC and we observe an unexpected change in behavior as the In_2O_3 barriers reach a certain thickness. In our third barrier layer study, we achieve a near-doubling in efficiency when Al_2O_3 is applied to a quantum dot-sensitized solar cell, a close analogue of the DSSC, wherein recombination more severely limits device performance.

In the second part of this work, we combine experimental and computational techniques to study the dye/anode interface and the orientation of dye molecules adsorbed on a TiO_2 surface. Near-edge X-ray absorption fine structure (NEXAFS) spectroscopy is used to measure the angles of individual bonds and in turn deduce the full geometry of adsorbed dye molecules. This result is compared to computational simulations using density functional theory-molecular dynamics (DFT-MD) of the same dye/TiO_2 system. Our results show remarkable correspondence between the experimental and computational approaches and signify important consequences for understanding the dye/anode interface in DSSCs as well as adsorbate/substrate studies more generally.

Acknowledgements

The work described in this dissertation represents the culmination of several years' effort. While not always clear from the finished product, this work was as much the result of false starts, dead ends, and unrelated detours through chemical engineering, physics, surface science, and chemistry as it was of the completed projects that constitute the primary chapters of this thesis. Making it through all of these aspects of the Ph.D. process (and making it out the other side) would not have been possible without contributions from a long list of people I would like to thank here.

First to thank is my advisor, Stacey Bent. Despite my minimal background outside of the biology end of the chemical engineering spectrum, Stacey was confident that my overarching interest in the energy arena would inspire my growth as a surface scientist, and I hope I was able to vindicate her trust. My research work was certainly not marked by early successes, and I very much appreciate Stacey's ability to prevent me from being discouraged by the slow progress during my first few years. Stacey was a great model for what a Ph.D. in the sciences ought to strive for. Working on dye (and quantum dot) sensitized solar cells was new for our lab, yet Stacey demonstrated how the important questions in DSSCs—as in any other field—can always be approached by asking how the fundamental processes at the molecular level control the behavior of large-scale systems. I would also like to thank the four other professors that served on my defense committee: Zhenan Bao, Chris Chidsey, Mike McGehee, and Alberto Salleo. Mike McGehee merits a great deal of thanks, as I spent the majority of my lab time with his group where I performed the solar cell fabrication and device-testing work. Mike was a great person to collaborate with, and I particularly appreciate his keen insight into the solar sector, from both the lab-scale and economy-wide ends of the spectrum—he is truly a solar guru. Mike does a great job facilitating collaboration as well, and the seamlessness with which I was able to work in his lab and with his graduate students went a long way to aiding my research.

I worked closely with several collaborators both inside and outside of the Bent group over the years. The Bent group I joined in 2008 has grown significantly in size during my time here. Much of what I learned in my early years was from my fellow

labmates, starting with our postdoc Jeff King and my fellow graduate students Xirong Jiang, Jess Kachian, Paul Loscutoff, Jonathan Bakke, Marja Mullings, and my classmate Nid Methaapanon. Jon Bakke was particularly instrumental in teaching me about atomic layer deposition and watching him build the Nona and TBSR reactors was one of the most educational experiences of my time here. Jon and I also collaborated significantly on both components of my thesis, working on metal oxide passivation layers and studying adsorbed dye layers at SSRL. The latter project was the source of many a memorable trip to the mysterious, James Bond-esque SSRL. It certainly would have been a struggle to work those long, bizarre synchrotron hours if I had not thoroughly enjoyed Jon's company. Jon proved to be a great mentor and source of conversation beyond the realm of ALD.

The work on DSSCs was first brought to Stanford by Brian Hardin and I-Kang Ding, both in the McGehee group and the work on DSSC and QDSSC devices in this thesis would not have been possible without their pioneering efforts. Brian and I-Kang provided much assistance in teaching me about DSSC device operation and fabrication (even if I could never truly match I-Kang's dexterity with a roll of Scotch tape). In addition to their own impressive DSSC results, Brian and I-Kang set the stage for many DSSC, QDSSC, and now PSSC research projects here at Stanford. I have also worked extensively over the years with their successors in the McGehee group, particularly George Margulis, Colin Bailie, and William Nguyen. George and Colin were really able to use their brief stints at EPFL to maximize their DSSC knowledge and the expertise they brought back with them (in addition to that which they already possessed) proved highly useful to everyone at Stanford interested in SSCs. In particular, they were instrumental in developing the transient photovoltage setup here which proved absolutely crucial in the recombination studies presented in this thesis. William is the namesake (and synthesizer) of the WN1 dye which factors into both halves of this thesis. Having the insight of an experienced chemist working on DSSCs was very valuable for all of us, and to that end, I would like to thank William's co-advisor Alan Sellinger as well. In addition to all of their assistance to my work, I very much enjoyed the time I spent working alongside George, Colin, and William. Given the large amount of time I spent in the McGehee lab, I would also like to thank many of the organic solar cell researchers

who I spent considerable time with. To mention just a few, George Burkhard, Eric Hoke (also of great assistance in the transient photovoltage setup), Jason Bloking, Zach Bailey, Toby Sachs-Quintana, Tomas Leijtens, Sean Sweetnam, and Billy Mateker all were valuable sources of help around the lab and great sources of conversation over the years.

On the quantum dot front, I worked very closely with two of my fellow Bent group members, Pendar Ardalan and Katie Roelofs. Pendar developed the SILAR and ALD processes for growing CdS quantum dots, and I was happy that some of the struggles I had getting SAMs to work in dye cells were able to help out Pendar's QDSSCs with much less difficulty. It should also be noted that Pendar set the bar for post-graduation travel at a height that may never be equaled, and his epic journeys are the source of great inspiration at this point in the Ph.D. process. Katie Roelofs took up the QD work in our group after Pendar's departure and she has been a great person to collaborate with over the past three years. As I taught Katie about the SSC work in our lab, she was always quick to provide an excellent question that really made me think critically about the various assumptions we utilize in our projects. Many of the projects and concepts discussed in this thesis will be continued in Katie's work, and I look forward to seeing what questions my fellow Tiger is able to answer in the SSC field.

In addition to the Bent group members that preceded me, I greatly benefited from working with several members that joined the group after I did; in approximately chronological order: Han Zhou, Keith Wong, Steve Herron, Art Wangperawong, Bo-Ram Lee, Sang Wook Park, Katie Pickrahn, Bonggeun Shong, Jukka Tanskanen, Yesheng Yee, Carl Hagglund, (the afore-mentioned) Katie Roelofs, Jon Servaites, Nuoya Yang, Scott Geyer, Chaiya Prasittichai, Fatemeh Hashemi, Rich Johnson, Adam Hultqvist, Pralay Santra, David Bergsman, and Axel Palmstrom. Katie Pickrahn, in addition to being a fantastic group social chair, did an excellent job maintaining the TBSR reactor, which was used to deposit the DSSC barrier layers. Jon taught her well, and always having this reactor available made planning device-making extremely easy. Jukka, probably the Bent group's first two-time post-doc, has been an invaluable collaborator. Jukka's expertise in quantum chemical calculations has been a tremendous asset for practically every Bent group member by this point. In the In_2O_3 and dye orientation

projects discussed in this dissertation, the insight gained from his work is invaluable. Jukka is also a great person to work with and I have enjoyed spending a good bit of time with him during his two stints in California. Two other post-docs in the group with previous experience in DSSCs, Carl and Chaiya, provided much helpful guidance over the past few years, and I thank them for much useful discussion. Along with Marja, Carl and Chiaya were probably my longest-standing officemates and we spent a great deal of time discussing non-lab stuff together as well (most frequently nutrition, coffee, and exercise). I would also like to mention two other post-docs, Pralay and Eva Unger (in the McGehee group), with whom I overlapped only briefly, but whose insight and helpful discussion I am very thankful for. I wish we had overlapped for a longer time, but Stanford is lucky to have both of them in the future.

I had the good fortune to collaborate on many different research projects over the years with groups both inside and out of Stanford. Katie and I worked with Orlando Trejo and John Xu, mechanical engineers in the Prinz group, on PbS quantum dots. I am hoping we are able to continue work in this area in the future, as we thought up many unique project possibilities that have yet to be pursued. Jon Bakke and I worked with Cong Trinh of the Thompson group down at USC on organic photovoltaics. This collaboration, which was facilitated by our funding organization, CAMP, provided a nice way for Jon and I to learn more about organic solar cells and we are glad our ALD coatings could proved for Cong. I would like to thank Rajib Mondal, a post-doc in the Bao group, for two things in particular: pointing out to me a new dye, YE05, that had recently been published, and then going ahead and synthesizing it for me. While we were never able to fully figure out the covalent dye linking project, using YE05 as an alternative to Z907 definitely got us further on down that road and also provided a helpful metric as an alternative to Z907 in device testing. Jon and I worked with many researchers at the Stanford Synchrotron and Radiation Laboratory (SSRL) over the years. Mike Toney spearheaded our project on examining the orientation of dye molecules. Although our work with XRR with Chad Miller and Chris Tassone did not pan out due to the thinness (and relative roughness) of our layers, I very much appreciate the time they took to work with us on our rather-difficult system. Dennis Nordlund is the NEXAFS expert at SSRL and without him the work on dye orientation would not have been

possible. Over the past several years I pestered Dennis innumerable times for help with NEXAFS data normalization and the like and he always responded if not hastily but extremely thoroughly—working with Dennis has certainly set the bar rather high for me when I hear the phrase "long meeting". I very much appreciate his patience over the years in explaining and (re-explaining) how NEXAFS works, how to do the experiments down at SSRL, and how to normalize and interpret the data, as well as his patience with our project's ambiguous results early on (with ruthenium dyes) that eventually yielded some very interesting conclusions.

During my time, I was also able to mentor several younger students doing summer research or rotations. Alas, much of the straightforward progress came during the last couple of years of my Ph.D. so I did not always have a clear project to guide them on. Regardless, all of these students were able to get some great work done, and I enjoyed working with all of them. Guarav Giri worked on the SAM project in its early days; Jon Proctor spent a summer looking at dye FTIR spectra; Priscila Barba worked on dye desorption measurements; Stephen Fried worked on the dye amide linking project and was a truly excellent tutor to me in organic chemistry; Juan Dominguez worked on devices with me and provided invaluable work on the QDSSC project under Katie's tutelage.

The Stanford Chemical Engineering Department provided invaluable help over the years. The staff does an excellent job taking care of you over the years and making sure everything is taken care of. I would like to thank Jeanne Cosby for welcoming me in as a prospective and first-year student and then, just a "couple years" later, making sure I had everything in line to graduate. Stauffer III could not operate without the work of Pam Juanes, Jeannie Lewandowski, and Pamela Dixon. I would especially like to thank Jeannie for all the purchasing questions over the years—I know I had some tricky ones between buying dyes from Australia and software from Europe. I would also like to thank the professors in the department for creating a very welcoming environment at Stanford and for being excellent teachers. I truly enjoyed the classes I took in my first two years here and definitely felt I was a better all-around chemical engineer for having taken them. I would like to thank Tom Jaramillo and Zhenan Bao for being my rotation

hosts in my first two quarters, I enjoyed working in both of their labs and the experience proved highly useful in my later research. To go one step further back, I would also like to thank the Chemical Engineering Department back at Princeton, and in particular my senior thesis advisor David Wood, for providing the basis for and inspiring me to pursue the ChemE path, a major I had not even strongly considered (or known much about) prior to college.

Cutting edge research in the field of nanotechnology is not an inexpensive undertaking. Two different sources of funding were critical in getting me and my projects through the last several years. I would like to thank the Hewlett family for their support through the Albion Walter Hewlett Stanford Graduate Fellowship which provided for my tuition and stipend for three years. My research funding was provided by the Center for Advanced Molecular Photovoltaics (CAMP) which was funded through a substantial (and perfectly-timed) five-year grant by the King Abdullah University of Science and Technology (KAUST) in Saudi Arabia (Award No. KUS-C1-015-21).

Outside of the direct interactions with colleagues and collaborators, there are many others whose friendship and support has been a very important part of my life over the last several years. Prior to even arriving at Stanford in the fall of 2007, I felt that I had already met many friends via the recruiting process. The older graduate students in the department were extremely welcoming and I developed many friendships that outlasted the years we overlapped. Bobby Feller is a stalwart of the fall football tailgating season (even if I see him much less in the ski/snowboard season that follows). Although Randy Lowe now lives in the southwest, I still get to see him when Stanford Football and his Bay Area travels allow. John Welsh was my Stanford "recruiting buddy" and we were able to bond over our identical middle names and shared Heps running background. John was one of my best friends at Stanford, and although he is now on the East Coast, he has served invaluably as someone I can harass via email with football or track article links I find online. It was also during the recruiting process—down in Austin, in fact, before Stanford—that I met my future roommate of four years, Nick Cordella. Nick and I quickly became close friends at Stanford. In addition to being a great roommate and a very funny guy, Nick was even more dedicated to Stanford sports

than me. When Nick and I moved off-campus after three years in Rains we were joined by two electrical engineers, Alok Vasudev and Paul Cristman. Although Alok would leave us after a year to "get married," this at least allowed the four of us to cap off our year together at an Indian wedding in Texas. Paul and I lived together another two years after that along with another electrical engineer, Mark Baybutt. Despite Mark being an Ohio State fan, he has been a great roommate for Paul and me (we at least have a two-thirds Penn State-fan-majority), although much like Bobby, the amount I see Mark diminishes after the football season, as he quickly enters the skiing/mountaineering/camping-in-the-snow season.

In addition to my roommates at Stanford, two of my roommates from Princeton ended up Bay Area grad students as well. Jonathan Charlesworth was my roommate for three years in college and he ended up doing his Ph.D. not too far away at UCSF. Although he has since made his way first to LA and now to Boston, overlapping for five years was a "good look," as JC would call it. We were joined for two years by our junior and senior year roommate, Clarke Smith, who got his MBA at Stanford. While the hard work of "networking" and travelling the world that all GSB students must go through prevented me from seeing Clarke as much as perhaps I expected, it was great to have him out here, even if he remains an East Coaster at heart. I would also like to recognize my other roommates from junior and senior year, all of whom made visits out to Stanford over the years: Jeff, Bryan (who is really cutting it close coming two weeks before graduation), Rob, Rob, Kenny, and Logan. While their visits were brief over the grand scheme of six years, they were all constant email contacts over the years (and to which I should also add my college friends Cam, Blake, Greg, and Cody) and their friendship is much appreciated. There are too many more friends at Stanford to all thank individually, but I would like to single out Jayson Jia and Hart Montgomery with whom I spent much time with over the years.

Obtaining a Ph.D. is not the sort of thing that comes out of nowhere. Rather, the foundations are developed over decades, and it is for this that I must thank my parents. From an early age, my parents not only demonstrated the value of hard work and learning, but also encouraged my natural curiosity and engineering bent (and here I must

also thank my five older siblings—Kristin, Jennifer, John, Courtney, and Kathryn—for encouraging/tolerating their nerdy younger brother). There was nothing my parents would not have done to further my education, and in addition to that, they were always present in my life, picking me up from innumerable sports practices and attending so many track meets over the years, and simply being around the house (even if they were often working).

Finally, I would like to thank my long-time girlfriend and now-fiancé Liz. Not only did Liz have the patience and fortitude to date a poor grad student living across the country for two years, but then after her own graduation, she moved to the West Coast without the obvious security of a grad school program like I had in my move. Not only did Liz have the wisdom to enter the downstream rather than upstream part of the solar industry, she has also been an incredibly supportive girlfriend and companion over the years. Liz has seamlessly interacted with more engineering grad students than one ought to have to, and she has been the most important part of my life in California. To her I give my thanks and a promise to, one day, even get a job in the real world.

Table of Contents

List of Figures xix

List of Tables xxxix

Chapter 1. Introduction & Background 1

1.1. Research Goals & Dissertation Outline 1

1.2. The Global Energy Landscape 4

1.3. Solar Cells (Photovoltaics) 7

1.4. Dye-Sensitized Solar Cells (DSSCs) 11

1.4.1. History and Background 11

1.4.2. Recombination in DSSCs 17

1.4.3. Recombination Barrier Layers 21

1.4.4. Dye Orientation 22

1.4.5. Quantum Dot-Sensitized Solar Cells (QDSSCs) 24

1.5. Collaborations & Copyright 25

1.6. References 26

Chapter 2. Experimental Methods 34

2.1. Atomic Layer Deposition (ALD) 34

2.2. Auger Electron Spectroscopy (AES) 37

2.3. Fabrication of Sensitized Solar Cells 39

2.4. Solar Cell Testing: Current-Voltage Curves 44

2.5. Transient Photovoltage & Photocurrent Measurements 46

2.6. Near-Edge X-Ray Absorption Fine Structure (NEXAFS) Spectroscopy 50

2.7. Quantum Chemical Calculations 53

2.7.1. Background 53

2.7.2. Relevance of Quantum Chemical Calculations to this Dissertation 56

2.8. References 57

Chapter 3. The Importance of Dye Chemistry and $TiCl_4$ Surface Treatment in the Behavior of Al_2O_3 Recombination Barrier Layers Deposited by Atomic Layer Deposition in Solid-State Dye-Sensitized Solar Cells 59

3.1. Introduction 59

3.2. Experimental Section 63

3.2.1. Nanostructured TiO_2 Substrates 63

3.2.2. ALD of Al_2O_3 63

3.2.3. ss-DSSC Device Fabrication 64

3.2.4. Device Measurements 65

3.3. Results & Discussion 67

3.3.1. Archetypal ss-DSSC 68

3.3.2. ss-DSSC with a thick (4.2 μm) TiO_2 active layer 69

3.3.3. Effect of Al_2O_3 barrier layers on TiO_2 not treated with $TiCl_4$ 72

3.3.4. An alternative ruthenium dye 74

3.3.5. Modeling J_{SC} as a function of Al_2O_3 growth behavior 78

3.4. Conclusions 82

3.5. Collaborations & Copyrights 83

3.6. References 84

Chapter 4. TiO_2 Conduction Band Modulation with In_2O_3 Recombination Barrier Layers in Solid-State Dye-Sensitized Solar Cells 88

4.1. Introduction 88

4.2. Materials & Methods 92

4.2.1. Preparation of Nanoporous TiO_2 Substrates 92

4.2.2. Atomic Layer Deposition and Characterization of In_2O_3 92

4.2.3. SS-DSSC Device Fabrication 93

4.2.4. Device Measurements 94
4.2.5. Computational Studies 95
4.3. Results & Discussion 96
4.3.1. Growth of In_2O_3 and Device Performance 96
4.3.2. Analysis of In_2O_3 Devices 101
4.3.3. Mechanisms of Recombination Rate Changes 107
4.4. Conclusions 112
4.5. Collaborations & Copyrights 113
4.6. References 114
Chapter 5. Efficiency Enhancement of Solid-State PbS Quantum Dot-Sensitized Solar Cells with Al_2O_3 Barrier Layer 118
5.1. Introduction 118
5.2. Experimental Details 121
5.2.1. Fabrication of Nanostructured TiO_2 Substrates 121
5.2.2. Atomic Layer Deposition of PbS and Al_2O_3 122
5.2.3. QDSSC Device Fabrication 124
5.2.4. Device Testing 124
5.2.5. Characterization via Transmission Electron Microscopy (TEM) and UV-Vis Spectroscopy 125
5.3. Results & Discussion 126
5.4. Conclusion 133
5.5. Collaborations & Copyrights 134
5.6. References 134
Chapter 6. The Dynamical Orientation of Large Molecules on Oxide Surfaces and its Implications for Dye-Sensitized Solar Cells 138
6.1. Introduction 138

6.2. Results & Discussion 144

6.2.1. Experimental and Simulated X-Ray Absorption Spectrum of WN1 Dye and Measured Orientation 144

6.2.2. Implications for DFT Simulations as a Predictive Tool for Device Performance 153

6.3. Conclusions 155

6.4. Materials & Methods 155

6.4.1. Fabrication of TiO_2-Dye Substrates 155

6.4.2. NEXAFS Measurements and Spectra-Fitting 156

6.4.3. Computational Details 157

6.5. Collaborations & Copyrights 160

6.6. References 160

Chapter 7. Conclusions & Outlook 164

7.1. Summary of Dissertation 164

7.2. Outlook on the Future of Sensitized Solar Cells 166

7.3. References 169

Appendix A: Phosphonic Acid SAM Recombination Barrier Layers 170

A.1. Introduction 170

A.2. Selection of Phosphonic Acids 171

A.3. Dye Adsorption on SAM-Coated TiO_2 174

A.4. Activation of Carboxylic Acid Groups 176

A.4.1. DCC/NHS Activation 176

A.4.2. EDC/NHS Activation 178

A.5. Conclusion 179

A.6. Outlook 180

A.7. Collaborations 180

A.8. References 180

Appendix B: CdS QDSSC Interface Engineering 182

B.1. Introduction 182

B.2. CdS QDSSCs with Phosphonic Acid SAMs 182

B.3. CdS QDSSCs with Al_2O_3 Barrier Layers 183

B.4. Growth of CdS QDs via Atomic Layer Deposition 184

B.5. Collaborations & Copyrights 185

B.6. References 185

Appendix C: NEXAFS Studies on Ruthenium Dyes 187

C.1. Introduction 187

C.2. Experimental Details 188

C.2.1. Metal Oxide Fabrication 188

C.2.2. Adsorbate Deposition 188

C.2.3. NEXAFS Experiments 189

C.3. Results & Discussion 190

C.3.1. *p*-Aminobenzyl Phosphonic Acid (ABPA) 190

C.3.2. Bi-isonicotinic Acid (BINA) 191

C.3.3. $Co(NCS)_2$ and Cu(NCS) 194

C.3.4. 2-(2,4-difluorophenyl) Pyridine 195

C.3.5. Z907 and YE05 Dye Powder 195

C.3.6. Dyes Adsorbed on Metal Oxide Substrates 196

C.3.7. Chenodeoxycholic Acid 199

C.4. Conclusions and Outlook 200

C.5. Collaborations 200

C.6. References 201

List of Figures

Figure 1-1: World energy production from 1965-2011, broken down by source, in terms of average power output. 1 TW of average output is equivalent to 8766 TWh or 29.9 quadrillion BTUs per year. Note that the values in the plot represent the energy released upon combustion (for example in the instance of coal), not the amount of energy successfully converted into electricity. Contributions from solar, wind, and "other" (which includes sources such as biofuels and geothermal energy production) are too small to see in the plot. In 2011, coal, oil, and natural gas accounted for 31%, 33%, and 24%, respectively, of world energy production. Data taken from the BP Statistical Review of World Energy 2012 [3]. 5

Figure 1-2: Cumulative global anthropogenic CO_2 emissions from fossil fuel combustion from 1965 - 2011 with three different future emission scenarios: one in which CO_2 emissions remain constant at 2011 levels, one in which the emissions rate continues at the linear growth rate it has followed since 1965, and one in which it follows the "A2" scenario outlined by the Intergovernmental Panel on Climate Change (IPCC) in 2000 and which emissions have closely matched from 2001-2011 [5]. The pink region identifies an uncertainty range of CO_2 cumulative emissions likely to lead to an atmospheric CO_2 concentration of 450 ppm, which is deemed necessary to, as likely as not, maintain net global warming below 2 °C [4]. The inset shows global CO_2 emissions per year from 1965-2011 along with the three future emission scenarios. CO_2 emissions data from 1965 – 2011 was taken from the BP 2012 Statistical Review [3] and emissions pre-1965 were taken from Boden *et al.* [6]. Note that the emissions targets technically refer to "CO_2-equivalent" concentrations to encompass other anthropogenic sources that either increase (*e.g.* methane) or decrease (*e.g.* aerosols) the net warming effect. Because at current levels these other forces approximately cancel out, the targets can be simplified and stated in terms of CO_2 [4]..... 6

Figure 1-3: Installed world photovoltaic capacity in MW from 1996-2011. The compound annual growth rate was 40% during this time period. Data taken from the BP Statistical Review of World Energy 2012 [3]. 7

Figure 1-4: Diagram of the *pn*-junction used in traditional inorganic photovoltaics. In a.), an *n*- and a *p*-type semiconductor are shown (with the same bandgap, typically indicative of different doping levels of the same material) with CB and VB indicating their conduction and valence bands, respectively, and E_F indicating the Fermi level in each semiconductor, which is a function of the doping levels. A *pn*-junction is formed as the two materials are brought together in b.), and the Fermi level is equalized across the two materials. In c.) a bias, V, is applied and the junction is no longer at equilibrium, resulting in the formation of quasi-Fermi levels (E_{Fp}, E_{Fn}) on each side of the junction. The junction is illuminated in d.); absorption of a photon results in an electron (green circle) being excited from the VB to the CB, leaving behind a positively-charged hole (red circle) in the VB. The electron-hole pair (or exciton) diffuses until it reaches the junction boundary in e.) where the electric field drives the separation the exciton. The electron is collected at the right contact (not shown) in f.) where it then proceeds to flow through a work-producing circuit (e.g. a light bulb) before reaching the left contact (not shown) where it will recombine with a hole, returning the solar cell to the state shown in d.). The amount of energy that can be extracted from each electron is a function of the applied voltage, V. 9

Figure 1-5: The AM 1.5G solar spectrum up to 1600 nm divided into the ultraviolet (UV), visible, and infrared ranges with the y-axis indicating the amount of power for a given wavelength of light. “AM” stands for “air mass”: AM 0 corresponds to the solar spectrum outside the Earth’s atmosphere while AM 1.0 indicates the light has passed through the length of atmosphere as if the sun were directly overhead. AM 1.5 well approximates the average atmospheric length sunlight travels through in order to reach Earth’s mid-latitudes. The dips in the spectrum correspond to the absorption of light by atmospheric gases such as O_2 (~760 nm) and H_2O (~950, ~1150, ~1300 nm). The AM 1.5G spectrum is available from the National Renewable Energy Laboratory [18]..... 10

Figure 1-6: Schematic of an archetypal dye-sensitized solar cell (DSSC). Starting with a glass substrate coated with the transparent conductor fluorine-doped tin oxide (FTO), a nanoporous TiO_2 film ~1 – 20 μm thick is deposited to serve as the photoanode. Dye molecules are then adsorbed onto the TiO_2 surface, typically through a solution-based process, to form a thin monolayer ~1 nm thick. The pores of the TiO_2 are then filled with the hole-transport material (HTM) which can be either liquid-based or solid-state. Finally, a back electrode is deposited; back electrodes are typically a thin metal film and material choice is related to the HTM. The schematic also identifies the basic light absorption and charge collection pathways: light shines through the transparent front electrode and is absorbed by a dye molecule, generating an excited electron-hole pair. The electron is injected into the TiO_2 where it diffuses to the front electrode while the hole diffuses through the HTM to the back electrode..... 12

Figure 1-7: Structures of the ruthenium dye N3, a.), organic D-π-A dye Y123, b.), and zinc porphyrin D-π-A dye YD2-*o*-C8, c.)..... 14

Figure 1-8: The solid-state organic hole-transport material spiro-OMeTAD (2,2',7,7'-tetrakis-(N,N-di-p-methoxyphenylamine)-9,9'-spirobifluorene). Spiro-OMeTAD, sometimes abbreviated as “spiro”, was used in the DSSCs fabricated in this thesis..... 16

Figure 1-9: Desirable (black) and undesirable (red) charge transfer processes at the Photoanode/Dye/HTM interface in a DSSC with a TiO_2 photoanode. In a.), light absorption excites an electron from the ground state to the excited state of a dye molecule (process 1). From the excited state, the electron can be injected into the TiO_2 (process 2), relax back to the ground state without being injected (process 4), or recombine with a hole in the HTM (process 5). Process 3 indicates the reduction (or regeneration) of the oxidized dye molecule by the HTM. B.) shows the possible recombination processes of an electron in TiO_2 with either an oxidized dye molecule (process 6; note the positive charge on the dye molecule implies here that process 3 has not yet occurred) or the HTM (process 7). Both processes 6 and 7 can originate with either conduction band electrons (as shown) or electrons residing in mid-bandgap states, which are indicated by the dashes

inside the TiO_2. The density of these states declines exponentially away from the conduction band. In a typical DSSC, process 2 is typically much faster than processes 4 and 5, which yields high electron injection efficiencies. Because dye regeneration (process 3) is rapid, process 6 is not significant in DSSCs and is typically ignored, but process 7, particularly when HTMs other than the iodide/triiodide redox couple are used, is important. 18

Figure 1-10: Schematic (not to scale) of the filling of mid-bandgap trap states in TiO_2 as a bias is applied to a solid-state DSSC. Empty states are indicated by dashes inside of the TiO_2, while the filling of these states is indicated by solid blue. The device voltage is equal to the potential difference between the Fermi level, E_F, inside the TiO_2 and the highest occupied molecular orbital (HOMO) of the hole-transport material (HTM). The highest achievable V_{OC} ($V_{OC\text{-}MAX}$) is limited by the TiO_2 conduction band level and HTM HOMO. 20

Figure 2-1: Schematic demonstrating the steps of the atomic layer deposition (ALD) process for a binary compound. In Step 1, a cleaned substrate is exposed to reactants (often in the presence of the purge gas or some other carrier gas) which bind to reactive surface groups (*e.g.* hydroxyl groups) but not each other. The reactant (like the counter-reactant) often consists of the desired element bound to ligands. In Step 2 the reactant dosage has ended and an inert purge gas is used to remove any residual reactant molecules along with ligands separated from adsorbed reactants. In Step 3 the counter-reactant is dosed into the chamber (again, often in the presence of the purge/carrier gas) and these molecules adsorb to surface-bound reactant molecules (but do not bind to each other). In Step 4 the reactor is again purged to remove residual counter-reactants and separated ligands, leaving an exposed counter-reactant surface which is ready to bind reactant molecules. Step 5 indicates the repeating of Steps 1 – 4 until the desired thickness is reached..... 35

Figure 2-2: Basic schematic of the "TBSR" hot wall tube reactor used to perform ALD in the DSSC barrier layer experiments described in this thesis. A computer graphical

interface is used to control most of the reactor conditions and automate the ALD process. Nitrogen carrier gas (it is also the purge gas) is introduced at the front of the reactor, near the loading door, upstream of the precursor (*i.e.* reactant/counter-reactant) lines and the substrates to be coated, which are located in the reactor body. The nitrogen flow is regulated by a mass flow controller. Several precursor manifold lines ("P") (and a pressure sensor, not shown) are oriented radially outward from the chamber, downstream of the N_2 and upstream of the reactor body. While only one valve is shown for the precursor line, in fact each precursor line has three valves: a manual valve, a needle valve to fine-tune the precursor doses, and a pneumatic ALD valve controlled by the computer interface. The vacuum pump, located downstream of the reactor body, pulls out excess precursors, reaction byproducts, and the purge/carrier gases while maintaining a reactor pressure ~100 mTorr during typical operation. Note that thermocouples and heat tape, which work with the computer program to regulate the temperature of the reactor body and precursor lines, are not shown. 37

Figure 2-3: Illustration of the relevant electron movements in an oxygen atom in X-ray photoelectron spectroscopy (XPS), Auger electron spectroscopy (AES), and X-ray fluorescence (XRF). Final states for each process are located below the dotted line. Filled green circles indicate electrons in the ground state in an oxygen atom while empty green circles indicate generated holes. The orbital naming conventions for AES and XRF are located on the left and those for XPS on the right. In XPS an X-ray is used to eject a core electron leaving a core-hole. The measured kinetic energy of the ejected electron is a function of both the incident X-ray energy and the binding energy of the core electron. Both the non-radiative Auger decay process (AES) and radiative fluorescent decay process (XRF) begin with the core-hole/final XPS state (note: in AES and XRF an electron beam rather than an X-ray can be used to generate the core-hole). In Auger decay an electron in a higher energy orbital falls down into the core-hole; the electron's resultant energy loss, if sufficiently high, can be imparted to another electron (the "Auger electron") and eject it from the oxygen atom. The process shown in this schematic would be labeled "KL_IL_{III}". In XRF, a photon rather than an Auger electron is released as the L_I electron falls into the core-hole. Note than in both AES and XRF, unlike in XPS, the

energy of the measured electron/photon is independent of the energy of the X-ray/electron used to generate the core-hole. 39

Figure 2-4: Fabrication scheme (not to scale) of DSSCs beginning with a 5 x 7.5 cm fluorine-doped tin oxide (FTO)-coated glass substrate (a) (Pilkington Glass, 15 Ω/□). A small strip of FTO in the middle of the substrate is etched using Zn powder and 4 M HCl, leaving (b). This step simplifies measurement of device area. A compact TiO_2 layer (~50 – 100 nm thick) to block recombination between FTO and spiro-OMeTAD is deposited by spray pyrolysis and annealed (c). The edges are masked in order to prevent deposition of TiO_2 atop the FTO contact, which may increase series resistance. A nanoporous TiO_2 layer (~2 μm thick) is added by doctor-blading a commercial paste (Dyesol) and annealing. Following a $TiCl_4$ chemical bath treatment, deposition of any metal oxide barrier layer, and sensitization (using either dye molecules or quantum dots) (not shown), pore-filling is performed by spin-coating a solution of spiro-OMeTAD in chlorobenzene, resulting in (e). Finally, a back silver electrode (~200 nm thick) is deposited by thermal evaporation under ultra-high vacuum; arrows indicate the direction of electron flow in a working device. Note that the dotted lines in (e) and (f) indicate that at this point in the fabrication process (specifically after the $TiCl_4$ chemical bath step) the larger 5 x 7.5 cm substrate has been cut into approximately 10 smaller substrates ~1.5 x 2 cm. Also note that the device schematics here are "upside-down" in the sense that while operating, the sun/light source would be below the glass; silver then serves as both the back electrode and a light reflector. 44

Figure 2-5: Photo of a completed DSSC substrate (~2 μm-thick TiO_2 active layer, WN1 dye) with five discrete devices defined by the Ag back electrodes. Note that the actual device areas are less than the full 16 mm^2 area of the Ag electrodes due to the etched FTO area (not visible in the photograph, but easily discernible by eye). 44

Figure 2-6: Examples of typical light and dark current density-voltage (*J-V*) curves for a solar cell in the light and in the dark. A solar cell is typically characterized by three metrics, the open-circuit voltage (V_{OC}), short-circuit current density (J_{SC}), and the fill

factor (not shown). The maximum power value (P_{MAX}, which is the product of associated current (J_{MP}) and voltage (V_{MP}) values) is related to the J_{SC} and V_{OC} through the fill factor, which is equal to the fraction of P_{MAX} over (J_{SC}*V_{OC}). An efficiency value for the solar cell can be calculated by dividing P_{MAX} by the light incident on the solar cell. In the *J-V* experiments described in this dissertation, a solar simulator utilizing a xenon arc lamp was used to mimic the Air Mass 1.5 G (AM1.5G) spectrum (see Figure 1-5). 46

Figure 2-7: Schematic of the equipment used to collect transient photovoltage measurements. A LabVIEW computer program is used to send commands to and receive data from the Circuit Specialists CSI3644A programmable power supply, Agilent 3300 function generator, Tektronix oscilloscope, and Keithley 2400 sourcemeter. The programmable power supply sets the bias light output. A function generator drives the LED pulse lamp and sends a timing trigger to the oscilloscope, which locks in the device voltage signal (note: in transient photocurrent measurements, a transimpedance amplifier connects the device current signal to the oscilloscope). The sourcemeter maintains the device at the desired current level (or voltage level in transient photocurrent measurements). 47

Figure 2-8: a.) Raw data along with a fitted curve for a transient photovoltage experiment. As the device current is kept constant, the pulse LED light results in an increased photovoltage (ΔV) which gradually disappears when the pulse light is turned off due to recombination of charge carriers. The transient data is fitted to an equation of the form $V(t) = V_0 + A*\exp(-t/\tau_R)$ where "A" is a pre-exponential factor and "τ_R" is the recombination lifetime; a shorter lifetime results in a faster decay of the photovoltage. b.) Differences in recombination lifetime are often readily apparent in the raw transient photovoltage data. In this example, photovoltage decay curves are shown for otherwise-identical solid-state DSSCs with 0, 1, and 3 ALD cycles of Al_2O_3 used as a recombination barrier layer at comparable photovoltages. Al_2O_3 increases the recombination lifetime, stretching out the photovoltage decay curves; more Al_2O_3 (*i.e.* a thicker recombination barrier layer) results in a larger lifetime enhancement. 48

Figure 2-9: Schematic demonstrating the meaning of device capacitance in two SSCs with TiO_2 photoanodes where a photoanode conduction band (C.B.) shift has occurred in one of the two devices. In a.), the filling of bandgap states in the TiO_2 as a voltage is applied is evident. In comparing the device on the left to the device on the right wherein the TiO_2 C.B. has been lowered, it is clear that at a given voltage fewer states are filled when the C.B. is higher. In b.) an additional pulse light (*e.g.* as in transient measurements) is turned on resulting in more electrons injected into TiO_2. Assuming that these charge carriers cannot be extracted from the device (as in transient photovoltage measurements), this results in an increase in the device photovoltage. Given the exponential distribution of TiO_2 bandgap states, for a given number of newly injected electrons (*i.e.* ΔQ) a device with a higher C.B. (left device) will undergo a larger increase in photovoltage (ΔV) than the device on the right with the lower C.B. As capacitance is defined by $\Delta Q/\Delta V$, the left device with the larger ΔV will have a lower differential capacitance at V_0 than the right device. 50

Figure 2-10: Simplified nitrogen K-edge NEXAFS spectrum demonstrating the relative energies and peak widths associated with excitation of core electrons into unoccupied π* and σ* orbitals as well as to the vacuum (indicated by the sharp ionization edge). When present in the molecule, π* orbitals are typically found below the ionization potential and have sharper peaks than the σ* transitions which are typically located at energies near or above the ionization potential. The intensity represented on the y-axis is effectively "counts per second" of whatever is being measured—*e.g.* Auger electrons, all electrons ("total electron yield"), photons—while the x-axis indicates the energy of the incident X-rays. The deconvolution of the total spectrum into discrete Gaussian (or Lorentzian) peaks (*i.e.* the dotted lines) as shown in the plot also indicates the manner in which spectra can be fitted for angle-resolved NEXAFS studies..... 52

Figure 2-11: Schematic of the basis behind angle-resolved NEXAFS studies. The probability of an atomic core electron being excited into an unoccupied molecular orbital—here drawn schematically as a π* orbital perpendicular to the plane of the adsorbate—is a function of the overlap of the electric field component of the incident,

polarized X-ray and the unoccupied orbital. As NEXAFS measures the intensity (*i.e.* frequency) of these transition, a larger peak results from the left (green) measurement where there is excellent overlap between the π* orbital and the electric-field component of the X-ray than in the right (orange) measurement where the substrate has been rotated relative to the X-ray source and there is less overlap. A representative plot of the resultant peaks showing intensity as a function of the photon energy (typically plotted in eV) is shown to the right. 53

Figure 3-1: Cross-sectional Auger electron spectroscopy line-scan after 10 ALD cycles of Al_2O_3 on a ~5 μm thick nanoporous TiO_2 film on a Si substrate. The line scan was performed through the middle of the scanning electron microscopy image, i.e. the 50% atomic concentration line. While the exact atomic concentration is subject to instrument sensitivity limits and baselines chosen, the data clearly indicate uniform growth of Al_2O_3 throughout the 5 μm thick TiO_2 film. 64

Figure 3-2: The three dye molecules used in the different studies: Z907, commonly used in ss-DSSCs; YE05, a Ru dye without isothiocyanate ligands that has demonstrated high efficiencies in liquid cells; WN1 a D-π-A metal-free dye with a cyanoacrylic acid attachment group. 66

Figure 3-3: Current Density-Voltage (*J-V*) curves for high performing 2 μm-thick devices with the Z907 dye as a function of the number of ALD cycles of Al_2O_3. Under 1 sun of illumination, (a), J_{SC} is reduced with thicker Al_2O_3 layers as electron injection is suppressed, while V_{OC} rises and then falls back down as the reduction in dark current is counteracted by the drop in photocurrent. In the dark, (b), onset of current occurs at higher voltages as more Al_2O_3 is deposited. 68

Figure 3-4: Electron lifetimes near the V_{MAX} (typically ~0.6 V depending on the number of ALD cycles) and V_{OC} of 2 μm thick Z907 $TiCl_4$-treated devices. Data represents the average of a subset of high-performing devices for which transient photovoltage measurements were performed. Error bars indicate standard deviations. 69

Figure 3-5: Electron Lifetimes for Z907 devices with thick TiO_2 active layers. Error bars indicate standard deviations. 70

Figure 3-6: Device efficiency of "normal" thickness (~2.2 μm) devices and devices with thick (~4.2 μm) active layers as a function of the number of ALD cycles. Thicker devices had somewhat higher efficiencies overall but the same overall trend of decreasing efficiency with increasing number of ALD cycles. Error bars indicate standard deviations. 71

Figure 3-7: J_{SC} as a function of the number of Al_2O_3 ALD cycles for devices that did and did not undergo the $TiCl_4$ treatment. Whereas for control devices without Al_2O_3 the $TiCl_4$ treatment improves J_{SC} ~35%, the $TiCl_4$ treatment has no effect on J_{SC} in devices with subsequent Al_2O_3 deposition. Error bars indicate standard deviations. 73

Figure 3-8: Electron lifetimes for devices with the Z907 dye without the $TiCl_4$ treatment for different numbers of ALD cycles. Error bars indicate standard deviations. 74

Figure 3-9: J_{SC}, normalized to devices with no Al_2O_3 recombination barriers, for the three dyes studied in ~2.2 μm $TiCl_4$-treated devices. The drop in current as more Al_2O_3 is deposited is much less severe with the WN1 D-π-A dye than with the two Ru dyes. 75

Figure 3-10: Electron lifetimes for devices with the YE05 dye for different numbers of ALD cycles. Error bars indicate standard deviations 76

Figure 3-11: Electron lifetimes for devices with the WN1 dye for different numbers of ALD cycles. Lifetimes are higher than in cells with Ru dyes, consistent with the higher V_{OC}'s observed in WN1 devices. Error bars indicate standard deviations 77

Figure 3-12: Comparison of the model for electron injection efficiency with experimentally-observed J_{SC}, normalized to devices without Al_2O_3, averaged over three trials using Ru dyes (Z907 on 2.2 and 4.2 μm active layers and the YE05 dye). The

model assumes the Al_2O_3 layer grows *via* an island process and therefore has a varying thickness at each cycle number. This model compared to one assuming uniform Al_2O_3 growth of complete layers at two different growth rates. Injection efficiency is also normalized to the Al_2O_3-free system, for which the kinetic rate constants yield a 99% injection efficiency..... 82

Figure 4-1: Cross-sectional Auger electron spectroscopy (AES) scan of 20 ALD cycles of In_2O_3 grown on a nanoporous TiO_2 substrate. The figure indicates that the ALD precursors are able to penetrate more than ~2 μm (the thickness of devices) into the nanoporous TiO_2 substrate. ALD was performed using the same conditions as used for the devices: 230 °C reactor temperature with pulse times of 10, 12 s and purge times of 30, 45 s for trimethylindium and H_2O, respectively. 93

Figure 4-2: TEM image of TiO_2 nanoparticles coated with 150 ALD cycles of In_2O_3, which can be seen to be approximately 1.5 - 2 nm thick. The sample was created by scraping onto an ultra-thin carbon grid TEM holder, TiO_2 nanoparticles from a standard photoanode (see methods) as used for devices in this study, which had been treated with 150 ALD cycles of In_2O_3. 97

Figure 4-3: Structure of the WN1 cyanoacrylic acid-based donor-π-acceptor dye used in the device studies. WN1 was synthesized as described in Ref. [51]. 98

Figure 4-4: Device data normalized to the performance of control (zero In_2O_3 cycles) devices in the same batch. "Delta V_{OC}" describes the average difference in the V_{OC} between In_2O_3-coated and control devices within the same batch. Device efficiencies, a.), are relatively constant from 0 – 10 In_2O_3 cycles as modest drops in J_{SC} are compensated by V_{OC} gains; it is primarily device-to-device variability in fill factor that dictates performance differences. After 15 In_2O_3 cycles, the drop-off in J_{SC}, b.), is not fully compensated by V_{OC} increases, c.), and overall device efficiency goes down. This is exacerbated by the net drop in V_{OC} after 30 cycles, although surprisingly, no further reduction in J_{SC} is observed. Error bars in c. indicate the standard deviation of the V_{OC}

changes with the device-to-device variability generally increasing at higher cycle numbers. 100

Figure 4-5. Current density-voltage (*J-V*) curves in the light, a.), and dark, b.), of representative devices for 0, 10, 15, and 30 In_2O_3 ALD cycles. The changes in V_{OC} are generally correlated to the onset of dark current. 101

Figure 4-6: Recombination lifetime data versus open-circuit voltage for different numbers of In_2O_3 cycles. Lifetimes generally increase with more In_2O_3 up to 15 ALD cycles, drop modestly from the peak after 20 cycles, and fall below the control devices after 30 cycles. Trend lines are drawn for 0, 15, and 30 cycles to demonstrate the large change in slope, *i.e.* dependence of recombination rate on bias, for 30 cycles versus all other cycle numbers and control cells. Note that lifetime variability was much higher in the 30 cycle devices than in other devices, similar to the higher V_{OC} variably also observed after 30 cycles, and one device exhibiting particularly low lifetimes and a large slope was chosen to illustrate the general trend. Other 30 cycle devices exhibited lifetimes similar to control cells, but with higher slopes. 102

Figure 4-7: Recombination lifetime (measured at V_{OC}) and V_{OC}, both under 1 sun illumination, as a function of the number of In_2O_3 ALD cycles for representative devices. To indicate the relatively high device variability of 30 cycle devices, data from a second device (unfilled symbols) were added for 0, 15, and 30 ALD cycles. 103

Figure 4-8: Capacitance, measured from transient photovoltage and photocurrent data, as a function of V_{OC} for three indicative In_2O_3 cycle numbers: 0 (control cells), 15 (highest observed V_{OC}'s), 30 (lowest observed V_{OC}'s). Fitted exponential trend lines are included for each device. Note that similar capacitance values are measured for all three cycle numbers and the fitted trend line slopes are roughly parallel. The shifting of these lines on the V_{OC} axis—approximately 120 mV lower for 30 cycles and 70 mV higher for 15 cycles, relative to the control—are indicative of a shift in the TiO_2 conduction band after deposition of In_2O_3. 104

Figure 4-9: a) PBE0-calculated relative energies (ΔE) and b) dipole moments perpendicular to the TiO_2 surface (z-component) as a function of fractional In_2O_3 surface coverage on anatase TiO_2 (101) surface. The relative energies are given with respect to a full monolayer of In_2O_3..... 105

Figure 4-10. PBE0-optimized anatase TiO_2 (101) surface structures with fractional In_2O_3 surface coverages of a) 0.25, b) 0.50, c) 0.75, and d) 1.0. Indium atoms are shown in green, oxygen in red, and titanium in gray. 106

Figure 4-11: Side views of the PBE0-optimized anatase TiO_2 (101) surface structures with fractional In_2O_3 surface coverages of a) 0.25, b) 0.50, c) 0.75, and d) 1.0 demonstrating the tilting of the In_2O_3 species on TiO_2..... 107

Figure 4-12: V_{OC} as a function of light intensity from a white LED array for all number of In_2O_3 ALD cycles tested. Intensity is measured in suns, with one sun equal to 100 mW/cm^2. Fit lines demonstrating the logarithmic dependence of V_{OC} on light intensity are also shown. The slope of these lines was observed to be consistent with recombination and V_{OC} (under the same illumination level) trends: the slope increased from 0 to 20 In_2O_3 cycles, indicating a stronger dependence of V_{OC} on light level, before dropping significantly after 30 ALD cycles..... 109

Figure 4-13: PBE0-calculated density of states (DOS) for pristine anatase TiO_2 (101) slab (top) and for TiO_2-In_2O_3 slabs with fractional In_2O_3 surface coverages of 0.25, 0.50, 0.75, and 1.0 (bottom). The states originating from In_2O_3 within the bandgap region for each coverage level are illustrated in the zoom-ins (right). 111

Figure 4-14: Schematic (not to scale) showing the effect of 15 and 30 In_2O_3 ALD cycles on the TiO_2 conduction band level and on recombination processes (red arrows). In a), which corresponds to control devices, there is no barrier layer to block recombination with holes in the hole-transport material (HTM) (recombination with oxidized dye molecules is ignored here for simplicity). Recombination can involve electrons in the

TiO_2 conduction band (top arrow) or in mid-bandgap trap states (bottom arrow). B) demonstrates an increase in TiO_2 band levels and a reduction in recombination rate, the effects of which are most apparent after 15 In_2O_3 ALD cycles. After 30 ALD cycles, c), the TiO_2 energy levels are lowered, the In_2O_3 bandgap is narrowed, and recombination occurs at a high rate and possibly involves In_2O_3 states. 112

Figure 5-1: Auger electron spectroscopy linescan of 10 ALD cycles of PbS grown on a nanoporous TiO_2 substrate with data reported in terms of signal intensity, a), and atomic concentration, b). The linescan was performed at the midpoint of the SEM image, i.e. the 100000 counts per second (CPS) line in a), and the 25% line in b). The nanoporous TiO_2 layer, approximately 5 µm thick, was deposited atop a silicon substrate which is at the far left of the SEM image, meaning that the top of the nanoporous TiO_2 film is at approximately the 6 µm mark. 123

Figure 5-2: Transmission electron micrographs of PbS QDs on nanoporous TiO_2 with (a) and without (b, c) an intermediate Al_2O_3 cycle. As seen in (a) and (b), the coverage of the QDs is not affected by Al_2O_3. (c) Lattice diffraction of the rock salt PbS QDs is captured with a measured lattice constant of 5.9 Å. 127

Figure 5-3: Schematics of the three configurations studied (not to scale). A: control devices with PbS quantum dots grown on TiO_2 nanoparticles, surrounded by the spiro-OMeTAD hole transport material (HTM). B: Al_2O_3 deposited after growth of quantum dots. In this configuration the Al_2O_3 barrier layer is expected to slow recombination involving electrons in TiO_2 and holes in the HTM. C: Al_2O_3 deposited prior to quantum dot growth. In this configuration the Al_2O_3 barrier layer is expected to slow recombination involving electrons in TiO_2 and holes in both the HTM and oxidized quantum dots. Configuration C yielded the highest device efficiencies. 127

Figure 5-4: a) UV-Vis absorbance spectra taken in transmission mode of nanoporous TiO_2 substrates on FTO coated with PbS QDs in the three different configurations studied. A TiO_2 control is also shown. No significant changes were observed when a

single ALD cycle of Al_2O_3 preceded PbS deposition, indicating that it did not lead to enhanced PbS nucleation. In all three configurations containing PbS QDs, the absorption onset occurs near 800 nm indicating a band gap for the largest QDs ~1.6 eV. b) UV-Vis spectra of full devices, measured in terms of spectral absorptance (percent of incident light absorbed), collected in an integrating sphere. As in a), no significant changes in light absorption were observed when a single ALD cycle of Al_2O_3 preceded PbS deposition indicating that it did not lead to enhanced PbS nucleation. All three spectra exhibit interference fringes common in thin films..... 129

Figure 5-5: Average device data for the PbS QDSSCs with and without Al_2O_3 barrier layers. Values were calculated by averaging the top two (of four) devices on each of four separate substrates for each configuration; therefore the values represent the average of eight different devices. Error bars indicate standard deviation of device parameters. .. 130

Figure 5-6: Incident photon-to-current efficiency (IPCE) averaged from multiple devices in each of the three configurations collected at zero bias. When Al_2O_3 precedes PbS QD growth, a substantial improvement in IPCE is observed. 131

Figure 5-7: Light, a), and dark, b), current-voltage (*J*-*V*) curves for typical devices of the three configurations studied. Whether deposited before or after the PbS quantum dots, a single cycle of Al_2O_3 suppressed the onset of dark current to a similar degree. The value in parentheses corresponds to a current-threshold voltage, that is, the voltage at which the dark current in the devices exceeded an arbitrary value (here, 0.4 mA/cm^2). These current threshold values are averaged over all the devices for that particular configuration. 132

Figure 5-8: Electron lifetimes for the three different device configurations as determined by fitting the photovoltage decay obtained from transient photovoltage experiments. At higher photovoltages the recombination suppression from depositing Al_2O_3 prior to PbS growth is readily apparent and is superior to Al_2O_3 deposited after PbS, although

recombination is also reduced in that configuration, particularly at lower photovoltages. Error bars indicate standard deviations of the several devices tested. 133

Figure 6-1: Structures of the relevant molecules in this study. a) WN1 dye molecule (R_1) and the reduced system used for DFT calculations (R_2). b) 2-Cyanoacrylic Acid (CAA) and c) Triphenylamine (TPA) reduced systems used to simulate X-ray absorption spectra. 143

Figure 6-2: Experimental NEXAFS spectrum of the WN1 dye powder compared to the theoretical X-ray absorption spectra for the 2-cyanoacrylic acid (CAA) and triphenylamine (TPA) substructures. The WN1 powder spectrum was normalized to 1.0 and the theoretical spectra to 0.8 for clarity. The theoretical spectra were shifted 0.3 eV to higher energy to match the first transition in the experimental spectrum. The first two peaks of the WN1 and CAA spectra, which show excellent agreement in relative energy and intensity, correspond to transitions into π* orbitals. 145

Figure 6-3: a) 3-D structure of the highly-planar 2-cyanoacrylic acid (CAA). b) **π1** ∗ orbital corresponding to the lowest energy peak of Figure 6-2. This orbital is located out of the plane of CAA, which is rotated here relative to a) for clarity. c) **π2** ∗ orbital corresponding to the second lowest energy peak in Figure 6-2. This orbital is located in the plane of CAA. An optimized geometry for CAA was obtained using a B3LYP hybrid functional and the orbitals, drawn using an isovalue of 0.05 in the Molekel software program [38], were calculated using the StoBe software [37] with BP86 functional. ... 145

Figure 6-4: a) Nitrogen K-edge NEXAFS spectra for a representative sample of the WN1 dye adsorbed on TiO_2 at five different incident X-ray angles (relative to the substrate surface plane). The lowest energy peak, **π1** ∗, increases in intensity as the incident angle is increased whereas the opposite trend is observed for the next lowest energy peak, **π2** ∗. b) Peaks used to fit the angle-resolved NEXAFS spectra (in this instance, the 20° spectrum), including five Gaussians and an arctangent function used for the ionization step-edge. c) Intensities from the Gaussian fitting of the raw data (red) versus the fitted

NEXAFS equation result (Eq. (3.3))) for the **π1** ∗ and **π2** ∗ peaks, which yielded angles of 63.0° and 45.1°, respectively. 147

Figure 6-5: Two views of the DFT-optimized ground state of the reduced WN1 system. In a), the angle associated with the **π1** ∗ orbital (Ψ_1) is shown. Ψ_1 dictates the tilt angle of the dye molecule and is calculated at 45.4° in the ground state DFT. b) shows an approximate view of the angle associated with the **π2** ∗ orbital (Ψ_2) which defines the angle of the C-N bond relative to the surface normal. Ψ_2 is found to be 51.2° from the DFT. For clarity, the inset shows the Ψ_2 angle in the simpler case where the cyanoacrylic acid group is completely upright (*i.e.* Ψ_1 = 90°); a low value for the Ψ_2 angle therefore would indicate the C-N bond is roughly parallel to the surface. Computational Analysis of WN1 Dye Orientation 148

Figure 6-6: Schematic structures and snapshots from the DFT-MD simulations (T = 300 K, side and front views at indicated times) for the binding configurations a) 1 with the dye bonding to the surface via two Ti-O bonds and b) 2 with the dye bonding to the surface via both Ti-O and Ti-N bonds. No periodic images of the unit cell and only the outermost atomic layers of the TiO_2 surface are shown in the snapshots for clarity. A video of the full DFT-MD simulation of binding configuration 1, is available as a digital supplementary file to this thesis. 150

Figure 6-7: a) Ψ_1 and Ψ_2 angles over time determined from atomic coordinates for all dye orientations produced by the 15 ps DFT-MD simulation (T = 300 K) on the TiO_2-WN1 system in binding configuration *1* with the dye binding to the surface via two Ti-O bonds. b) Cumulative average Ψ_1 and Ψ_2 angles from the DFT-MD simulation (*i.e.* averaged from time 0 to time *t*) as a function of simulation length. 153

Figure 6-8: Total energies during the 15 ps DFT-MD simulation with a time step of 1.5 fs and during the 5 ps control simulation with a time step of 1 fs of the TiO_2-WN1 system in binding configuration 1. The total energies are given relative to the averaged total energy from the 15 ps simulation. 159

Figure A-1: Phosphonic acids studied: aminomethyl phosphonic acid (AMPA), 3-aminopropyl phosphonic acid (APPA), *p*-aminobenzyl phosphonic acid (ABPA), 3-phosphopropionic acid (PPA), butyl phosphonic acid (BPA), and octadecyl phosphonic acid (ODPA). 172

Figure A-2: FTIR spectra of phosphonic acid SAMs adsorbed on nanoporous TiO_2, normalized to bare TiO_2. Various important and characteristic peaks are indicated. 174

Figure A-3: The ruthenium-based dyes Z907, a.), and YE05, b.), used in the phosphonic acid SAM studies. 175

Figure A-4: FTIR spectra of the Z907 dye adsorbed on phosphonic acid SAM-covered nanoporous TiO_2, normalized to spectra taken after the SAM deposition, prior to dye adsorption. "Bare" indicates that the TiO_2 was not coated with a SAM prior to dye adsorption. Various important and characteristic peaks are indicated. 175

Figure A-5: Activation of a carboxylic acid using N,N'-dicyclohexylcarbodiimide (DCC) and N-hydroxysuccinimide (NHS). The reaction yields an activated acid and the insoluble byproduct N,N'-dicyclohexylurea (DHCU). 176

Figure A-6: FTIR spectra of octanoic acid and NHS-activated octanoic acid adsorbed on APPA-coated nanoporous TiO_2. Spectra normalized to corresponding spectrum of APPA SAM on TiO_2. 177

Figure A-7: Activation of a carboxylic acid using 1-ethyl-3-(3-dimethylaminopropyl) carbodiimide (EDC) and N-hydroxysuccinimide (NHS). 178

Figure B-1: Schematic of the two different device configurations studied in Ref. [30] based on the placement of the Al_2O_3 barrier layer and the recombination processes that each placement is expected to impede. Figure reprinted with permission from Ref. [30]. Copyright 2013 American Chemical Society. (Image courtesy of Katherine Roelofs). 183

Figure B-2: TEM image of a CdS quantum dot grown on nanoporous TiO_2. Reprinted from Ref. [33] with permission from John Wiley & Sons, Ltd. (Image courtesy of Han Bo-Ram Lee). 184

Figure C-1: Molecules studied in this appendix include: a.) *p*-aminobenzyl phosphonic acid (ABPA); b.) chenodeoxycholic acid; c.) bi-isonicotinic acid (BINA); d.) 2-(2,4-difluorophenyl) pyridine; e.) Z907 dye; f.) YE05 dye. 190

Figure C-2: Angle-resolved NEXAFS carbon K-edge spectra for ABPA. 191

Figure C-3: NEXAFS K-edge spectra for BINA powder and BINA adsorbed from solution onto anatase TiO_2. Spectra for the BINA powder are shown in a.) for carbon and b.) for nitrogen. Angle-resolved NEXAFS spectra of BINA adsorbed on TiO_2 are shown in c.) for carbon and d.) for nitrogen (which uses the same color scheme for angles as c.). In both of the angle-resolved plots a clear angular-dependence is visible. Note that the nitrogen spectra were shifted 1.05 eV to lower energy based on literature references and subsequent beam time experiments of the same materials. 193

Figure C-4: NEXAFS carbon, a.), and nitrogen, b.), K-edge spectra of $Co(NCS)_2$ and Cu(NCS) powders. 194

Figure C-5: Carbon K-edge NEXAFS spectrum of 2-(2,4-difluorophenyl) pyridine. Molecule was studied in the gas phase. 195

Figure C-6: NEXAFS carbon, a.), and nitrogen, b.), K-edge spectra of Z907 and YE05 dye powders. 196

Figure C-7: Angle-resolved carbon K-edge NEXAFS spectra of Z907 adsorbed on anatase TiO_2, a.), ZrO_2, b.), and Al_2O_3, c.). 197

Figure C-8: Angle-resolved carbon K-edge NEXAFS spectra of YE05 adsorbed on anatase TiO_2, a.), amorphous TiO_2, b.), ZrO_2, c.), and Al_2O_3, d.), ZnO, e.), and MgO, f.). 199

Figure C-9: Carbon K-edge NEXAFS spectrum of chenodeoxycholic acid powder, a.), and adsorbed on anatase TiO_2, b.). 200

List of Tables

Table 3-1 Device parameters for five different trials of solid-state tested at standard AM 1.5 illumination. Parameters represent the average of the top 50% of devices (ranked by efficiency), a set ranging in number from 7 - 20 depending on trial and treatment. The "Quantified Dark Current Onset" represents the voltage at which current in a dark *J-V* curve exceeds 2 mA/cm^2 and is used to capture the suppression of recombination in cells and is, unlike V_{OC}, independent of photocurrent. Unless noted otherwise, devices used the Z907 dye, were ~2.2 μm thick, and had undergone the $TiCl_4$ surface treatment prior to Al_2O_3 deposition. 67

Table 3-2: Al_2O_3 growth parameters used in model. Al_2O_3 thickness and variance were taken from Tien *et al*. [65]. θ was adjusted upwards 0.25 from the same source to better match values reported by Mäkinen and coworkers [70, 71]. Data for three cycles were interpolated from the values for one, two, and five cycles. 80

Table 3-3: Representative *k* values used in the model. Values taken from Ref. [19]. 81

Table 4-1: Average device parameters for the different numbers of In_2O_3 ALD cycles studied. 99

Table 4-2: Slope of V_{OC} versus the log of light intensity (Figure 4-12) as a function of In_2O_3 ALD cycles. 109

Table 5-1: Average atomic concentrations measured using TEM-EDS. The atomic shells used for each element are denoted inside parentheses next to the respective element. .. 125

Table 5-2: Average device parameters for the three configurations tested. A substantial improvement in efficiency was achieved by performing a single ALD cycle of Al_2O_3 prior to PbS growth whereas no improvement was observed with a single Al_2O_3 ALD cycle after PbS growth. The efficiency improvement is driven by a large increase in J_{SC}

and a smaller increase in V_{OC}. Values were obtained by taking the average of the top two of four devices (~10 mm^2 in area) on a given substrate and then averaging over the four substrates tested with each configuration. 130

Table 6-1: Energies of the investigated TiO_2-WN1systems in binding configurations 1 and 2 for the WN1 without the C_6H_{13} alkyl chains and the WN1 truncated after the thiophene rings. The energies in kcal/mol are given relative to the binding configuration 2 structures. 151

Table 6-2: Compilation of the two angles calculated from NEXAFS, DFT optimization, and DFT-MD. 155

Chapter 1. Introduction & Background

1.1. Research Goals & Dissertation Outline

The subject of the work described in this dissertation is a particular class of photovoltaics—*i.e.* solar cells—called dye-sensitized solar cells (DSSCs) and their close analogue, quantum dot-sensitized solar cells (QDSSCs). These two types of solar cells, more broadly referred to as "sensitized solar cells" (SSCs), are a particularly interesting and attractive area of study because they operate in a much different fashion than typical solar cells available on the commercial market today such as those using silicon (Si), cadmium telluride (CdTe), and copper indium gallium selenide (CIGS) absorbing layers. What fundamentally differentiates SSCs from these more traditional solar cells is the separation of light harvesting and charge transfer processes. Whereas in traditional photovoltaics the light absorption occurs in a planar layer on the order of ~1 - 200 μm thick, in SSCs the absorbing layer (*i.e.* of dye molecules or quantum dots) is on the order of 1 nm. As will be described in greater detail later on in this introductory chapter, light absorption in a solar cell generates an electron-hole pair. In a traditional device this electron-hole pair must diffuse a relatively long distance before the Coulombic attraction between the electron and hole is overcome and they can be separated; if they are not separated quickly enough, the electron-hole pair will relax down to the ground state and no energy will be collected from the absorbed photon. In a SSC on the other hand, this separation happens almost instantaneously because the electron-hole pair is generated right at an interface that facilitates the charge separation.

The necessary consequence of the ultrathin absorbing layer in a SSC, however, is that a very high surface area substrate must be used in order to harvest a large percentage of the incident light. In a typical SSC, for example the archetypal DSSC developed in the 1990s, the substrate is a nanoporous TiO_2 film ~10 μm thick. While the absorbing film of dye molecules attached to the TiO_2 surface is only ~1 nm thick, the nanoporous TiO_2 film has a surface area approximately 1000 times the geometric area (*i.e.* the footprint of the device), meaning that the effective thickness of absorbing material is actually ~1 μm, similar to the absorbing layer thickness in CdTe and CIGS devices. All solar cells suffer

from efficiency-diminishing charge recombination processes, such as the electron-hole relaxation process described above for traditional photovoltaics. In SSCs, the dominant recombination processes occur at interfaces in the device; the substantial interfacial area of SSCs means that there are many places where this recombination process can occur.

Making an efficient SSC therefore requires a high degree of control over and understanding of interfaces, in particular the interfaces that exist between the light-absorbing material and the high surface area substrate and between the light-absorbing material and the "hole-transport material" (HTM). The remaining sections of this introductory chapter are devoted to describing in detail the processes that occur at these interfaces and to motivating, more broadly, photovoltaic research. Following an introduction to the most important experimental techniques utilized in the research described here (Chapter 2) are four chapters that constitute the primary novel research presented in this dissertation. This research can effectively be broken down into an "engineering" component and a "characterization" component. The engineering component focuses on work performed to modify the high surface area substrate prior to deposition of the light-absorbing material in order to slow down deleterious recombination processes. In Chapter 3 a comprehensive examination of Al_2O_3 recombination barriers in solid-state DSSCs is performed to help understand the wide range of results previously reported in the literature for liquid-based DSSCs and to guide the future development of barrier layers. We observe large changes in device behavior after depositing less than 2 Å (less than a full monolayer) of Al_2O_3 which indicates that an extremely fine control over the recombination barrier growth rate is crucial. Large differences in the behavior of two classes of dye molecules demonstrate how the energy levels of the absorbing material play a significant role in determining how much a recombination barrier—which is generally designed to be insulating—interferes with desirable charge transfer processes.

The observations with Al_2O_3 barrier layers motivate the search for a barrier layer that can be deposited with a lower growth rate and that is less insulating than Al_2O_3. Fitting these criteria, In_2O_3 was examined as a barrier layer, also in solid-state DSSCs (Chapter 4). Work with In_2O_3 reveals the ability to substantially reduce recombination

with significantly less concomitant blocking of desirable charge transfer processes as compared to Al_2O_3 recombination barriers. Once the In_2O_3 barrier layers reach a certain thickness, however, their "barrier" properties disappear in rather remarkable fashion. Quantum chemical computational studies help better explain this intriguing phenomenon.

The work with Al_2O_3 barrier layers in a solid-state DSSC also motivates an investigation in a device where charge collection efficiency is much lower—*i.e.* recombination is a more severe problem. To this end, Al_2O_3 barrier layers are employed in a QDSSC using PbS quantum dots and a substantial (near doubling) of efficiency is achieved (Chapter 5). In addition to the impressive device-enhancing results, this chapter also describes a method to deposit a barrier layer and an absorbing material in a single process, which opens the door for *in situ* studies of the barrier/absorber interface.

Chapter 6 describes the "characterization" facet of this dissertation. In this study, an organic dye molecule—which was used in both the Al_2O_3 and In_2O_3 DSSC barrier layer studies—is adsorbed on a planar TiO_2 substrate (chosen to serve as a model for the high surface area substrate) and studied using the synchrotron radiation technique near-edge X-ray absorption fine structure (NEXAFS) spectroscopy. NEXAFS is particularly well-suited for directly measuring the orientation of adsorbed molecules and these results are compared to an in-depth computational study using the advanced simulation technique density functional theory-molecular dynamics (DFT-MD) of the same dye-TiO_2 system. The motivation for this study is two-fold: to gain a comprehensive understanding of the specific dye in question, which is quite similar in structure to a widely-used class of high-performing dyes, and to assess the ability of computational studies—which are commonly used to predict and understand a variety of phenomena critical to device performance—to capture real world behavior.

Following a summation of this work and perspective on the future of sensitized solar cells (Chapter 7), three appendices are included describing additional studies related to the work described in Chapter 3,Chapter 4, Chapter 5, and Chapter 6. In Appendix A: an organic means of recombination blocking in DSSCs (in contrast to the inorganic metal oxide layers described above) is presented which involves the formation of a covalent bond to link dye molecules to a self-assembled monolayer of phosphonic acids pre-

deposited on the high surface area substrate. In Appendix B: studies examining the use of both inorganic and organic recombination barriers in CdS QDSSCs are briefly summarized in addition to a study that uses a novel quantum dot growth technique, atomic layer deposition, which was also used to grow the PbS quantum dots in Chapter 5. In Appendix C: studies examining the NEXAFS spectra of ruthenium-based dyes adsorbed on a variety of metal oxide substrates are reported.

1.2. The Global Energy Landscape

Average global power consumption today is in excess of 16 TW and that figure is expected to nearly double to approximately 30 TW by 2050 [1, 2] due to continued population growth and gains in standard of living in the developing world. World energy production, which grew at a compound annual growth rate (CAGR) of 2.6% from 1965 – 2011, is shown in Figure 1-1. As is evident in the plot, the dominant sources of energy production are the fossil fuels coal, petroleum, and natural gas, accounting for nearly 90% of all production in 2011 (the remainder being primarily nuclear and hydropower). A scale-up of energy production to reach the 30 TW of forecasted demand by midcentury would require an aggressive expansion of fossil fuel development difficult in its own right, but further compounded by the need to reduce global CO_2 emissions.

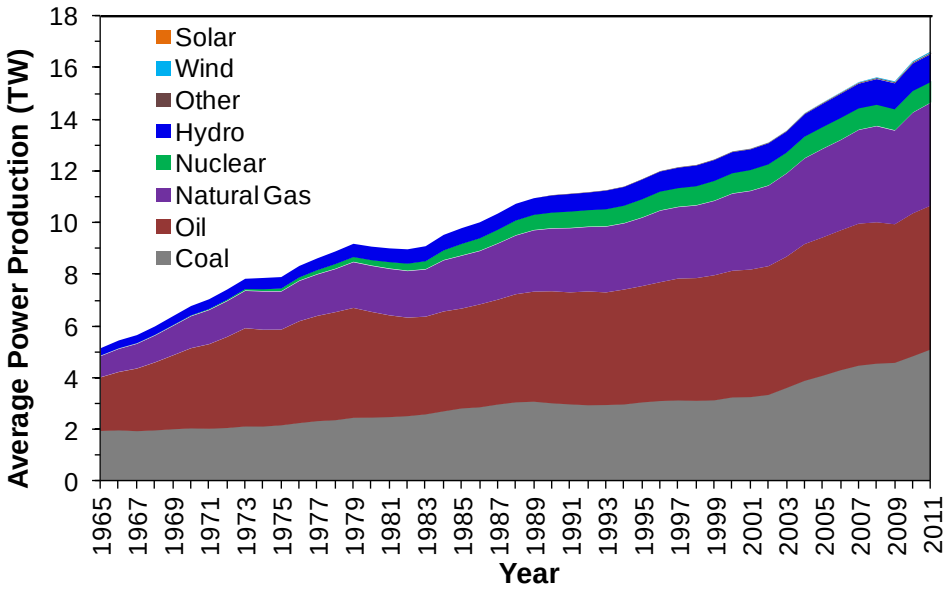


Figure 1-1: World energy production from 1965-2011, broken down by source, in terms of average power output. 1 TW of average output is equivalent to 8766 TWh or 29.9 quadrillion BTUs per year. Note that the values in the plot represent the energy released upon combustion (for example in the instance of coal), not the amount of energy successfully converted into electricity. Contributions from solar, wind, and "other" (which includes sources such as biofuels and geothermal energy production) are too small to see in the plot. In 2011, coal, oil, and natural gas accounted for 31%, 33%, and 24%, respectively, of world energy production. Data taken from the BP Statistical Review of World Energy 2012 [3].

Due to the radiative forcing of CO_2 in the atmosphere—*i.e.* its role as a greenhouse gas—the molecule's release affects global climate to such a degree that if left unchecked, continued CO_2 emissions could have substantial negative consequences for the world's population. According to the Intergovernmental Panel on Climate Change (IPCC), cumulative 21st century anthropogenic CO_2 emissions should be kept below approximately 1800 gigatonnes (or ~2800 gigatonnes when including pre-2000 emissions) in order to maintain the atmospheric CO_2 concentration below 450 parts per million (ppm) [4]. This 450 ppm figure, while somewhat arbitrary, is chosen because if atmospheric CO_2 concentration is stabilized at this level, then mean global temperature rise relative to pre-industrial levels is ~50% likely to be restricted to less than 2 °C [4]. What is clear from Figure 1-2 is that even in the quite conservative scenario in which CO_2 emissions remain constant at current levels, the 450 ppm threshold will likely be surpassed in the next 50 years with higher CO_2 concentrations leading to increasingly severe changes in the climate.

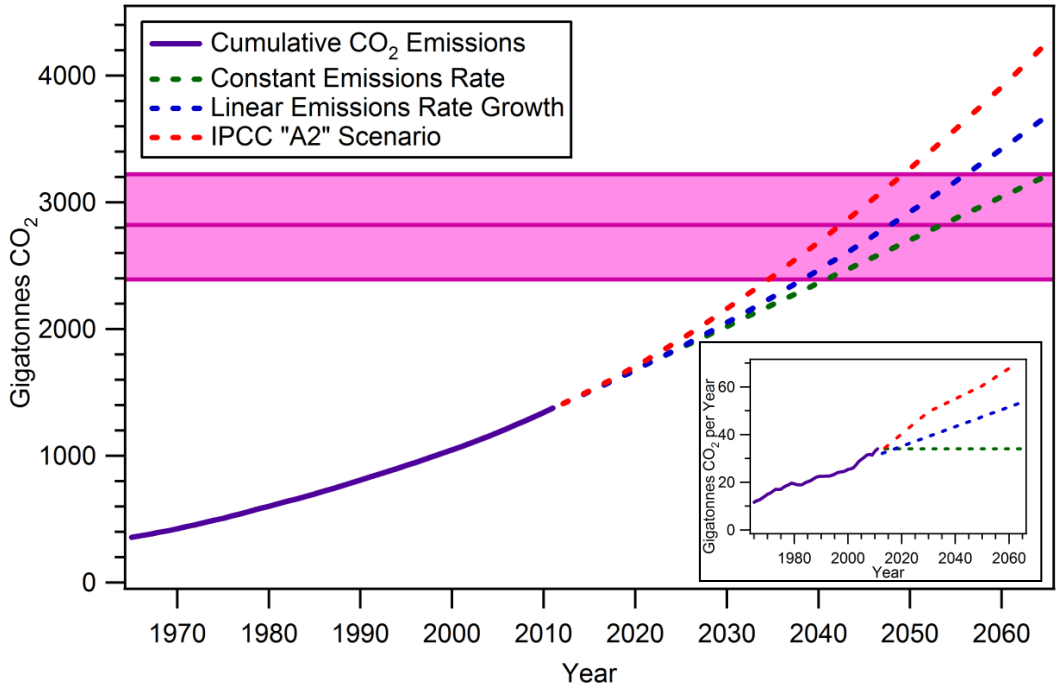


Figure 1-2: Cumulative global anthropogenic CO_2 emissions from fossil fuel combustion from 1965 - 2011 with three different future emission scenarios: one in which CO_2 emissions remain constant at 2011 levels, one in which the emissions rate continues at the linear growth rate it has followed since 1965, and one in which it follows the "A2" scenario outlined by the Intergovernmental Panel on Climate Change (IPCC) in 2000 and which emissions have closely matched from 2001-2011 [5]. The pink region identifies an uncertainty range of CO_2 cumulative emissions likely to lead to an atmospheric CO_2 concentration of 450 ppm, which is deemed necessary to, as likely as not, maintain net global warming below 2 °C [4]. The inset shows global CO_2 emissions per year from 1965-2011 along with the three future emission scenarios. CO_2 emissions data from 1965 – 2011 was taken from the BP 2012 Statistical Review [3] and emissions pre-1965 were taken from Boden *et al.* [6]. Note that the emissions targets technically refer to "CO_2-equivalent" concentrations to encompass other anthropogenic sources that either increase (*e.g.* methane) or decrease (*e.g.* aerosols) the net warming effect. Because at current levels these other forces approximately cancel out, the targets can be simplified and stated in terms of CO_2 [4].

As the combustion of fossil fuels constitutes the primary source of anthropogenic CO_2 emissions, meeting 21st century energy needs for the planet is therefore a two-fold challenge: increasing energy production to improve the quality of living in a growing world and converting our current energy portfolio to one with significantly reduced carbon emissions; a 15 TW problem is in reality a 30 TW problem. Identifying technologies to transform the energy landscape is truly one of scale: what sources can provide several TWs of energy with minimal CO_2 emissions? According to the U.S. Department of Energy [7], the total extractable wind energy throughout the world is at most 4 TW, 2 TW for tidal energy, and 12 TW for geothermal energy. Building one 1

GW nuclear power plant every single day for the next 40 years would only yield 14.6 TW—and would bring uranium usage rates to an unsustainably high level. In contrast, 120,000 TW of solar energy strikes the earth's surface at each moment [7]. Producing tens of TWs of power from solar energy requires converting only a small portion—less than 0.1%—of this energy source.

As Figure 1-1 indicates, however, solar power currently constitutes a near-negligible percentage of global energy production—approximately 0.04% in 2011 [3]. On the other hand, as Figure 1-3 demonstrates, photovoltaic production capacity is increasing rapidly, with a CAGR of 40% from 1996 – 2011 [3]. Further adoption of solar energy, which will lead to the expansion of an industry that saw $77 billion in revenue in 2012 [8], necessitates a continued reduction in system cost which can be driven by improvements in device efficiency, reductions in materials and manufacturing cost, reductions in installation cost, and reductions in permitting costs. Reaching the TW scale requires that solar energy conversion be both ubiquitous and inexpensive.

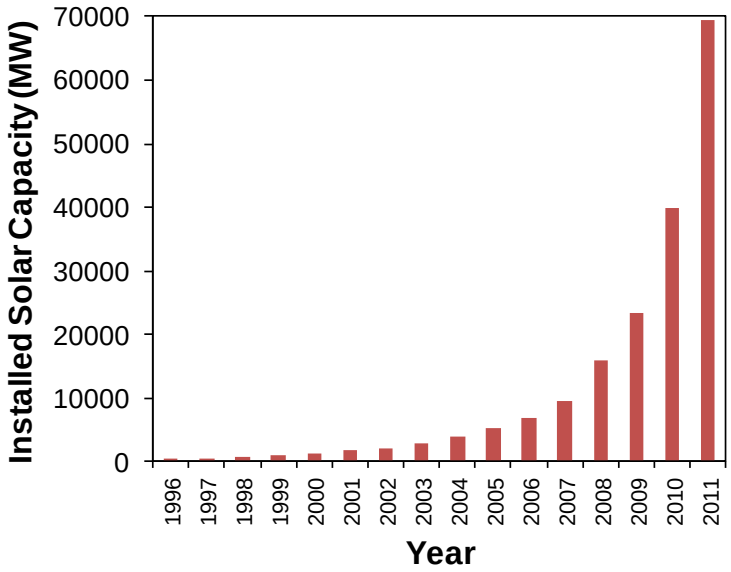


Figure 1-3: Installed world photovoltaic capacity in MW from 1996-2011. The compound annual growth rate was 40% during this time period. Data taken from the BP Statistical Review of World Energy 2012 [3].

1.3. Solar Cells (Photovoltaics)

The modern silicon solar cell got its start at Bell Labs in the 1950s and exhibited an impressive 6% efficiency [9, 10]. Since then, progress on silicon solar cells has

increased efficiencies to 25% [11] with substantial gains in other high-efficiency technologies that use light-absorbing materials such as cadmium telluride (CdTe), copper indium gallium selenide (CIGS), and gallium arsenide (GaAs) [12]. Many extensive reviews and textbooks on solar cells are available [13-15], but it is important to introduce the basic operation and design considerations for photovoltaics here. In contrast to the dye-sensitized solar cells described below, the essential operating fundamentals of inorganic photovoltaic devices, such as those listed above, are quite similar to one another and are illustrated in Figure 1-4. A *p*-type and an *n*-type semiconductor (these can be of the same material (*e.g.* as in Si cells) or different materials (*e.g.* as in CdTe cells)) are brought into contact with one another to form a *pn*-junction with at least one of the semiconductors having a bandgap well-matched to the solar spectrum (Figure 1-4b); a photon of incident light is absorbed in the solar cell (Figure 1-4d) generating an excited electron-hole pair; this electron-hole pair will, if successfully extracted, diffuse to the *pn*-junction where the junction's electric field will assist in separating the electron and hole, accelerating one of the charge carriers to its terminal electrode (Figure 1-4e); a harvested charge carrier will perform some sort of useful work on its way to the opposite electrode where it will then recombine with a charge carrier of the opposite sign (Figure 1-4f).

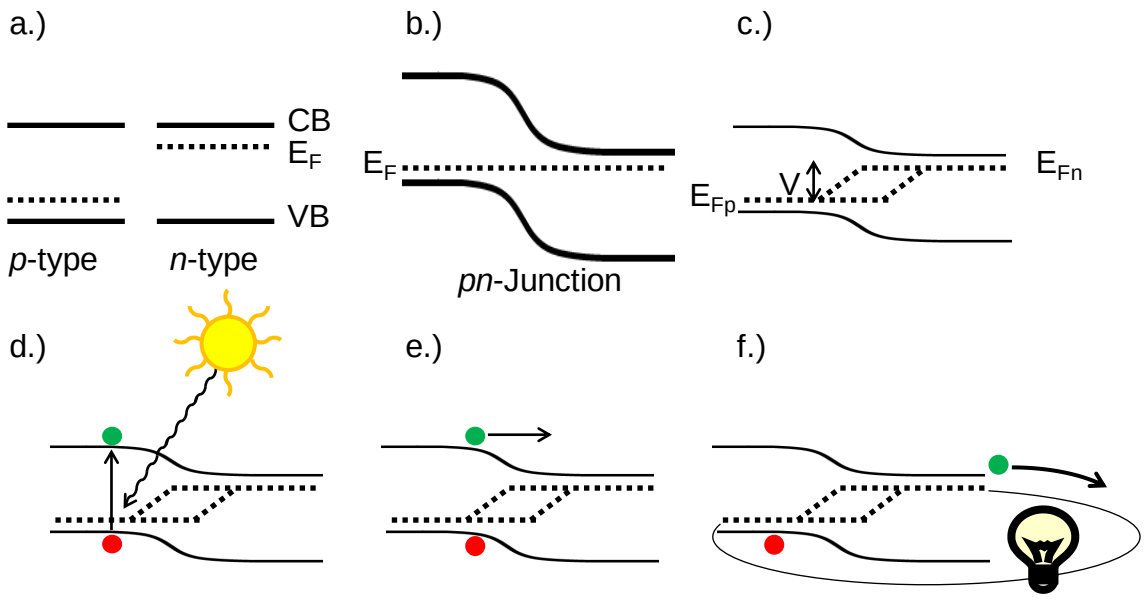


Figure 1-4: Diagram of the *pn*-junction used in traditional inorganic photovoltaics. In a.), an *n*- and a *p*-type semiconductor are shown (with the same bandgap, typically indicative of different doping levels of the same material) with CB and VB indicating their conduction and valence bands, respectively, and E_F indicating the Fermi level in each semiconductor, which is a function of the doping levels. A *pn*-junction is formed as the two materials are brought together in b.), and the Fermi level is equalized across the two materials. In c.) a bias, *V*, is applied and the junction is no longer at equilibrium, resulting in the formation of quasi-Fermi levels (E_{Fp}, E_{Fn}) on each side of the junction. The junction is illuminated in d.); absorption of a photon results in an electron (green circle) being excited from the VB to the CB, leaving behind a positively-charged hole (red circle) in the VB. The electron-hole pair (or exciton) diffuses until it reaches the junction boundary in e.) where the electric field drives the separation the exciton. The electron is collected at the right contact (not shown) in f.) where it then proceeds to flow through a work-producing circuit (e.g. a light bulb) before reaching the left contact (not shown) where it will recombine with a hole, returning the solar cell to the state shown in d.). The amount of energy that can be extracted from each electron is a function of the applied voltage, *V*.

Several material qualities are needed to produce a high-efficiency solar cell. For one, the absorbing material must have a high absorption coefficient in the energy-dense visible and near-infrared domains of the solar spectrum (Figure 1-5). In a standard single-junction device, the maximum possible power output is bounded by the product of the number of photons absorbed and the amount of energy that can be extracted from each electron-hole pair generated by the absorption of a photon. This latter quantity is limited by the bandgap of the absorbing material: ultimately you can absorb more photons by choosing a material with a lower bandgap, but the amount of energy that can be extracted from each of those photons is then capped by the material's bandgap. This implies, then, that given the solar spectrum of Figure 1-5, there is some optimal value for the material bandgap that would yield the highest efficiency for ideal device behavior.

This so-called "Shockley-Queisser Limit" was first described in 1961 [16] and yields an efficiency of 31% with a bandgap of 1.3 eV (~954 nm) (note: an active area of research in "third generation photovoltaics" is to exceed this limit by extracting the excess energy imparted to electron-hole pairs by photons above the bandgap energy, which, in the Shockley-Queisser analysis, is assumed to be lost to charge-carrier thermalization) [17].

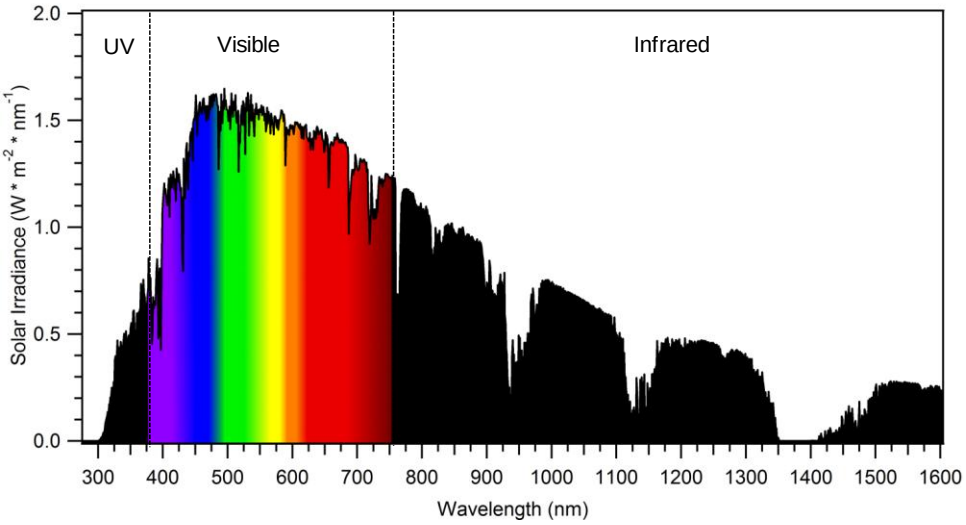


Figure 1-5: The AM 1.5G solar spectrum up to 1600 nm divided into the ultraviolet (UV), visible, and infrared ranges with the y-axis indicating the amount of power for a given wavelength of light. "AM" stands for "air mass": AM 0 corresponds to the solar spectrum outside the Earth's atmosphere while AM 1.0 indicates the light has passed through the length of atmosphere as if the sun were directly overhead. AM 1.5 well approximates the average atmospheric length sunlight travels through in order to reach Earth's mid-latitudes. The dips in the spectrum correspond to the absorption of light by atmospheric gases such as O_2 (~760 nm) and H_2O (~950, ~1150, ~1300 nm). The AM 1.5G spectrum is available from the National Renewable Energy Laboratory [18].

In order to approach the physical limits imposed by spectrum-overlap and charge carrier energy, a solar cell must be built to efficiently extract charge carriers while they are in a high energy state as the excited charge carrier may relax to the ground state via a recombination process before it is extracted and performs useful work. Recombination may involve a radiative process (the rate of which is a function of the material's absorption coefficient), an Auger process, or a trap-mediated process (such as may occur at grain boundaries or due to defect states in the solar cell). These inorganic solar cells are termed "minority carrier devices" because these recombination processes involve the decay of an excited minority carrier, *e.g.* the electron shown in the Figure 1-4d. A high recombination rate (or, equivalently, a short minority carrier lifetime) can lead to both

reduced device current (from poor charge collection efficiency) and achievable device voltage (due to increased dark current, which is undesirable and flows in the opposite direction of the photo-generated current). In order to minimize recombination, efficiently extract excited charge carriers, and achieve high device performance, it is crucial to place the exciton-splitting junction near where most of the photons are absorbed and use high-purity materials with low defect concentrations.

In dye-sensitized solar cells, which are described in detail in the next section, recombination again plays an important role. However, in dye-sensitized solar cells both desirable and undesirable charge transfer processes are qualitatively different than in inorganic devices.

1.4. Dye-Sensitized Solar Cells (DSSCs)

DSSCs are the subject of several in-depth reviews and textbook chapters and some particularly notable and informative ones cited here include: a textbook chapter by Grätzel and Durrant which provides perhaps the most accessible introduction to DSSCs [19]; an extensive review by Hagfeldt *et al*. which is the most comprehensive available and touches on all elements of DSSC engineering principles [20]; a review by Baxter focusing on the commercialization of DSSCs and relevant material considerations when scaling from the lab to module level [21]; and a forward-looking review by Hardin *et al*. that focuses on novel techniques critical to reaching the efficiency limits of DSSCs [22]. The following sections provide an overview of the history and progress of DSSCs, their fundamental operating principles, their advantages over traditional photovoltaics, and particular areas of DSSC research relevant to this dissertation: charge recombination and the orientation of adsorbed dye molecules. Quantum-dot sensitized solar cells (QDSSCs) are also discussed.

1.4.1. History and Background

The archetypal dye-sensitized solar cell was first reported in 1991 by O'Regan and Grätzel, and the latter's importance in the device's development has led to the DSSC also being called the "Grätzel cell" [23]. While dye-based solar energy conversion had been performed previously, the 1991 paper represented a substantial leap forward for the field due to its use of a high surface area, nanoporous TiO_2 substrate which enabled

appreciable light absorption and, coupled with an advance in dye design, appreciable photocurrent generation. In contrast to previous reports of sub-1% efficient devices, Grätzel and O'Regan's dye cell efficiency was over 7%, launching intense research into the field of DSSCs that has only accelerated in the two decades since. A schematic that well-illustrates both the 1991 Grätzel cell and the DSSCs fabricated and described in this dissertation is shown in Figure 1-6. A step-by-step guide to DSSC fabrication can be found in Section 2.3, which also provides more detailed insight into some of the design considerations associated with the device components shown in Figure 1-6.

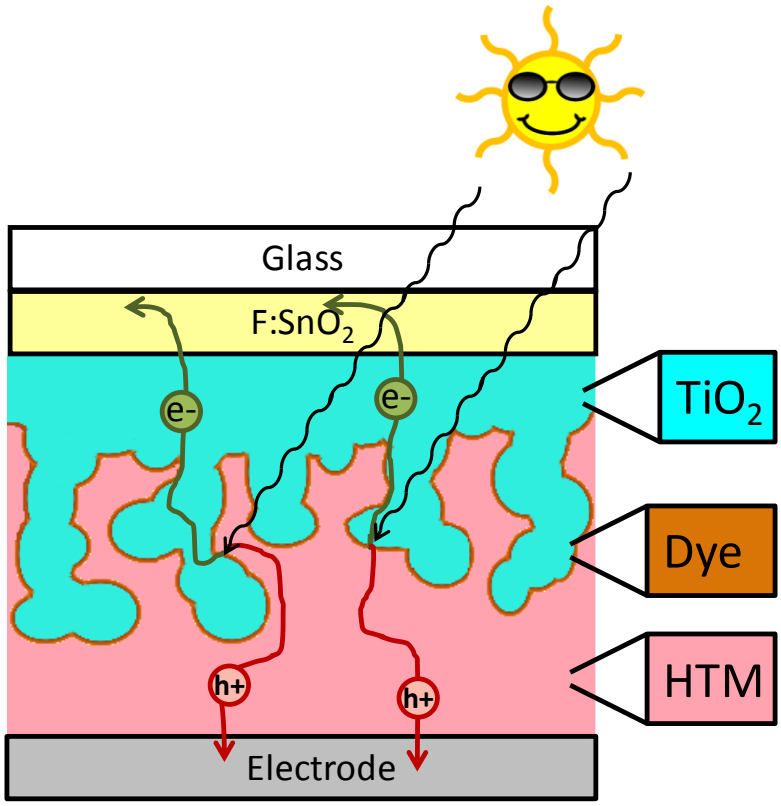


Figure 1-6: Schematic of an archetypal dye-sensitized solar cell (DSSC). Starting with a glass substrate coated with the transparent conductor fluorine-doped tin oxide (FTO), a nanoporous TiO_2 film ~1 – 20 µm thick is deposited to serve as the photoanode. Dye molecules are then adsorbed onto the TiO_2 surface, typically through a solution-based process, to form a thin monolayer ~1 nm thick. The pores of the TiO_2 are then filled with the hole-transport material (HTM) which can be either liquid-based or solid-state. Finally, a back electrode is deposited; back electrodes are typically a thin metal film and material choice is related to the HTM. The schematic also identifies the basic light absorption and charge collection pathways: light shines through the transparent front electrode and is absorbed by a dye molecule, generating an excited electron-hole pair. The electron is injected into the TiO_2 where it diffuses to the front electrode while the hole diffuses through the HTM to the back electrode.

The circuitous movement of the electron and hole charge carriers shown in Figure 1-6 is indicative of an important characteristic of DSSCs, that charge collection is driven by diffusion rather than drift. Diffusion tends to be much slower than electric field-driven transport (*i.e.* drift) but this is counteracted by a practical advantage of the Grätzel cell design: unlike the traditional solar cells described in Section 1.3 above, DSSCs are "majority carrier devices"—TiO_2 is an *n*-type semiconductor and is responsible for bringing electrons to the front electrode, while the HTM brings holes to the rear electrode. Because minority carrier lifetimes are, as a result, not critical for device operation, there is less need for ultrapure materials [23]. Coupled with the fact that earth-abundant, inexpensive materials can be used for all of the DSSC components, this results in a solar cell technology that can be scaled to high production volumes at low cost.

A second advantage of the DSSC architecture is that its various components can be tuned independently of one another, opening up limitless research avenues for DSSC progress and expanding the number of possible commercial applications. Perhaps the subject of most research is modification of the dye structure to better facilitate light absorption and charge collection. The dye used in the 1991 DSSC was a metallorganic molecule with a ruthenium atom at the center. The N3 ruthenium dye (Figure 1-7a) was developed shortly thereafter [24] and quickly became a staple of DSSC research as well as a starting point for further dye modification. Ru dyes are desirable due to their wide absorption bands in the visible spectrum, strong attachment to TiO_2 through -COOH groups, and their ability to rapidly inject electrons into TiO_2, which is facilitated by a metal-to-ligand charge transfer (MLCT) process in which light absorption excites an electron from the Ru atom into an orbital localized near the -COOH groups of the dye ligands (*i.e.* in close proximity to the TiO_2 surface) [20]. Ru dyes, however, are not without disadvantages, namely their inclusion of ruthenium, a highly rare element, and their relatively weak absorption coefficients.

These shortcomings motivated the development of all-organic "donor-π-bridge-acceptor (D-π-A) dyes which provide even greater freedom for chemical modification, have stronger (though typically narrower) light absorption spectra, are non-toxic, and use earth-abundant materials [20]. The basic structure of these D-π-A dyes is that a donor

region, where the highest occupied molecular orbital is localized (HOMO), is located far away from the surface attaching groups but is connected to it by a conjugated π backbone. The lowest unoccupied molecular orbital (LUMO) is localized near the attaching group (typically –COOH as in the Ru dyes) so that, as in the Ru dyes, the light excitation yields an excited electron located in close proximity to the TiO_2 surface, allowing for rapid injection. The most common structure for these dyes involves a triphenylamine-based donor group and a cyanoacrylic acid-based acceptor group. The WN1 dye used in Chapter 3, Chapter 4, and Chapter 6 has such a structure, as does the dye Y123 shown in Figure 1-7b. Y123 was co-sensitized with a zinc porphyrin D-π-A dye (Figure 1-7c) (representing another class of dye molecules not discussed in this thesis) to achieve the DSSC efficiency record of 12.3% [25].

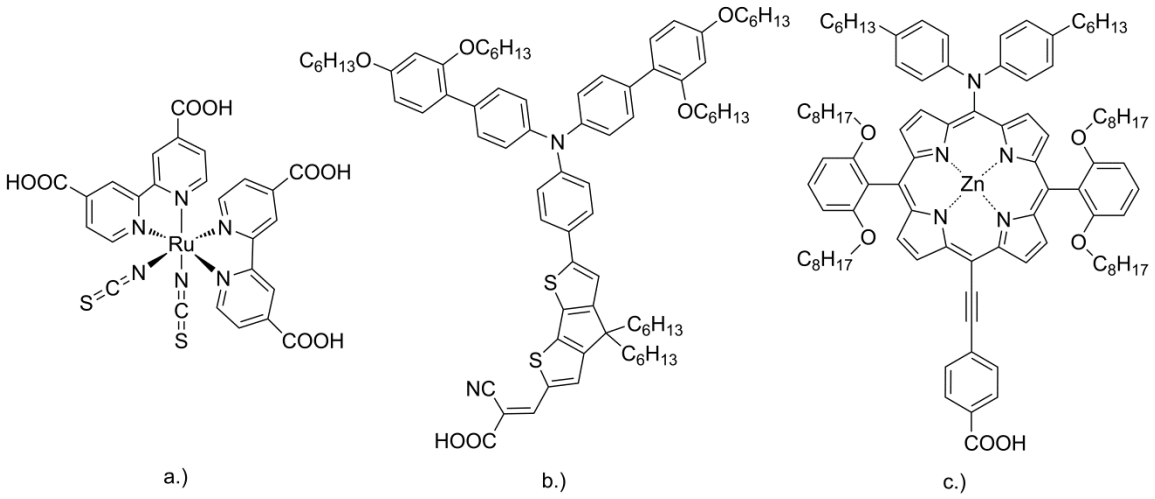


Figure 1-7: Structures of the ruthenium dye N3, a.), organic D-π-A dye Y123, b.), and zinc porphyrin D-π-A dye YD2-*o*-C8, c.).

The world record 12.3% efficiency DSSC also provides an excellent example of engineering of the HTM. In this device the iodide/triiodide redox couple was exchanged for a cobalt (II)/(III)-based redox couple [25]. The reason for this swap is to enable a higher device V_{OC}; the iodide/triiodide redox couple has a large overpotential for dye reduction (also referred to as "regeneration") whereas cobalt has a reduced driving force for this reaction, enabling a higher maximum V_{OC} (the maximum achievable V_{OC} is bound by the TiO_2 conduction band level and the redox potential (or HOMO) of the HTM; see Section 1.4.2 below) [20]. The use of the cobalt HTM system, however, brings with it

new engineering challenges for DSSCs. Compared to the small size of the I^- and I_3^- ions, the $Co^{II/III}$ tris(bipyridyl) molecule in the redox system employed by Yella *et al*. is approximately the same size as the N3 dye in Figure 1-7a; movement of holes in DSSCs requires the diffusion of these redox species from oxidized dye molecules to the back electrode (Figure 1-6) and the slower diffusion of the large Co-based molecules leads to constraints in pore diameter and photoanode thickness [25]. A second consideration which will be discussed in more detail in Section 1.4.2 below is that recombination from the TiO_2 photoanode to the Co-based complexes is much faster than to iodide/triiodide.

While the cobalt system discussed above is able to achieve high V_{OC}'s and efficiencies, it does not fix one important practical problem of the iodide/triiodide system: both redox systems are liquid-based. This has obvious implications for DSSC commercialization and it is desirable to eliminate the need for impenetrable sealing as a fabrication requirement (the iodide system also has the further disadvantage of being corrosive to many back electrode materials) [20]. This consideration has motivated research into solid-state HTMs. Several inorganic HTMs have been developed such as CuI [26], CuSCN [27, 28], and most recently, $CsSnI_3$, which achieved an impressive 8.5% efficiency, the record for solid-state inorganic HTMs [29]. Organic solid-state HTMs have also been studied, including both polymers, such as P3HT (Poly(3-hexylthiophene-2,5-diyl)) [30], and small molecules, of which the most widely-used is spiro-OMeTAD (2,2',7,7'-tetrakis-(*N*,*N*-di-*p*-methoxyphenylamine)-9,9'-spirobifluorene) [31]. Spiro-OMeTAD was used in the DSSCs and QDSSCs studied in this dissertation and its structure is shown in Figure 1-8. To date, the efficiency record for a spiro-based DSSC is 7.2%, achieved in 2011 [32].

In contrast to liquid HTMs where hole transport occurs via the diffusion of charged molecules, charge transport in solid-state HTMs occurs via a hole hopping process. As with the cobalt liquid redox couple, solid-state HTMs typically suffer from a higher recombination rate than the iodide/triiodide redox couple. Solid-state HTMs must also overcome the pore-filling engineering problem. In order to successfully regenerate dye molecules and extract holes, the HTM must reach the bottom of the DSSC nanopores and conformally coat the dye-covered photoanode [33]. The high recombination rate and

difficulties involved with pore-filling result in an optimal photoanode thickness of only ~2 μm for spiro-based DSSCs in contrast to the ~10 μm thickness typical of liquid DSSCs [34]. This limits the amount of light that can be harvested in the cell and accounts for the large efficiency gap between solid-state DSSCs and liquid DSSCs.

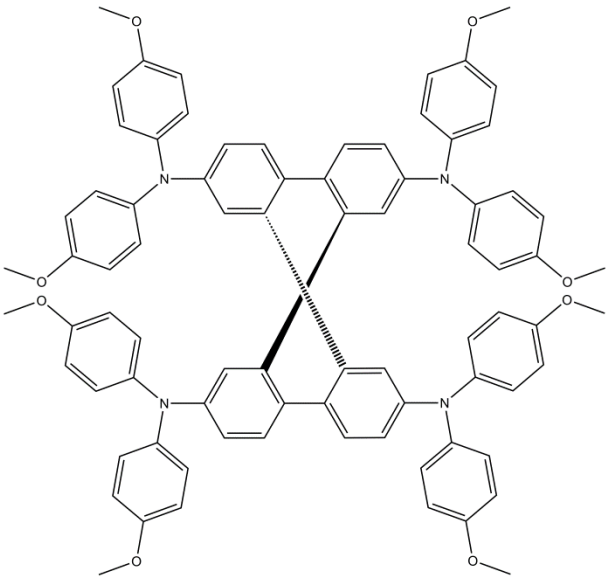


Figure 1-8: The solid-state organic hole-transport material spiro-OMeTAD (2,2',7,7'-tetrakis-(N,N-di-p-methoxyphenylamine)-9,9'-spirobifluorene). Spiro-OMeTAD, sometimes abbreviated as "spiro", was used in the DSSCs fabricated in this thesis.

There are also several areas of active research into modifying other components of the DSSC not specifically related to the research described in this dissertation. While TiO_2 is the most commonly-used material for the photoanode, there are many studies examining SnO_2 and ZnO [20]. Research into ZnO is motivated by its high electron diffusion rate, which hastens the extraction of electrons injected by dye molecules. The disadvantages of using ZnO are that it suffers from a higher recombination rate and is less stable than TiO_2 [35]. SnO_2 has a lower conduction band level than TiO_2 which can be advantageous when using dye molecules or (quantum dots) with low LUMO levels that are not able to inject electrons into TiO_2 or ZnO (which has band level positions similar to TiO_2). The downside to this lower conduction band, however, is that it typically results in a lower device V_{OC}. Like ZnO, SnO_2 has a higher electron diffusion length but faster recombination rate than TiO_2 [20]. In addition to chemical composition

of the photoanode, many studies have examined different high-surface area nanostructures that have potential advantages in charge transport rate and ease of pore-filling [20, 36]. Other areas of DSSC research seek to aid commercialization. One particularly important goal to this end is to replace the glass base of DSSCs with a flexible substrate [20, 21, 37]. Another important research area for DSSC commercialization is the development of inexpensive back electrodes, which are traditionally made of platinum in iodide-based cells and precious metals such as gold or silver in solid-state DSSCs [20, 21, 38].

1.4.2. Recombination in DSSCs

The motivation for the "engineering" component of this thesis is the reduction of the recombination rate in spiro-based solid-state DSSCs (ss-DSSCs) with the goal of bridging the liquid-solid device efficiency gap. While Figure 1-6 illustrates the successful collection of charge carriers on the micron-scale, the charge transfer pathways of most relevance to recombination—and therefore to the work contained in this dissertation—occur at the photoanode/dye/HTM interface (which in the DSSCs in Chapter 3 and Chapter 4, is a TiO_2/dye/spiro-OMeTAD interface). These processes are shown in Figure 1-9, both immediately after light absorption (Figure 1-9a) and after electron injection into TiO_2 (Figure 1-9b).

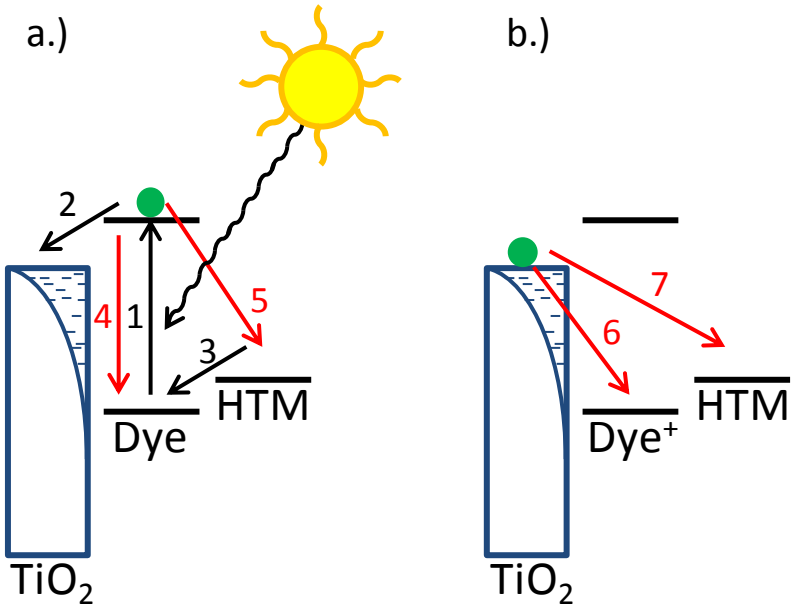


Figure 1-9: Desirable (black) and undesirable (red) charge transfer processes at the Photoanode/Dye/HTM interface in a DSSC with a TiO_2 photoanode. In a.), light absorption excites an electron from the ground state to the excited state of a dye molecule (process 1). From the excited state, the electron can be injected into the TiO_2 (process 2), relax back to the ground state without being injected (process 4), or recombine with a hole in the HTM (process 5). Process 3 indicates the reduction (or regeneration) of the oxidized dye molecule by the HTM. B.) shows the possible recombination processes of an electron in TiO_2 with either an oxidized dye molecule (process 6; note the positive charge on the dye molecule implies here that process 3 has not yet occurred) or the HTM (process 7). Both processes 6 and 7 can originate with either conduction band electrons (as shown) or electrons residing in mid-bandgap states, which are indicated by the dashes inside the TiO_2. The density of these states declines exponentially away from the conduction band. In a typical DSSC, process 2 is typically much faster than processes 4 and 5, which yields high electron injection efficiencies. Because dye regeneration (process 3) is rapid, process 6 is not significant in DSSCs and is typically ignored, but process 7, particularly when HTMs other than the iodide/triiodide redox couple are used, is important.

The use of HTMs other than iodide/triiodide typically results in the acceleration of process 7 (Figure 1-9). Recombination with the iodide/triiodide redox couple is particularly slow because it is a two-step process and the hole-transporting ions in fact carry a negative formal charge [39]. Recombination with alternative liquid HTMs (*e.g.* cobalt) as well as with solid-state HTMs, however, is a single electron process and proceeds at a much faster rate—on the microsecond timescale compared to the millisecond timescale of the iodide/triiodide redox couple [39]. Faster recombination means that photogenerated charge carriers are less likely to be successfully extracted from the solar cell. Faster recombination can result in a drop in the three critical device parameters that determine efficiency: J_{SC}, which indicates the number of charge carriers

that can be extracted with zero applied bias; V_{OC} which indicates the bias at which net current is zero (*i.e.* photocurrent and dark current completely cancel out); and fill factor, which is a fraction defined as the maximum power (current times voltage) produced by the solar cell divided by the product of J_{SC} and V_{OC} (note: these parameters are described in more depth in Section 2.4, which discusses current-voltage device measurements).

While Figure 1-9b depicts recombination involving electrons in the conduction band of TiO_2, in fact, recombination can also involve electrons that lie in the bandgap of TiO_2. Nanoporous TiO_2 is characterized by an exponential distribution of trap states located within the TiO_2 bandgap. These states play an important role in electron diffusion, as electrons in the conduction band are constantly falling into and being released from these traps [20]. With respect to recombination, many of these states are theorized to be located near the surface of the TiO_2 nanoparticles, placing them in close proximity to holes travelling through the HTM. As a consequence of the exponential distribution of these mid-bandgap states below the conduction band and the trap-release model of electron diffusion, there is a strong dependence of recombination rate on applied voltage. As a bias is applied to a DSSC, these bandgap states are filled, raising the quasi-Fermi level (E_F) inside the TiO_2, as shown in Figure 1-10.

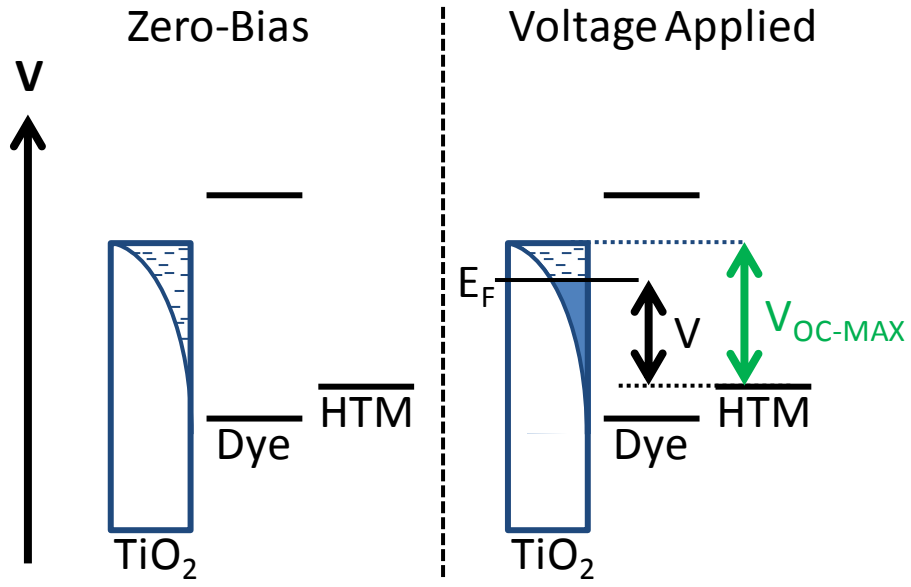


Figure 1-10: Schematic (not to scale) of the filling of mid-bandgap trap states in TiO_2 as a bias is applied to a solid-state DSSC. Empty states are indicated by dashes inside of the TiO_2, while the filling of these states is indicated by solid blue. The device voltage is equal to the potential difference between the Fermi level, E_F, inside the TiO_2 and the highest occupied molecular orbital (HOMO) of the hole-transport material (HTM). The highest achievable V_{OC} ($V_{OC\text{-}MAX}$) is limited by the TiO_2 conduction band level and HTM HOMO.

From the perspective of recombination solely through conduction band states, an increase in recombination rate would be expected as E_F increases due to the increased probability of conduction band states being occupied. For recombination involving bandgap/trap states, there are two considerations for recombination rate as a function of bias: the first is that increases in bias lead to an exponential increase in the population of filled bandgap states; the second is that the new states filled with each ΔV increase in bias have a larger driving force for recombination than those states deeper into the bandgap (in contrast to recombination solely from conduction band states, where the driving force for recombination is independent of applied bias). The first consideration leads to an increase in the recombination rate—which is the product of the electron concentration, n, and recombination rate constant, k_R—with increased bias due to an increase of n, and the second consideration would also be expected to lead to an increase in recombination—through an increase in k_R—but in fact it does not. This is because this recombination reaction is believed to reside in the Marcus inverted regime wherein an increase in driving force leads, unexpectedly, to a decrease in k_R [40]. This drop in k_R, however,

does not substantially affect the relationship of recombination rate with bias and the dominant trend is an increased recombination rate with increased bias [39].

Much research has been done to better understand the nature of the recombination process in liquid and solid-state DSSCs and the conclusion of the most thorough assessments suggest that recombination processes involving both conduction band and mid-bandgap states are important [40, 41]. Understanding these recombination pathways has also informed the development of strategies to minimize recombination and thereby improve device performance. One such strategy is to passivate the TiO_2 surface and eliminate the surface states that contribute to recombination. A $TiCl_4$ chemical bath treatment of the nanopoprous-TiO_2 photoanode has proven to be particularly advantageous for this purpose and is now a standard part of the DSSC fabrication process [42-45]. Lithium ions and the molecule *tert*-butyl pyridine have also been demonstrated to reduce recombination, and the addition of these species to the HTM has also become a standard part of DSSC fabrication [46]. These additives diminish the Coulombic attraction that helps drive recombination by screening the charges at the TiO_2/HTM interface.

1.4.3. Recombination Barrier Layers

Another means of slowing down recombination is the application of an insulating layer to the photoanode surface that traps in electrons, providing separation from holes in the HTM, and serves as a potential barrier to recombination. These so-called "barrier layers" were first developed in DSSCs by Palomares *et al.* through the chemical bath deposition (CBD) of a thin Al_2O_3 layer atop a nanoporous TiO_2 photoanode prior to dye adsorption [47]. These barrier layers can both passivate surface sites as well as serve as a tunneling barrier to recombination involving both conduction band and mid-bandgap electrons. The work by Palomares *et al*. motivated several similar studies of CBD barrier layers made of Al_2O_3 [28, 47-52], SiO_2 [48], ZrO_2 [48, 53], MgO [49, 54], $SrTiO_3$ [50], Nb_2O_5 [50], $CaCO_3$ [55, 56], In_2O_3 [53], and HfO_2 [57]. Another popular means of growing such barrier layers is via atomic layer deposition (ALD) [58], which, compared to the CBD method, provides superior growth rate control and the ability to better penetrate nanoporous substrates and achieve uniform growth [59]. ALD has been used to

grow barrier layers made of Al_2O_3 [60-72], HfO_2 [66, 73], ZrO_2 [74], SiO_2 [75, 76], and Ga_2O_3 [77].

These studies—using both CBD and ALD growth methods—identified several important characteristics of barrier layers. As mentioned, they can suppress recombination by both passivating surface states and serving as a tunneling barrier. They can generate a surface dipole on the photoanode that, depending on direction, can either lift or lower the photoanode conduction band (which can in turn raise or lower the device V_{OC}). Barrier layers must readily adsorb dye molecules like the photoanode they are deposited upon (hence the popularity of metal oxide barriers); otherwise less light will be absorbed and device current will drop. Given their insulating nature, barrier layers can also inhibit the desirable injection of electrons into the photoanode (Figure 1-9, process 2) which can lead to a decrease in electron collection efficiency and device current. The inhibition of this electron injection process is a function of the barrier layer thickness, its conduction band level, the dye LUMO level, and the excited state relaxation rate constant of the dye (Figure 1-9, process 4), which injection is ultimately competing against. This concept has been studied in depth previously in the literature with Al_2O_3, which is possibly the most commonly-used barrier layer material [59, 64].

With these characteristics in mind, the ideal application scenario for a barrier layer to achieve a large improvement in device efficiency involves: a device with a high baseline recombination rate, a barrier layer that readily adsorbs dye molecules, a barrier layer that can be deposited at a low growth rate, a barrier layer that exerts a surface dipole that pulls up the photoanode conduction band, and a barrier layer with a conduction band level higher than the photoanode's but lower than the dye LUMO. Fulfilling all of these criteria is not trivial, but the barrier layers described in this dissertation (Chapter 3, Chapter 4, and Chapter 5) come close, being metal oxides, used in conjunction with the spiro-OMeTAD HTM (*i.e.* high recombination rate), and deposited via ALD at low growth rates on the order of 1 Å / ALD cycle.

1.4.4. Dye Orientation

The motivation for the "characterization" component of this thesis is to better understand the orientation and binding configuration of dye molecules adsorbed on the

anatase (101) TiO_2 surface, which is the surface structure of the TiO_2 nanoparticles that compose the most popular DSSC photoanode [20]. At a broader level, Chapter 6 uses a sophisticated experimental measurement to determine the orientation of a particular organic D-π-A dye and compares it to computational studies of the same system in order to assess the ability of simulations to capture real-world behavior. The orientation of adsorbed dye molecules has important implications for device performance. While DSSC dyes are typically designed such that the LUMO is localized near the surface-binding group, dye conformation dictates the proximity of the dye HOMO to the photoanode surface. Having the HOMO close to the photoanode can result in an increase in recombination (Figure 1-9, process 6) while having it oriented away from the surface can increase its proximity to the HTM and speed dye regeneration (Figure 1-9, process 3), which further reduces the possibility of recombination with the oxidized dye (Figure 1-9, process 6) [78]. Orientation affects how dye molecules will pack on the surface, which dictates the maximum achievable surface coverage as well as the accessibility of the HTM to the photoanode surface, which can speed recombination (Figure 1-9, process 7) [79]. Orientation impacts the role played by dye dipoles in raising or lowering the photoanode conduction band. Taking as an example organic D-π-A dyes such as the one shown in Figure 1-7b, dye molecules tend to have characteristic dipoles due to the placement of electron donating (the "donor") and electron withdrawing (the "acceptor") groups at opposite ends of the structure. This typically results in a dipole that points away from the electron-rich binding group of the dye and so has the ability to raise the photoanode conduction band (thereby improving device V_{OC}) [80-82]. Because this dipole vector essentially lies in the backbone of the dye, the dye orientation dictates what the surface normal component of the dipole will be (note: only the surface normal component of the dipole affects the photoanode conduction band level). As will be discussed in Chapter 6, very few direct measurements of dye orientation have been performed experimentally; rather, orientation has typically been surmised through a combination of computational studies and inferences made from device performance. The work presented in this dissertation serves to bridge the computational/experimental divide to improve understanding and future prediction of dye orientation.

1.4.5. Quantum Dot-Sensitized Solar Cells (QDSSCs)

While QDSSCs—having their own acronym—are sometimes classified as comprising a distinct type of solar cell, they instead represent a modular modification of the DSSC design in which the absorbing material is changed from a monolayer of adsorbed dye molecules to a coating of nanometer-scale particles of semiconductor materials [83, 84]. Quantum dots (QDs) are so-called because their small size leads to a quantization—rather than a continuum—of energy states. This quantization of states leads to a larger optical gap than that found in the corresponding bulk material and so the optical gap (and therefore light absorption properties) becomes a function of the QD size. In this way, QD absorbers can be tuned for optimal band alignment and light absorption in the solar cell.

The most commonly used QDSSC absorbing materials are chalcogenide semiconductors such as Sb_2S_3 [85-89], In_2S_3 [90], CdS [91-98], CdSe [99-102], and PbS [103-111]. The absorbing materials can be either grown directly on the photoanode surface via a gas phase or solution process or grown *ex situ* and then deposited onto the photoanode and attached via a linker molecule. Note that while not the subject of the work described in this thesis, a subtle modification of the QDSSC is the "extremely thin absorber" (ETA) solar cell in which a continuous thin film—rather than discrete quantum dots—of the absorbing material is grown on the photoanode. This can be advantageous when the bulk material already possesses desirable band level energies, for instance as in the Sb_2S_3 references cited above. This ETA/QDSSC distinction, however, is one of nomenclature rather than of fundamental composition and operating principles.

As noted in Section 1.1 above, QDSSCs and DSSCs can be grouped into the broader category of "sensitized solar cells" (SSCs). While the preceding discussion in this section (1.4) has been specifically geared towards DSSCs, as with QDSSCs versus ETA cells, the distinction between QDSSCs and DSSCs is primarily one of nomenclature rather than design and operation. There are, however, important differences in relevant recombination pathways between DSSCs and QDSSCs. Because QDs typically have a lower surface coverage than dye molecules, there is a larger interfacial contact area between the photoanode and the HTM, which results in enhanced recombination (Figure

1-9, process 7) (note that this is not the case with ETA cells wherein the absorber fully coats the photoanode surface). Additionally, recombination to oxidized QDs is more significant than to oxidized dye molecules (Figure 1-9, process 6). This is due to both the nature of the photoanode/QD interface—QDs for example, have been shown to introduce mid-bandgap states into TiO_2 [112]—as well as the relatively slow regeneration of oxidized QDs as compared to oxidized dye molecules [113].

QDSSCs are relatively younger than their DSSC counterparts and they have a longer path to go to reach their theoretical limits, with the best devices to date (Sb_2S_3 ETA cells) demonstrating efficiencies just over 6% [87, 114]. One reason for this is that QDSSC (and ETA) cells have been designed in large part using considerations and parameters optimized for DSSCs that may not necessarily apply to QDSSCs. Another reason for this is that unlike dye molecules, QDs in a QDSSC are typically heterogeneous, differing in size, energy levels, and concentration of defect and surface states, all of which can reduce performance and make characterization difficult. There remains, therefore, much room for performance enhancement and improved understanding of QDSSCs. With respect to the barrier layers described for DSSCs in Section 1.4.3 above, QDSSCs offer some attractive qualities. The generally higher recombination rates and the relevance of recombination to both oxidized QDs and to the HTM in QDSSCs means that barrier layers may yield substantial improvements in device performance, and this is in fact what is observed in Chapter 5. Furthermore, the fact that metal oxide barrier layers can also be grown on the QDs themselves (in contrast to dye molecules) enables barrier layer research to provide insight into charge transfer processes between the absorbing material and the HTM; this too is described in Chapter 5 and Appendix B:.

1.5. Collaborations & Copyright

The research described in this dissertation could not have been carried out with the extensive help of others. Following each chapter and appendix is a subsection acknowledging the role of collaborators in the respective work. Relevant copyright information for research that has already been published in journals is also included in these subsections.

1.6. References

[1] Royal Dutch Shell, Energy Scenarios to 2050, The Hague, Netherlands, 2008.
[2] G. Doucet, Deciding the Future: Energy Policy Scenarios to 2050, World Energy Council, London, United Kingdom, 2007.
[3] BP, Statistical Review of World Energy 2012, 2012.
[4] Intergovernmental Panel on Climate Change, Contribution of Working Groups I, II and III to the Fourth Assessment Report of the Intergovernmental Panel on Climate Change, Geneva, Switzerland, 2007.
[5] N. Nakicenovic, J. Alcamo, G. Davis, B. de Vries, J. Fenhann, S. Gaffin, K. Gregory, A. Grübler, T. Yong Jung, T. Kram, E. Lebre La Rovere, L. Michaelis, S. Mori, T. Morita, W. Pepper, H. Pitcher, L. Price, K. Riahi, A. Roehrl, H.-H. Rogner, A. Sankovski, M. Schlesinger, P. Shukla, S. Smith, R. Swart, S. van Rooijen, N. Victor, Z. Dadi, Emissions Scenarios, Intergovernmental Panel on Climate Change, Geneva, Switzerland, 2000.
[6] T. Boden, B. Andres, G. Marland, Carbon Dioxide Information Analysis Center, 2012.
[7] N.S. Lewis, G. Crabtree, Basic Research Needs for Solar Energy Utilization: Report of the basic energy sciences workshop on solar energy utilization, April 18-21, 2005, U.S. Department of Energy, 2005.
[8] A. Sharma, H. Wicht, The Global Solar Power Industry for 2013: Predictions and Prospects for the Year Ahead, Englewood, Colorado, 2012.
[9] D.M. Chapin, C.S. Fuller, G.L. Pearson, Journal of Applied Physics 25/5 (1954) 676.
[10] M.B. Prince, Journal of Applied Physics 26/5 (1955) 534.
[11] J. Zhao, A. Wang, M.A. Green, F. Ferrazza, Applied Physics Letters 73/14 (1998) 1991.
[12] M.A. Green, K. Emery, Y. Hishikawa, W. Warta, E.D. Dunlop, Progress in Photovoltaics: Research and Applications 21/1 (2013) 1.
[13] T.M. Razykov, C.S. Ferekides, D. Morel, E. Stefanakos, H.S. Ullal, H.M. Upadhyaya, Solar Energy 85/8 (2011) 1580.
[14] A.L. Fahrenbruch, R.H. Bube, Fundamentals of Solar Cells: Photovoltaic Solar Energy Conversion, Academic Press, 1983.
[15] J. Nelson, The Physics of Solar Cells, Imperial College Press, 2003.
[16] W. Shockley, H.J. Queisser, Journal of Applied Physics 32/3 (1961) 510.
[17] G. Conibeer, Materials Today 10/11 (2007) 42.
[18] NREL, ASTM G173-03 Tables, http://rredc.nrel.gov/solar/spectra/am1.5/.
[19] M.D. Archer, A.J. Nozik (Eds.), Nanostructured and Photoelectrochemical Systems for Solar Photon Conversion, Imperial College Press, London, 2008.
[20] A. Hagfeldt, G. Boschloo, L. Sun, L. Kloo, H. Pettersson, Chemical Reviews 110/11 (2010) 6595.
[21] J.B. Baxter, Journal of Vacuum Science & Technology A: Vacuum, Surfaces, and Films 30/2 (2012) 020801.
[22] B.E. Hardin, H.J. Snaith, M.D. McGehee, Nat Photon 6/3 (2012) 162.
[23] B. O'Regan, M. Grätzel, Nature 353/6346 (1991) 737.

[24] M.K. Nazeeruddin, A. Kay, I. Rodicio, R. Humphry-Baker, E. Mueller, P. Liska, N. Vlachopoulos, M. Grätzel, Journal of the American Chemical Society 115/14 (1993) 6382.
[25] A. Yella, H.-W. Lee, H.N. Tsao, C. Yi, A.K. Chandiran, M.K. Nazeeruddin, E.W.-G. Diau, C.-Y. Yeh, S.M. Zakeeruddin, M. Grätzel, Science 334/6056 (2011) 629.
[26] K. Tennakone, G.R.R.A. Kumara, A.R. Kumarasinghe, K.G.U. Wijayantha, P.M. Sirimanne, Semiconductor Science and Technology 10/12 (1995) 1689.
[27] G.R.R.A. Kumara, A. Konno, G.K.R. Senadeera, P.V.V. Jayaweera, D.B.R.A. De Silva, K. Tennakone, Solar Energy Materials and Solar Cells 69/2 (2001) 195.
[28] B.C. O'Regan, S. Scully, A.C. Mayer, E. Palomares, J. Durrant, The Journal of Physical Chemistry B 109/10 (2005) 4616.
[29] I. Chung, B. Lee, J. He, R.P.H. Chang, M.G. Kanatzidis, Nature 485/7399 (2012) 486.
[30] P. Ravirajan, A.M. Peiró, M.K. Nazeeruddin, M. Grätzel, D.D.C. Bradley, J.R. Durrant, J. Nelson, The Journal of Physical Chemistry B 110/15 (2006) 7635.
[31] U. Bach, D. Lupo, P. Comte, J.E. Moser, F. Weissortel, J. Salbeck, H. Spreitzer, M. Grätzel, Nature 395/6702 (1998) 583.
[32] J. Burschka, A. Dualeh, F. Kessler, E. Baranoff, N.-L. Cevey-Ha, C. Yi, M.K. Nazeeruddin, M. Grätzel, Journal of the American Chemical Society 133/45 (2011) 18042.
[33] I.K. Ding, N. Tétreault, J. Brillet, B.E. Hardin, E.H. Smith, S.J. Rosenthal, F. Sauvage, M. Grätzel, M.D. McGehee, Advanced Functional Materials 19/15 (2009) 2431.
[34] L. Schmidt-Mende, S.M. Zakeeruddin, M. Grätzel, Applied Physics Letters 86/1 (2005) 3504.
[35] Q. Zhang, C.S. Dandeneau, X. Zhou, G. Cao, Advanced Materials 21/41 (2009) 4087.
[36] N. Tetreault, M. Grätzel, Energy & Environmental Science 5/9 (2012) 8506.
[37] M. Toivola, J. Halme, K. Miettunen, K. Aitola, P.D. Lund, International Journal of Energy Research 33/13 (2009) 1145.
[38] K.S. Lee, Y. Lee, J.Y. Lee, J.-H. Ahn, J.H. Park, ChemSusChem 5/2 (2012) 379.
[39] H.J. Snaith, L. Schmidt-Mende, Advanced Materials 19/20 (2007) 3187.
[40] P. Salvador, M.G. Hidalgo, A. Zaban, J. Bisquert, The Journal of Physical Chemistry B 109/33 (2005) 15915.
[41] G. Schlichthörl, S.Y. Huang, J. Sprague, A.J. Frank, The Journal of Physical Chemistry B 101/41 (1997) 8141.
[42] P.M. Sommeling, B.C. O'Regan, R.R. Haswell, H.J.P. Smit, N.J. Bakker, J.J.T. Smits, J.M. Kroon, J.A.M. van Roosmalen, The Journal of Physical Chemistry B 110/39 (2006) 19191.
[43] B.C. O'Regan, J.R. Durrant, P.M. Sommeling, N.J. Bakker, The Journal of Physical Chemistry C 111/37 (2007) 14001.
[44] S.-W. Lee, K.-S. Ahn, K. Zhu, N.R. Neale, A.J. Frank, The Journal of Physical Chemistry C 116/40 (2012) 21285.
[45] A. Marchioro, A. Dualeh, A. Punzi, M. Grätzel, J.-E. Moser, The Journal of Physical Chemistry C 116/51 (2012) 26721.

[46] J. Kruger, R. Plass, L. Cevey, M. Piccirelli, M. Grätzel, U. Bach, Applied Physics Letters 79/13 (2001) 2085.
[47] E. Palomares, J.N. Clifford, S.A. Haque, T. Lutz, J.R. Durrant, Chemical Communications/14 (2002) 1464.
[48] E. Palomares, J.N. Clifford, S.A. Haque, T. Lutz, J.R. Durrant, Journal of the American Chemical Society 125/2 (2003) 475.
[49] K.M.P. Bandaranayake, M.K. Indika Senevirathna, P.M.G.M. Prasad Weligamuwa, K. Tennakone, Coordination Chemistry Reviews 248/13-14 (2004) 1277.
[50] Y. Diamant, S. Chappel, S.G. Chen, O. Melamed, A. Zaban, Coordination Chemistry Reviews 248/13-14 (2004) 1271.
[51] X.-T. Zhang, H.-W. Liu, T. Taguchi, Q.-B. Meng, O. Sato, A. Fujishima, Solar Energy Materials and Solar Cells 81/2 (2004) 197.
[52] S.-Q. Fan, Y. Geng, C. Kim, S. Paik, J. Ko, Materials Chemistry and Physics 132/2-3 (2012) 943.
[53] D.B. Menzies, Q. Dai, L. Bourgeois, R.A. Caruso, Y.-B. Cheng, G.P. Simon, L. Spiccia, Nanotechnology 18/12 (2007) 125608.
[54] P. Docampo, P. Tiwana, N. Sakai, H. Miura, L. Herz, T. Murakami, H.J. Snaith, The Journal of Physical Chemistry C 116/43 (2012) 22840.
[55] Z.-S. Wang, M. Yanagida, K. Sayama, H. Sugihara, Chemistry of Materials 18/12 (2006) 2912.
[56] S. Lee, J. Young Kim, K. Sun Hong, H. Suk Jung, J.-K. Lee, H. Shin, Solar Energy Materials and Solar Cells 90/15 (2006) 2405.
[57] P. Ramasamy, M.-S. Kang, H.-J. Cha, J. Kim, Materials Research Bulletin 48/1 (2013) 79.
[58] J.R. Bakke, K.L. Pickrahn, T.P. Brennan, S.F. Bent, Nanoscale 3/9 (2011) 3482.
[59] J. Guo, C. She, T. Lian, The Journal of Physical Chemistry C 111/25 (2007) 8979.
[60] M. Law, L.E. Greene, A. Radenovic, T. Kuykendall, J. Liphardt, P. Yang, The Journal of Physical Chemistry B 110/45 (2006) 22652.
[61] T.W. Hamann, O.K. Farha, J.T. Hupp, The Journal of Physical Chemistry C 112/49 (2008) 19756.
[62] C. Lin, F.-Y. Tsai, M.-H. Lee, C.-H. Lee, T.-C. Tien, L.-P. Wang, S.-Y. Tsai, Journal of Materials Chemistry 19/19 (2009) 2999.
[63] T.-C. Tien, F.-M. Pan, L.-P. Wang, C.-H. Lee, Y.-L. Tung, S.-Y. Tsai, C. Lin, F.-Y. Tsai, S.-J. Chen, Nanotechnology 20/30 (2009) 305201.
[64] L.J. Antila, M.J. Heikkilä, V. Aumanen, M. Kemell, P. Myllyperkiö, M. Leskelä, J.E.I. Korppi-Tommola, The Journal of Physical Chemistry Letters 1/2 (2009) 536.
[65] T.-C. Tien, F.-M. Pan, L.-P. Wang, F.-Y. Tsai, C. Lin, The Journal of Physical Chemistry C 114/21 (2010) 10048.
[66] M. Shanmugam, M.F. Baroughi, D. Galipeau, Thin Solid Films 518/10 (2010) 2678.
[67] M.J. DeVries, M.J. Pellin, J.T. Hupp, Langmuir 26/11 (2010) 9082.
[68] C. Prasittichai, J.T. Hupp, The Journal of Physical Chemistry Letters 1/10 (2010) 1611.
[69] A.M. Spokoyny, T.C. Li, O.K. Farha, C.W. Machan, C. She, C.L. Stern, T.J. Marks, J.T. Hupp, C.A. Mirkin, Angewandte Chemie International Edition 49/31 (2010) 5339.

[70] L.J. Antila, M.J. Heikkilä, V. Mäkinen, N. Humalamäki, M. Laitinen, V. Linko, P. Jalkanen, J. Toppari, V. Aumanen, M. Kemell, P. Myllyperkiö, K. Honkala, H. Häkkinen, M. Leskelä, J.E.I. Korppi-Tommola, The Journal of Physical Chemistry C 115/33 (2011) 16720.
[71] V. Mäkinen, K. Honkala, H. Häkkinen, The Journal of Physical Chemistry C 115/18 (2011) 9250.
[72] T.P. Brennan, J.R. Bakke, I.K. Ding, B.E. Hardin, W.H. Nguyen, R. Mondal, C.D. Bailie, G.Y. Margulis, E.T. Hoke, A. Sellinger, M.D. McGehee, S.F. Bent, Physical Chemistry Chemical Physics 14/35 (2012) 12130.
[73] B. Bills, M. Shanmugam, M.F. Baroughi, Thin Solid Films 519/22 (2011) 7803.
[74] T.C. Li, M.S. Goes, F. Fabregat-Santiago, J. Bisquert, P.R. Bueno, C. Prasittichai, J.T. Hupp, T.J. Marks, Journal of Physical Chemistry C 113/42 (2009) 18385.
[75] M. Shanmugam, B. Bills, M.F. Baroughi, Materials Research Society Symposium Proceedings 1260/T10 (2010) 1.
[76] H.-J. Son, X. Wang, C. Prasittichai, N.C. Jeong, T. Aaltonen, R.G. Gordon, J.T. Hupp, Journal of the American Chemical Society 134/23 (2012) 9537.
[77] A.K. Chandiran, N. Tetreault, R. Humphry-Baker, F. Kessler, E. Baranoff, C. Yi, M.K. Nazeeruddin, M. Grätzel, Nano Letters (2012).
[78] M. Pastore, F. De Angelis, Physical Chemistry Chemical Physics 14/2 (2012) 920.
[79] T. Marinado, K. Nonomura, J. Nissfolk, M.K. Karlsson, D.P. Hagberg, L. Sun, S. Mori, A. Hagfeldt, Langmuir 26/4 (2009) 2592.
[80] W.H. Howie, F. Claeyssens, H. Miura, L.M. Peter, Journal of the American Chemical Society 130/4 (2008) 1367.
[81] P. Chen, J.H. Yum, F.D. Angelis, E. Mosconi, S. Fantacci, S.-J. Moon, R.H. Baker, J. Ko, M.K. Nazeeruddin, M. Grätzel, Nano Letters 9/6 (2009) 2487.
[82] A. Dualeh, F. De Angelis, S. Fantacci, T. Moehl, C. Yi, F. Kessler, E. Baranoff, M.K. Nazeeruddin, M. Grätzel, The Journal of Physical Chemistry C 116/1 (2012) 1572.
[83] G. Hodes, D. Cahen, Accounts of Chemical Research 45/5 (2012) 705.
[84] P.V. Kamat, Accounts of Chemical Research (2012) 1906.
[85] J.A. Chang, J.H. Rhee, S.H. Im, Y.H. Lee, H.-j. Kim, S.I. Seok, M.K. Nazeeruddin, M. Grätzel, Nano Letters 10/7 (2010) 2609.
[86] S.-J. Moon, Y. Itzhaik, J.-H. Yum, S.M. Zakeeruddin, G. Hodes, M. Grätzel, The Journal of Physical Chemistry Letters 1/10 (2010) 1524.
[87] S.H. Im, C.-S. Lim, J.A. Chang, Y.H. Lee, N. Maiti, H.-J. Kim, M.K. Nazeeruddin, M. Grätzel, S.I. Seok, Nano Letters 11/11 (2011) 4789.
[88] J.A. Chang, S.H. Im, Y.H. Lee, H.-j. Kim, C.-S. Lim, J.H. Heo, S.I. Seok, Nano Letters 12/4 (2012) 1863.
[89] H. Wedemeyer, J. Michels, R. Chmielowski, S. Bourdais, T. Muto, M. Sugiura, G. Dennler, J. Bachmann, Energy & Environmental Science (2013) 67.
[90] S.K. Sarkar, J.Y. Kim, D.N. Goldstein, N.R. Neale, K. Zhu, C.M. Elliott, A.J. Frank, S.M. George, The Journal of Physical Chemistry C 114/17 (2010) 8032.
[91] M. Shalom, S. Dor, S. Rühle, L. Grinis, A. Zaban, The Journal of Physical Chemistry C 113/9 (2009) 3895.
[92] C.-F. Chi, P. Chen, Y.-L. Lee, I.P. Liu, S.-C. Chou, X.-L. Zhang, U. Bach, Journal of Materials Chemistry 21/43 (2011) 17534.

[93] H. Choi, R. Nicolaescu, S. Paek, J. Ko, P.V. Kamat, ACS Nano 5/11 (2011) 9238.
[94] P. Ardalan, T.P. Brennan, H.-B.-R. Lee, J.R. Bakke, I.K. Ding, M.D. McGehee, S.F. Bent, ACS Nano 5/2 (2011) 1495.
[95] T.P. Brennan, P. Ardalan, H.-B.-R. Lee, J.R. Bakke, I.K. Ding, M.D. McGehee, S.F. Bent, Advanced Energy Materials 1/6 (2011) 1169.
[96] Q. Zhang, X. Guo, X. Huang, S. Huang, D. Li, Y. Luo, Q. Shen, T. Toyoda, Q. Meng, Physical Chemistry Chemical Physics 13/10 (2011) 4659.
[97] Z. Yang, C.-Y. Chen, C.-W. Liu, C.-L. Li, H.-T. Chang, Advanced Energy Materials 1/2 (2011) 259.
[98] K.E. Roelofs, T.P. Brennan, J.C. Dominguez, C.D. Bailie, G.Y. Margulis, E.T. Hoke, M.D. McGehee, S.F. Bent, The Journal of Physical Chemistry C 117/11 (2013) 5584.
[99] S.-Q. Fan, D. Kim, J.-J. Kim, D.W. Jung, S.O. Kang, J. Ko, Electrochemistry Communications 11/6 (2009) 1337.
[100] S.-Q. Fan, B. Fang, J.H. Kim, B. Jeong, C. Kim, J.-S. Yu, J. Ko, Langmuir 26/16 (2010) 13644.
[101] H.J. Lee, D.W. Chang, S.-M. Park, S.M. Zakeeruddin, M. Grätzel, M.K. Nazeeruddin, Chemical Communications 46/46 (2010) 8788.
[102] X.-Y. Yu, B.-X. Lei, D.-B. Kuang, C.-Y. Su, Journal of Materials Chemistry 22/24 (2012) 12058.
[103] S.-m. Yang, C.-h. Huang, J. Zhai, Z.-s. Wang, L. Jiang, Journal of Materials Chemistry 12/5 (2002) 1459.
[104] R. Plass, S. Pelet, J. Krueger, M. Grätzel, U. Bach, The Journal of Physical Chemistry B 106/31 (2002) 7578.
[105] B.-R. Hyun, Y.-W. Zhong, A.C. Bartnik, L. Sun, H.D. Abruña, F.W. Wise, J.D. Goodreau, J.R. Matthews, T.M. Leslie, N.F. Borrelli, ACS Nano 2/11 (2008) 2206.
[106] H.J. Lee, P. Chen, S.-J. Moon, F.d.r. Sauvage, K. Sivula, T. Bessho, D.R. Gamelin, P. Comte, S.M. Zakeeruddin, S.I. Seok, M. Grätzel, M.K. Nazeeruddin, Langmuir 25/13 (2009) 7602.
[107] H. Lee, H.C. Leventis, S.-J. Moon, P. Chen, S. Ito, S.A. Haque, T. Torres, F. Nüesch, T. Geiger, S.M. Zakeeruddin, M. Grätzel, M.K. Nazeeruddin, Advanced Functional Materials 19/17 (2009) 2735.
[108] A. Braga, S. Giménez, I. Concina, A. Vomiero, I.n. Mora-Seró • , The Journal of Physical Chemistry Letters 2/5 (2011) 454.
[109] H.J. Snaith, A. Stavrinadis, P. Docampo, A.A.R. Watt, Solar Energy 85/6 (2011) 1283.
[110] L. Etgar, T. Moehl, S. Gabriel, S.G. Hickey, A. Eychmüller, M. Grätzel, ACS Nano 6/4 (2012) 3092.
[111] J.-W. Lee, D.-Y. Son, T.K. Ahn, H.-W. Shin, I.Y. Kim, S.-J. Hwang, M.J. Ko, S. Sul, H. Han, N.-G. Park, Sci. Rep. 3 (2013) 1.
[112] I. Hod, V. González-Pedro, Z. Tachan, F. Fabregat-Santiago, I. Mora-Seró, J. Bisquert, A. Zaban, The Journal of Physical Chemistry Letters 2/24 (2011) 3032.
[113] H.C. Leventis, F. O'Mahony, J. Akhtar, M. Afzaal, P. O'Brien, S.A. Haque, Journal of the American Chemical Society 132/8 (2010) 2743.
[114] W. Guo, Y. Shen, M. Wu, T. Ma, Chemical Communications 48/49 (2012) 6133.
[115] R.L. Puurunen, Journal of Applied Physics 97/12 (2005) 121301.

[116] T. Suntola, Materials Science Reports 4/5 (1989) 261.
[117] J.R. Bakke, Atomic Layer Deposition of Materials for Applications to Photovoltaics, Stanford University, Stanford, 2011.
[118] P. Auger, J. Phys. Radium 6/6 (1925) 205.
[119] K.D. Childs, B.A. Carlson, L.A. LaVanier, J.F. Moulder, D.F. Paul, W.F. Stickle, D.G. Watson (Eds.), Handbook of Auger Electron Spectroscopy, Physical Electronics, Inc., Eden Praire, Minnesota, 1995.
[120] R.E. Weber, W.T. Peria, Journal of Applied Physics 38/11 (1967) 4355.
[121] L.A. Harris, Journal of Applied Physics 39/3 (1968) 1419.
[122] L.A. Harris, Journal of Applied Physics 39/3 (1968) 1428.
[123] L. Kavan, M. Grätzel, Electrochimica Acta 40/5 (1995) 643.
[124] S. Ito, P. Chen, P. Comte, M.K. Nazeeruddin, P. Liska, P. Péchy, M. Grätzel, Progress in Photovoltaics: Research and Applications 15/7 (2007) 603.
[125] N.R. Neale, N. Kopidakis, J. van de Lagemaat, M. Grätzel, A.J. Frank, The Journal of Physical Chemistry B 109/49 (2005) 23183.
[126] I.-K. Ding, Pore Filling and Light Trapping of Solid-State Dye-Sensitized Solar Cells, Stanford University, Stanford, 2011.
[127] H.J. Snaith, M. Grätzel, Advanced Materials 19/21 (2007) 3643.
[128] H.J. Snaith, A.J. Moule, C. Klein, K. Meerholz, R.H. Friend, M. Grätzel, Nano Letters 7/11 (2007) 3372.
[129] B.C. O'Regan, F. Lenzmann, The Journal of Physical Chemistry B 108/14 (2004) 4342.
[130] P.R.F. Barnes, K. Miettunen, X. Li, A.Y. Anderson, T. Bessho, M. Grätzel, B.C. O'Regan, Advanced Materials 25/13 (2013) 1881.
[131] J. Stöhr, K. Baberschke, R. Jaeger, R. Treichler, S. Brennan, Physical Review Letters 47/5 (1981) 381.
[132] J. Stöhr, NEXAFS Spectroscopy, Springer-Verlag, Berlin, 1992.
[133] J. Stöhr, D.A. Outka, Physical Review B 36/15 (1987) 7891.
[134] G. Hähner, Chemical Society Reviews 35/12 (2006) 1244.
[135] J. Kohanoff, Electronic Structure Calculations for Solids and Molecules, Cambridge, New York, 2006.
[136] C.J. Cramer, Essentials of Computational Chemistry: heories and Models, John Wiley & Sons, Ltd., Hoboken, NJ, USA, 2005.
[137] D. Sholl, J.A. Steckel, Density Functional Theory: A Practical Introduction, John Wiley & Sons, Ltd., Hoboken, NJ, 2009.
[138] A.D. Becke, The Journal of Chemical Physics 98/2 (1993) 1372.
[139] K. Hermann, L.G.M. Pettersson, M.E. Casida, C. Daul, A. Goursot, A. Koester, E. Proynov, A. St-Amant, D.R. Salahub, V. Carravetta, H. Duarte, C. Friedrich, N. Godbout, J. Guan, C. Jamorski, M. Leboeuf, M. Leetmaa, M. Nyberg, S. Patchkovskii, L. Pedocchi, F. Sim, L. Triguero, A. Vela, 2011.
[140] N. Cai, S.-J. Moon, L. Cevey-Ha, T. Moehl, R. Humphry-Baker, P. Wang, S.M. Zakeeruddin, M. Grätzel, Nano Letters 11/4 (2011) 1452.
[141] Q. Yu, Y. Wang, Z. Yi, N. Zu, J. Zhang, M. Zhang, P. Wang, ACS Nano 4/10 (2010) 6032.

[142] J. Melas-Kyriazi, I.K. Ding, A. Marchioro, A. Punzi, B.E. Hardin, G.F. Burkhard, N. Tétreault, M. Grätzel, J.-E. Moser, M.D. McGehee, Advanced Energy Materials 1/3 (2011) 407.
[143] E. Palomares, J.N. Clifford, S.A. Haque, T. Lutz, J.R. Durrant, Chemical Communications/14 (2002).
[144] J.W. Ondersma, T.W. Hamann, The Journal of Physical Chemistry C 114/1 (2010) 638.
[145] R.L. Puurunen, W. Vandervorst, Journal of Applied Physics 96/12 (2004) 7686.
[146] Y. Noma, T. Kado, D. Ogata, Y. Hara, S. Hayase, Japanese Journal of Applied Physics 47/1 (2008) 505.
[147] V. Ganapathy, B. Karunagaran, S.-W. Rhee, Journal of Power Sources 195/15 (2010) 5138.
[148] A.C. Dillon, A.W. Ott, J.D. Way, S.M. George, Surface Science 322/1-3 (1995) 230.
[149] M.D. Groner, F.H. Fabreguette, J.W. Elam, S.M. George, Chemistry of Materials 16/4 (2004) 639.
[150] T.-C. Tien, F.-M. Pan, L.-P. Wang, F.-Y. Tsai, C. Lin, Thin Solid Films 520/6 (2012) 1745.
[151] T. Leijtens, I.K. Ding, T. Giovenzana, J.T. Bloking, M.D. McGehee, A. Sellinger, ACS Nano 6/2 (2012) 1455.
[152] T. Bessho, E. Yoneda, J.-H. Yum, M. Guglielmi, I. Tavernelli, H. Imai, U. Rothlisberger, M.K. Nazeeruddin, M. Grätzel, Journal of the American Chemical Society 131/16 (2009) 5930.
[153] W.H. Nguyen, C.D. Bailie, M. Grätzel, M.D. McGehee, A. Sellinger, In prep. (2012).
[154] X. Liu, W. Zhang, S. Uchida, L. Cai, B. Liu, S. Ramakrishna, Advanced Materials 22/20 (2010) E150.
[155] P. Wang, S.M. Zakeeruddin, J.E. Moser, M.K. Nazeeruddin, T. Sekiguchi, M. Grätzel, Nat Mater 2/6 (2003) 402.
[156] J.E. Kroeze, N. Hirata, S. Koops, M.K. Nazeeruddin, L. Schmidt-Mende, M. Grätzel, J.R. Durrant, Journal of the American Chemical Society 128/50 (2006) 16376.
[157] J.R. Jennings, L.M. Peter, The Journal of Physical Chemistry C 111/44 (2007) 16100.
[158] F. Fabregat-Santiago, J. Bisquert, L. Cevey, P. Chen, M. Wang, S.M. Zakeeruddin, M. Grätzel, Journal of the American Chemical Society 131/2 (2009) 558.
[159] L. Schmidt-Mende, J.E. Kroeze, J.R. Durrant, M.K. Nazeeruddin, M. Grätzel, Nano Letters 5/7 (2005) 1315.
[160] M. Grätzel, Accounts of Chemical Research 42/11 (2009) 1788.
[161] F. De Angelis, S. Fantacci, A. Selloni, M. Grätzel, M.K. Nazeeruddin, Nano Letters 7/10 (2007) 3189.
[162] F. De Angelis, S. Fantacci, A. Selloni, M.K. Nazeeruddin, M. Grätzel, The Journal of Physical Chemistry C 114/13 (2010) 6054.
[163] D.P. Hagberg, J.-H. Yum, H. Lee, F. De Angelis, T. Marinado, K.M. Karlsson, R. Humphry-Baker, L. Sun, A. Hagfeldt, M. Grätzel, M.K. Nazeeruddin, Journal of the American Chemical Society 130/19 (2008) 6259.

[164] P. Wang, S.M. Zakeeruddin, J.E. Moser, R. Humphry-Baker, P. Comte, V. Aranyos, A. Hagfeldt, M.K. Nazeeruddin, M. Grätzel, Advanced Materials 16/20 (2004) 1806.
[165] D. Kuang, S. Ito, B. Wenger, C. Klein, J.-E. Moser, R. Humphry-Baker, S.M. Zakeeruddin, M. Grätzel, Journal of the American Chemical Society 128/12 (2006) 4146.
[166] R.L. Puurunen, Chemical Vapor Deposition 10/3 (2004) 159.
[167] P. de Rouffignac, J.-S. Park, R.G. Gordon, Chemistry of Materials 17/19 (2005) 4808.
[168] D.-J. Lee, J.-Y. Kwon, J.I. Lee, K.-B. Kim, The Journal of Physical Chemistry C 115/31 (2011) 15384.

Chapter 2. Experimental Methods

This chapter of the thesis describes relevant background information on the major fabrication and analytical methods used to build and study experimental samples. The chapter begins with an introduction to atomic layer deposition (ALD) which was extensively used to create sub-nanometer metal oxide barrier layers for dye/quantum dot-sensitized solar cell (SSC generally, DSSC or QDSSC specifically) devices, grow quantum dots, and synthesize thin, smooth TiO_2 films for use in synchrotron studies. Auger electron spectroscopy (AES), which was useful in studying the growth of thin ALD films in nanoporous substrates, is then described. A detailed, step-by-step explanation of how SSC devices were constructed is then provided followed by the two important device analysis techniques employed: current-voltage (*J*-*V*) measurements and transient photovoltage/photocurrent measurements. Near-edge X-ray absorption fine structure (NEXAFS) spectroscopy, a synchrotron-based technique used to study dye orientation on planar substrates, is then discussed. Finally, a brief background on quantum chemical calculations is provided along with a discussion of the role played by computational studies in parts of this dissertation.

2.1. Atomic Layer Deposition (ALD)

Atomic layer deposition (ALD) was independently developed in the Soviet Union in the 1960s [115] and by Suntola and coworkers in Finland in the 1970s [116]. Two significant advantages over other deposition technologies that have inspired wide-scale research into ALD are its extremely fine thickness control (at the sub-nanometer level) and ability to conformally coat high aspect ratio nanostructured substrates. These two properties of ALD arise from the principles upon which it is based: in ALD, growth is surface reaction-controlled and proceeds in self-limited steps. At a basic level ALD involves: the saturation of one reactant (that serves as the source of one element, hence the commonly-used term “precursor”) on a substrate surface under conditions in which reactant molecules will adsorb on atoms on the native surface or on chemisorbed counter-reactant atoms but not on each other; the purging of residual unadsorbed reactants and reaction byproducts from the reactor; the introduction of a counter-reactant that either

serves as a precursor for a second element (*e.g.* oxygen in a metal oxide) and allows subsequent adsorption of the first reactant or simply prepares the surface for further adsorption of the first reactant (*e.g.* as in ALD of a pure metal film); purging of residual unadsorbed counter-reactants and reaction byproducts; repetition of the preceding steps (which constitute one "cycle") until the film reaches the desired thickness. These steps (in the case of a binary compound) are shown schematically in Figure 2-1.

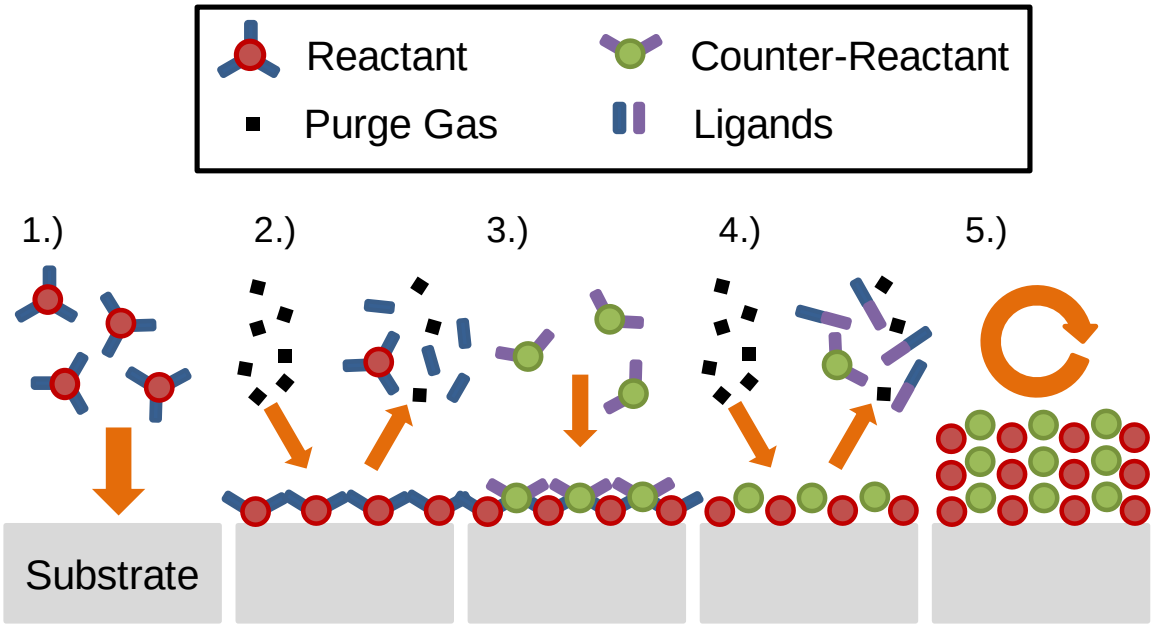


Figure 2-1: Schematic demonstrating the steps of the atomic layer deposition (ALD) process for a binary compound. In Step 1, a cleaned substrate is exposed to reactants (often in the presence of the purge gas or some other carrier gas) which bind to reactive surface groups (*e.g.* hydroxyl groups) but not each other. The reactant (like the counter-reactant) often consists of the desired element bound to ligands. In Step 2 the reactant dosage has ended and an inert purge gas is used to remove any residual reactant molecules along with ligands separated from adsorbed reactants. In Step 3 the counter-reactant is dosed into the chamber (again, often in the presence of the purge/carrier gas) and these molecules adsorb to surface-bound reactant molecules (but do not bind to each other). In Step 4 the reactor is again purged to remove residual counter-reactants and separated ligands, leaving an exposed counter-reactant surface which is ready to bind reactant molecules. Step 5 indicates the repeating of Steps 1 – 4 until the desired thickness is reached.

The self-limited steps of the ALD process (Steps 1 and 3 in Figure 2-1) require a careful selection of reactant/precursor molecules and operating conditions (*e.g.* temperature, pressure, exposure time). In this "ALD window" reactants will only chemisorb on counter-reactant-terminated surfaces. The maximum growth rate per cycle, therefore, is limited by the saturation surface coverage of the precursors and is no more than one monolayer per cycle. In order to perform ALD, it is imperative to have a reactor

capable of controlling the substrate temperature, introducing reactants and counter-reactants into the chamber, and removing excess precursors and reaction products from the chamber so that the reactants and counter-reactants are in isolation from one another. A simplified description and schematic of the reactor used in the dye-sensitized solar cell (DSSC) experiments described in this thesis ("TBSR") is found in Figure 2-2. A more detailed description of TBSR and ALD reactors in general can be found in Ref. [117].

The advantages of ALD, particularly its highly-controllable growth rate and ability to conformally coat high aspect ratio substrates, are particularly well-suited to sensitized solar cell applications. In work described in the body of this dissertation ALD was used to both deposit ultrathin recombination barrier layers and light-absorbing quantum dots throughout a nanoporous TiO_2 substrate. For the barrier layer application, very fine growth rate control is crucial: as described in Section 1.4.3 (and as becomes clear in Chapter 3 and Chapter 4), there is a fine line between suppressing undesirable recombination processes and blocking necessary forward charge injection processes. The gas-phase delivery of precursor molecules and self-limited nature of ALD also makes it possible to grow such barrier layers in a uniform manner throughout a several-micron-thick nanoporous substrate; this renders analysis of the thickness-dependent behavior of SSCs much simpler than if barrier thickness was a function of substrate depth. ALD is also capable of growing small nanoparticles. ALD is used in this fashion to grow light-absorbing quantum dots (QDs) in Chapter 5 and Appendix B:. The advantages in the QD-growth application are similar to those in the barrier layer fabrication: fine control over QD size is necessary to optimize light absorption and charge injection and avoid pore-blocking and again it is highly advantageous to have uniform growth throughout the nanoporous substrate. Although it plays a lesser role, ALD was also used in the dye orientation study described in Chapter 6. In this application ALD was useful for its ability to fabricate thin, smooth films of TiO_2.

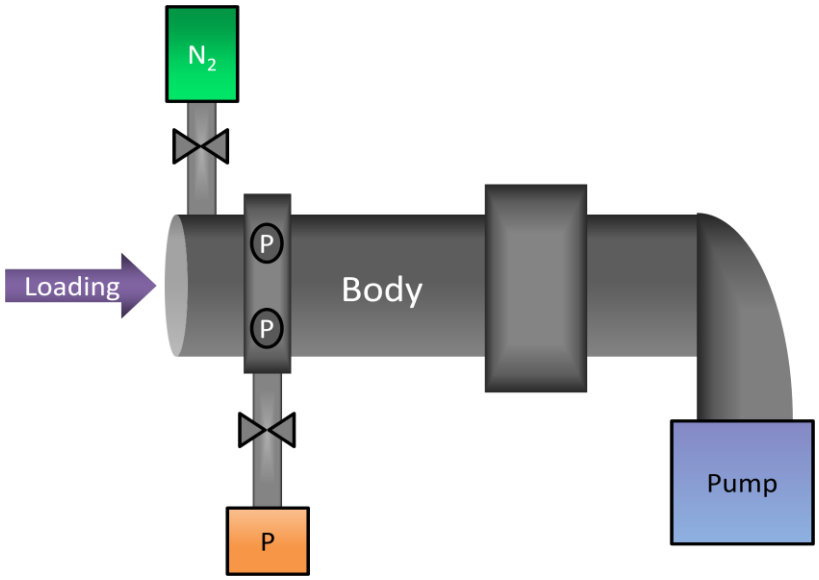


Figure 2-2: Basic schematic of the "TBSR" hot wall tube reactor used to perform ALD in the DSSC barrier layer experiments described in this thesis. A computer graphical interface is used to control most of the reactor conditions and automate the ALD process. Nitrogen carrier gas (it is also the purge gas) is introduced at the front of the reactor, near the loading door, upstream of the precursor (*i.e.* reactant/counter-reactant) lines and the substrates to be coated, which are located in the reactor body. The nitrogen flow is regulated by a mass flow controller. Several precursor manifold lines ("P") (and a pressure sensor, not shown) are oriented radially outward from the chamber, downstream of the N_2 and upstream of the reactor body. While only one valve is shown for the precursor line, in fact each precursor line has three valves: a manual valve, a needle valve to fine-tune the precursor doses, and a pneumatic ALD valve controlled by the computer interface. The vacuum pump, located downstream of the reactor body, pulls out excess precursors, reaction byproducts, and the purge/carrier gases while maintaining a reactor pressure ~100 mTorr during typical operation. Note that thermocouples and heat tape, which work with the computer program to regulate the temperature of the reactor body and precursor lines, are not shown.

2.2. Auger Electron Spectroscopy (AES)

AES involves the detection of an electron that has been ejected from an atom following an Auger decay process, which was first observed—and is so named—by Pierre Auger in the 1920s [118]. The Auger decay process, which is shown schematically in Figure 2-3 alongside the related processes relevant in X-ray photoelectron spectroscopy (XPS) and X-ray fluorescence (XRF), begins with the core-hole created in the XPS process. A second electron within the same atom then falls into the core-hole and the energy released by this process, rather than result in the emission of a photon (as in XRF), ejects a *third* electron within the same atom, resulting in a doubly-charged atom. The third electron that is ejected (*i.e.* the "Auger" electron) has a kinetic energy that is independent of the energy used to originally create the core-hole. The Auger process is conventionally named by the shells of the three electrons which it

involves, for example the KL_IL_{III} Auger process in Figure 2-3. To a first approximation, the kinetic energy of the Auger electron in an "ABC" Auger process, KE_C, is defined by [119]:

$$KE_C = \left(BE_A(Z) - BE_B(Z+\Delta)\right) - BE_C(Z+\Delta) \quad (2.1)$$

Where *KE* and *BE* refer to kinetic and binding energy, respectively, *Z* indicates the atomic number, and Δ, typically in the range of 0.5 to 1.5, helps to account for the fact that the binding energies of B and C are affected by the presence of the core-hole (*e.g.* as in the "Z+1" approximation). Because the kinetic energies of various Auger processes differ widely from element to element, AES is capable of elemental analysis.

While the Auger process was first observed in the 1920s, AES, given the requirement of ultrahigh vacuum, was not thoroughly developed until several decades later [120-122]. The widespread use of AES for elemental detection today is due in large part to three particularly attractive qualities [119]. One, the low mean-free path of electrons (which are detected in AES) means that AES is extremely surface sensitive. Two, the probability of Auger decay, which is inversely related to the probability of XRF, is higher in low-Z elements and AES therefore serves as a complement to XRF (which is preferable for heavy elements). Three, because AES measurements are independent of how the core-hole is generated, an electron beam can be used; electron beams can be much more highly focused than X-rays which means that, in contrast to XPS, AES has an extremely high spatial resolution, on the order of 10 nanometers.

The elemental detection capabilities and high spatial resolution of AES proved useful in this dissertation for the purpose of determining whether or not a particular ALD process was able to uniformly grow a desired material throughout a given depth of a nanoporous TiO_2 structure. The ability to perform ALD throughout such a nanostructured substrate is primarily a function of reactant exposure time, reactant size, and pore diameter and it is therefore not necessarily obvious whether or not uniform growth will result. In order to gauge this, several cycles of the ALD process in question were performed on a nanoporous TiO_2 layer (deposited on a silicon wafer which, in contrast to FTO-coated glass, did not suffer from charging effects); the wafer was then cut down the middle and an AES linescan was performed on the newly

exposed cross-section of the nanoporous layer. The linescan could then be matched up with a scanning electron microscopy (SEM) image of the analyzed cross-section in order to determine the extent of penetration (see Chapter 3 and Chapter 4).

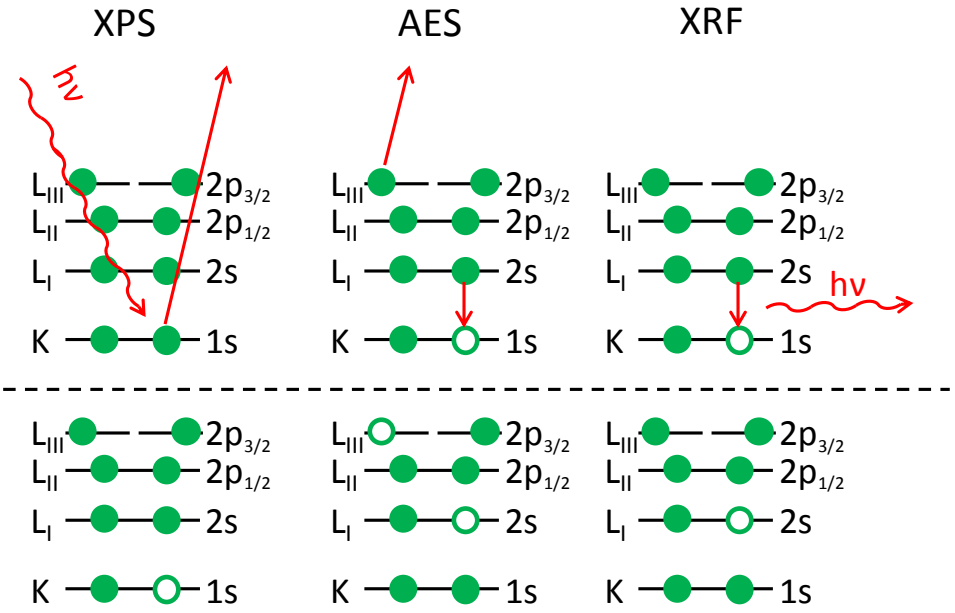


Figure 2-3: Illustration of the relevant electron movements in an oxygen atom in X-ray photoelectron spectroscopy (XPS), Auger electron spectroscopy (AES), and X-ray fluorescence (XRF). Final states for each process are located below the dotted line. Filled green circles indicate electrons in the ground state in an oxygen atom while empty green circles indicate generated holes. The orbital naming conventions for AES and XRF are located on the left and those for XPS on the right. In XPS an X-ray is used to eject a core electron leaving a core-hole. The measured kinetic energy of the ejected electron is a function of both the incident X-ray energy and the binding energy of the core electron. Both the non-radiative Auger decay process (AES) and radiative fluorescent decay process (XRF) begin with the core-hole/final XPS state (note: in AES and XRF an electron beam rather than an X-ray can be used to generate the core-hole). In Auger decay an electron in a higher energy orbital falls down into the core-hole; the electron's resultant energy loss, if sufficiently high, can be imparted to another electron (the "Auger electron") and eject it from the oxygen atom. The process shown in this schematic would be labeled "KL_IL_{III}". In XRF, a photon rather than an Auger electron is released as the L_I electron falls into the core-hole. Note than in both AES and XRF, unlike in XPS, the energy of the measured electron/photon is independent of the energy of the X-ray/electron used to generate the core-hole.

2.3. Fabrication of Sensitized Solar Cells

The breakthrough of O'Regan and Grätzel in developing the first highly-efficient dye-sensitized solar cell (DSSC) was the use of a high-surface area nanoporous TiO_2 substrate which allowed for adsorption of a large number of dye molecules, and hence, substantially increased light absorption and device current [23]. While some details of

this original design have been modified, the basic model remains the same for the devices described in this thesis (Figure 1-6).

The fabrication process begins with a 5 x 7.5 cm substrate of glass coated with fluorine-doped tin oxide (FTO) (Figure 2-4a), a commonly used transparent electrode. Note that FTO is preferred over indium tin oxide (ITO), another common transparent conductor, because FTO is less expensive and more stable [19]. In order to provide an easily-measured device area in the completed solar cells, a strip down the middle of the substrate is etched away by mixing zinc powder and 4 M HCl for approximately one minute, leaving Figure 2-4b. Scotch tape is used to mask the sides. Due to the low charge mobility in TiO_2 and spiro-OMeTAD [39], the hole transport material (HTM) used in the SSCs presented in this thesis, there is minimal lateral collection of charge carriers; therefore the area where FTO has been etched away does not contribute to charge collection.

Following a step in which the substrate is cleaned by a series of sonication and rinsing steps (15 minutes each in 10% Extran® solution, acetone, and isopropanol) and 20 minutes exposure in a UV-ozone oven, a compact layer of TiO_2 (~50-100 nm thick) is applied to the middle of the substrate via spray pyrolysis [123]. Here the outer sides of the substrate are masked with pieces of glass in order to preserve a clean FTO surface for electrical contact in device testing and eliminating any series resistance contributions from an additional TiO_2 layer (Figure 2-4c). The role of the compact TiO_2 layer is to prevent any contact between the FTO electrode and spiro-OMeTAD through pinholes in the nanoporous TiO_2 layer, which would otherwise short circuit the solar cell [31]. A solution of titanium diisopropoxide bis(acetylacetonate) and ethanol (9:1 ethanol v/v) is prepared and the cleaned substrate is heated to 450 °C after which spray pyrolysis is performed using air as the carrier gas.

Next, the nanoporous TiO_2 layer is deposited by doctor-blading a TiO_2 paste [124] atop the compact TiO_2 layer and then annealing at 450 °C, yielding Figure 2-4d. The commercial TiO_2 paste used in these experiments (20 nm particles, Dyesol 18NR-T) can be diluted with terpineol in order to reduce its viscosity which in turn alters the thickness of the resultant TiO_2 layer. A 1:1 w/w dilution of the commercial paste with

terpineol was used to fabricate TiO_2 layers approximately 2 µm thick, which is the standard for SSCs using spiro-OMeTAD [34]. Approximately 300 µL of the diluted commercial paste was doctor-bladed at a speed of 25 mm/s to coat a single substrate. The subsequent anneal step sinters TiO_2 nanoparticles together yielding a high-surface area substrate through which electrons can travel.

After formation of the nanoporous TiO_2 layer (Figure 2-4d) a chemical bath treatment of the substrate with $TiCl_4$ is performed. Despite many studies of this process, it is not entirely clear how this treatment improves short-circuit current density (J_{SC}), and resultantly efficiency, in SSCs. However, it has been indicated that this process increases the size of TiO_2 nanoparticles, lowers surface area but increases dye adsorption, and lowers the TiO_2 conduction band (improving electron injection) [42-44]. The $TiCl_4$ treatment step involves soaking substrates (specifically the TiO_2 nanoporous layers) in a 0.02 M aqueous $TiCl_4$ solution for 12-16 hours and then annealing again at 450 °C.

Following the $TiCl_4$ treatment step, substrates are typically cut into smaller pieces, approximately 1.5 x 2 cm (meaning each of the larger substrates yields 10 smaller substrates). Many of the devices described in this thesis include metal oxide barrier layers which were grown using ALD (Section 2.1). Unless otherwise specified, these barrier layers were grown after the $TiCl_4$ treatment and prior to sensitizing the TiO_2 substrates with either dye molecules or quantum dots. The role of these barrier layers, which herein include Al_2O_3 and In_2O_3, is described in detail in Section 1.4.3.

In order to build a DSSC, substrates (with or without a barrier layer) are dipped in a solution (typically composed of an alcohol or acetonitrile-alcohol mixture) containing the desired dye molecule. Solvent, concentration and dip time are a function of the dye utilized: for instance, the ruthenium dyes discussed in this thesis (Z907 and YE05) require long dip-times of ~20 hours, whereas the organic dye (WN1) only requires 3 hours. Furthermore, some dyes, including organic dyes like WN1, are typically co-dissolved with an additive such as chenodeoxycholic acid in order to reduce dye aggregation and improve DSSC performance [125]. Regardless of the dye chosen, it is imperative to heat the substrates prior to the sensitization step: this evaporates any adsorbed H_2O molecules on the TiO_2 surface, which interferes with dye attachment [126].

Following the sensitization process, the substrates are removed and dipped into pure solvent in order to remove physisorbed dye molecules. For the PbS QDSSCs discussed in this thesis, sensitization is performed via ALD. However, there are many other common ways to grow quantum dots including chemical bath deposition (CBD) [91] and (SILAR) [94].

Following sensitization with either dyes or quantum dots, the hole transport material (HTM) spiro-OMeTAD (2,2',7,7'-tetrakis-(*N*,*N*-di-*p*-methoxyphenylamine)-9,9'-spirobifluorene) [31], which is used in all of the SSCs described in this thesis, was deposited by spin-coating a solution of spiro-OMeTAD dissolved in chlorobenzene, resulting in Figure 2-4e. While the archetypal O'Regan and Grätzel device [23] uses an iodide/triiodide redox couple in solution, and the current record efficiency DSSC uses a liquid-based cobalt redox couple [25], solid-state HTMs like spiro-OMeTAD have been the subject of much interest due to the practical considerations (*e.g.* long-term storage and electrode corrosion) associated with liquid HTMs. Unlike liquid HTMs, however, successfully filling the nanopores of a SSC with solid-state HTMs presents a challenge. The importance of the pore-filling step, therefore, cannot be overstated.

As with the TiO_2 paste, the concentration of spiro-OMeTAD in chlorobenzene affects its viscosity and in-turn its behavior when spin-coated [33]. For 2 µm thick TiO_2 films, a concentration of 225 mg spiro-OMeTAD per mL chlorobenzene was used. This results in a large filling fraction of the nanopores as well as an overlayer of the HTM that is neither too thin (which can lead to shunting) nor too thick (which increases series resistance). In order to boost cell performance, two additives are added to the spiro-OMeTAD solution prior to spin-coating: *tert*-butyl pyridine (*t*BP) and lithium ions (lithium bis-(trifluoromethylsulfonyl)imide salt) in ratios of 1:10.3 µL:mg of spiro-OMeTAD for *t*BP, and 1:4.8 µL:mg of spiro-OMeTAD for the lithium salt (170 mg mL^{-1} in acetonitrile). It is important to add the tBP to the spiro-OMTAD solution first as the lithium compound is highly soluble in *t*BP [46]. Whereas in liquid SSCs *t*BP and lithium ion have opposite effects on the conduction band energy (with *t*BP raising the TiO_2 conduction band level and Li^+ lowering it) and in turn recombination kinetics, in solid-state SSCs both reduce the recombination rate [46]. Spin-coating was performed by

adding ~30 µL of the spiro-OMeTAD solution (with additives) per ~3 cm^2 substrate active layer with a pipette, smoothing the solution over the device area with a glass rod, and immediately spinning for ~30 seconds at 2000 revolutions per minute.

After being stored overnight in a desiccator, the substrates are then placed into an evaporator which is pumped down to ultrahigh vacuum (~10^{-6} torr). Silver is then thermally evaporated onto the substrates through a mask; 5 nm are deposited at 0.2 Å/s and an additional 195 nm at 5 Å/s, resulting in a 200 nm thick back electrode. This final structure is shown schematically in Figure 2-4f and a photograph of a completed device is in Figure 2-5 (minus the external circuitry). Note that gold is often used in the literature for the back electrode in solid-state SSCs. This is because gold forms a Schottky barrier with TiO_2 which prevents device shunting [127]. However, provided that there is a spiro-OMeTAD overlayer to separate the nanoporous TiO_2 active layer and the back contact, such shunting is not an issue; silver is then preferred due to its lower cost and better reflectivity profile [128]. Prior to testing, the completed solar cells were again placed overnight in a desiccator: this allows partial oxidation of the silver contact, which is beneficial for solar cell performance [128].

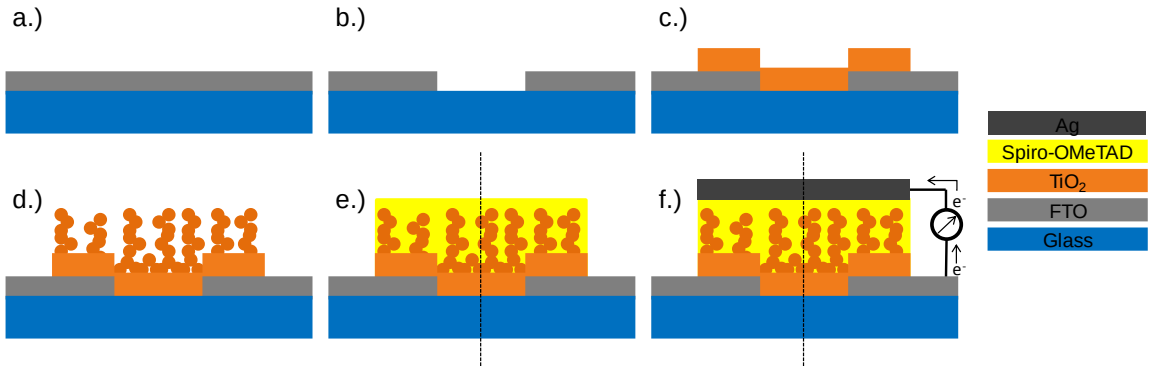


Figure 2-4: Fabrication scheme (not to scale) of DSSCs beginning with a 5 x 7.5 cm fluorine-doped tin oxide (FTO)-coated glass substrate (a) (Pilkington Glass, 15 Ω/□). A small strip of FTO in the middle of the substrate is etched using Zn powder and 4 M HCl, leaving (b). This step simplifies measurement of device area. A compact TiO_2 layer (~50 – 100 nm thick) to block recombination between FTO and spiro-OMeTAD is deposited by spray pyrolysis and annealed (c). The edges are masked in order to prevent deposition of TiO_2 atop the FTO contact, which may increase series resistance. A nanoporous TiO_2 layer (~2 µm thick) is added by doctor-blading a commercial paste (Dyesol) and annealing. Following a $TiCl_4$ chemical bath treatment, deposition of any metal oxide barrier layer, and sensitization (using either dye molecules or quantum dots) (not shown), pore-filling is performed by spin-coating a solution of spiro-OMeTAD in chlorobenzene, resulting in (e). Finally, a back silver electrode (~200 nm thick) is deposited by thermal evaporation under ultra-high vacuum; arrows indicate the direction of electron flow in a working device. Note that the dotted lines in (e) and (f) indicate that at this point in the fabrication process (specifically after the $TiCl_4$ chemical bath step) the larger 5 x 7.5 cm substrate has been cut into approximately 10 smaller substrates ~1.5 x 2 cm. Also note that the device schematics here are "upside-down" in the sense that while operating, the sun/light source would be below the glass; silver then serves as both the back electrode and a light reflector.

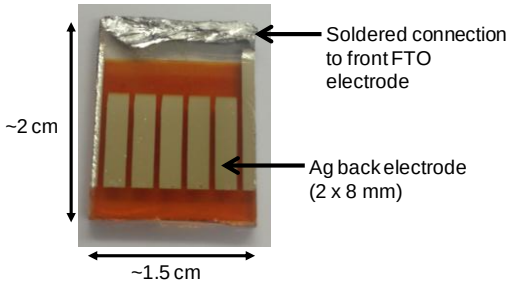


Figure 2-5: Photo of a completed DSSC substrate (~2 µm-thick TiO_2 active layer, WN1 dye) with five discrete devices defined by the Ag back electrodes. Note that the actual device areas are less than the full 16 mm^2 area of the Ag electrodes due to the etched FTO area (not visible in the photograph, but easily discernible by eye).

2.4. Solar Cell Testing: Current-Voltage Curves

The most basic characterization of a finished solar cell is to measure its current output as a function of applied bias. By performing this measurement under a quantified light source one can determine the solar cell's efficiency. These Current-Voltage (*I-V*) measurements (or, Current Density-Voltage (*J-V*), to account for the device area) have

certain features that are used to characterize device performance. Before examining the characteristics of a *J-V* curve under illumination it is useful to describe a solar cell's behavior in the dark. The dark current in a solar cell, which flows opposite to the desired direction for energy extraction, has a value of zero with no bias applied and rises exponentially as the forward (positive) bias is increased (Figure 2-6). Analysis of dark current can be useful in understanding the role of barrier layers (such as those studied in this dissertation) because the charge transfer pathways relevant in recombination processes are also frequently involved in the flow of dark current.

When light is shined onto the solar cell a photocurrent flows in the desired direction, opposite to the dark current. As described in Chapter 1, the process of photocurrent collection is fundamentally difference in SSCs than in typical inorganic solar cells (*e.g.*, Si, CdTe, CIGS). In a DSSC, photocurrent originates when a photon of light excites an electron in a dye molecule to a higher energy level, wherefrom it injects into the photoanode and diffuses to the front electrode where its high energy content can be harvested before proceeding to the back electrode. When there is no applied bias (and therefore no dark current) the solar cell current output is purely a function of the photocurrent; this value is termed short-circuit current density (J_{SC}) (Figure 2-6). At a basic level the J_{SC} reflects the solar cell's ability to absorb light and efficiently collect charge carriers.

The lack of an applied bias, however, means that there is no difference in energy level between the front and back electrodes and no energy is extracted from the photo-generated charge carriers. The light current curve in the fourth quadrant of Figure 2-6 represents where the solar cell is generating power. As the forward bias is increased, more energy is extracted from each charge carrier, but the dark current increasingly competes with the photocurrent. Eventually the dark current fully cancels out the photocurrent; at this point there is no net current flow in the solar cell and the bias at which this occurs is termed the open-circuit voltage (V_{OC}). The J_{SC} and V_{OC} effectively indicate upper bounds for the maximum number of charge carriers that can be collected in the forward bias regime and how much energy can be extracted from each charge carrier. There exists some optimal bias (V_{MP}) less than the V_{OC} at which the power

output—which is current times voltage—of the solar cell will be highest (P_{MAX}); this is called the maximum power point. The "fill factor" of a solar cell relates this P_{MAX} to the J_{SC} and V_{OC} performance bounds according to the equation below:

$$Fill\ Factor = \frac{P_{MAX}}{J_{SC} * V_{OC}} = \frac{J_{MP} * V_{MP}}{J_{SC} * V_{OC}} \tag{2.2}$$

The fill factor, typically reported as a percentage or fraction (less than one), gives an indication of how efficiently photocurrent is extracted under forward bias; a low fill factor can be indicative of a large amount of undesirable charge recombination or series resistance in the cell.

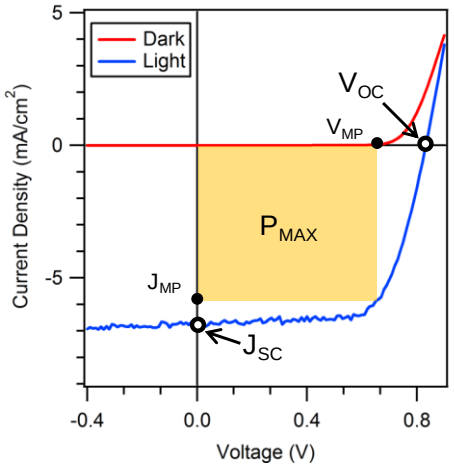


Figure 2-6: Examples of typical light and dark current density-voltage (*J-V*) curves for a solar cell in the light and in the dark. A solar cell is typically characterized by three metrics, the open-circuit voltage (V_{OC}), short-circuit current density (J_{SC}), and the fill factor (not shown). The maximum power value (P_{MAX}, which is the product of associated current (J_{MP}) and voltage (V_{MP}) values) is related to the J_{SC} and V_{OC} through the fill factor, which is equal to the fraction of P_{MAX} over (J_{SC}*V_{OC}). An efficiency value for the solar cell can be calculated by dividing P_{MAX} by the light incident on the solar cell. In the *J-V* experiments described in this dissertation, a solar simulator utilizing a xenon arc lamp was used to mimic the Air Mass 1.5 G (AM1.5G) spectrum (see Figure 1-5).

2.5. Transient Photovoltage & Photocurrent Measurements

Transient photovoltage (TPV) measurement is an advanced SSC characterization technique that features prominently in this dissertation because it provides a means of quantifying the recombination lifetime of charge carriers in the TiO_2 photoanode, and hence, can indicate the effectiveness of recombination blocking layers. The basic principles behind TPV measurements as developed by O'Regan *et al.* [129, 130] are as

follows. A constant "bias" light is shone onto a solar cell and an electrical sourcemeter (a Keithley 2400 was used in this dissertation) keeps the device current constant. Most commonly this measurement is performed at open-circuit (where current equals zero) but any point on a *J-V* curve can be sampled: in other words, the current chosen locks in a particular photovoltage in the device. A pulse light (typically of an intensity about 5% that of the bias light) is then flashed on, resulting in additional light absorption and injection of excited electrons into the photoanode in the device. A simplified diagram of the setup used to conduct the transient measurements in this dissertation is shown in Figure 2-7.

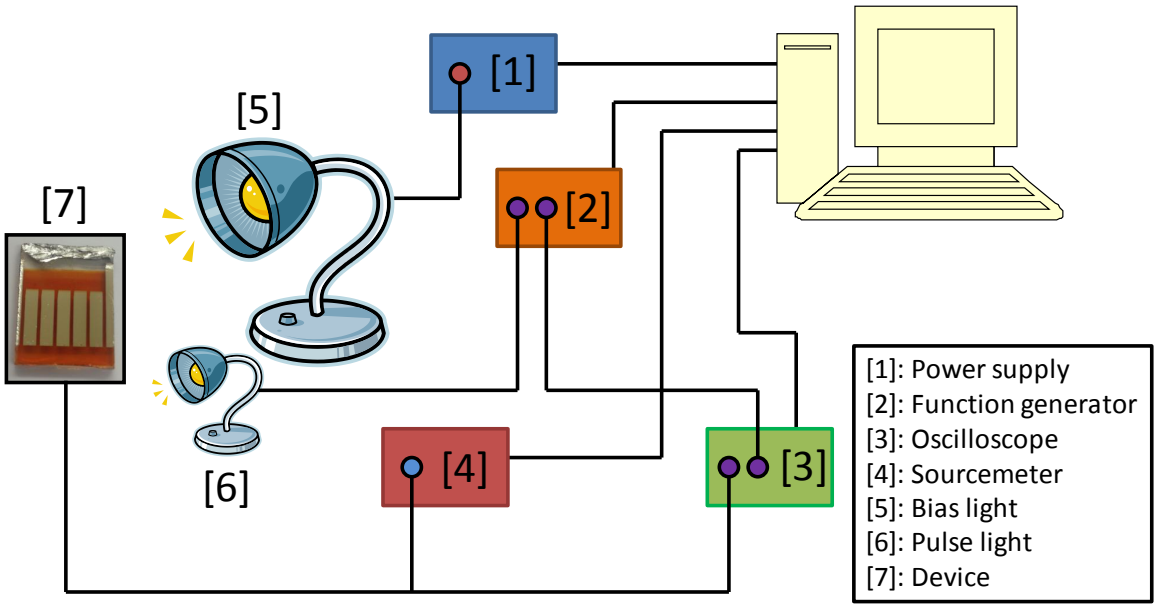


Figure 2-7: Schematic of the equipment used to collect transient photovoltage measurements. A LabVIEW computer program is used to send commands to and receive data from the Circuit Specialists CSI3644A programmable power supply, Agilent 3300 function generator, Tektronix oscilloscope, and Keithley 2400 sourcemeter. The programmable power supply sets the bias light output. A function generator drives the LED pulse lamp and sends a timing trigger to the oscilloscope, which locks in the device voltage signal (note: in transient photocurrent measurements, a transimpedance amplifier connects the device current signal to the oscilloscope). The sourcemeter maintains the device at the desired current level (or voltage level in transient photocurrent measurements).

Because the device current is being held constant during a TPV measurement, the additional electrons injected when the pulse light is turned on have no means of being extracted in a normal fashion; rather than increase the device current, the pulse light instead increases the concentration of electrons in the photoanode, raising its Fermi level

and thereby the photovoltage by ΔV (see Figure 1-10). The pulse light is then shut off (typical pulse on/off times are ~50 ms each) and the device photovoltage decays down to its baseline value under the bias light (V_0) as electrons in the photoanode recombine with holes in the light-absorbing material or HTM. Examples of typical TPV data are shown in Figure 2-8.

The rate of photovoltage decay is therefore an indication of the recombination reaction rate (with recombination rate being equal to one divided by the recombination lifetime, τ_R). Recombination lifetime can be determined by fitting TPV data to an equation like that in Figure 2-8a; a least-squares fitting can be performed (with the error defined by the difference between the "Fit" equation value and the measured photovoltage) to yield values for, using the nomenclature of Figure 2-8a, V_0, A, and τ_R.

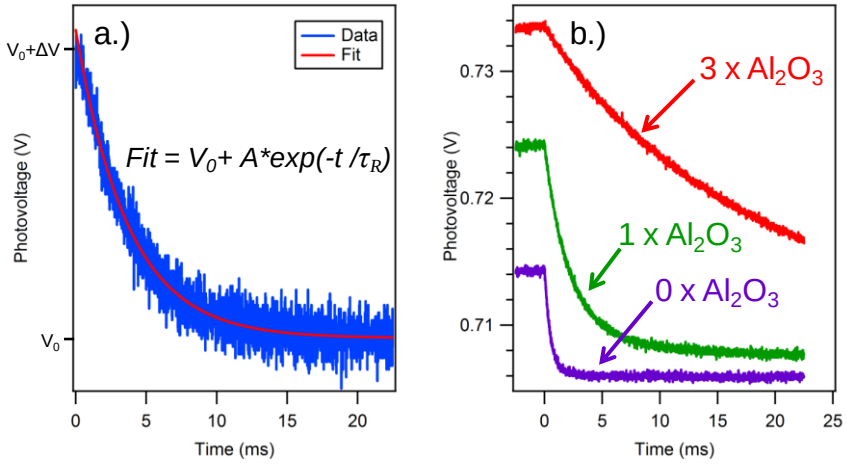


Figure 2-8: a.) Raw data along with a fitted curve for a transient photovoltage experiment. As the device current is kept constant, the pulse LED light results in an increased photovoltage (ΔV) which gradually disappears when the pulse light is turned off due to recombination of charge carriers. The transient data is fitted to an equation of the form $V(t) = V_0 + A*\exp(-t/\tau_R)$ where "A" is a pre-exponential factor and "τ_R" is the recombination lifetime; a shorter lifetime results in a faster decay of the photovoltage. b.) Differences in recombination lifetime are often readily apparent in the raw transient photovoltage data. In this example, photovoltage decay curves are shown for otherwise-identical solid-state DSSCs with 0, 1, and 3 ALD cycles of Al_2O_3 used as a recombination barrier layer at comparable photovoltages. Al_2O_3 increases the recombination lifetime, stretching out the photovoltage decay curves; more Al_2O_3 (*i.e.* a thicker recombination barrier layer) results in a larger lifetime enhancement.

Transient photocurrent (TPC) measurements are fundamentally similar to TPV measurements. The primary differences are that as opposed to the current being held constant, in TPC measurements a sourcemeter holds the device voltage constant. This

means that when the pulse light is turned on and additional electrons are injected into the photoanode, photovoltage is constant but photocurrent increases. When the light is turned off, the photocurrent decays down to its baseline value; as with photovoltage in TPV measurements, the decay follows an exponential form but is in this instance a function not of the recombination rate, but of the extraction rate of electrons from the photoanode (note: the photocurrent decay can in fact also be a function of the recombination rate, but this is typically only a necessary consideration in far forward bias where the recombination rate is high). TPC measurements are typically conducted to measure the extraction rate of electrons from the photoanode, which when the photoanode thickness is known, allows determination of the electron diffusion length.

In the work described in this dissertation, however, TPC measurements are primarily a means of determining device capacitance. Device capacitance (C) is defined as $\Delta Q/\Delta V$, that is, the amount of additional charge (ΔQ) associated with a given change in voltage (ΔV). Device capacitance measurements are a particularly simple way of identifying movement of the photoanode conduction band such as can be caused by the introduction of a surface dipole on the photoanode (*e.g.* from an adsorbed dye monolayer or deposition of a thin metal oxide barrier layer). The concept and calculation of capacitance (specifically a "differential capacitance" defined at a given photovoltage, V_0) is illustrated in Figure 2-9. An increase in light intensity (Figure 2-9b) results in a certain number of additional electrons being injected into the photoanode (ΔQ); the filling of the bandgap states within the photoanode raises the Fermi level and in turn the device photovoltage by the amount ΔV. The change in photovoltage for a given ΔQ is a function of the position of the baseline photovoltage (V_0) relative to the conduction band. As such, a change in differential capacitance at the same photovoltage from one device to another typically indicates a movement of the conduction band.

The TPV and TPC measurements described above are one way to calculate ΔQ and ΔV, and in turn, C. TPV measurements performed at open-circuit yield a change in photovoltage, ΔV. Integrating the photocurrent decay from a TPC measurement using the same pulse light intensity at short-circuit (*i.e.* at low bias so as to render recombination

losses negligible) yields the corresponding ΔQ enabling calculation of C, which is typically normalized to the device area.

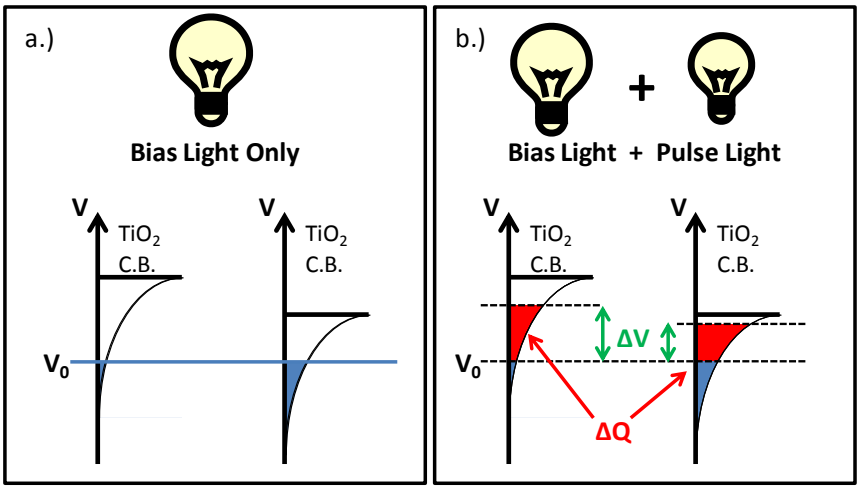


Figure 2-9: Schematic demonstrating the meaning of device capacitance in two SSCs with TiO_2 photoanodes where a photoanode conduction band (C.B.) shift has occurred in one of the two devices. In a.), the filling of bandgap states in the TiO_2 as a voltage is applied is evident. In comparing the device on the left to the device on the right wherein the TiO_2 C.B. has been lowered, it is clear that at a given voltage fewer states are filled when the C.B. is higher. In b.) an additional pulse light (*e.g.* as in transient measurements) is turned on resulting in more electrons injected into TiO_2. Assuming that these charge carriers cannot be extracted from the device (as in transient photovoltage measurements), this results in an increase in the device photovoltage. Given the exponential distribution of TiO_2 bandgap states, for a given number of newly injected electrons (*i.e.* ΔQ) a device with a higher C.B. (left device) will undergo a larger increase in photovoltage (ΔV) than the device on the right with the lower C.B. As capacitance is defined by $\Delta Q/\Delta V$, the left device with the larger ΔV will have a lower differential capacitance at V_0 than the right device.

2.6. Near-Edge X-Ray Absorption Fine Structure (NEXAFS) Spectroscopy

NEXAFS is a technique first developed in the 1980's that probes unoccupied molecular orbitals [131]. The most comprehensive reference on NEXAFS was written by one of its pioneers, Joachim Stöhr [132], but more concise introductions to the field are also available [133, 134]. In a NEXAFS measurement the incident X-ray energy, beginning below the ionization potential of the core electrons being studied, is gradually increased past (up to 50 eV [134]) the ionization edge. In this "near (ionization) edge" region, the incident X-ray is able to excite core electrons (typically from the K-shell) into unoccupied molecular orbitals as well as to vacuum (in the latter instance, this effectively represents the XPS process shown in Figure 2-3). Just as in the AES and XRF processes shown in Figure 2-3, the excitation of the core electron to either unoccupied high energy

orbitals or to vacuum creates a core-hole which can decay in either a radiative or non-radiative (Auger) process, resulting in the emission of a photon or Auger electron, respectively.

In a typical NEXAFS experiment in an ultrahigh vacuum chamber, detectors are set up which can measure ejected electrons ("Total electron yield", TEY) and emitted photons ("Fluorescence yield", FY) as well as elastically-scattered Auger electrons ("Auger electron yield", AEY). TEY, AEY, and FY can be of different utility depending upon the element being studied, the desired surface sensitivity, and the necessary signal-to-background ratio [134]. A simplified NEXAFS spectrum is shown in Figure 2-10. Antibonding π^* orbitals are typically the lowest energy unoccupied orbitals (in a molecule with π-bonding) and they are usually located at energies below the ionization edge. Peaks corresponding to transitions of core electrons into these orbitals are typically much narrower than σ^* peaks, which are located at higher energies, near or above the ionization edge. NEXAFS measurements can yield detailed information about a system's frontier molecular orbitals, and the intensity and energetic position of the peaks like those illustrated in Figure 2-10 are strongly influenced by the chemical environment in which they are located.

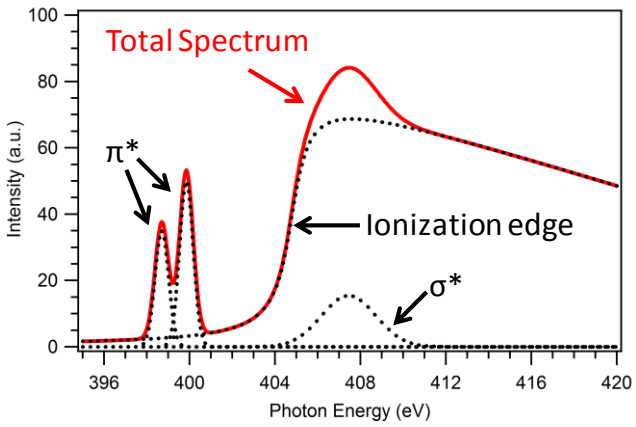


Figure 2-10: Simplified nitrogen K-edge NEXAFS spectrum demonstrating the relative energies and peak widths associated with excitation of core electrons into unoccupied π* and σ* orbitals as well as to the vacuum (indicated by the sharp ionization edge). When present in the molecule, π* orbitals are typically found below the ionization potential and have sharper peaks than the σ* transitions which are typically located at energies near or above the ionization potential. The intensity represented on the y-axis is effectively "counts per second" of whatever is being measured—*e.g.* Auger electrons, all electrons ("total electron yield"), photons—while the x-axis indicates the energy of the incident X-rays. The deconvolution of the total spectrum into discrete Gaussian (or Lorentzian) peaks (*i.e.* the dotted lines) as shown in the plot also indicates the manner in which spectra can be fitted for angle-resolved NEXAFS studies.

Because NEXAFS measurements require a tunable, monochromatic X-ray source, a synchrotron radiation source is needed (the NEXAFS experiments described in this dissertation were performed at Stanford Synchrotron Radiation Laboratory). This synchrotron radiation has a further advantage: it is highly polarized. The probability for a core-valence electronic transition (which is effectively what the various AEY, TEY, and FY detection schemes measure) is a strong function of the overlap of the electric field component of the incident radiation and the shape of the final state (*i.e.* π* or σ* orbital). This means that adjusting the angle between the incident radiation and the sample should yield different intensities for the same electronic transitions if the unoccupied final state orbital in question has a particular orientation: specifically, the intensity (*i.e.* transition probability) is maximized when there is strong overlap of the incident radiation's electric field vector and the vector that characterizes the largest spatial extent of the unoccupied orbital. This characteristic is illustrated schematically in Figure 2-11 where the orientation of an adsorbate's π* orbital affects how its intensity varies with the incident X-ray angle. By performing the NEXAFS measurement on a sample at two or more incident angles and fitting the resultant peak intensities, the orientation of various orbitals

can be calculated using the NEXAFS equation, which is derived for a number of different scenarios (*e.g.* the directionality of the π* orbitals of a benzene is defined by a single vector, whereas the σ* orbitals of the benzene ring span a plane, requiring the use of a different equation) in Ref. [132]. The NEXAFS equation for one particular scenario is described in Chapter 6 where angle-resolved NEXAFS measurements were used to determine the orientation of dye molecule adsorbed on TiO_2.

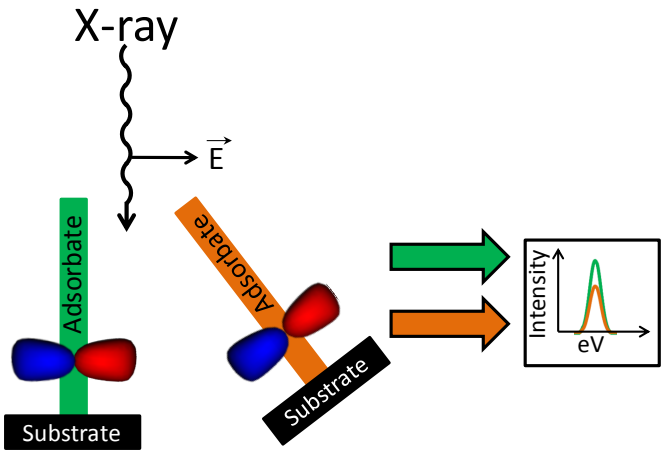


Figure 2-11: Schematic of the basis behind angle-resolved NEXAFS studies. The probability of an atomic core electron being excited into an unoccupied molecular orbital—here drawn schematically as a π* orbital perpendicular to the plane of the adsorbate—is a function of the overlap of the electric field component of the incident, polarized X-ray and the unoccupied orbital. As NEXAFS measures the intensity (*i.e.* frequency) of these transition, a larger peak results from the left (green) measurement where there is excellent overlap between the π* orbital and the electric-field component of the X-ray than in the right (orange) measurement where the substrate has been rotated relative to the X-ray source and there is less overlap. A representative plot of the resultant peaks showing intensity as a function of the photon energy (typically plotted in eV) is shown to the right.

2.7. Quantum Chemical Calculations

2.7.1. Background

As high-powered, economical computational capabilities become ever more accessible, quantum chemical calculations become an increasingly-useful way of learning about the physical behavior of molecular systems at the atomic level. Such calculations can be used as both a predictive and explanatory tool for a number of phenomena of interest including, among many others, molecular structure, binding energy, electronic structure, and infrared radiation absorption. The field of quantum calculations is extremely deep, and numerous textbooks (from which the background described here was

developed) are available on the subject [135-137]; therefore the following discussion will briefly outline in very broad terms the critical elements that underpin the field and discuss the particular relevance of quantum calculations to work described in this dissertation.

The starting point for quantum calculation is the foundational time-independent Schrödinger Equation (2.3):

$$\widehat{H}\Psi = E\Psi \tag{2.3}$$

that describes the wavefunction (Ψ) of a system in relation to the Hamiltonian operator ($\widehat{H}$) which when operated on a wavefunction yields the system's energy as the eigenvalue, E. The system's energy, which is a sum of kinetic and potential energy contributions, is also defined as the expectation value of the Hamiltonian:

$$< \Psi \left| \widehat{H} \right| \Psi > = E \tag{2.4}$$

The general goal of many quantum chemical calculations is to find the ground-state energy (E_0) of a system for which, based on the variational principle, an upper bound can be determined by minimizing the expectation value of the Hamiltonian. While simple in form, this equation becomes incredibly complex—effectively a quantum many-body problem—as the system size grows and analytical solutions are only available for the most trivial systems (*e.g.* the hydrogen atom).

Quantum chemical calculation methods therefore find means of simplifying the estimation of the ground-state energy. For electrons, the potential energy term of the Hamiltonian can be further decomposed into interactions with protons in the atom's nucleus and interactions with other electrons. While the nuclear-electron interactions can be well-described simply by Coulombic forces, the electron-electron interactions are more complex: in addition to electron-electron Coulombic repulsion, two additional significant energetic contributions arise based on the fact that electron locations are correlated (that is, the presence of electron "A" at location *x* precludes electron "B" from also being located at *x*; this gives rise to a "correlation energy" term) and, as fermions, must follow the Pauli Exclusion Principle (this gives rise to an "exchange energy" term).

One of the earliest approximations (going all the way back to the 1920s) was the *ab initio* Hartree-Fock "self-consistent field" algorithm wherein a many-electron wavefunction is approximated as the product of many one-electron wavefunctions. Hartree-Fock is an iterative process wherein the wavefunction for an electron is guessed, the Coulombic forces from the other electrons are calculated (thereby generating a mean electric field), the orbital of the first electron is adjusted accordingly, and the calculation then proceeds to the next electron in the system. This process is repeated until the orbitals, within some convergence constraint, no longer change. While in this method the exchange energy term can be exactly calculated, the treatment of the Coulombic interactions as a mean-field effect of several discrete one-electron systems means that in Hartree-Fock, correlation interactions are neglected. Hartree-Fock has served as the starting point for many more advanced calculation methods—which typically yield more accurate results at the expense of greater computational cost—by, for example, approximating correlation effects and using more detailed mathematical descriptions of electron orbitals (*i.e.* basis sets).

The primary alternative to Hartree-Fock-based approaches is density functional theory (DFT), developed by Walter Kohn, Pierre Hohenberg, and Lu Jeu Sham in the 1960s. The premise of DFT is that rather than rely on the wavefunction as in Hartree-Fock methods, the electron density, $\rho(\vec{r})$, is used. The electron density uniquely determines a system's external potential and ground-state wave function and, therefore, the system's energy. This means that the Hamiltonian used to calculate the system's energy can be reformulated in terms of electron density rather than wavefunction. As in Hartree-Fock, the Hamiltonian can be decomposed into various energetic contributions, which in DFT are "functionals" of the electron density: kinetic energy, electron-nuclear interactions, electron-electron interactions, and "everything else", which includes various correlation and exchange contributions and is denoted E_{XC}. In addition to the use of a variety of basis sets (as in Hartree-Fock methods) to describe the electron density, developments in DFT theory have led to a number of different methods to approximate the E_{XC} functional. The development of accurate E_{XC} functionals—including some "hybrid" functionals that incorporate Hartree-Fock exchange (*e.g.* "B3LYP" [138])—in

the 1980's and 1990's has led to DFT being a very popular choice for quantum chemical calculations due its combination of relatively high accuracy and excellent speed.

2.7.2. Relevance of Quantum Chemical Calculations to this Dissertation

The chapters on In_2O_3 barrier layers (Chapter 4) and NEXAFS studies of dye orientation (Chapter 6) include significant theoretical components to complement the experimental results, and the motivations for these calculations fall generally into three categories. In the In_2O_3 study, DFT was used to probe an anatase (101) TiO_2 slab (using periodic boundary conditions) coated with sub-monolayer to monolayer amounts of In_2O_3 in order to observe the possible formation of a surface dipole on the TiO_2 (which has implications for solar cell V_{OC}) and introduction of intra-bandgap states that could play a role in interfacial charge transfer. In this study the determination of the ground-state energy (*i.e.* structural optimization) of the TiO_2-In_2O_3 system led to facile calculation of dipoles (based on charge density gradients) and the density of states (DOS).

DFT methods were used to predict both the energies and geometry of the excited state of a dye molecule in order to inform the NEXAFS measurements. The StoBe-deMon software [139] was used to probe the ground state and an excited state that results from a core electron being excited into an unoccupied orbital, as occurs in the X-ray absorption process. This analysis was pivotal in understanding the origin of peaks observed in the NEXAFS spectra and the implications of these peaks' angular intensities with regards to the orientation of adsorbed dye molecules.

In the same chapter, traditional DFT methods and DFT-molecular dynamics (DFT-MD) studies were performed to compare the experimental (NEXAFS) dye orientation data with theoretical calculations. As with the In_2O_3 study, an anatase TiO_2 slab with periodic boundary conditions was used as the starting point. For this application a periodic system provided substantial benefits over a cluster system in that the periodic boundary conditions allow for dye-dye interactions on a substrate with realistic dye surface coverage. The dye molecule under study was adsorbed onto the surface and a structural optimization was performed to determine the ground state geometry. This ground-state geometry then served as the starting structure for a DFT-MD simulation. The basic concept behind DFT-MD is that DFT is used to calculate the

forces present on atoms in the system and then classical physics (*i.e.* Newton's equation of motion) is used to determine the movement of atoms in a given time step at the desired temperature (the temperature affects the atomic velocities); at the end of the time step, DFT is then used to calculate the forces present in the new atomic configuration and the cycle repeats. The advantage of DFT-MD is that a high level of theory can be used to develop an understanding of how a system behaves in a realistic environment: a DFT-MD simulation provides a much clearer picture of how a dye-TiO_2 system behaves during a NEXAFS measurement than a ground-state traditional DFT optimization. Indeed, the DFT-MD simulation results indicate remarkable agreement with the NEXAFS measurements.

2.8. References

[1] R.L. Puurunen, Journal of Applied Physics 97/12 (2005) 121301.
[2] T. Suntola, Materials Science Reports 4/5 (1989) 261.
[3] J.R. Bakke, Atomic Layer Deposition of Materials for Applications to Photovoltaics, Stanford University, Stanford, 2011.
[4] P. Auger, J. Phys. Radium 6/6 (1925) 205.
[5] K.D. Childs, B.A. Carlson, L.A. LaVanier, J.F. Moulder, D.F. Paul, W.F. Stickle, D.G. Watson (Eds.), Handbook of Auger Electron Spectroscopy, Physical Electronics, Inc., Eden Praire, Minnesota, 1995.
[6] R.E. Weber, W.T. Peria, Journal of Applied Physics 38/11 (1967) 4355.
[7] L.A. Harris, Journal of Applied Physics 39/3 (1968) 1419.
[8] L.A. Harris, Journal of Applied Physics 39/3 (1968) 1428.
[9] B. O'Regan, M. Grätzel, Nature 353/6346 (1991) 737.
[10] M.D. Archer, A.J. Nozik (Eds.), Nanostructured and Photoelectrochemical Systems for Solar Photon Conversion, Imperial College Press, London, 2008.
[11] H.J. Snaith, L. Schmidt-Mende, Advanced Materials 19/20 (2007) 3187.
[12] L. Kavan, M. Grätzel, Electrochimica Acta 40/5 (1995) 643.
[13] U. Bach, D. Lupo, P. Comte, J.E. Moser, F. Weissortel, J. Salbeck, H. Spreitzer, M. Grätzel, Nature 395/6702 (1998) 583.
[14] S. Ito, P. Chen, P. Comte, M.K. Nazeeruddin, P. Liska, P. Péchy, M. Grätzel, Progress in Photovoltaics: Research and Applications 15/7 (2007) 603.
[15] L. Schmidt-Mende, S.M. Zakeeruddin, M. Grätzel, Applied Physics Letters 86/1 (2005) 3504.
[16] P.M. Sommeling, B.C. O'Regan, R.R. Haswell, H.J.P. Smit, N.J. Bakker, J.J.T. Smits, J.M. Kroon, J.A.M. van Roosmalen, The Journal of Physical Chemistry B 110/39 (2006) 19191.
[17] B.C. O'Regan, J.R. Durrant, P.M. Sommeling, N.J. Bakker, The Journal of Physical Chemistry C 111/37 (2007) 14001.
[18] S.-W. Lee, K.-S. Ahn, K. Zhu, N.R. Neale, A.J. Frank, The Journal of Physical Chemistry C 116/40 (2012) 21285.

[19] N.R. Neale, N. Kopidakis, J. van de Lagemaat, M. Grätzel, A.J. Frank, The Journal of Physical Chemistry B 109/49 (2005) 23183.
[20] I.-K. Ding, Pore Filling and Light Trapping of Solid-State Dye-Sensitized Solar Cells, Stanford University, Stanford, 2011.
[21] M. Shalom, S. Dor, S. Rühle, L. Grinis, A. Zaban, The Journal of Physical Chemistry C 113/9 (2009) 3895.
[22] P. Ardalan, T.P. Brennan, H.-B.-R. Lee, J.R. Bakke, I.K. Ding, M.D. McGehee, S.F. Bent, ACS Nano 5/2 (2011) 1495.
[23] A. Yella, H.-W. Lee, H.N. Tsao, C. Yi, A.K. Chandiran, M.K. Nazeeruddin, E.W.-G. Diau, C.-Y. Yeh, S.M. Zakeeruddin, M. Grätzel, Science 334/6056 (2011) 629.
[24] I.K. Ding, N. Tétreault, J. Brillet, B.E. Hardin, E.H. Smith, S.J. Rosenthal, F. Sauvage, M. Grätzel, M.D. McGehee, Advanced Functional Materials 19/15 (2009) 2431.
[25] J. Kruger, R. Plass, L. Cevey, M. Piccirelli, M. Grätzel, U. Bach, Applied Physics Letters 79/13 (2001) 2085.
[26] H.J. Snaith, M. Grätzel, Advanced Materials 19/21 (2007) 3643.
[27] H.J. Snaith, A.J. Moule, C. Klein, K. Meerholz, R.H. Friend, M. Grätzel, Nano Letters 7/11 (2007) 3372.
[28] B.C. O'Regan, F. Lenzmann, The Journal of Physical Chemistry B 108/14 (2004) 4342.
[29] P.R.F. Barnes, K. Miettunen, X. Li, A.Y. Anderson, T. Bessho, M. Grätzel, B.C. O'Regan, Advanced Materials 25/13 (2013) 1881.
[30] J. Stöhr, K. Baberschke, R. Jaeger, R. Treichler, S. Brennan, Physical Review Letters 47/5 (1981) 381.
[31] J. Stöhr, NEXAFS Spectroscopy, Springer-Verlag, Berlin, 1992.
[32] J. Stöhr, D.A. Outka, Physical Review B 36/15 (1987) 7891.
[33] G. Hähner, Chemical Society Reviews 35/12 (2006) 1244.
[34] J. Kohanoff, Electronic Structure Calculations for Solids and Molecules, Cambridge, New York, 2006.
[35] C.J. Cramer, Essentials of Computational Chemistry: heories and Models, John Wiley & Sons, Ltd., Hoboken, NJ, USA, 2005.
[36] D. Sholl, J.A. Steckel, Density Functional Theory: A Practical Introduction, John Wiley & Sons, Ltd., Hoboken, NJ, 2009.
[37] A.D. Becke, The Journal of Chemical Physics 98/2 (1993) 1372.
[38] K. Hermann, L.G.M. Pettersson, M.E. Casida, C. Daul, A. Goursot, A. Koester, E. Proynov, A. St-Amant, D.R. Salahub, V. Carravetta, H. Duarte, C. Friedrich, N. Godbout, J. Guan, C. Jamorski, M. Leboeuf, M. Leetmaa, M. Nyberg, S. Patchkovskii, L. Pedocchi, F. Sim, L. Triguero, A. Vela, 2011.

Chapter 3. The Importance of Dye Chemistry and $TiCl_4$ Surface Treatment in the Behavior of Al_2O_3 Recombination Barrier Layers Deposited by Atomic Layer Deposition in Solid-State Dye-Sensitized Solar Cells

Atomic layer deposition (ALD) was used to fabricate Al_2O_3 recombination barriers in solid-state dye-sensitized solar cells (ss-DSSCs) employing an organic hole transport material (HTM) for the first time. Al_2O_3 recombination barriers of varying thickness were incorporated into efficient ss-DSSCs utilizing the Z907 dye adsorbed onto a 2-µm-thick nanoporouos TiO_2 active layer and the HTM spiro-OMeTAD. The impact of Al_2O_3 barriers was also studied in devices employing different dyes, with increased active layer thicknesses, and with substrates that did not undergo the $TiCl_4$ surface treatment. In all instances, electron lifetimes (as determined by transient photovoltage measurements) increased and dark current was suppressed after Al_2O_3 deposition. However, only when the $TiCl_4$ treatment was eliminated did device efficiency increase; in all other instances efficiency decreased due to a drop in short-circuit current. These results are attributed in the former case to the similar effects of Al_2O_3 ALD and the $TiCl_4$ surface treatment whereas the insulating properties of Al_2O_3 hinder charge injection and lead to current loss in $TiCl_4$-treated devices. The impact of Al_2O_3 barrier layers was unaffected by doubling the active layer thickness or using an alternative ruthenium dye, but a metal-free donor-π-acceptor dye exhibited a much smaller decrease in current due to its higher excited state energy. We develop a model employing prior research on Al_2O_3 growth and dye kinetics that successfully predicts the reduction in device current as a function of ALD cycles and is extendable to different dye/barrier systems.

3.1. Introduction

Given the bountiful energy resource provided by the sun, research of photovoltaic devices has accelerated in the past several years with the promise of providing for increased future energy demands. Recent progress in dye-sensitized solar cells (DSSCs)

[20, 22, 23] has improved the record device efficiency to over 12% at one sun intensity [25]. Widespread adoption of DSSC technology, however, will for reliability reasons likely necessitate reaching these high efficiencies in devices wherein the liquid redox electrolyte that regenerates oxidized dye molecules is replaced with a solid-state material. While a recent advance with an inorganic *p*-type semiconductor hole transport material (HTM) led to an 8.5% efficient solid-state DSSC (ss-DSSC) [29], organic HTM ss-DSSCs have only reached efficiencies of ~6-7% due to reduced light absorption compared to liquid DSSCs [32, 140]. Performance of organic HTM ss-DSSCs degrades when the TiO_2 active layer becomes much thicker than ~2 μm, as compared to the 5 – 15 μm thick TiO_2 used in high-efficiency liquid cells [140, 141]. As a result, the surface area available to adsorb dye molecules is reduced with a concomitant drop in light absorption. The thickness limits in ss-DSSCs are due, at least in the case of the most commonly used organic HTM spiro-OMeTAD (2,2',7,7'-tetrakis-(*N*,*N*-di-*p*-methoxyphenylamine)-9,9'-spirobifluorene) [31], to poor charge collection and a high charge recombination rate between electrons diffusing through the TiO_2 and holes in the spiro-OMeTAD. The recombination rate is high because it involves a single electron transfer step (as compared to the multistep process in the analogous pathway when the iodide/triiodide redox couple is employed) and the recombination rate increases further as the active layer thickness is increased due to a reduced pore-filling fraction of the spiro-OMeTAD, which limits separation of electrons and holes [33, 39, 142].

In order to limit this recombination process in both liquid and solid-state DSSCs, insulating metal oxide layers have been applied to the TiO_2 surface prior to dye adsorption. Recombination is impeded through a variety of mechanisms including passivation of surface trap sites, dielectric screening of electrons and holes, and by the presence of an electron tunneling barrier. In the first reports of such recombination barriers, the oxides, including SiO_2, ZrO_2, Nb_2O_5, and Al_2O_3, were deposited through solution methods and device efficiencies were improved [48, 50, 143]. The solution methods, however, only provide nanometer-level thickness resolution for the oxide shells and there are difficulties in producing a uniform coverage throughout the depth of the TiO_2 active layer [59]. Atomic layer deposition (ALD) has been used in many photovoltaic applications because ALD, in contrast to the solution methods referenced

above, offers angstrom-level thickness control and conformal coverage on high aspect ratio surfaces [58]. These attributes are obviously attractive for DSSC barrier layers and some recent reports have used ALD as the deposition method for several of the same materials grown *via* the solution method [61-63, 65-70, 73-75, 77, 144]. It is important to note that for the Al_2O_3 system discussed in this paper, ALD does not yield atomically smooth films. While the roughness is much less than in solution-grown films, the sub-monolayer growth-per-cycle rate of Al_2O_3 means that at low cycle numbers (≤ 5) the thickness variation in Al_2O_3 layers is of significance. This growth behavior has been described in detail elsewhere [62, 65, 71, 145] and its relevance to the work here will be detailed below.

While there have been many studies on metal oxide barrier layers grown by either ALD or solution deposition, the majority employed the iodide/triiodide redox couple where recombination is not a significant obstacle in limiting device efficiency; despite this, many improvements in device efficiency have still been reported. Some studies have examined liquid alternatives to the iodide system that promise higher achievable open-circuit voltage (V_{OC}) but suffer from higher recombination rates [61, 67, 69, 77], while others have examined *p*-type semiconductor-based ss-DSSCs [28, 51]. Only two studies have studied the effect of barrier layers with organic HTMs in TiO_2 DSSCs. Noma *et al.* improved device performance with poly(3-hexylthiophene) (P3HT) as the HTM using solution-deposited Al_2O_3 but do not report device efficiencies [146]. Li *et al.* studied the effect of ALD-grown ZrO_2 barrier layers in spiro-based ss-DSSCs and they observed large efficiency gains. Their control devices, however, suffered from low efficiencies (< 0.3%) [74], so it remains unknown whether similar gains can be achieved in a high-performing ss-DSSC. Furthermore, it has been noted [52, 58] that few studies have used nanoporous TiO_2 substrates treated with $TiCl_4$ prior to barrier layer growth [52, 53], which is known to yield large device efficiency gains by increasing the short-circuit current (J_{SC}) [42, 43]. No studies to our knowledge have combined ALD-grown barrier layers with $TiCl_4$-treated TiO_2 substrates.

While many metal oxides have been used as barrier layers, there is much work focusing on Al_2O_3 in particular. Al_2O_3 is attractive due to its wide bandgap [48], high

isoelectric point (which can enhance dye adsorption) [48, 147], and ability to raise the TiO_2 conduction band edge (which can improve the V_{OC}) [50, 63]. With respect to growth via ALD, Al_2O_3 is a particularly well-studied system [148] and ALD can be performed at very low temperatures (< 50 °C) [149]. On the other hand, the high conduction band of Al_2O_3 will inhibit electron injection from an excited dye state into TiO_2 and therefore if the Al_2O_3 barrier layer is too thick, device current will drop as relaxation of the dye excited state competes with electron injection via tunneling. This phenomenon has been observed throughout the literature but there are large discrepancies in the optimal Al_2O_3 shell thickness, ranging from 2 Å to 2 nm [62, 147]. Efficiency improvements with thick coatings have been reported with both solution methods and ALD, so it is not simply due to the inhomogeneous coatings created with the solution method.

The application of a metal oxide barrier layer should improve the collection efficiency of electrons successfully injected into TiO_2 by reducing the number of charge carriers lost *via* recombination. While this may offset or outweigh the loss of charge carriers that fail to inject in devices with poor charge collection efficiency, which is not the case at short-circuit in spiro-based ss-DSSCs [140], a barrier layer's primary benefit to DSSC performance is likely to be through an increase in V_{OC} due to a drop in dark current. The expected result of depositing a barrier layer, therefore, is to see an increasing V_{OC} and decreasing J_{SC} as the barrier thickness increases, and the goal is to identify an optimum barrier thickness where V_{OC} gains outweigh J_{SC} losses.

In order to better understand the conflicting results reported for optimal Al_2O_3 barrier layer thicknesses, in this paper we report our findings for ALD-deposited Al_2O_3 barriers in a variety of ss-DSSCs and we identify relevant variables. Beginning with an archetypal optimized ss-DSSC—Z907 dye, ~2 µm thick $TiCl_4$-treated nanoporous TiO_2, spiro-OMeTAD HTM—we observe the effect on device performance of varying numbers of Al_2O_3 ALD cycles. Transient photovoltage and dark current measurements are used to quantify the recombination-blocking abilities of Al_2O_3 layers. By comparing the behavior of Al_2O_3-coated substrates with and without $TiCl_4$ treatment we gain insight into $TiCl_4$'s mechanism of action. Thick TiO_2 substrates are used to probe the effect of

lengthened electron collection distances and our results indicate that even when the active layer thickness is doubled, recombination is not significantly exacerbated and high device efficiencies are possible. By comparing the behavior of the Z907 dye with an alternative Ru dye and a metal-free organic dye we demonstrate the importance of dye chemistry on current collection. Finally, using experimental and theoretical literature reports on the nature of Al_2O_3 growth *via* ALD at low cycle numbers [62, 65, 71, 145, 150], we develop a model to describe the dependence of device current on the number of ALD cycles.

3.2. Experimental Section

3.2.1. Nanostructured TiO_2 Substrates

As described elsewhere [151], glass substrates coated with fluorine-doped tin (15 Ω/□, Pilkington) were etched with 4 M HCl and Zn to create desired transparent electrode patterns. Substrates were then coated with a thin (~50 nm) TiO_2 compact layer by aerosol spray pyrolysis using air as a carrier gas at 450 °C. Nanoporous TiO_2 was deposited by doctor-blading a commercial paste (Dyesol 18NR-T) diluted with terpineol (Sigma-Aldrich) and annealing at 450 °C resulting in a film thickness of ~2.2 μm as measured by a Dektak profilometer. To make thicker TiO_2 films, substrates were heated at 125 °C for ten minutes prior to a second doctor-blading step. The $TiCl_4$ treatment was carried out by immersing the nanostructured TiO_2 in an acidic 0.02 M aqueous $TiCl_4$ solution overnight at room temperature and then annealing by slowly heating to 450 °C and maintaining for 30 minutes.

3.2.2. ALD of Al_2O_3

ALD was performed in a custom-built, traveling-wave, hot wall, tube furnace-type reactor with five radially-oriented precursor manifolds and a N_2 carrier gas line. The substrate temperature was maintained at 175 °C. The precursors, trimethylaluminum (TMA) (Sigma-Aldrich) and water, were held at room temperature. Following a similar process as Lin *et al.* [62], TMA was pulsed for 5 s and allowed to soak (that is, the reaction chamber was isolated from the vacuum pump and the precursor manifold valve was closed) for an additional 40 s. After evacuating for 70 s, H_2O was pulsed for 3 s and allowed to soak for an additional 40 s; subsequent cycles commenced after evacuating for 70 s. The growth rate of this process over 100 cycles on a Si (100) wafer with a native

oxide as measured by a spectroscopic ellipsometer (Woollam Alpha SE) was ~1.6 Å/cycle, somewhat higher than the ~1.0 Å/cycle rate measured using a shorter process involving 0.5 s precursor pulses and 10 s purges (with no soak steps). We believe that the higher growth rate is a result of the soaking procedure used to ensure Al_2O_3 growth throughout the highly porous TiO_2 substrates. Growth of Al_2O_3 throughout the nanoporous TiO_2 was verified by Auger electron spectroscopy (AES) (PHI 700) of cross-sections of a 5 µm thick TiO_2 layer (Figure 3-1).

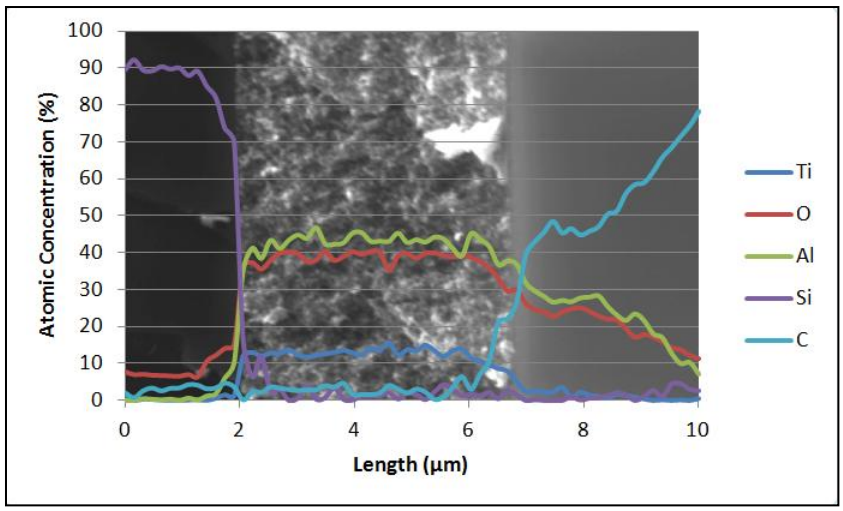


Figure 3-1: Cross-sectional Auger electron spectroscopy line-scan after 10 ALD cycles of Al_2O_3 on a ~5 µm thick nanoporous TiO_2 film on a Si substrate. The line scan was performed through the middle of the scanning electron microscopy image, i.e. the 50% atomic concentration line. While the exact atomic concentration is subject to instrument sensitivity limits and baselines chosen, the data clearly indicate uniform growth of Al_2O_3 throughout the 5 µm thick TiO_2 film.

3.2.3. ss-DSSC Device Fabrication

Nanostructured TiO_2 substrates with or without an Al_2O_3 coating were heated at 500 °C for 30 min and cooled to 80 °C prior to immersion in dye solutions. Dye solutions were made as follows: 0.3 mM Z907 dye (Dyesol, DNH2) in a 1:1 (v/v) solution of acetonitrile and *tert*-butanol; 0.3 mM YE05 dye, synthesized and purified as per Bessho *et al.* [152], in ethanol; 0.1 mM WN1 dye, synthesized and purified as per Nguyen *et al.* [153], with 1 mM chenodeoxycholic acid in a 1:1 (v/v) solution of acetonitrile and *tert*-butanol. The immersion step was carried out overnight for Z907 and YE05 and for 4 hours for WN1. After removal, Z907 and WN1 substrates were rinsed in acetonitrile; YE05 substrates were rinsed in ethanol. UV-Visible spectroscopy studies of

Z907 dye uptake (performed with a Cary 6000i spectrometer) indicated that Al_2O_3 layers did not reduce dye adsorption. For 2-µm-thick substrates, pore-filling of the spiro-OMeTAD hole-transporting material was performed by dissolving 225 mg mL^{-1} of spiro-OMeTAD (Lumtec) in chlorobenzene. *Tert*-butylpyridine was added to the solution at the ratio of 1:10.3 µL:mg of spiro-OMeTAD, and lithium bis-(trifluoromethylsulfonyl)imide salt (170 mg mL^{-1} in acetonitrile) was added at the ratio of 1:4.8 µL:mg of spiro-OMeTAD. For 4 µm thick substrates, the spiro-OMeTAD concentration was increased to 288 mg mL^{-1} with the additive ratios held constant. The solutions were deposited on TiO_2 substrates (30 µL per 3 cm^2 substrates) and spin-coated at 2000 RPM for 30 s. 200 nm thick Ag rear electrodes were deposited *via* thermal evaporation under vacuum below 10^{-6} torr.

3.2.4. Device Measurements

Current-voltage (*J-V*) curves were collected for devices with an average area of 8 mm^2 using a Xe lamp AM 1.5 solar simulator calibrated to 1 sun as described elsewhere [151]. Devices were light-soaked until maximum efficiencies were reached (~10-20 minutes). Constant current transient photovoltage measurements were performed with a setup like those described in more detail elsewhere [43, 129, 142]. Devices were light biased at 1 sun using a white LED array. A Keithley 2400 SourceMeter was used to maintain the current of a specified photovoltage in 0.1 V steps. A 50 ms square-wave pulse of light was applied using a white LED (~0.05 suns) while maintaining a constant current, resulting in an increased photovoltage. The decay of this photovoltage was fitted to determine a recombination lifetime.

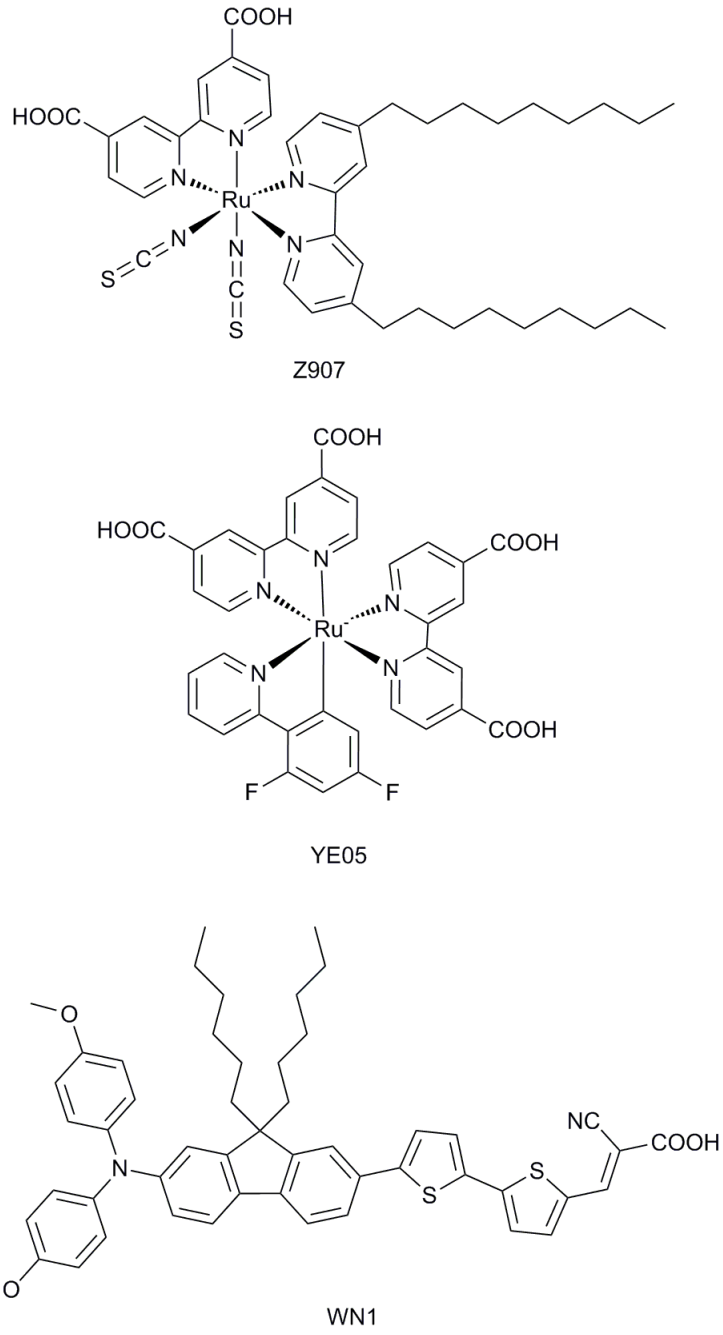


Figure 3-2: The three dye molecules used in the different studies: Z907, commonly used in ss-DSSCs; YE05, a Ru dye without isothiocyanate ligands that has demonstrated high efficiencies in liquid cells; WN1 a D-π-A metal-free dye with a cyanoacrylic acid attachment group.

3.3. Results & Discussion

Table 3-1 Device parameters for five different trials of solid-state tested at standard AM 1.5 illumination. Parameters represent the average of the top 50% of devices (ranked by efficiency), a set ranging in number from 7 - 20 depending on trial and treatment. The "Quantified Dark Current Onset" represents the voltage at which current in a dark *J-V* curve exceeds 2 mA/cm^2 and is used to capture the suppression of recombination in cells and is, unlike V_{OC}, independent of photocurrent. Unless noted otherwise, devices used the Z907 dye, were ~2.2 µm thick, and had undergone the $TiCl_4$ surface treatment prior to Al_2O_3 deposition.

Device Type	# ALD Cycles	J_{SC} (mA/cm2)	V_{OC} (V)	Quantified Dark Current Onset (V)	Fill Factor	Efficiency (%)
Archetypal ss-DSSCs	0	6.03	0.78	0.78	0.65	3.02
	1	4.66	0.82	0.83	0.66	2.53
	2	2.92	0.82	0.85	0.71	1.71
	3	1.07	0.84	0.90	0.68	0.61
	5	0.43	0.76	0.88	0.70	0.23
4 µm TiO_2 Cells	0	7.92	0.77	0.78	0.54	3.27
	1	7.07	0.78	0.81	0.56	3.10
	2	3.75	0.75	0.77	0.60	1.68
	3	1.97	0.82	0.89	0.61	0.98
No $TiCl_4$-Treatment	0	4.55	0.80	0.81	0.69	2.51
	1	4.74	0.80	0.80	0.73	2.74
	2	2.74	0.81	0.81	0.73	1.62
	3	1.11	0.79	0.83	0.73	0.64
YE05 Dye	0	4.37	0.76	0.78	0.68	2.26
	1	3.13	0.76	0.78	0.70	1.67
	2	1.37	0.73	0.80	0.68	0.68
	3	0.85	0.77	0.90	0.55	0.36
WN1 Dye	0	5.79	0.87	0.88	0.70	3.50
	1	5.69	0.88	0.88	0.70	3.49
	2	3.86	0.93	0.94	0.71	2.53
	3	2.94	0.95	0.97	0.71	1.97
	5	1.77	0.93	0.99	0.66	1.07

3.3.1. Archetypal ss-DSSC

Despite the recent development of alternative HTMs [151, 154], spiro-OMeTAD has continued to be the most widely-used organic HTM in ss-DSSCs, and many studies have reported optimal device thicknesses of ~2 µm. The Z907 dye, a modified version of the N3 dye with long alkyl chains on one of its bipyridine ligands [155], has been used for many of the foundational studies of solid-state devices [33, 34, 156-158] and as such, serves as a natural choice for the baseline studies presented here of 2 µm thick ss-DSSCs incorporating an Al_2O_3 barrier layer. Z907, along with the YE05 and WN1 dyes we also studied (*vide infra*), is shown in Figure 3-2. While the alkyl chains of Z907 are effective in increasing the distance between the TiO_2 surface and spiro-OMeTAD, ss-DSSCs still suffer from a high recombination rate leading to low open-circuit voltages. As such, we hoped to improve device performance in these cells by depositing an Al_2O_3 barrier layer atop the TiO_2 prior to dye attachment.

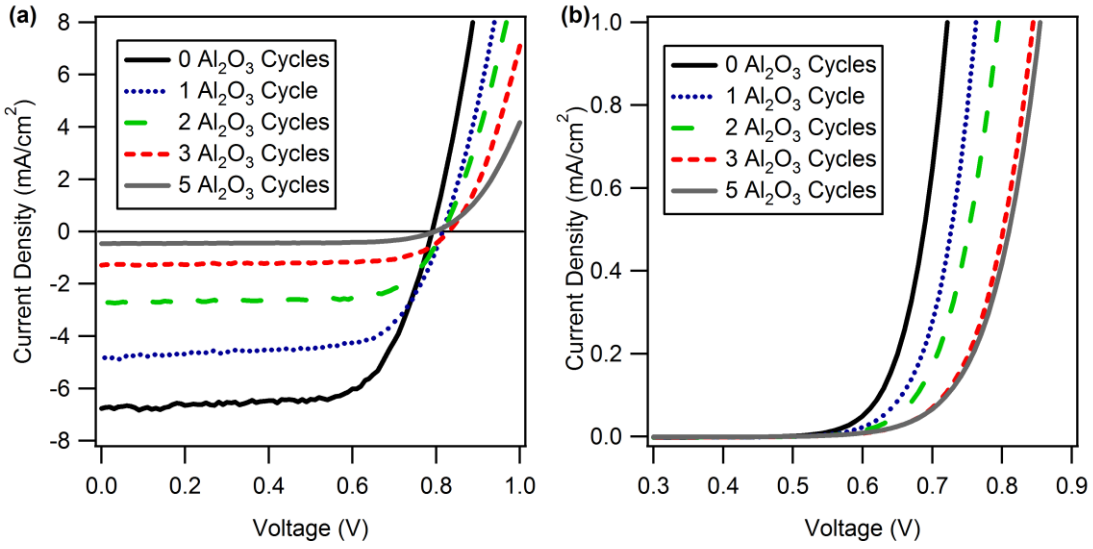


Figure 3-3: Current Density-Voltage (*J-V*) curves for high performing 2 µm-thick devices with the Z907 dye as a function of the number of ALD cycles of Al_2O_3. Under 1 sun of illumination, (a), J_{SC} is reduced with thicker Al_2O_3 layers as electron injection is suppressed, while V_{OC} rises and then falls back down as the reduction in dark current is counteracted by the drop in photocurrent. In the dark, (b), onset of current occurs at higher voltages as more Al_2O_3 is deposited.

The results (Figure 3-3 and Table 3-1) demonstrate that Al_2O_3 barrier layers are effective in delaying the onset of dark current, raising device V_{OC} (including one device with a V_{OC} of 0.89 V after three ALD cycles), and increasing the recombination lifetimes at voltages near the maximum power point of the cell (V_{MAX}) (Figure 3-4). Deposition of

Al_2O_3 on nanoporous TiO_2 has been shown to have minor effects on the TiO_2 conduction band level [28, 70, 144], and so we attribute these significant changes to the Al_2O_3 serving as a tunneling barrier to recombination. Despite these improvements in V_{OC} and electron lifetimes, however, the overall device efficiency declines, even after one ALD cycle, due to a drop in J_{SC} that is larger than the V_{OC} gains. The rapid dropoff in current is attributed to the failure of the dyes to inject electrons through the insulating Al_2O_3 and is so severe that by five ALD cycles the photocurrent is so low as to result in a net *drop* in V_{OC} relative to the control cells. Consistent with work by O'Regan *et al.* [28], the large increase in electron lifetimes (*i.e.* decrease in recombination rates) (Figure 3-4) suggests that the Al_2O_3 improves V_{OC} primarily by acting as a "tunnel barrier," although contributions from dipole and surface passivation effects cannot be excluded.

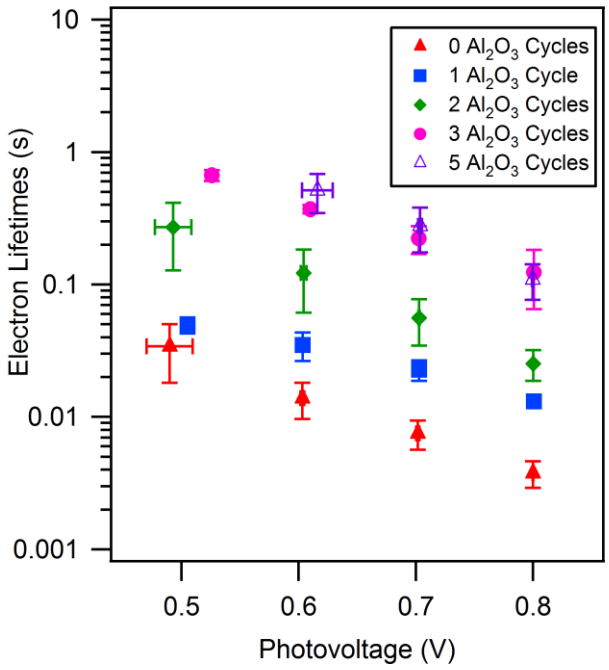


Figure 3-4: Electron lifetimes near the V_{MAX} (typically ~0.6 V depending on the number of ALD cycles) and V_{OC} of 2 µm thick Z907 $TiCl_4$-treated devices. Data represents the average of a subset of high-performing devices for which transient photovoltage measurements were performed. Error bars indicate standard deviations.

3.3.2. ss-DSSC with a thick (4.2 µm) TiO_2 active layer

The significant increases in ss-DSSC efficiency records over the past decade have come not through increasing light absorption *via* thicker active layers but, largely, from advances in dye design; optimal reported device thicknesses have stubbornly hovered

near 2 µm [32, 34, 128, 140]. Device thicknesses have remained limited due to high recombination rates and inadequate pore-filling of the HTM, the latter further exacerbating the former by constraining the distance between electrons in the TiO_2 and holes in the HTM thereby decreasing the tunneling distance for charge recombination. As the TiO_2 active layer is thickened it approaches the electron diffusion length in ss-DSSCs; therefore we studied the effect of Al_2O_3 recombination barriers in thicker devices anticipating that the benefit of suppressed recombination would be more apparent than in 2 µm cells.

The results, however, (Table 3-1) indicate the same trend in device performance as observed in thin cells. Although recombination is suppressed (Figure 3-5) and V_{OC} is improved (with the exception of 2 ALD cycles), the benefits do not outweigh the drop in J_{SC} and efficiency, as with 2 µm cells, is not improved with Al_2O_3 recombination barriers (Figure 3-6). Notably, we actually observe a modest improvement of 0.2% in efficiency for the devices without the Al_2O_3 barrier as the TiO_2 thickness is essentially doubled and even greater efficiency improvements are observed after one and three ALD cycles.

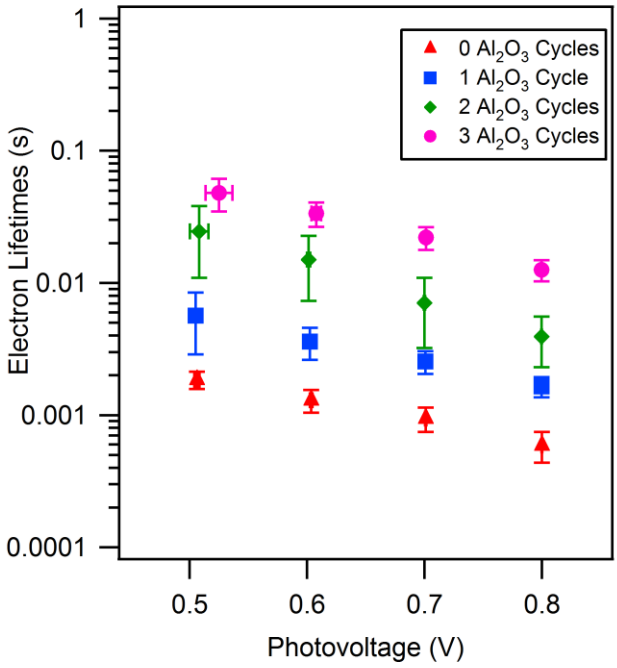


Figure 3-5: Electron Lifetimes for Z907 devices with thick TiO_2 active layers. Error bars indicate standard deviations.

Compared to the 2 µm devices, the thick cells have improved J_{SC}'s, lower fill factors, and relatively unchanged or slightly lower V_{OC}'s. The improved current is due to the larger number of adsorbed dye molecules in the thicker TiO_2 films coupled with effective charge collection. The drop in fill factor as thickness is increased is most likely due to increased series resistance due to the longer charge collection pathway. Notably the fill factor drop is less significant in the two and three ALD cycles cells where device current is lower. While the V_{OC} for Al_2O_3-treated devices is lower than in the 2 µm cells, the drop is not severe, and the similar recombination lifetimes indicate that recombination is not appreciably increased. In summary, our results indicate that V_{OC} and electron lifetimes do not significantly diminish and that, contrary to reports in the past [34], efficient ss-DSSCs can be made with active layers twice the "optimal" 2 µm thickness. However, the fact that high V_{OC}'s are attainable means that recombination barrier layers are not significantly more desirable in thick devices than in 2 µm devices.

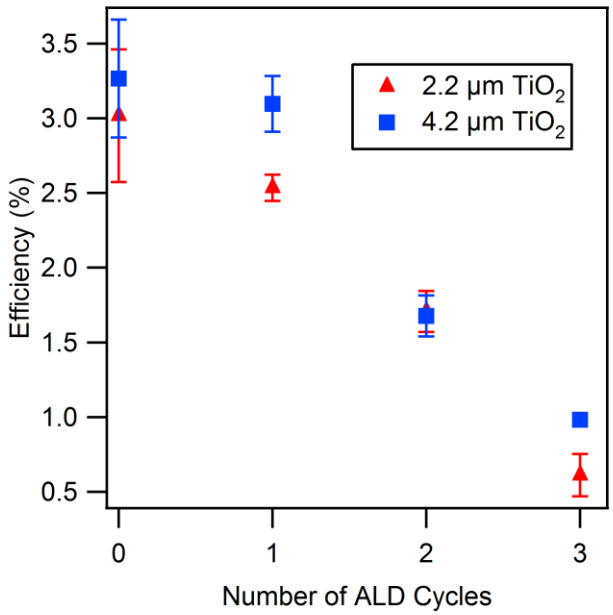


Figure 3-6: Device efficiency of "normal" thickness (~2.2 µm) devices and devices with thick (~4.2 µm) active layers as a function of the number of ALD cycles. Thicker devices had somewhat higher efficiencies overall but the same overall trend of decreasing efficiency with increasing number of ALD cycles. Error bars indicate standard deviations.

3.3.3. Effect of Al_2O_3 barrier layers on TiO_2 not treated with $TiCl_4$

The highest efficiency DSSCs, both liquid and solid-state, use TiO_2 substrates that have undergone a $TiCl_4$ chemical bath treatment. The large performance gains result from an increased J_{SC}, while fill factor and V_{OC} are relatively unaffected [42, 43]. The exact mechanism of this improvement has been studied in detail in liquid cells, and some of the key findings are summarized here: TiO_2 particle radii increase by ~1 nm; surface area decreases, but dye adsorption increases; the increases in J_{SC} are much greater than can be accounted for through increased dye adsorption and the primary cause of the higher J_{SC} appears to be improved charge separation [42, 43]. The improved charge separation has been attributed to a lowering of the TiO_2 conduction band and passivation of surface trap states.

Despite the importance of this treatment step, only one study that looked at Al_2O_3 barrier layers used $TiCl_4$-treated substrates. The improvements the authors observed using solution-deposited Al_2O_3 shells were varied with the dyes used and not as significant as in many of the reports using untreated TiO_2 [52]. Further, while some have suggested ALD deposition of Al_2O_3 as a replacement to the $TiCl_4$ treatment, no one has compared the effect of ALD of Al_2O_3 versus the $TiCl_4$ treatment.

As our results demonstrate (Table 3-1), the effect of the $TiCl_4$ treatment is striking—but only for the control cells *without* Al_2O_3. As shown in Figure 3-7, the $TiCl_4$ treatment results in a large increase in J_{SC} (over 30%), as seen elsewhere in the literature. Interestingly, however, the J_{SC} of cells with even one ALD cycle of the Al_2O_3 barrier layers is unchanged by $TiCl_4$ treatment. While Al_2O_3 improves average efficiency in untreated devices from 2.51% to 2.74%, $TiCl_4$ treatment is more effective, boosting the efficiency to 3.02%. The results, therefore, do not show ALD of Al_2O_3 to be superior to $TiCl_4$ treatment purely in terms of performance enhancement but they do suggest that an ALD layer be a potential substitute for the $TiCl_4$ treatment as a low electron affinity oxide can act as both a passivating agent and tunneling barrier.

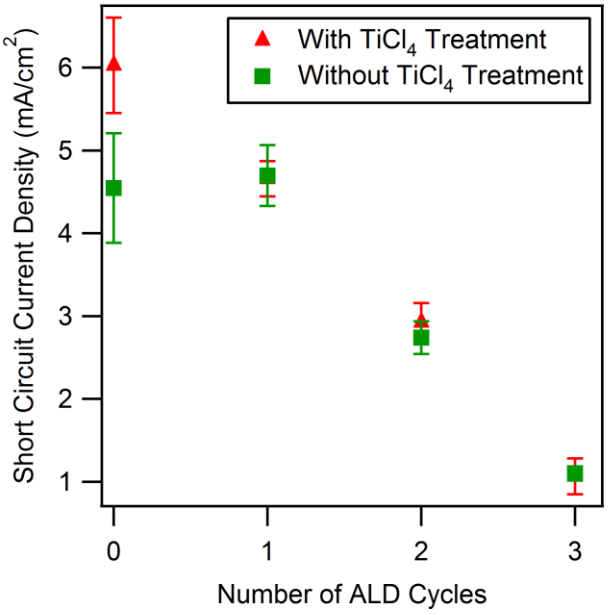


Figure 3-7: J_{SC} as a function of the number of Al_2O_3 ALD cycles for devices that did and did not undergo the $TiCl_4$ treatment. Whereas for control devices without Al_2O_3 the $TiCl_4$ treatment improves J_{SC} ~35%, the $TiCl_4$ treatment has no effect on J_{SC} in devices with subsequent Al_2O_3 deposition. Error bars indicate standard deviations.

The interesting behavior of J_{SC} as a function of $TiCl_4$ and Al_2O_3 treatments offers some insight into the mechanism by which the $TiCl_4$ treatment improves ss-DSSCs. In particular, whereas in all other trials using ruthenium dyes we observe a dropoff in J_{SC} of at least 10% (and sometimes much greater) after 1 ALD cycle, when $TiCl_4$ treatment is not performed, we instead observe an improvement in J_{SC} (Table 3-1). There is little change in electron lifetime in Z907 ss-DSSCs after $TiCl_4$ treatment (Figure 3-4 and Figure 3-8). Because recombination is believed to be a transport-limited (not surface state-limited) process, this is not inconsistent with the $TiCl_4$ treatment passivating surface states [28]. This suggests that the improved current is not a consequence of suppressed recombination leading to greater charge collection efficiency of injected electrons. The lack of current drop after 1 ALD cycle on substrates without the $TiCl_4$ treatment indicates that Al_2O_3 may be growing at TiO_2 surface sites that either resist dye adsorption or electron injection—sites that contribute little or nothing to device current unless the $TiCl_4$ treatment is performed. In this scenario, tunneling through a thin Al_2O_3 layer is preferable to having no dye, or a surface site on the TiO_2 that completely resists electron injection. After the first ALD cycle, however, current drops as the Al_2O_3 layers become

too thick and there are diminishing returns in terms of further TiO_2 passivation. It is also possible that one Al_2O_3 cycle has, like the $TiCl_4$ treatment, a beneficial effect on the TiO_2 conduction band, easing injection; this mechanism and the passivation theory are not mutually exclusive and both may contribute. Whatever the mechanism, as Figure 3-7 shows, J_{SC} is completely independent of $TiCl_4$ treatment if Al_2O_3 is deposited.

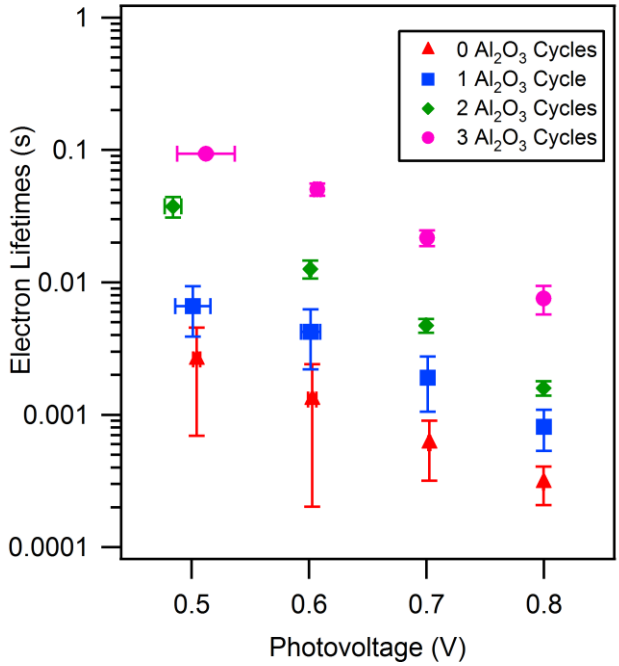


Figure 3-8: Electron lifetimes for devices with the Z907 dye without the $TiCl_4$ treatment for different numbers of ALD cycles. Error bars indicate standard deviations.

3.3.4. An alternative ruthenium dye

It has been suggested that the Z907 dye is particularly well-suited for ss-DSSCs because its long alkyl chains hold spiro-OMeTAD away from the TiO_2 surface [34, 159]. In order to determine if this property of the Z907 dye inhibits further improvement in $TiCl_4$-treated devices through recombination barriers, we tested a different Ru-centered dye, YE05 (Figure 3-2). YE05 is the first dye lacking the isothiocyanate ligands common to all other high-performing Ru dyes (including Z907) that is reported to achieve high efficiencies in liquid cells, although it has not been heretofore tested in ss-DSSCs [152, 160]. Despite the removal of the isothiocyanate ligands, which have been identified as the least chemically stable components of Ru dyes, YE05 is very similar to its closest analogue, the N3 dye, in terms of energetics and device performance. Furthermore, like

the N3 dye it is "homoleptic," meaning it has identical bypyridine ligands each with two carboxylic acid groups capable of attachment to an oxide surface, in contrast to the heteroleptic Z907. The four carboxylic acid groups also imply that YE05 lacks the alkyl chains of Z907 useful for recombination suppression.

The results with the YE05 dye, however, are qualitatively the same as those observed in the standard Z907 devices (Table 3-1). We observe a sharp dropoff in J_{SC} that more than outweighs the benefit of blocking recombination—indeed the drop in photocurrent is sufficiently severe so as to preclude any notable boost in V_{OC} despite the reduced dark current. The reduction of current relative to Al_2O_3-free devices as a function of the number of ALD cycles closely matches that of Z907 (Figure 3-9).

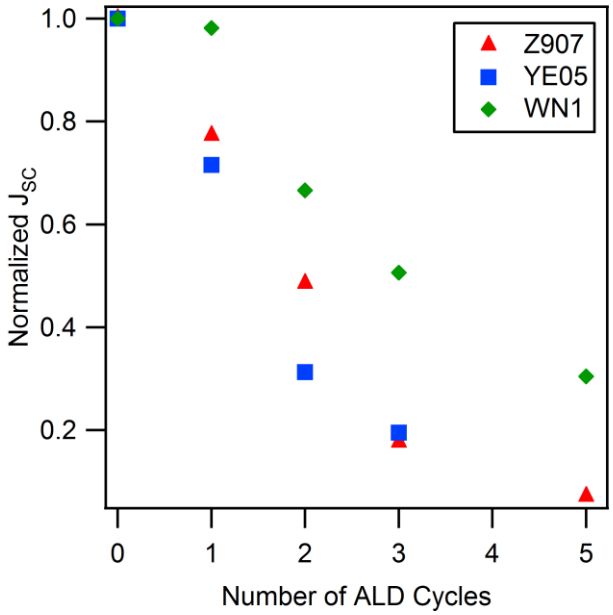


Figure 3-9: J_{SC}, normalized to devices with no Al_2O_3 recombination barriers, for the three dyes studied in ~2.2 µm $TiCl_4$-treated devices. The drop in current as more Al_2O_3 is deposited is much less severe with the WN1 D-π-A dye than with the two Ru dyes.

Surprisingly, YE05 devices without Al_2O_3 barriers do not suffer from a high recombination rate; in fact the electron lifetimes are somewhat higher than in Z907 devices (Figure 3-10). One possibility for the low recombination rate could be the manner in which the YE05 dye attaches to the surface, which computational studies have suggested is through three different carboxylic acid groups, as in other homoleptic dyes [161, 162]. In this orientation the dye ligands are more spread out over the TiO_2 surface,

hindering access of the HTM. Our data may also indicate that improved understanding of HTM pore-filling and proper additive concentrations (*i.e.* Li ions and *tert*-butyl pyridine) over the years has reduced the need for recombination blocking *via* alkyl chains on Ru dyes.

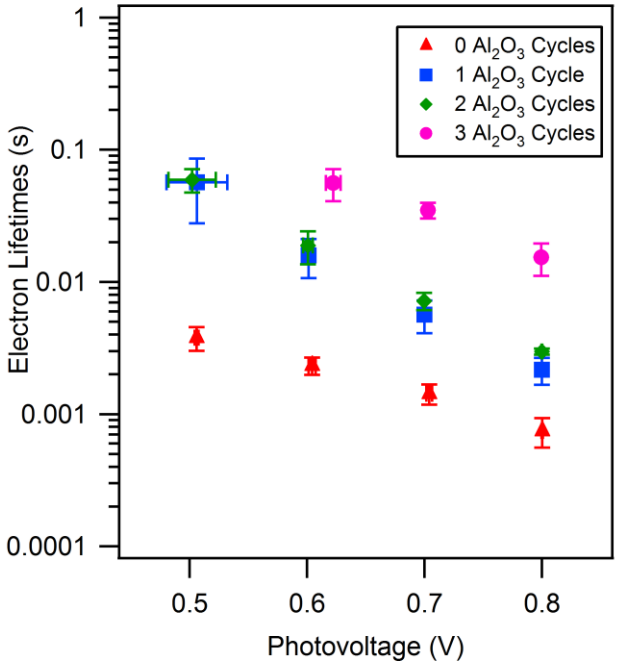


Figure 3-10: Electron lifetimes for devices with the YE05 dye for different numbers of ALD cycles. Error bars indicate standard deviations.

3.5 A metal-free organic donor-π-acceptor dye

Metal-free organic dyes have, due to their high molar extinction coefficients, become more prevalent in organic HTM ss-DSSCs, including the latest record devices [32, 140]. One of the most common dye designs is "D-π-A" (donor-π-acceptor) where a "donor" group is localized away from the TiO_2 surface and connected by a conjugated backbone to an acceptor group bound to the surface, frequently cyanoacrylic acid [163]. In order to compare the behavior of metal-free and Ru dyes when Al_2O_3 barrier layers are involved, we studied the WN1 dye (Figure 3-2) developed by Nguyen *et al.* [153].

The most striking result is that the reduction of current upon addition of the insulating Al_2O_3 layers is not nearly as severe with WN1 as it is with the Z907 and YE05 Ru dyes (Figure 3-9). We observe only a 2% drop in J_{SC} after one ALD cycle and ~50%

after three cycles, as compared to ~80% after three cycles with the two Ru dyes. At the same time, we observe longer electron lifetimes (Figure 3-11) and reduced dark current as more Al_2O_3 is deposited, just as with the Ru dyes, and V_{OC} gains with the organic dye are larger (Table 3-1) because the current drop is reduced—one device with three ALD cycles achieved a V_{OC} of 0.98 V, over 100 mV higher than the average Al_2O_3-free device. Only recent work by Fan *et al.* [52] (with Al_2O_3) and Chandiran *et al.* [77] (with Ga_2O_3) have examined cyanoacrylic acid organic dyes with metal oxide barrier layers. Fan *et al.* note that the degree of current drop after Al_2O_3 deposition is a strong function of the LUMO level of the dye [52]. LUMO levels in cyanoacrylic acid D-π-A dyes have been observed throughout the literature to be several hundred mVs higher than in Ru dyes, [52, 160, 163-165] and this is true for the dyes studied here: WN1, Z907, and YE05 have LUMO levels of -1.26, -0.79, and -0.76 V, respectively, *versus* the normal hydrogen electrode (NHE) [152, 153]. We believe that this gap (0.47 V from Z907 to WN1) is responsible for the improved performance of WN1; the higher LUMO levels of D-π-A dyes relative to Ru dyes means that injection efficiency is less sensitive to the presence of Al_2O_3 layers.

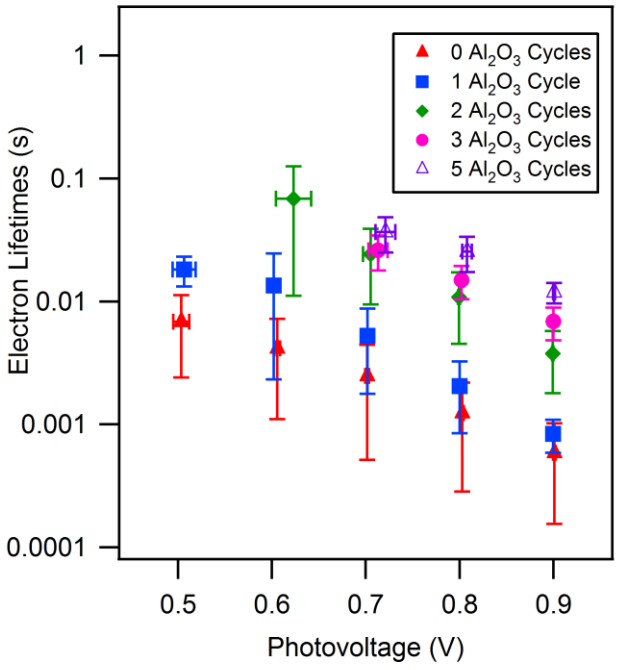


Figure 3-11: Electron lifetimes for devices with the WN1 dye for different numbers of ALD cycles. Lifetimes are higher than in cells with Ru dyes, consistent with the higher V_{OC}'s observed in WN1 devices. Error bars indicate standard deviations.

While the modified cells do not realize an overall efficiency gain—the best Al_2O_3-treated devices, 1 ALD cycle, have a negligible 0.01% reduction in overall efficiency (a small improvement in V_{OC} is offset by a small drop in J_{SC})—the WN1 results offer an important lesson for future progress in recombination barriers in ss-DSSCs. While the degree of charge injection suppression is also a function of the metal oxide chosen, our results clearly demonstrate the importance of dye selection. Generally-speaking, when using an insulating barrier layer with a high conduction band, a dye with a high LUMO level offers a much greater chance of achieving V_{OC} gains without large declines in J_{SC}. The implication of this is that while tunneling barriers may be complementary to current high-performance D-π-A dyes, improving solar cell absorption in the red-infrared spectrum by using a low optical gap dye with a low LUMO level may require using a less-insulating barrier, using no barrier at all, or, in a two-dye cell, selectively adsorbing the high LUMO dye on the barrier layer and the low LUMO dye on exposed TiO_2.

3.3.5. Modeling J_{SC} as a function of Al_2O_3 growth behavior

The ease of growing Al_2O_3 through either solution deposition or ALD and its high conduction band well-suited for insulating applications has resulted in a wealth of studies using both theoretical and experimental methods to probe its growth process and ability to slow down charge transfer on TiO_2. Tying together these disparate studies, we developed a model to better understand the large drop in current observed with Ru dyes as the number of Al_2O_3 ALD cycles was increased.

Various studies have suggested an island or random growth process for Al_2O_3 [63, 70, 145, 150]. In the former process, Al_2O_3 nucleates at surface defect sites and then preferentially grows on already-deposited Al_2O_3 rather than the substrate, whereas in the latter, growth occurs at any site with equal probability. Importantly, at low cycle numbers Al_2O_3 is not believed to grow *via* a two-dimensional process in which growth occurs at the lowest-lying sites on the substrate [166]; in other words, the Al_2O_3 barrier layer is not uniformly thick and a surface roughness exists. Tien and coworkers studied the growth of Al_2O_3 on nanoporous TiO_2 at low cycle numbers using transmission electron microscopy (TEM) and found a range of layer thicknesses present, in addition to

some uncoated regions [62, 63, 65]. Mäkinen and coworkers have used density functional theory (DFT) studies to examine the growth of Al_2O_3 on anatase TiO_2 and the resultant spatial separation from the TiO_2 of dyes adsorbed on Al_2O_3 [70, 71]. Both theoretical and experimental studies indicate that the growth rate of Al_2O_3 islands at low cycle numbers is approximately twice that (~2 Å/cycle) seen for average growth over a large number of cycles (~1 Å/cycle). In part, this can be understood by the fact that for example after the first cycle, if 50% of the surface is covered by Al_2O_3 islands 2 Å thick, the islands are growing at 2 Å/cycle but the growth rate over the entire surface is only 1 Å/cycle.

Accordingly, understanding the surface coverage is also very important, and there is less agreement on this than on the reported growth rates. Tien *et al*. developed a geometric model that uses X-ray photoelectron spectroscopy (XPS) to calculate a surface coverage, θ, and for one ALD cycle they found 25% coverage [65]. Mäkinen and coworkers, however, used simulations corroborated by experiments to determine a surface coverage of 50-75% after one ALD cycle [70, 71]. They attribute the gap between their coverage estimates and those reported by Tien *et al*. to be due to the assumptions of the XPS model that do not account for the fact that the nanospheres are sintered together. Given the wide range reported, for our model we assumed an average θ value of 50% after 1 ALD cycle and adjusted the θ's reported by Tien *et al*. for larger numbers of cycles accordingly. In order to model the thickness of the deposited Al_2O_3 islands we used the average values and standard deviations reported by Tien *et al*. and assumed a Gaussian distribution; these values, θ, and their corresponding number of ALD cycles are listed in Table 3-2.

Table 3-2: Al_2O_3 growth parameters used in model. Al_2O_3 thickness and variance were taken from Tien *et al*. [65]. θ was adjusted upwards 0.25 from the same source to better match values reported by Mäkinen and coworkers [70, 71]. Data for three cycles were interpolated from the values for one, two, and five cycles.

# ALD Cycles	Al_2O_3 Coverage, θ	Average Al_2O_3 Thickness (nm)	Al_2O_3 Thickness Standard Deviation (nm)
1	0.50	0.20	0.10
2	0.65	0.50	0.20
3	0.75	0.67	0.27
5	0.96	1.00	0.40

Many studies have examined the rates associated with charge transfer steps in Ru dyes. Electron injection is highly efficient when considering a Ru dye on a TiO_2 surface because the injection rate is much faster than the excited state decay rate. The addition of an insulating layer like Al_2O_3 is expected to slow down the injection processes which will result in appreciably lower injection efficiencies if the new injection rate is no longer much faster than the decay rate. This slowdown of electron transfer through an insulating medium can be understood to follow an exponential decay as thickness—and therefore tunneling distance—is increased, as described by Equation (2.3), where *d* is thickness and β is the tunneling attenuation factor.

$$Injection\ Rate \propto e^{-\beta * d} \tag{3.1}$$

Work by Guo *et al*. found a β value of 1.65 $Å^{-1}$ for the N3 Ru dye adsorbed on an Al_2O_3 overlayer [59]; in other words, a 10-Å-thick Al_2O_3 layer will slow down charge injection by a factor of ~40000. The final inputs to our model are the kinetic parameters of a Ru dye on TiO_2. While these values vary with dye and environment, we chose the representative *k* values shown in Table 3-3. While measuring all of these parameters specifically for the YE05 and Z907 dyes in our devices would be ideal, the device results indicate the fundamental similarity in behavior of these two Ru dyes and so we have used the β and *k* values measured with other chemically similar Ru dyes. Furthermore, because electron injection was not directly measured in our experiments, J_{SC} values, normalized to the J_{SC} of control devices without Al_2O_3 layers, are used as a proxy for electron injection efficiency. Charge collection efficiency at zero bias is very high even without recombination barriers in ss-DSSCs, and so the presence of insulating barrier

layers is not expected to yield large changes in J_{SC} irrespective of reduced electron injection efficiency [140].

Table 3-3: Representative *k* values used in the model. Values taken from Ref. [19].

Process	Abbreviation	k value (s^{-1})
Electron injected into TiO_2 from dye excited singlet state	$k_{s\text{-}inj}$	10^{12}
Electron injected into TiO_2 from dye excited triplet state	$k_{t\text{-}inj}$	10^{10}
Transition from singlet to triplet state	$k_{s\text{-}t}$	10^{13}
Decay of excited singlet state	$k_{s\text{-}dec}$	10^{10}
Decay of excited triplet state	$k_{t\text{-}dec}$	10^{8}

In the model, a number of surface sites are generated with Al_2O_3 overlayer thicknesses randomly generated using the parameters in Table 3-2. At each site effective injection rates (k'_{s-inj}, k'_{t-inj}) are calculated as per Equation (3.2)**(6.1** . The percentage of absorbed photons that lead to electrons successfully injected into the TiO_2 from the singlet ($P_{s\text{-}inj}$) and triplet ($P_{t\text{-}inj}$) states are given by Equation (3.3) and Equation (3.4), respectively. The injection figure then is simply the sum of $P_{s\text{-}inj}$ and $P_{t\text{-}inj}$.

$$k'_{inj} = k_{inj} * \mathrm{e}^{-\beta * d} \tag{3.2}$$

$$P_{s-inj} = \frac{k'_{s-inj}}{k_{s-dec} + k_{s-t} + k'_{s-inj}} \tag{3.3}$$

$$P_{t-inj} = \left(\frac{k_{s-t}}{k_{s-dec} + k_{s-t} + k'_{s-inj}}\right)\left(\frac{k'_{t-inj}}{k_{t-dec} + k'_{t-inj}}\right) \tag{3.4}$$

As shown in Figure 3-12, the sigmoidal shape of the model closely matches the deterioration of J_{SC} with more ALD cycles. The island growth model (*i.e.* mimicking that described by Tien *et al.* [65]) is contrasted to a uniform growth model in which the Al_2O_3 is assumed to proceed in homogeneously thick layers at the bulk growth rate. Using the measured 1.6 Å/cycle growth rate, a uniform growth assumption predicts a more severe current dropoff at higher cycle numbers than that observed and a better fit is achieved by the island growth model. The model demonstrates the important interplay between the physics of electron transfer and the growth behavior of a given ALD system in predicting

device performance. This model is further applicable to different dye/barrier layer systems given an understanding of the barrier growth process and the relevant charge transfer kinetics, and therefore provides a foundation for a more informed choice of dye and barrier type.

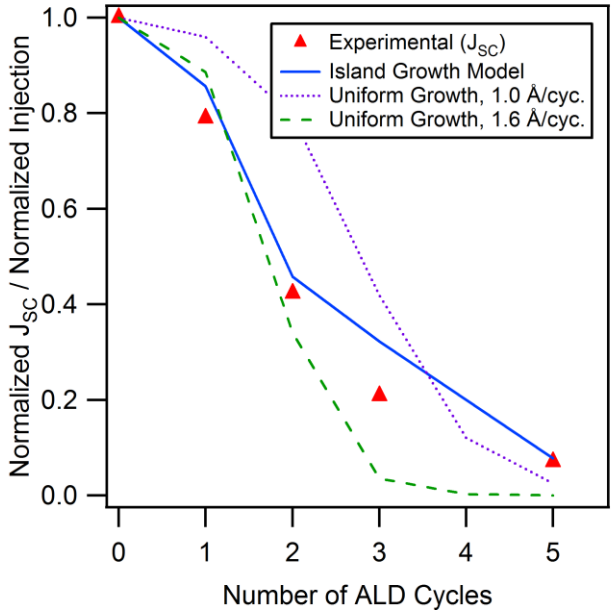


Figure 3-12: Comparison of the model for electron injection efficiency with experimentally-observed J_{SC}, normalized to devices without Al_2O_3, averaged over three trials using Ru dyes (Z907 on 2.2 and 4.2 µm active layers and the YE05 dye). The model assumes the Al_2O_3 layer grows *via* an island process and therefore has a varying thickness at each cycle number. This model compared to one assuming uniform Al_2O_3 growth of complete layers at two different growth rates. Injection efficiency is also normalized to the Al_2O_3-free system, for which the kinetic rate constants yield a 99% injection efficiency.

3.4. Conclusions

Al_2O_3 recombination barrier layers less than ~1 nm thick were deposited *via* ALD in ss-DSSCs using spiro-OMeTAD as the HTM while varying the device thickness, choice of dye, and use of the $TiCl_4$ surface treatment. The barrier layers were highly effective at reducing dark current and increasing electron lifetimes in the TiO_2, an effect which was amplified by depositing a larger number of ALD cycles, but in most cases the Al_2O_3 resulted in a reduction in J_{SC} and an overall drop in device efficiency attributed to reduced electron injection efficiency. This was observed even when the TiO_2 active layer thickness was doubled to over 4 µm, which surprisingly resulted in an overall improvement in device performance contrary to that observed elsewhere. When the

$TiCl_4$ treatment step was not performed, an increase in J_{SC} and efficiency was observed. Although this improvement was not greater than that achieved by performing the $TiCl_4$ treatment step without adding an Al_2O_3 layer, ALD offers a route to improve device efficiency when the $TiCl_4$ process is not feasible. The importance of dye choice was also demonstrated, as an organic D-π-A dye suffered much less current loss after Al_2O_3 deposition than the two Ru dyes tested. The large drops in J_{SC} with increasing Al_2O_3 ALD were more consistent with results in liquid DSSCs reported by Lin *et al.* and Antila *et al.* than those reported by Ganapathy *et al*. and Shanmugam *et al.*, as the latter two both achieved optimal device performance after 10 or more Al_2O_3 ALD cycles [62, 66, 70, 147]. In sum, our results suggest that while V_{OC} gains are achievable, recombination is not so significant a problem in an efficient, optimized TiO_2-based ss-DSSC that reductions in current can be ignored. If the dye/barrier combination is not chosen properly, the drop in J_{SC} can more than offset improvements in V_{OC}. Finally, a model was developed tying together work in the literature on the growth of Al_2O_3 on TiO_2 and charge transfer rates in dye/oxide systems. The model is effective in predicting the dropoff in current observed in our ss-DSSCs with Ru dyes, and serves as a platform for predicting deleterious drops in electron injection efficiency for other dye/barrier layer systems. Looking forward, despite the fact that Al_2O_3 only grows at 1-2 Å/cycle, both the model and experimental data demonstrate that J_{SC} can vary substantially from one ALD cycle to the next, even when the chosen dye has a high energy LUMO. Predicting the band energies of ultra-thin films—and therefore charge injection efficiency through such a film—from bulk properties is difficult. Therefore, when choosing a barrier layer material, rather than simply extrapolating from bulk properties, it may serve to select an oxide with a low growth rate ALD process (*e.g.* Y_2O_3 or In_2O_3) [167, 168]. The smaller the growth rate, the better the probability of identifying a barrier thickness and coverage that improves overall efficiency—regardless of the substrate and device architecture used.

3.5. Collaborations & Copyrights

This chapter is adopted from work originally published in the Royal Society of Chemistry journal *Physical Chemistry Chemical Physics* [72] and is reproduced by

permission of the PCCP Owner Societies. This project was originally developed with Jonathan Bakke, I-Kang Ding, and Brian Hardin. William Nguyen synthesized the WN1 dye in the lab of Alan Sellinger and Rajib Mondal synthesized the YE05 dye in the lab of Zhenan Bao. Colin Bailie, George Margulis, and Eric Hoke built the equipment setup used to perform the transient photovoltage experiments. Device fabrication and testing were performed in the lab of Michael McGehee.

3.6. References

[1] B. O'Regan, M. Grätzel, Nature 353/6346 (1991) 737.
[2] A. Hagfeldt, G. Boschloo, L. Sun, L. Kloo, H. Pettersson, Chemical Reviews 110/11 (2010) 6595.
[3] B.E. Hardin, H.J. Snaith, M.D. McGehee, Nat Photon 6/3 (2012) 162.
[4] A. Yella, H.-W. Lee, H.N. Tsao, C. Yi, A.K. Chandiran, M.K. Nazeeruddin, E.W.-G. Diau, C.-Y. Yeh, S.M. Zakeeruddin, M. Grätzel, Science 334/6056 (2011) 629.
[5] I. Chung, B. Lee, J. He, R.P.H. Chang, M.G. Kanatzidis, Nature 485/7399 (2012) 486.
[6] N. Cai, S.-J. Moon, L. Cevey-Ha, T. Moehl, R. Humphry-Baker, P. Wang, S.M. Zakeeruddin, M. Grätzel, Nano Letters 11/4 (2011) 1452.
[7] J. Burschka, A. Dualeh, F. Kessler, E. Baranoff, N.-L. Cevey-Ha, C. Yi, M.K. Nazeeruddin, M. Grätzel, Journal of the American Chemical Society 133/45 (2011) 18042.
[8] Q. Yu, Y. Wang, Z. Yi, N. Zu, J. Zhang, M. Zhang, P. Wang, ACS Nano 4/10 (2010) 6032.
[9] U. Bach, D. Lupo, P. Comte, J.E. Moser, F. Weissortel, J. Salbeck, H. Spreitzer, M. Grätzel, Nature 395/6702 (1998) 583.
[10] H.J. Snaith, L. Schmidt-Mende, Advanced Materials 19/20 (2007) 3187.
[11] I.K. Ding, N. Tétreault, J. Brillet, B.E. Hardin, E.H. Smith, S.J. Rosenthal, F. Sauvage, M. Grätzel, M.D. McGehee, Advanced Functional Materials 19/15 (2009) 2431.
[12] J. Melas-Kyriazi, I.K. Ding, A. Marchioro, A. Punzi, B.E. Hardin, G.F. Burkhard, N. Tétreault, M. Grätzel, J.-E. Moser, M.D. McGehee, Advanced Energy Materials 1/3 (2011) 407.
[13] E. Palomares, J.N. Clifford, S.A. Haque, T. Lutz, J.R. Durrant, Chemical Communications/14 (2002).
[14] E. Palomares, J.N. Clifford, S.A. Haque, T. Lutz, J.R. Durrant, Journal of the American Chemical Society 125/2 (2003) 475.
[15] Y. Diamant, S. Chappel, S.G. Chen, O. Melamed, A. Zaban, Coordination Chemistry Reviews 248/13-14 (2004) 1271.
[16] J. Guo, C. She, T. Lian, The Journal of Physical Chemistry C 111/25 (2007) 8979.
[17] J.R. Bakke, K.L. Pickrahn, T.P. Brennan, S.F. Bent, Nanoscale 3/9 (2011) 3482.
[18] T.W. Hamann, O.K. Farha, J.T. Hupp, The Journal of Physical Chemistry C 112/49 (2008) 19756.

[19] T.C. Li, M.S. Goes, F. Fabregat-Santiago, J. Bisquert, P.R. Bueno, C. Prasittichai, J.T. Hupp, T.J. Marks, Journal of Physical Chemistry C 113/42 (2009) 18385.
[20] C. Lin, F.-Y. Tsai, M.-H. Lee, C.-H. Lee, T.-C. Tien, L.-P. Wang, S.-Y. Tsai, Journal of Materials Chemistry 19/19 (2009) 2999.
[21] T.-C. Tien, F.-M. Pan, L.-P. Wang, C.-H. Lee, Y.-L. Tung, S.-Y. Tsai, C. Lin, F.-Y. Tsai, S.-J. Chen, Nanotechnology 20/30 (2009) 305201.
[22] J.W. Ondersma, T.W. Hamann, The Journal of Physical Chemistry C 114/1 (2010) 638.
[23] T.-C. Tien, F.-M. Pan, L.-P. Wang, F.-Y. Tsai, C. Lin, The Journal of Physical Chemistry C 114/21 (2010) 10048.
[24] M. Shanmugam, M.F. Baroughi, D. Galipeau, Thin Solid Films 518/10 (2010) 2678.
[25] M. Shanmugam, B. Bills, M.F. Baroughi, Materials Research Society Symposium Proceedings 1260/T10 (2010) 1.
[26] C. Prasittichai, J.T. Hupp, The Journal of Physical Chemistry Letters 1/10 (2010) 1611.
[27] M.J. DeVries, M.J. Pellin, J.T. Hupp, Langmuir 26/11 (2010) 9082.
[28] A.M. Spokoyny, T.C. Li, O.K. Farha, C.W. Machan, C. She, C.L. Stern, T.J. Marks, J.T. Hupp, C.A. Mirkin, Angewandte Chemie International Edition 49/31 (2010) 5339.
[29] B. Bills, M. Shanmugam, M.F. Baroughi, Thin Solid Films 519/22 (2011) 7803.
[30] L.J. Antila, M.J. Heikkilä, V. Mäkinen, N. Humalamäki, M. Laitinen, V. Linko, P. Jalkanen, J. Toppari, V. Aumanen, M. Kemell, P. Myllyperkiö, K. Honkala, H. Häkkinen, M. Leskelä, J.E.I. Korppi-Tommola, The Journal of Physical Chemistry C 115/33 (2011) 16720.
[31] A.K. Chandiran, N. Tetreault, R. Humphry-Baker, F. Kessler, E. Baranoff, C. Yi, M.K. Nazeeruddin, M. Grätzel, Nano Letters (2012).
[32] R.L. Puurunen, W. Vandervorst, Journal of Applied Physics 96/12 (2004) 7686.
[33] V. Mäkinen, K. Honkala, H. Häkkinen, The Journal of Physical Chemistry C 115/18 (2011) 9250.
[34] X.-T. Zhang, H.-W. Liu, T. Taguchi, Q.-B. Meng, O. Sato, A. Fujishima, Solar Energy Materials and Solar Cells 81/2 (2004) 197.
[35] B.C. O'Regan, S. Scully, A.C. Mayer, E. Palomares, J. Durrant, The Journal of Physical Chemistry B 109/10 (2005) 4616.
[36] Y. Noma, T. Kado, D. Ogata, Y. Hara, S. Hayase, Japanese Journal of Applied Physics 47/1 (2008) 505.
[37] S.-Q. Fan, Y. Geng, C. Kim, S. Paik, J. Ko, Materials Chemistry and Physics 132/2-3 (2012) 943.
[38] D.B. Menzies, Q. Dai, L. Bourgeois, R.A. Caruso, Y.-B. Cheng, G.P. Simon, L. Spiccia, Nanotechnology 18/12 (2007) 125608.
[39] P.M. Sommeling, B.C. O'Regan, R.R. Haswell, H.J.P. Smit, N.J. Bakker, J.J.T. Smits, J.M. Kroon, J.A.M. van Roosmalen, The Journal of Physical Chemistry B 110/39 (2006) 19191.
[40] B.C. O'Regan, J.R. Durrant, P.M. Sommeling, N.J. Bakker, The Journal of Physical Chemistry C 111/37 (2007) 14001.

[41] V. Ganapathy, B. Karunagaran, S.-W. Rhee, Journal of Power Sources 195/15 (2010) 5138.
[42] A.C. Dillon, A.W. Ott, J.D. Way, S.M. George, Surface Science 322/1-3 (1995) 230.
[43] M.D. Groner, F.H. Fabreguette, J.W. Elam, S.M. George, Chemistry of Materials 16/4 (2004) 639.
[44] T.-C. Tien, F.-M. Pan, L.-P. Wang, F.-Y. Tsai, C. Lin, Thin Solid Films 520/6 (2012) 1745.
[45] T. Leijtens, I.K. Ding, T. Giovenzana, J.T. Bloking, M.D. McGehee, A. Sellinger, ACS Nano 6/2 (2012) 1455.
[46] T. Bessho, E. Yoneda, J.-H. Yum, M. Guglielmi, I. Tavernelli, H. Imai, U. Rothlisberger, M.K. Nazeeruddin, M. Grätzel, Journal of the American Chemical Society 131/16 (2009) 5930.
[47] W.H. Nguyen, C.D. Bailie, M. Grätzel, M.D. McGehee, A. Sellinger, In prep. (2012).
[48] B.C. O'Regan, F. Lenzmann, The Journal of Physical Chemistry B 108/14 (2004) 4342.
[49] X. Liu, W. Zhang, S. Uchida, L. Cai, B. Liu, S. Ramakrishna, Advanced Materials 22/20 (2010) E150.
[50] P. Wang, S.M. Zakeeruddin, J.E. Moser, M.K. Nazeeruddin, T. Sekiguchi, M. Grätzel, Nat Mater 2/6 (2003) 402.
[51] L. Schmidt-Mende, S.M. Zakeeruddin, M. Grätzel, Applied Physics Letters 86/1 (2005) 3504.
[52] J.E. Kroeze, N. Hirata, S. Koops, M.K. Nazeeruddin, L. Schmidt-Mende, M. Grätzel, J.R. Durrant, Journal of the American Chemical Society 128/50 (2006) 16376.
[53] J.R. Jennings, L.M. Peter, The Journal of Physical Chemistry C 111/44 (2007) 16100.
[54] F. Fabregat-Santiago, J. Bisquert, L. Cevey, P. Chen, M. Wang, S.M. Zakeeruddin, M. Grätzel, Journal of the American Chemical Society 131/2 (2009) 558.
[55] H.J. Snaith, A.J. Moule, C. Klein, K. Meerholz, R.H. Friend, M. Grätzel, Nano Letters 7/11 (2007) 3372.
[56] L. Schmidt-Mende, J.E. Kroeze, J.R. Durrant, M.K. Nazeeruddin, M. Grätzel, Nano Letters 5/7 (2005) 1315.
[57] M. Grätzel, Accounts of Chemical Research 42/11 (2009) 1788.
[58] F. De Angelis, S. Fantacci, A. Selloni, M. Grätzel, M.K. Nazeeruddin, Nano Letters 7/10 (2007) 3189.
[59] F. De Angelis, S. Fantacci, A. Selloni, M.K. Nazeeruddin, M. Grätzel, The Journal of Physical Chemistry C 114/13 (2010) 6054.
[60] D.P. Hagberg, J.-H. Yum, H. Lee, F. De Angelis, T. Marinado, K.M. Karlsson, R. Humphry-Baker, L. Sun, A. Hagfeldt, M. Grätzel, M.K. Nazeeruddin, Journal of the American Chemical Society 130/19 (2008) 6259.
[61] P. Wang, S.M. Zakeeruddin, J.E. Moser, R. Humphry-Baker, P. Comte, V. Aranyos, A. Hagfeldt, M.K. Nazeeruddin, M. Grätzel, Advanced Materials 16/20 (2004) 1806.
[62] D. Kuang, S. Ito, B. Wenger, C. Klein, J.-E. Moser, R. Humphry-Baker, S.M. Zakeeruddin, M. Grätzel, Journal of the American Chemical Society 128/12 (2006) 4146.

[63] R.L. Puurunen, Chemical Vapor Deposition 10/3 (2004) 159.
[64] M.D. Archer, A.J. Nozik (Eds.), Nanostructured and Photoelectrochemical Systems for Solar Photon Conversion, Imperial College Press, London, 2008.
[65] P. de Rouffignac, J.-S. Park, R.G. Gordon, Chemistry of Materials 17/19 (2005) 4808.
[66] D.-J. Lee, J.-Y. Kwon, J.I. Lee, K.-B. Kim, The Journal of Physical Chemistry C 115/31 (2011) 15384.
[67] T.P. Brennan, J.R. Bakke, I.K. Ding, B.E. Hardin, W.H. Nguyen, R. Mondal, C.D. Bailie, G.Y. Margulis, E.T. Hoke, A. Sellinger, M.D. McGehee, S.F. Bent, Physical Chemistry Chemical Physics 14/35 (2012) 12130.

Chapter 4. TiO_2 Conduction Band Modulation with In_2O_3 Recombination Barrier Layers in Solid-State Dye-Sensitized Solar Cells

Atomic layer deposition (ALD) was used to grow sub-nanometer indium oxide recombination barriers in a solid-state dye-sensitized solar cell (DSSC) based on the spiro-OMeTAD hole-transport material (HTM) and the WN1 donor-π-acceptor organic dye. While optimal device performance was achieved after 3-10 ALD cycles, 15 ALD cycles (~2 Å of In_2O_3) was observed to be optimal for increasing open-circuit voltage (V_{OC}) with an average improvement of over 100 mV, including one device with an extremely high V_{OC} of 1.00 V. An unexpected phenomenon was observed after 15 ALD cycles: the increasing V_{OC} trend reversed and after 30 ALD cycles V_{OC} dropped by over 100 mV relative to control devices without any In_2O_3. To explore possible causes of the non-monotonic behavior resulting from In_2O_3 barrier layers, we conducted several device measurements, including transient photovoltage experiments and capacitance calculations, as well as density functional theory (DFT) studies. Our results suggest that the V_{OC} gains observed in the first 20 ALD cycles are due to both a surface dipole that pulls up the TiO_2 conduction band and recombination suppression. After 30 ALD cycles, however, both effects are reversed: the surface dipole of the In_2O_3 layer reverses direction, lowering the TiO_2 conduction band, and mid-bandgap states introduced by In_2O_3 accelerate recombination, leading to a reduced V_{OC}.

4.1. Introduction

Dye-sensitized solar cells (DSSCs), first developed by Grätzel and coworkers in the 1990s [1], represent a promising photovoltaic design due to their competitive efficiencies, use of inexpensive materials, and high degree of modularity opening up several different application areas [2, 3]. Recent progress in DSSCs has yielded efficiencies in excess of 12% in liquid cells [4] and over 8% in solid-state cells [5, 6]. Meanwhile, efforts continue in replacing dye molecules with alternative absorbers such as chalcogenides [7] and perovskites [8, 9] while maintaining the nanoporous photoanode and other features of the archetypal DSSC design. Regardless of absorbing material, a

critical issue in all of these devices is managing the rate of detrimental charge transfer processes inherent to the high surface area design.

In a DSSC, undesirable interfacial charge recombination reactions occur when an electron that has been injected by a dye molecule into the metal oxide photoanode (*e.g.* TiO_2, SnO_2, ZnO) recombines with a hole located in either an oxidized dye molecule or the hole-transport material (HTM). Because reduction of oxidized dye molecules (*i.e.* regeneration) by the HTM is relatively fast, recombination with oxidized dye molecules has a smaller impact on charge collection efficiency than does the photoanode-HTM recombination process [10]. This process is particularly important when alternatives to the iodide/triiodide redox couple, which has remained a popular choice for the HTM since the original 1991 device, are employed. Although high efficiencies have been achieved with iodide/triiodide HTMs, the large overpotential for dye regeneration caps the maximum achievable open-circuit voltage (V_{OC}), ultimately limiting device efficiency [11]. This has motivated alternative liquid redox couples (such as cobalt-based systems) which offer lower overpotentials but have higher recombination rates [4, 12]. Substituting the iodide/triiodide HTM with a solid-state HTM has the potential to both improve device V_{OC} and provide an added practical advantage of eliminating the liquid component of the cell, and thus difficulties due to corrosion and leakage. Like the cobalt redox system, however, both organic [13] and inorganic [14] solid-state HTMs exhibit much higher recombination rates than the iodide/triiodide system.

In order to reduce this photoanode-HTM recombination process, many studies have examined thin (nanometer-scale), passivating, insulating, barrier layers deposited atop the photoanode in a "core-shell" fashion prior to dye adsorption. Starting with Palomares *et al*. [15], several studies have used chemical bath deposition (CBD) to grow metal oxides such as Al_2O_3 [14-21], SiO_2 [17], ZrO_2 [16, 17, 22], MgO [16, 18, 23], $SrTiO_3$ [19], Nb_2O_5 [19], $CaCO_3$ [24, 25], In_2O_3 [16, 22], and HfO_2 [26]. While these CBD-grown barrier layers have often proved effective in improving device performance, the CBD technique is limited by its relatively low thickness resolution (on the order of 1 nm) and inhomogeneous growth rate throughout the photoanode film [27]. This has inspired barrier layer studies using atomic layer deposition (ALD), which offers finer

thickness control (on the order of Ångstroms) and the ability to uniformly coat high aspect ratio substrates [28], of many similar insulating oxides: Al_2O_3 [29-41], HfO_2 [35, 42], ZrO_2 [43], SiO_2 [44, 45], and Ga_2O_3 [12]. Despite the wealth of barrier layer studies—grown using either CBD or ALD—relatively few have focused on solid-state DSSCs [14, 20, 23, 41, 43, 46], particularly the commonly-used organic HTM spiro-OMeTAD (2,2',7,7'-tetrakis-(*N*,*N*-di-*p*-methoxyphenylamine)-9,9'-spirobifluorene) [13] which suffers from a high recombination rate [23, 41, 43].

The primary mechanisms by which a metal oxide barrier layer can improve device performance are well described by O'Regan *et al*. [14]: it can passivate surface defect sites that serve as recombination centers; it can act as an insulating wall between the photoanode and both oxidized dye molecules and the HTM, thereby serving as a tunneling barrier to recombination; it can introduce a surface dipole which raises the photoanode's conduction band. In the first two mechanisms, the reduction of recombination can increase the charge collection efficiency (raising the short-circuit current density, J_{SC}, and/or fill factor) and reduce dark current (raising V_{OC}), while in the dipole mechanism an upward shift of the photoanode conduction band also lifts the Fermi level inside the photoanode, raising V_{OC}. None of these mechanisms are mutually exclusive and all three can play a part in improving device performance, but it has been observed in Al_2O_3 and Ga_2O_3 on TiO_2, for example, that the tunneling barrier mechanism is dominant whereas in MgO on SnO_2 a conduction band shift is dominant [12, 14, 23]. The insulating nature of these barrier layers, however, can also reduce device performance if the barrier unduly hinders electron injection from the dye into the photoanode. It has been observed that once the barrier layers reach a certain critical thickness, losses in electron injection efficiency outweigh any gains from reducing recombination and/or raising the photoanode conduction band [41].

In our previous work with spiro-OMeTAD-based solid-state DSSCs (ss-DSSCs) using Al_2O_3 barrier layers [41] we observed that given the growth rate of Al_2O_3 and its highly insulating nature, the critical thickness is reached in as early as one ALD cycle if the efficiency-enhancing $TiCl_4$ treatment [47] is also performed. Charge collection efficiency at zero bias is in fact quite high in spiro-based TiO_2 ss-DSSCs [48] and

appreciably increasing J_{SC} is therefore difficult; in order to improve device efficiency then, V_{OC} and fill factor gains must be significant relative to any reduction in electron injection efficiency. The lessons from Al_2O_3 motivate finding a metal oxide layer that is less insulating and can be deposited at a lower growth rate than the 1 Å/ALD cycle typical of Al_2O_3. One potentially attractive ALD barrier layer material is In_2O_3. Whereas the conduction band of bulk Al_2O_3 is approximately 4.0 V higher than that of TiO_2 [17], the bulk conduction band of In_2O_3 is only ~300 mV higher than that of TiO_2 [49]. Further, an ALD process was recently reported by Lee *et al*. which uses H_2O and trimethylindium (TMI) as precursors [50]: not only did they report a rather low growth rate (~0.4 Å/ALD cycle), but the precursors are small molecules, which facilitates complete penetration of a nanoporous photoanode.

In this report we describe our investigation of the effect of In_2O_3 barrier layers grown via the TMI/H_2O ALD process on TiO_2-based ss-DSSCs using spiro-OMeTAD as the HTM and an organic donor-π-acceptor (D-π-A) dye as the sensitizer. For In_2O_3 layers up to 2 Å thick, we observe behavior consistent with typical metal oxide barrier layers: V_{OC} rises and recombination lifetimes increase, although J_{SC} drops as the layers approach ~2 Å, consistent with decreased electron injection efficiency. As the In_2O_3 layers increase in thickness from ~2 to 4 Å, however, their impact on device operation fundamentally changes. Surprisingly, no further current loss is observed and the large increases in V_{OC} and recombination lifetimes are reversed such that by the time the In_2O_3 layer is ~4 Å thick, device V_{OC} is more than 100 mV lower than in cells without In_2O_3 layers. In order to better understand this phenomenon, we analyzed the behavior of electron lifetime and device capacitance as a function of In_2O_3 layer thickness. With insight gained from density functional theory (DFT) simulations of In_2O_3 atop TiO_2, we attribute the observed behavior to the following phenomena: the large V_{OC} and lifetime gains for thin In_2O_3 layers are due to both the tunnel barrier effect and a favorable surface dipole directed away from the photoanode surface that raises the TiO_2 conduction band. After a critical thickness is reached (~2-4 Å, corresponding to approximately a full monolayer coverage), the V_{OC} and lifetime trends are reversed as the In_2O_3-induced dipole changes direction, lowering the TiO_2 conduction band, and In_2O_3 introduces intra-band gap states that accelerate, rather than suppress, recombination. Our results

demonstrate the promise of very thin In_2O_3 barrier layers grown using the TMI/H_2O ALD process for improving electron lifetime and V_{OC} with minimal current loss and illustrate the sometimes unanticipated and non-linear behavior of metal oxide systems as they transition from sub-monolayers to continuous films.

4.2. Materials & Methods

4.2.1. Preparation of Nanoporous TiO_2 Substrates

Nanoporous TiO_2 substrates were prepared in the same manner as in our report on Al_2O_3 barrier layers [41]. Briefly, fluorine-doped tin oxide (FTO)-coated glass (15 Ω/□, Pilkington) substrates were masked with tape and etched with 4 M HCl and Zn powder in order to create the desired front electrode pattern. A compact TiO_2 layer (~50 nm thick) was then deposited via spray pyrolysis of titanium diisopropoxide bis(acetylacetonate) (Aldrich) diluted in ethanol with air as a carrier gas at 450 °C. The nanoporous TiO_2 photoanode was subsequently deposited by doctor-blading a commercial paste (Dyesol 18NR-T) diluted at a 1:1 (w/w) ratio with terpineol (Sigma-Aldrich) and annealing at 450 °C, resulting in a film thickness of ~2.2 μm as measured by a Dektak profilometer. All substrates then underwent a $TiCl_4$ chemical bath deposition: nanoporous TiO_2 was coated overnight with an acidic 0.02 M aqueous $TiCl_4$ solution at room temperature and subsequently annealed by slowly heating to and then maintaining at 450 °C for 30 minutes.

4.2.2. Atomic Layer Deposition and Characterization of In_2O_3

ALD was performed in a custom-built, traveling-wave, hot wall, tube furnace-type reactor with five radially-oriented precursor manifolds and a N_2 carrier gas line. Following Lee *et al*. [50], trimethylindium (Strem) and H_2O were chosen as the reactants. Substrates were maintained at 230 °C (approximately in the middle of the 200 – 250 °C ALD window described by Lee *et al*.) and a single ALD cycle consisted of a 10 s pulse of trimethylindium, 30s purge, 12 s pulse of H_2O, and a 45 s purge. Like Lee *et al*., we noted the necessity for very large H_2O exposures in order to grow In_2O_3; while our total H_2O exposure level per cycle was similar (~ 2 Torr*s), our growth rate, measured on a Si (100) wafer with a native oxide by a spectroscopic ellipsometer (Woollam Alpha SE), was ~0.2 Å/cycle, somewhat lower than the ~0.4 Å reported by Lee *et al.* but

advantageous given the requirement for maximal barrier layer thickness control. A PHI 700 scanning Auger nanoprobe was used to perform Auger electron spectroscopy (AES) on cross-sections of nanoporous TiO_2 substrates in order to verify the growth of In_2O_3 throughout a 2 µm film (Figure 4-1).

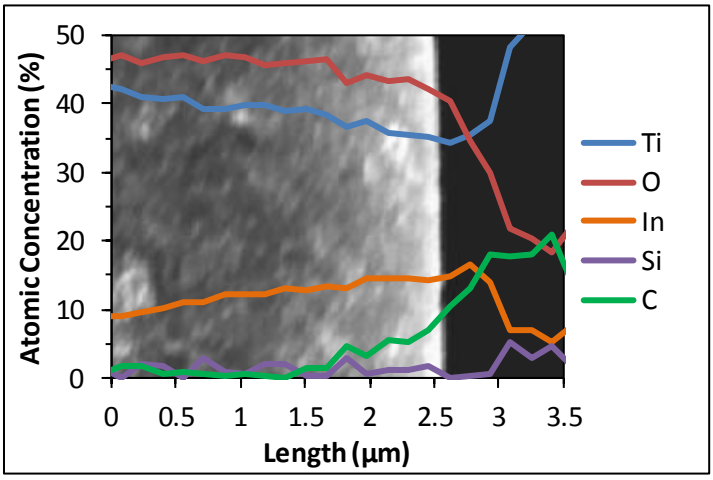


Figure 4-1: Cross-sectional Auger electron spectroscopy (AES) scan of 20 ALD cycles of In_2O_3 grown on a nanoporous TiO_2 substrate. The figure indicates that the ALD precursors are able to penetrate more than ~2 µm (the thickness of devices) into the nanoporous TiO_2 substrate. ALD was performed using the same conditions as used for the devices: 230 °C reactor temperature with pulse times of 10, 12 s and purge times of 30, 45 s for trimethylindium and H_2O, respectively.

4.2.3. SS-DSSC Device Fabrication

Following the desired number of In_2O_3 ALD cycles, substrates were heated at 500 °C for 30 minutes to remove any surface-adsorbed H_2O and cooled to 80 °C prior to immersion for 3 hours in a solution of the WN1 D-π-A dye (0.1 mM) and chenodeoxycholic acid (1 mM) in 1:1 (v/v) acetonitrile:*tert*-butanol. Synthesis of WN1 was as described elsewhere [51]. The rest of the device preparation was the same as in our Al_2O_3 report [41]. Following immersion in the WN1 solution, devices were removed and rinsed in acetonitrile. Pore-filling of the spiro-OMeTAD HTM was conducted by dissolving 225 mg mL^{-1} of spiro-OMeTAD (Lumtec) in chlorobenzene. *Tert*-butylpyridine was added to the solution at the ratio of 1:10.3 µL:mg of spiro-OMeTAD, and lithium bis-(trifluoromethylsulfonyl)imide salt (170 mg mL^{-1} in acetonitrile) was added at the ratio of 1:4.8 µL:mg of spiro-OMeTAD. The solutions were deposited on TiO_2 substrates (30 µL per 3 cm^2 substrates) and spin-coated at 2000 RPM for 30 s. Rear

electrodes of 200 nm thick Ag were deposited *via* thermal evaporation under vacuum below 10^{-6} torr.

4.2.4. Device Measurements

The resultant devices had an active area of ~10.5 mm^2. Current density-voltage (*J-V*) curves were collected in a downward (high to low bias) sweep direction with 40 ms sweep delay using a Xe arc lamp AM 1.5 solar simulator calibrated to 1 sun (100 mW/cm^2) as described elsewhere [52]. Devices were light-soaked ~30 minutes in order to reach maximum efficiencies. Three batches of twelve substrates, with five individual devices on each substrate, were fabricated and measured. Each batch consisted of four control substrates (zero ALD cycles) as well as four each of two different numbers of In_2O_3 ALD cycles. In order to determine reliable device parameter data, the bottom-performing two devices on each substrate (based on efficiency) were discarded and the remaining three (highest efficiency) devices on each substrate were averaged to give an average efficiency for that substrate. The substrate with the lowest average efficiency among each set of four substrates was then discarded and the data presented in this paper represents the average parameters of the top-performing three substrates (9 devices for each number of In_2O_3 ALD cycles, 27 devices for control cells across all three batches). The behavior of control cells was also used to better account for variations in device performance across batches (*vide infra*).

Transient photovoltage (TPV) and photocurrent (TPC) experiments as developed by O'Regan and coworkers [53, 54] were performed on a subset of high-performing devices using a white LED array as the bias light with a white LED pulse light driven by an Agilent function generator. For TPV measurements, a programmable power supply was used to adjust the bias light output from ~1 to 0.01 suns. A Keithley 2400 Sourcemeter was used to maintain the cell at open-circuit (zero current) while under the bias light and after initiating a 50 ms square-wave pulse of approximately 5% of the bias light intensity (in some instances cleaner data was obtained using 25 or 100 ms pulses; this was found to not affect the fitted recombination lifetimes). The decay of the V_{OC} once the pulse light was turned off was measured by a Tektronix oscilloscope and fitted to a single exponential in order to determine recombination lifetimes. TPC experiments

were conducted at short-circuit (zero bias) conditions in a similar fashion with a transimpedance amplifier used to convert the device's current into a voltage signal for the oscilloscope. As described by Docampo *et al*. [23], measuring the total amount of charge (Q) collected from a light pulse (measured by summing the area under the fitted current decay curve) as well as the change in photovoltage from the same pulse and bias intensity enables calculation of the differential capacitance (C): $C = \Delta Q/\Delta V_{OC}$.

V_{OC} as a function of light intensity data was obtained using the white LED bias light array and varying the light intensity with a programmable power supply as in the transient measurements. Light intensity was measured by the current produced by a reference Si photodiode with IR cutoff filter. The V_{OC} as a function of light intensity data (and resultant slopes) obtained using this approach were found to closely agree with measurements obtained by using a neutral density optical filter with the Xe arc lamp solar simulator described above.

4.2.5. Computational Studies

Periodic DFT calculations of TiO_2 and TiO_2-In_2O_3 slabs using the PBE0 [55, 56] functional were performed by the Gaussian 09 [57] and CRYSTAL09 [58] programs. Full structural optimizations of the slabs were performed using an all-electron def2-SVP basis [59, 60] for O, a modified def2-SVP for In, and a 86-51G* basis, which has previously been utilized for anatase TiO_2 (110) and (101) surfaces [61], for Ti. These basis sets were necessary for In and Ti to avoid functions with small exponents that often give rise to numerical difficulties and degradations of performance in periodic calculations utilizing atomic centered basis sets. The modification of the In basis was performed by calculating the energy of an In atom in a periodic box by systematically increasing the values of the most diffuse s and p exponents at 10% intervals until convergence was reached during self consistent field (SCF) procedure. Using this approach, the most diffuse s and p exponents were modified from 0.061 to 0.104 and 0.050 to 0.085, respectively (the utilized basis is given in the Supporting Information). 28-electron scalar relativistic effective core potentials (ECP) were used to describe the core electrons of indium [62]. This computational approach provided optimized crystal structures for rutile and anatase TiO_2, and for cubic In_2O_3 within 2% of the experimental

ones in terms of lattice parameters. An anatase (101) surface was simulated by a 2x4 slab model having a thickness of 12 atomic layers and unit cell stoichiometry of $Ti_{32}O_{64}$. A structurally analogous surface model has been previously utilized in the investigation of sensitization of TiO_2 nanoparticles [63, 64]. A monolayer of stoichiometric In_2O_3 was generated on TiO_2 by placing In atoms on top of surface oxygens and connecting the In atoms by oxygens according to In_2O_3 stoichiometry, followed by full structural optimization. Submonolayer In_2O_3 coverages of 0.25, 0.50, and 0.75 were constructed by systematically removing In_2O_3 units from the monolayer system and allowing the resulting structures to fully relax. Relative energies for the different In_2O_3 coverages on TiO_2 were determined from $\Delta E = [E_{TiO2\text{-}In2O3} - (E_{TiO2} + n_{In2O3} * E_{In2O3})]/n_{In2O3}$, where $E_{TiO2\text{-}In2O3}$, E_{TiO2}, and E_{In2O3} are the total energies of the TiO_2-In_2O_3 slab, pristine TiO_2 slab, and cubic In_2O_3 bulk per In_2O_3 unit. The term n_{In2O3} refers to the number of In_2O_3 units in the unit cell of a TiO_2-In_2O_3 slab. CRYSTAL09 was utilized in the structural optimizations and in the electronic density of states (DOS) calculations, whereas Gaussian 09 was utilized to tabulate surface dipole moments for the investigated systems. 18 Legendre polynomials were utilized to expand the calculated DOS as implemented in CRYSTAL09.

4.3. Results & Discussion

4.3.1. Growth of In_2O_3 and Device Performance

Transmission electron microscopy (TEM) was performed to assess the growth rate of In_2O_3 on nanoporous TiO_2 in comparison to planar silicon wafers. As shown in Figure 4-2, for 150 ALD cycles the resulting thickness was approximately 1.5-2 nm, indicating a growth rate of approximately 0.10 - 0.13 Å/cycle, somewhat lower than the 0.2 Å/cycle growth rate measured on planar Si via ellipsometry. This discrepancy in growth rate could be due to the different measurement techniques used or to relatively slower nucleation on TiO_2 versus SiO_2. This implies that the In_2O_3 barrier layers grown in this study, which were deposited in 3 to 30 ALD cycles, ranged from ~0.3 to ~4 Å thick. Note that these thicknesses are mostly lower than the thickness of one monolayer, which is approximately 3 Å as suggested by the DFT-optimized structures. The TEM images indicate that growth is highly conformal on the high-aspect ratio TiO_2 surface,

although thicker regions are observed at junctions formed between nanoparticles. For all but the largest number of ALD cycles studied, the "barrier layers" are in fact sub-monolayers; this is typical of the growth process of many ALD films (*e.g.* Al_2O_3) [34] and so for low cycle numbers, "thickness" should be interpreted as a nominal or average value.

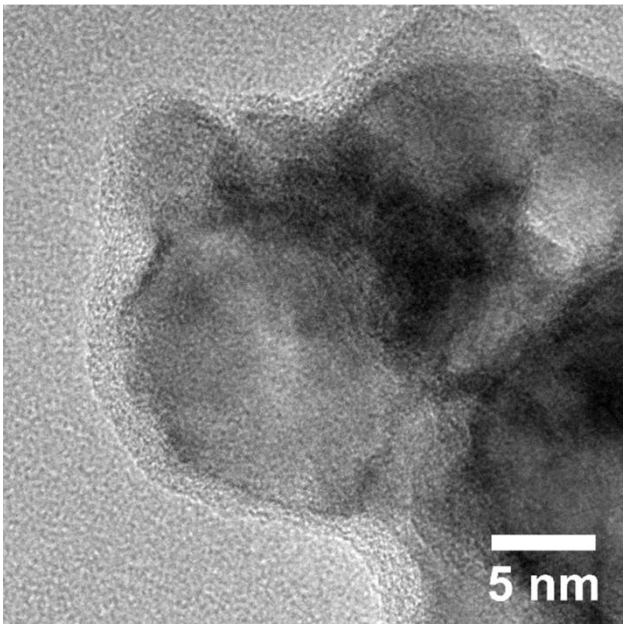


Figure 4-2: TEM image of TiO_2 nanoparticles coated with 150 ALD cycles of In_2O_3, which can be seen to be approximately 1.5 - 2 nm thick. The sample was created by scraping onto an ultra-thin carbon grid TEM holder, TiO_2 nanoparticles from a standard photoanode (see methods) as used for devices in this study, which had been treated with 150 ALD cycles of In_2O_3.

In this study, In_2O_3 barrier layers were grown using 3, 5, 10, 15, 20, and 30 ALD cycles and compared to devices with no In_2O_3 (referred to herein as "control cells"). Prior to In_2O_3 ALD, and also in those devices with no In_2O_3, the $TiCl_4$ treatment was performed, which passivates TiO_2 surface states and typically leads to large improvements in device J_{SC} [47]. Although this ultimately limits the potential performance enhancement of also depositing In_2O_3 layers, it provides a sounder basis of comparison for assessing In_2O_3's potential. A cyanoacrylic acid-based D-π-A dye, WN1 (Figure 4-3), was used in all devices. Our previous work with Al_2O_3 demonstrated that the relatively high lowest unoccupied molecular orbital (LUMO) typical of such organic dyes (in comparison to most ruthenium-based dyes) renders them less susceptible to current losses due to the inhibition of electron injection that inevitably occurs when

inserting an insulating layer in between dye molecules and the photoanode [41]. The low growth rate of the TMI/H_2O ALD system was further beneficial for delaying the inhibition of electron injection.

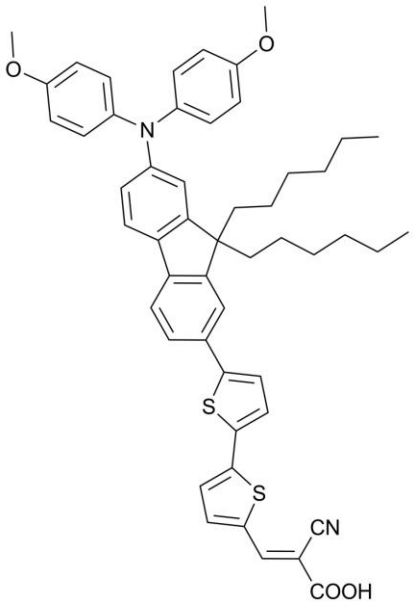


Figure 4-3: Structure of the WN1 cyanoacrylic acid-based donor-π-acceptor dye used in the device studies. WN1 was synthesized as described in Ref. [51].

Average device results for each number of In_2O_3 ALD cycles are shown in Table 4-1. For 0 – 10 ALD cycles, device efficiency was relatively unchanged: improvements in V_{OC} were offset by small decreases in J_{SC} with substrate-to-substrate variability in fill factor also playing a role. At 15 cycles, the V_{OC} peaks but the drop in J_{SC} is sufficiently large so as to result in an overall efficiency loss. Surprisingly, in contrast to expected barrier layer behavior, from 15 to 30 cycles J_{SC} is relatively constant but V_{OC} instead drops. It is interesting to note that in a previous study of In_2O_3 barrier layers in liquid DSSCs (which also included a $TiCl_4$ treatment prior to In_2O_3 deposition), Menzies *et al.* observed similar trends of a smaller magnitude: initial increase in V_{OC}, later drop in V_{OC}, with ~25% decrease in J_{SC} [22]. These results were achieved, however, with thicker In_2O_3 layers ranging from 5 to 10 Å—*i.e.* their thinnest layers were approximately as thick as the thickest In_2O_3 layers reported here.

Table 4-1: Average device parameters for the different numbers of In_2O_3 ALD cycles studied.

In_2O_3 Cycles	J_{SC} (mA/cm^2)	V_{OC} (V)	Fill Factor	Efficiency (%)
0	7.61	0.83	0.55	3.49
3	7.13	0.88	0.56	3.49
5	7.44	0.89	0.49	3.26
10	6.28	0.88	0.62	3.44
15	4.97	0.94	0.59	2.77
20	5.46	0.85	0.60	2.77
30	4.75	0.72	0.54	1.85

In order to isolate batch-to-batch fluctuation in device parameters, In_2O_3-treated cells were normalized to control cells within the same batch and data for normalized efficiency, J_{SC}, and V_{OC} are shown in Figure 4-4. As in Table 4-1, the efficiency for 0 – 10 ALD cycles is relatively unchanged with performance peaking at 10 cycles, a modest improvement of 5% relative to control cells. More interesting are the trends in J_{SC} and V_{OC}. Normalized J_{SC} drops significantly from about 95% to under 70% as the number of ALD cycles is increased from 5 to 15 but from 15 to 30 ALD cycles, the J_{SC} is essentially constant. With regards to changes in J_{SC}, there are two related means by which a recombination barrier layer may impede electron injection: one, by establishing a potential barrier between the dye excited state and the TiO_2 conduction band, and two, in the instance where the barrier layer conduction band is lower than the dye excited state energy but higher than the TiO_2 conduction band, by spatially separating the dye and TiO_2 thereby reducing the strong orbital overlap between the dye LUMO and TiO_2 d-band orbitals that typically accelerates electron transfer [65]. It is surprising, therefore, that these considerations appear relevant as the barrier thickness is increased from 0 to 15 cycles but not when increasing the barrier layer even further. Overall, the maximum J_{SC} reduction of ~30% is much lower than the ~70% drop we previously observed with the same dye after five ALD cycles of Al_2O_3 [41].

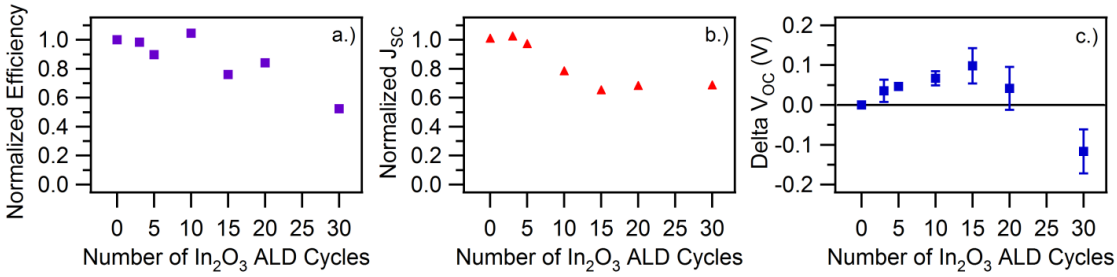


Figure 4-4: Device data normalized to the performance of control (zero In_2O_3 cycles) devices in the same batch. "Delta V_{OC}" describes the average difference in the V_{OC} between In_2O_3-coated and control devices within the same batch. Device efficiencies, a.), are relatively constant from 0 – 10 In_2O_3 cycles as modest drops in J_{SC} are compensated by V_{OC} gains; it is primarily device-to-device variability in fill factor that dictates performance differences. After 15 In_2O_3 cycles, the drop-off in J_{SC}, b.), is not fully compensated by V_{OC} increases, c.), and overall device efficiency goes down. This is exacerbated by the net drop in V_{OC} after 30 cycles, although surprisingly, no further reduction in J_{SC} is observed. Error bars in c. indicate the standard deviation of the V_{OC} changes with the device-to-device variability generally increasing at higher cycle numbers.

The behavior of V_{OC} as more In_2O_3 is deposited is also intriguing. For a barrier layer that decreases recombination by serving as a tunneling barrier, it is expected that the thicker the barrier layer, the greater the recombination suppression and the larger the V_{OC} boost (notwithstanding any V_{OC} losses associated with large drops in current). The In_2O_3 results appear to follow this trend for 0 to 15 cycles and large gains in excess of 100 mV are achieved. One 15 cycle "champion V_{OC}" device had a very large V_{OC} of 1.00 V; to our knowledge, only two other spiro-OMeTAD-based DSSCs with a V_{OC} as high as 1 V have been reported before [63, 66]. However, the V_{OC} gains reverse after 15 cycles and by 30 In_2O_3 cycles, there is in fact a substantial drop in V_{OC} of over 100 mV relative to control cells, with the V_{OC} of one device as low as 0.66 V, representing a range of 340 mV from the highest device V_{OC} at 15 ALD cycles to the lowest device V_{OC} at 30 ALD cycles. This unusual V_{OC} change occurs while current is essentially unchanged, suggesting that the nature of the In_2O_3 barrier layers fundamentally changes as they grow.

4.3.2. Analysis of In_2O_3 Devices

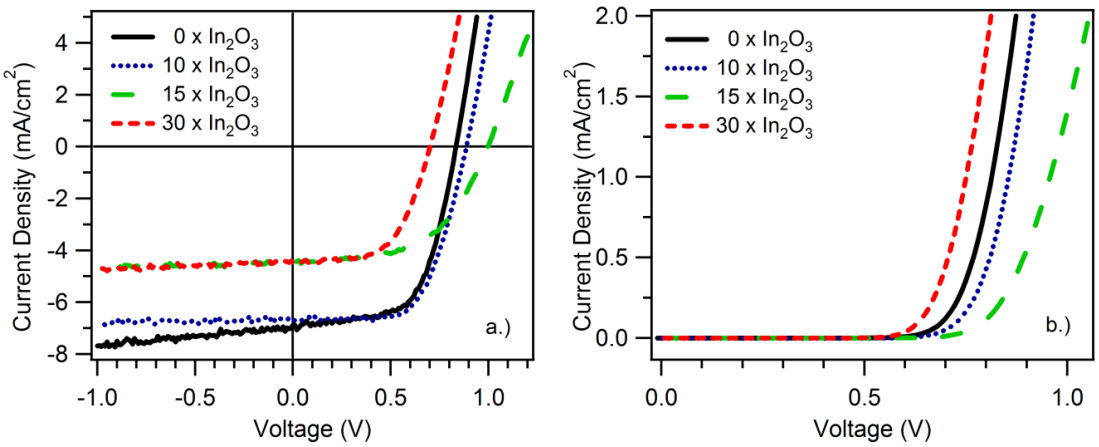


Figure 4-5. Current density-voltage (*J-V*) curves in the light, a.), and dark, b.), of representative devices for 0, 10, 15, and 30 In_2O_3 ALD cycles. The changes in V_{OC} are generally correlated to the onset of dark current.

Current density-voltage (*J-V*) plots of representative devices in the light and in the dark (Figure 4-5) exhibit no obvious changes in solar cell behavior not captured by the device parameter values (Table 4-1). In order to better understand the mechanism behind the large rise—and then fall—in V_{OC} as In_2O_3 is deposited, we performed transient photovoltage (TPV) measurements at open-circuit (modulating the bias light intensity) in order to measure recombination lifetimes (τ_r), which are plotted in Figure 4-6 for all of the ALD cycle numbers. As with V_{OC} data, a distinct pattern emerges: from 0 to 15 cycles, lifetimes increase both as a function of light intensity and V_{OC}—*i.e.* the curves are shifted up and to the right in the plot; at 20 cycles, lifetime is still much larger than in control cells but not as high as at 15 cycles; at 30 cycles, the lifetime data is fundamentally different. The lifetime drops to below even that of control cells and furthermore, the slope of the data is markedly different. Fitting the data to an equation of the form

$$\tau_r = A * \exp(-m * V_{OC}) \quad (1)$$

where A is an exponential prefactor and m characterizes the slope, we find that m is confined to the narrow range of 14 to 17 from 0 to 20 cycles (fit lines for 0, 15, and 30 cycles are shown in Figure 4-6). At 30 cycles, however, m jumps up to 47, indicating a much stronger dependence of recombination rate on photovoltage. We note that the drop

in lifetime and increase in slope in the 30 cycle device in Figure 4-6 were more severe than in other 30 cycle devices but the trends—drop-off in lifetime to approximately that of control cells, increase in *m* (to 39 on average)—were universal. This device-to-device variability also appears in the relatively large V_{OC} error bars for 30 ALD cycles in Figure 4-4c and we believe that this is due to a high sensitivity of In_2O_3 barrier layer behavior to small differences in thickness/coverage when the layers are approximately one monolayer. Figure 4-7 shows device V_{OC} and τ_r, both under 1 sun of illumination. The strong correlation between the two series of data is striking and clearly indicates that the changes in V_{OC} are not solely due to movement of the conduction band: if that were the case, the lifetime at one sun would be largely independent of the V_{OC}. This suggests that at least for the first 20 ALD cycles, In_2O_3 is acting as a recombination barrier.

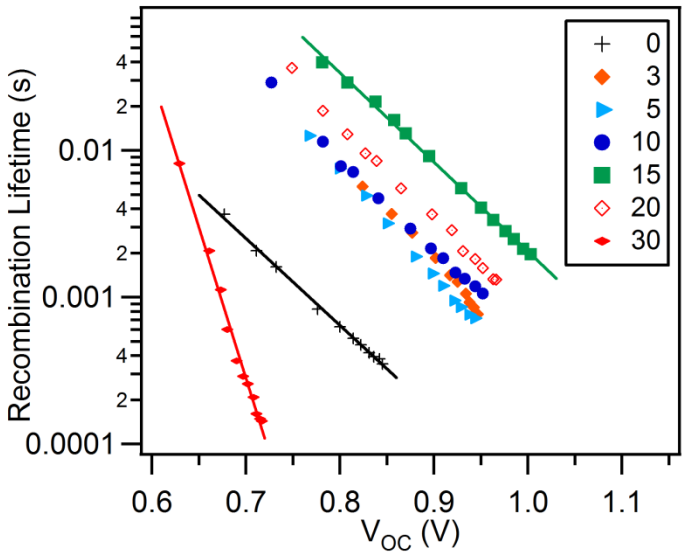


Figure 4-6: Recombination lifetime data versus open-circuit voltage for different numbers of In_2O_3 cycles. Lifetimes generally increase with more In_2O_3 up to 15 ALD cycles, drop modestly from the peak after 20 cycles, and fall below the control devices after 30 cycles. Trend lines are drawn for 0, 15, and 30 cycles to demonstrate the large change in slope, *i.e.* dependence of recombination rate on bias, for 30 cycles versus all other cycle numbers and control cells. Note that lifetime variability was much higher in the 30 cycle devices than in other devices, similar to the higher V_{OC} variably also observed after 30 cycles, and one device exhibiting particularly low lifetimes and a large slope was chosen to illustrate the general trend. Other 30 cycle devices exhibited lifetimes similar to control cells, but with higher slopes.

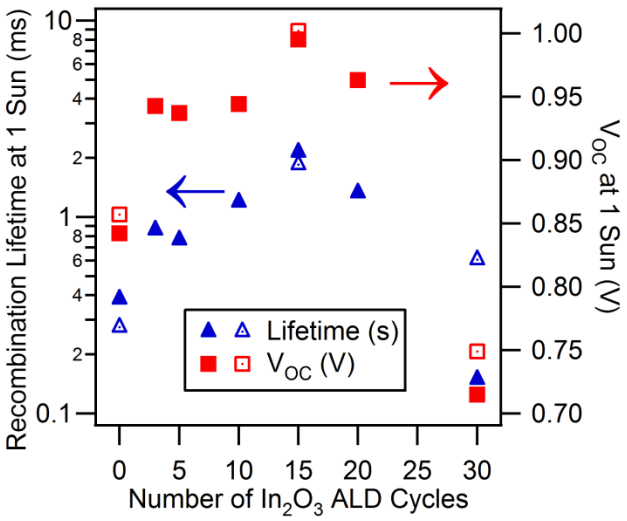


Figure 4-7: Recombination lifetime (measured at V_{OC}) and V_{OC}, both under 1 sun illumination, as a function of the number of In_2O_3 ALD cycles for representative devices. To indicate the relatively high device variability of 30 cycle devices, data from a second device (unfilled symbols) were added for 0, 15, and 30 ALD cycles.

Figure 4-6 and Figure 4-7, however, do not exclude the possibility that In_2O_3 exerts a surface dipole that affects the level of the TiO_2 conduction band. In order to measure such an effect, capacitance values were measured for the control samples as well as the extreme cases of 15 and 30 ALD cycles (Figure 4-8). The premise of capacitance measurements is that trap states in the bandgap of TiO_2 are the dominant source of device capacitance in DSSCs and the distribution of these states relative to the TiO_2 conduction band is fixed [54]. This implies that the same capacitance value measured in two devices at different voltages indicates a movement of the TiO_2 conduction band; this effect has been used to study conduction band shifts due to dipoles induced by dye molecules [63] and barrier layers [23]. The fact that all three devices shown in Figure 4-8 exhibit similar capacitance values at very different voltages is consistent with movement of the TiO_2 conduction band. At a capacitance value of ~10 μF/cm^2 the 15 cycle curve is shifted approximately +70 mV and the 30 cycle curve approximately -120 mV relative to the control device. These shifts are in comparison to changes in V_{OC} relative to the control device at one sun of +140 mV and -130 mV for 15 and 30 ALD cycles, respectively. In other words, shifts in the TiO_2 conduction band appear to account for most of the drop in V_{OC} obtained after 30 cycles, but only about half of the increase in V_{OC} after 15 ALD cycles. These shifts also aid analysis of the recombination data in Figure 4-6.

Accounting for the +70 mV shift after 15 In_2O_3 cycles (*i.e.* moving the 15 cycle τ_r versus V_{OC} curve 70 mV to the left and then comparing lifetime values) indicates that recombination is still approximately 20 times slower in 15 In_2O_3 ALD cycle devices than in control devices (and as is apparent in Figure 4-7, even if offset the full 140 mV, recombination is still ~6 times slower in 15 cycle devices than control cells). On the other hand, when 30 cycle devices are offset according to the conduction band shift they exhibit only slightly faster recombination (by a factor of two) than control cells at one sun, as shown in Figure 4-7.

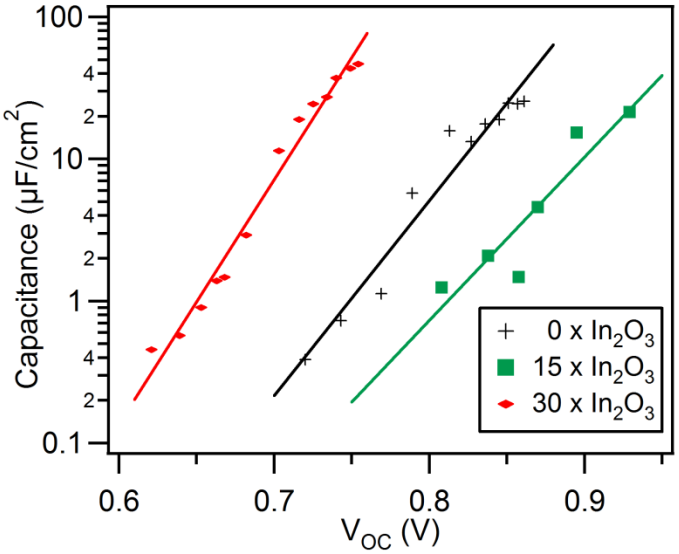


Figure 4-8: Capacitance, measured from transient photovoltage and photocurrent data, as a function of V_{OC} for three indicative In_2O_3 cycle numbers: 0 (control cells), 15 (highest observed V_{OC}'s), 30 (lowest observed V_{OC}'s). Fitted exponential trend lines are included for each device. Note that similar capacitance values are measured for all three cycle numbers and the fitted trend line slopes are roughly parallel. The shifting of these lines on the V_{OC} axis—approximately 120 mV lower for 30 cycles and 70 mV higher for 15 cycles, relative to the control—are indicative of a shift in the TiO_2 conduction band after deposition of In_2O_3.

To see if the shift in the TiO_2 conduction band indicated by the capacitance data could be due to a change in the surface dipole induced by In_2O_3 as it transitions from sub-monolayer to monolayer coverages, we simulated different surface coverages of In_2O_3 on the TiO_2 anatase (101) surface by periodic DFT calculations using a PBE0 functional (for details see the Computational Studies section). In addition to surface dipoles, the calculations provided access to the relative energies of the different In_2O_3 coverages on TiO_2. The relative energies and surface dipole moments perpendicular to the TiO_2

surface (z-direction) for the different TiO_2-In_2O_3 systems are illustrated in Figure 4-9 and the optimized structures in Figure 4-10. Note that a positive dipole moment refers to a dipole pointing, from the negative charge to the positive charge, outward from the surface; such a dipole can induce an upward shift in the TiO_2 CB, which has been demonstrated to be beneficial for solid-state DSSCs [63]. The calculations demonstrate the formation of a surface dipole perpendicular to the TiO_2 surface due to In_2O_3 and suggest the strength of this dipole increases as a function of In_2O_3 coverage, up to a coverage of 0.75. At a full monolayer coverage the direction of the moment is reversed.

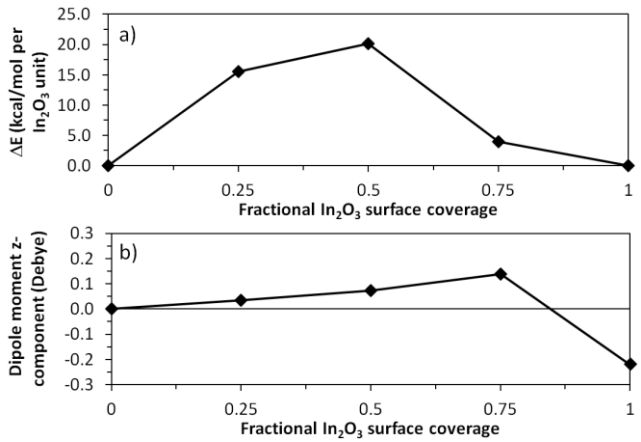


Figure 4-9: a) PBE0-calculated relative energies (Δ*E*) and b) dipole moments perpendicular to the TiO_2 surface (z-component) as a function of fractional In_2O_3 surface coverage on anatase TiO_2 (101) surface. The relative energies are given with respect to a full monolayer of In_2O_3.

The dipole originates from polar In-O and O-Ti bonds in the In_2O_3 surface species; the orientation of these bonds determines the direction of the surface dipoles. The In_2O_3 clusters are tilted on the surface at submonolayer coverages to maximize coordination of In atoms to neighboring oxygen atoms (see Figure 4-10), resulting in bond orientations that give rise to positive dipoles. In contrast, such strong tilting is not necessary to maximize In coordination at a full monolayer coverage, causing changes in the orientations of the polar In-O and O-Ti bonds and reversing the dipole moment direction (Figure S2 illustrates the orientations of the In_2O_3 species). The relative energies calculated for the different coverages are high at 0.50 and below, and decrease sharply as the In_2O_3 coverage increases up to a full monolayer. The lower coverages are energetically less favorable due to separated surface In_2O_3 clusters having In species coordinated to 4 oxygen atoms, whereas at higher coverages coordination of In to a larger number of oxygen atoms becomes feasible due to decreased separation between the In_2O_3

clusters (see Figure 4-10 and Figure 4-11). Notably, In atoms in cubic In_2O_3 are coordinated to six oxygen atoms. Overall, our PBE0 calculations demonstrate the formation of surface dipoles pointing outward from the TiO_2 surface at submonolayer In_2O_3 coverages. An inversion in the dipole takes place at a full monolayer coverage, generally in agreement with the trend observed in V_{OC} as a function of In_2O_3 ALD cycles. This inversion in dipole agrees with the observed changes in V_{OC} as a function of In_2O_3 ALD cycles. The magnitudes of the dipoles introduced by sub-monolayer In_2O_3 are small in magnitude, below 0.2 D, as compared with those introduced by dye molecules (typically several D). This is partly counteracted, however, by the extremely close proximity of the In_2O_3 dipoles to the TiO_2 surface, which should amplify their effect on the TiO_2 conduction band.

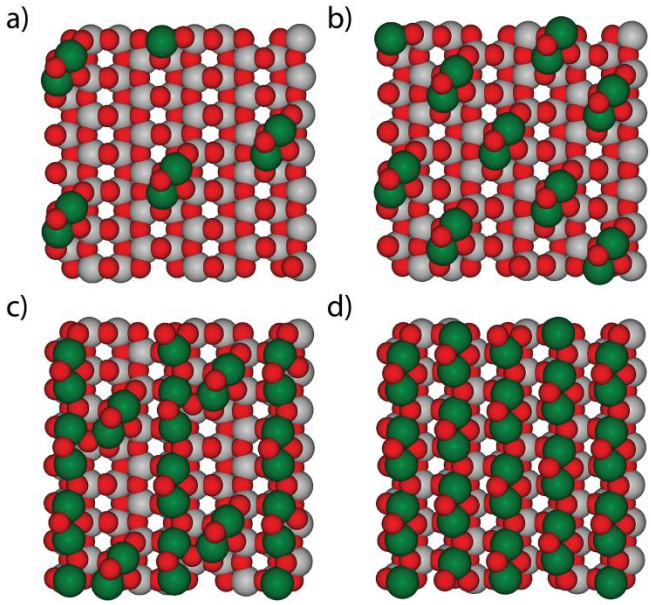


Figure 4-10. PBE0-optimized anatase TiO_2 (101) surface structures with fractional In_2O_3 surface coverages of a) 0.25, b) 0.50, c) 0.75, and d) 1.0. Indium atoms are shown in green, oxygen in red, and titanium in gray.

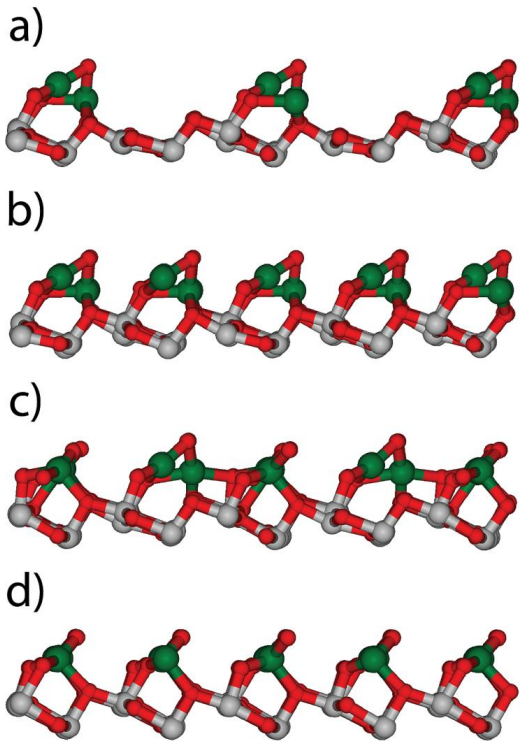


Figure 4-11: Side views of the PBE0-optimized anatase TiO_2 (101) surface structures with fractional In_2O_3 surface coverages of a) 0.25, b) 0.50, c) 0.75, and d) 1.0 demonstrating the tilting of the In_2O_3 species on TiO_2.

4.3.3. Mechanisms of Recombination Rate Changes

The change in dipole direction indicated by the DFT calculations helps explain the TiO_2 conduction band shift suggested by the capacitance data in Figure 4-8. It still remains, however, to explain why In_2O_3 strongly reduces the recombination rate only when a very thin layer is deposited. Previous work in the literature has examined the relationship between V_{OC} and light intensity and its implications for understanding recombination pathways [67-70]. In order to gain insight into whether this may explain the effect of In_2O_3 barrier layers, we measured V_{OC} while adjusting the light intensity over two orders of magnitude from approximately 0.01 sun to 1 sun. Figure 4-12 shows V_{OC}-intensity curves in a semi-log plot for all numbers of In_2O_3 ALD cycles. The slopes of the lines fitted to this data are shown in Table 4-2 in terms of the increase in V_{OC} (in mV) associated with a factor of ten increase in light intensity (*i.e.* $dVoc / dlog_{10}(I)$, or V_{OC} per decade). The same general trend seen with V_{OC} and with lifetime is observed here: there is an increase in slope as more In_2O_3 is deposited, with a plateau from 10 to 20 cycles, followed by a large drop when 30 In_2O_3 cycles are deposited. We note that the values observed here for 0 – 20 cycles are in line with those previously reported for both

liquid and solid-state devices [67-70]. The recombination analysis developed by Schlichthörl *et al.* and Salvador *et al*. indicates that if recombination primarily involves TiO_2 conduction band states, a slope of 60 mV/decade is expected because the recombination rate constant will be independent of device voltage [67, 69]. In contrast, the reaction rate constant for recombination involving bandgap (or surface) states is not constant with voltage—as states higher in the bandgap are filled as voltage is increased—and therefore the 60 mV/decade figure no longer applies. The large deviations from 60 mV/decade measured in DSSCs are indicative of the role played by TiO_2 bandgap states in recombination [67, 69]. Because V_{OC} indicates the bias at which the rate of electron injection into the TiO_2 equals the rate of recombination, a higher slope implies that for a given increase in electron injection rate (*i.e.* light intensity), a relatively larger increase in voltage must be applied before the recombination rate fully matches the injection rate. In other words, the increased slope observed after deposition of In_2O_3 up to 20 cycles indicates that recombination increases more slowly than in control cells as the bias is increased, suggesting that the recombination rate constant is reduced. This could be indicative of In_2O_3 serving as a tunneling barrier to recombination from TiO_2 bandgap states and/or—as this is observed with sub-monolayer coverages of In_2O_3—the passivation of surface states that act as recombination centers.

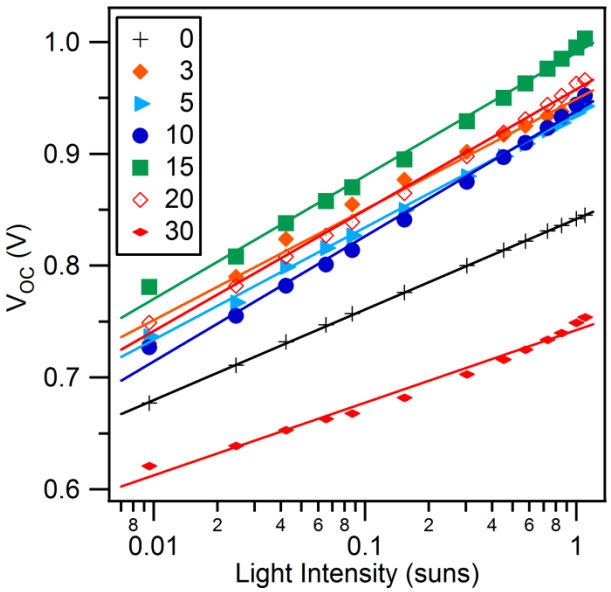


Figure 4-12: V_{OC} as a function of light intensity from a white LED array for all number of In_2O_3 ALD cycles tested. Intensity is measured in suns, with one sun equal to 100 mW/cm^2. Fit lines demonstrating the logarithmic dependence of V_{OC} on light intensity are also shown. The slope of these lines was observed to be consistent with recombination and V_{OC} (under the same illumination level) trends: the slope increased from 0 to 20 In_2O_3 cycles, indicating a stronger dependence of V_{OC} on light level, before dropping significantly after 30 ALD cycles.

Table 4-2: Slope of V_{OC} versus the log of light intensity (Figure 4-12) as a function of In_2O_3 ALD cycles.

In_2O_3 Cycles	$d(V_{OC}\ (mV)) / d(\log_{10}(Intensity))$
0	81
3	99
5	100
10	112
15	110
20	108
30	65

There are several possible explanations for the severe drop in slope after 30 ALD cycles. As the increase in slope observed after 3 – 20 cycles was attributed to a decrease in the recombination rate constant, the decrease in slope may indicate an increase in the recombination rate constant. This could occur due to the formation of states in the In_2O_3 layer that act as recombination centers. To investigate the potential of In_2O_3 to introduce states into the bandgap of TiO_2, we return to the DFT calculations where we also

calculated density of state (DOS) contributions from the constituent atoms to the total DOS for pristine TiO_2 and the TiO_2-In_2O_3 systems, the results of which are illustrated in Figure 4-13. The calculated DOS demonstrates bandgap narrowing as a function of increasing In_2O_3 coverage, in particular at In_2O_3 coverages of 0.75 and 1.0 (full monolayer). The narrowing is caused by O states from In_2O_3 being introduced to the valence band region, and both O and In states from In_2O_3 to the conduction band (CB) region. The sub-CB states may provide additional pathways for recombination [69], and their increasing density seen in Figure 4-13 as a function of coverage correlates with the lifetime measurements (Figure 4-6) suggesting a different recombination process in the device with 30 ALD cycles of In_2O_3 as compared to the devices with less In_2O_3. Overall, the DFT calculations suggest that the In_2O_3 barrier layer introduces both changes in and new states near TiO_2 valence and conduction bands, especially close to monolayer coverages, and these changes may cause a fundamental change in the recombination process when approaching close to monolayer coverages of In_2O_3 on TiO_2.

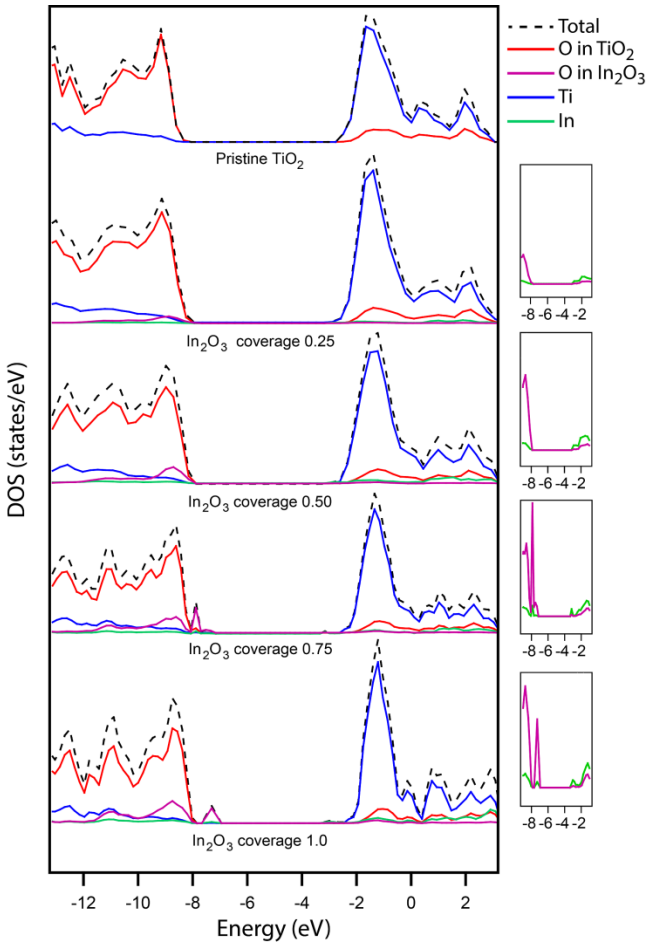


Figure 4-13: PBE0-calculated density of states (DOS) for pristine anatase TiO_2 (101) slab (top) and for TiO_2-In_2O_3 slabs with fractional In_2O_3 surface coverages of 0.25, 0.50, 0.75, and 1.0 (bottom). The states originating from In_2O_3 within the bandgap region for each coverage level are illustrated in the zoom-ins (right).

It is notable that the slope of the V_{OC} after 30 In_2O_3 cycles approaches the 60 mV/decade value associated with conduction band-dominated recombination. If, as the DFT calculations suggest, In_2O_3 introduces bandgap states at a particular energy level, then we should expect them to have, like the conduction band states and in contrast to the exponential tail of bandgap states that occupy a wide range of energy levels, a constant recombination activation energy associated with them, and such an explanation is consistent with the near-sixty slope value in Table 4-2. Finally, the In_2O_3 bandgap narrowing indicated by the DOS calculations as coverage is increased may also explain the unexpected behavior of the device J_{SC}. As described above, for a model barrier layer it is anticipated that electron injection efficiency will approach zero as the layer thickness increases, however, as shown in Figure 4-4, J_{SC} is essentially constant from 15 to 30 ALD

cycles. One explanation for this is that the increasing thickness of the In_2O_3 layer is cancelled out by its decreasing conduction band level due to the bandgap narrowing. In other words, the barrier layer is becoming thicker but less insulating. The observations of In_2O_3 barrier layer behavior as a function of thickness and coverage with regards to band movement, recombination, and electron injection are summarized in Figure 4-14.

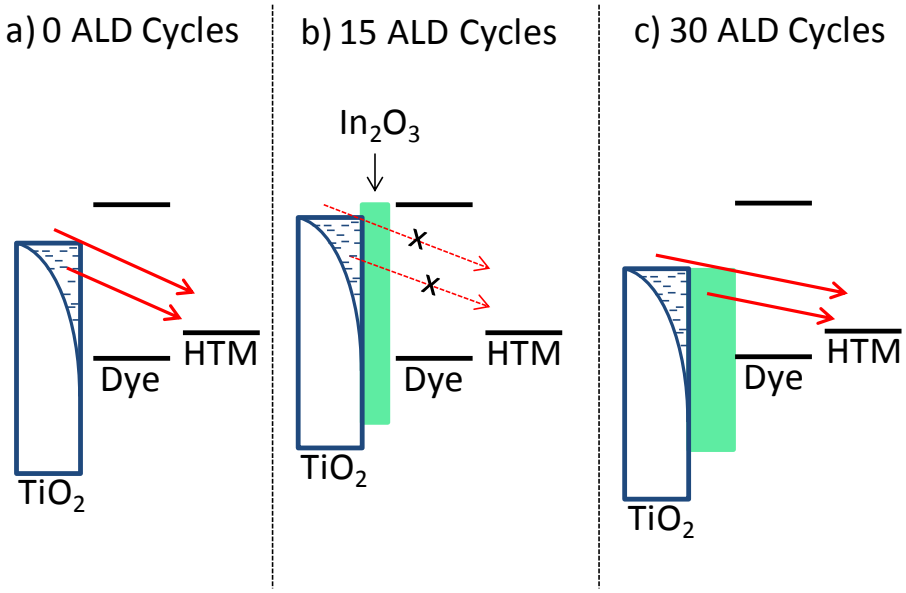


Figure 4-14: Schematic (not to scale) showing the effect of 15 and 30 In_2O_3 ALD cycles on the TiO_2 conduction band level and on recombination processes (red arrows). In a), which corresponds to control devices, there is no barrier layer to block recombination with holes in the hole-transport material (HTM) (recombination with oxidized dye molecules is ignored here for simplicity). Recombination can involve electrons in the TiO_2 conduction band (top arrow) or in mid-bandgap trap states (bottom arrow). B) demonstrates an increase in TiO_2 band levels and a reduction in recombination rate, the effects of which are most apparent after 15 In_2O_3 ALD cycles. After 30 ALD cycles, c), the TiO_2 energy levels are lowered, the In_2O_3 bandgap is narrowed, and recombination occurs at a high rate and possibly involves In_2O_3 states.

4.4. Conclusions

ALD-grown In_2O_3 barrier layers were studied in solid-state DSSCs. For submonolayer In_2O_3 coverages (up to 20 ALD cycles), significant V_{OC} improvements were achieved, with an average improvement of over 100 mV after 15 ALD cycles, leading to a peak V_{OC} of 1.00 V. Loss in J_{SC} was relatively low, as compared to Al_2O_3 barrier layer layers, with a minimal decrease at fewer than 10 ALD cycles and only a 30% drop after 20 cycles. The behavior of In_2O_3-coated devices changed substantially as barrier layers approached a full monolayer, with a significant drop in average V_{OC} of over 110 mV after 30 ALD cycles but without any further J_{SC} loss. Recombination lifetime

measurements indicated much slower recombination in devices with high V_{OC}'s, whereas no recombination suppression was observed for the thickest In_2O_3 films that also exhibited the reduced V_{OC}. Capacitance measurements indicated a shift in the TiO_2 conduction band that accounts for roughly half of the V_{OC} improvements seen for thinner In_2O_3 layers and most of the V_{OC} decrease seen with the thickest layer. DFT computational studies examining various In_2O_3 surface coverages provide a possible explanation for the movement in the TiO_2 conduction band, revealing a change in the direction of the In_2O_3-induced dipole moment as coverage was increased. The large decrease in recombination rate observed for thinner In_2O_3 layers was attributed to a surface passivation and/or a tunneling barrier effect, whereas the faster recombination rate of the thicker films was attributed to the introduction of mid-bandgap states that serve as recombination centers. Our results demonstrate the feasibility of using ultrathin In_2O_3 layers to improve device V_{OC} and provide insight into competing effects that may be introduced by dielectric interface layers, including barrier properties, surface dipoles, and interface states.

4.5. Collaborations & Copyrights

This chapter is currently in preparation to be submitted for publication. Jukka Tanskanen performed the DFT analysis provided in this chapter. Katherine Roelofs performed the TEM analysis. The In_2O_3 ALD process was developed with John To. This barrier layer project was originally developed with Jonathan Bakke, I-Kang Ding, and Brian Hardin. William Nguyen synthesized the WN1 dye in the lab of Alan Sellinger. Device fabrication and testing were performed in the lab of Michael McGehee. Colin Bailie and George Margulis provided advice for constructing the transient photovoltage/photocurrent setup and Chaiya Prasittichai offered helpful discussion in analyzing device data.

4.6. References

[1] B. O'Regan, M. Grätzel, Nature 353/6346 (1991) 737.
[2] A. Hagfeldt, G. Boschloo, L. Sun, L. Kloo, H. Pettersson, Chemical Reviews 110/11 (2010) 6595.
[3] B.E. Hardin, H.J. Snaith, M.D. McGehee, Nat Photon 6/3 (2012) 162.
[4] A. Yella, H.-W. Lee, H.N. Tsao, C. Yi, A.K. Chandiran, M.K. Nazeeruddin, E.W.-G. Diau, C.-Y. Yeh, S.M. Zakeeruddin, M. Grätzel, Science 334/6056 (2011) 629.
[5] I. Chung, B. Lee, J. He, R.P.H. Chang, M.G. Kanatzidis, Nature 485/7399 (2012) 486.
[6] J. Burschka, A. Dualeh, F. Kessler, E. Baranoff, N.-L. Cevey-Ha, C. Yi, M.K. Nazeeruddin, M. Grätzel, Journal of the American Chemical Society 133/45 (2011) 18042.
[7] G. Hodes, D. Cahen, Accounts of Chemical Research 45/5 (2012) 705.
[8] M.M. Lee, J. Teuscher, T. Miyasaka, T.N. Murakami, H.J. Snaith, Science 338/6107 (2012) 643.
[9] H.-S. Kim, C.-R. Lee, J.-H. Im, K.-B. Lee, T. Moehl, A. Marchioro, S.-J. Moon, R. Humphry-Baker, J.-H. Yum, J.E. Moser, M. Grätzel, N.-G. Park, Sci. Rep. 2 (2012) 1.
[10] H.J. Snaith, L. Schmidt-Mende, Advanced Materials 19/20 (2007) 3187.
[11] G. Boschloo, A. Hagfeldt, Accounts of Chemical Research 42/11 (2009) 1819.
[12] A.K. Chandiran, N. Tetreault, R. Humphry-Baker, F. Kessler, E. Baranoff, C. Yi, M.K. Nazeeruddin, M. Grätzel, Nano Letters (2012).
[13] U. Bach, D. Lupo, P. Comte, J.E. Moser, F. Weissortel, J. Salbeck, H. Spreitzer, M. Grätzel, Nature 395/6702 (1998) 583.
[14] B.C. O'Regan, S. Scully, A.C. Mayer, E. Palomares, J. Durrant, The Journal of Physical Chemistry B 109/10 (2005) 4616.
[15] E. Palomares, J.N. Clifford, S.A. Haque, T. Lutz, J.R. Durrant, Chemical Communications/14 (2002) 1464.
[16] A. Kay, M. Grätzel, Chemistry of Materials 14/7 (2002) 2930.
[17] E. Palomares, J.N. Clifford, S.A. Haque, T. Lutz, J.R. Durrant, Journal of the American Chemical Society 125/2 (2003) 475.
[18] K.M.P. Bandaranayake, M.K. Indika Senevirathna, P.M.G.M. Prasad Weligamuwa, K. Tennakone, Coordination Chemistry Reviews 248/13-14 (2004) 1277.
[19] Y. Diamant, S. Chappel, S.G. Chen, O. Melamed, A. Zaban, Coordination Chemistry Reviews 248/13-14 (2004) 1271.
[20] X.-T. Zhang, H.-W. Liu, T. Taguchi, Q.-B. Meng, O. Sato, A. Fujishima, Solar Energy Materials and Solar Cells 81/2 (2004) 197.
[21] S.-Q. Fan, Y. Geng, C. Kim, S. Paik, J. Ko, Materials Chemistry and Physics 132/2-3 (2012) 943.
[22] D.B. Menzies, Q. Dai, L. Bourgeois, R.A. Caruso, Y.-B. Cheng, G.P. Simon, L. Spiccia, Nanotechnology 18/12 (2007) 125608.
[23] P. Docampo, P. Tiwana, N. Sakai, H. Miura, L. Herz, T. Murakami, H.J. Snaith, The Journal of Physical Chemistry C 116/43 (2012) 22840.
[24] Z.-S. Wang, M. Yanagida, K. Sayama, H. Sugihara, Chemistry of Materials 18/12 (2006) 2912.

[25] S. Lee, J. Young Kim, K. Sun Hong, H. Suk Jung, J.-K. Lee, H. Shin, Solar Energy Materials and Solar Cells 90/15 (2006) 2405.
[26] P. Ramasamy, M.-S. Kang, H.-J. Cha, J. Kim, Materials Research Bulletin 48/1 (2013) 79.
[27] J. Guo, C. She, T. Lian, The Journal of Physical Chemistry C 111/25 (2007) 8979.
[28] J.R. Bakke, Atomic Layer Deposition of Materials for Applications to Photovoltaics, Stanford University, Stanford, 2011.
[29] M. Law, L.E. Greene, A. Radenovic, T. Kuykendall, J. Liphardt, P. Yang, The Journal of Physical Chemistry B 110/45 (2006) 22652.
[30] T.W. Hamann, O.K. Farha, J.T. Hupp, The Journal of Physical Chemistry C 112/49 (2008) 19756.
[31] C. Lin, F.-Y. Tsai, M.-H. Lee, C.-H. Lee, T.-C. Tien, L.-P. Wang, S.-Y. Tsai, Journal of Materials Chemistry 19/19 (2009) 2999.
[32] T.-C. Tien, F.-M. Pan, L.-P. Wang, C.-H. Lee, Y.-L. Tung, S.-Y. Tsai, C. Lin, F.-Y. Tsai, S.-J. Chen, Nanotechnology 20/30 (2009) 305201.
[33] L.J. Antila, M.J. Heikkilä, V. Aumanen, M. Kemell, P. Myllyperkiö, M. Leskelä, J.E.I. Korppi-Tommola, The Journal of Physical Chemistry Letters 1/2 (2009) 536.
[34] T.-C. Tien, F.-M. Pan, L.-P. Wang, F.-Y. Tsai, C. Lin, The Journal of Physical Chemistry C 114/21 (2010) 10048.
[35] M. Shanmugam, M.F. Baroughi, D. Galipeau, Thin Solid Films 518/10 (2010) 2678.
[36] M.J. DeVries, M.J. Pellin, J.T. Hupp, Langmuir 26/11 (2010) 9082.
[37] C. Prasittichai, J.T. Hupp, The Journal of Physical Chemistry Letters 1/10 (2010) 1611.
[38] A.M. Spokoyny, T.C. Li, O.K. Farha, C.W. Machan, C. She, C.L. Stern, T.J. Marks, J.T. Hupp, C.A. Mirkin, Angewandte Chemie International Edition 49/31 (2010) 5339.
[39] L.J. Antila, M.J. Heikkilä, V. Mäkinen, N. Humalamäki, M. Laitinen, V. Linko, P. Jalkanen, J. Toppari, V. Aumanen, M. Kemell, P. Myllyperkiö, K. Honkala, H. Häkkinen, M. Leskelä, J.E.I. Korppi-Tommola, The Journal of Physical Chemistry C 115/33 (2011) 16720.
[40] V. Mäkinen, K. Honkala, H. Häkkinen, The Journal of Physical Chemistry C 115/18 (2011) 9250.
[41] T.P. Brennan, J.R. Bakke, I.K. Ding, B.E. Hardin, W.H. Nguyen, R. Mondal, C.D. Bailie, G.Y. Margulis, E.T. Hoke, A. Sellinger, M.D. McGehee, S.F. Bent, Physical Chemistry Chemical Physics 14/35 (2012) 12130.
[42] B. Bills, M. Shanmugam, M.F. Baroughi, Thin Solid Films 519/22 (2011) 7803.
[43] T.C. Li, M.S. Goes, F. Fabregat-Santiago, J. Bisquert, P.R. Bueno, C. Prasittichai, J.T. Hupp, T.J. Marks, Journal of Physical Chemistry C 113/42 (2009) 18385.
[44] M. Shanmugam, B. Bills, M.F. Baroughi, Materials Research Society Symposium Proceedings 1260/T10 (2010) 1.
[45] H.-J. Son, X. Wang, C. Prasittichai, N.C. Jeong, T. Aaltonen, R.G. Gordon, J.T. Hupp, Journal of the American Chemical Society 134/23 (2012) 9537.
[46] Y. Noma, T. Kado, D. Ogata, Y. Hara, S. Hayase, Japanese Journal of Applied Physics 47/1 (2008) 505.

[47] P.M. Sommeling, B.C. O'Regan, R.R. Haswell, H.J.P. Smit, N.J. Bakker, J.J.T. Smits, J.M. Kroon, J.A.M. van Roosmalen, The Journal of Physical Chemistry B 110/39 (2006) 19191.
[48] N. Cai, S.-J. Moon, L. Cevey-Ha, T. Moehl, R. Humphry-Baker, P. Wang, S.M. Zakeeruddin, M. Grätzel, Nano Letters 11/4 (2011) 1452.
[49] Y. Xu, M.A.A. Schoonen, American Mineralogist 85/3-4 (2000) 543.
[50] D.-J. Lee, J.-Y. Kwon, J.I. Lee, K.-B. Kim, The Journal of Physical Chemistry C 115/31 (2011) 15384.
[51] W.H. Nguyen, C.D. Bailie, J. Burschka, T. Moehl, M. Grätzel, M.D. McGehee, A. Sellinger, Chemistry of Materials 25/9 (2013) 1519.
[52] T. Leijtens, I.K. Ding, T. Giovenzana, J.T. Bloking, M.D. McGehee, A. Sellinger, ACS Nano 6/2 (2012) 1455.
[53] B.C. O'Regan, F. Lenzmann, The Journal of Physical Chemistry B 108/14 (2004) 4342.
[54] P.R.F. Barnes, K. Miettunen, X. Li, A.Y. Anderson, T. Bessho, M. Grätzel, B.C. O'Regan, Advanced Materials 25/13 (2013) 1881.
[55] J.P. Perdew, K. Burke, M. Ernzerhof, Physical Review Letters 77/18 (1996) 3865.
[56] C. Adamo, V. Barone, The Journal of Chemical Physics 110/13 (1999) 6158.
[57] M.J. Frisch, G.W. Trucks, H.B. Schlegel, G.E. Scuseria, M.A. Robb, J.R. Cheeseman, G. Scalmani, V. Barone, B. Mennucci, G.A. Petersson, H. Nakatsuji, M. Caricato, X. Li, H.P. Hratchian, A.F. Izmaylov, J. Bloino, G. Zheng, J.L. Sonnenberg, M. Hada, M. Ehara, K. Toyota, R. Fukuda, J. Hasegawa, M. Ishida, T. Nakajima, Y. Honda, O. Kitao, H. Nakai, T. Vreven, J. Montgomery, J. A., J.E. Peralta, F. Ogliaro, M. Bearpark, J.J. Heyd, E. Brothers, K.N. Kudin, V.N. Staroverov, R. Kobayashi, J. Normand, K. Raghavachari, A. Rendell, J.C. Burant, S.S. Iyengar, J. Tomasi, M. Cossi, N. Rega, J.M. Millam, M. Klene, J.E. Knox, J.B. Cross, V. Bakken, C. Adamo, J. Jaramillo, R. Gomperts, R.E. Stratmann, O. Yazyev, A.J. Austin, R. Cammi, C. Pomelli, J.W. Ochterski, R.L. Martin, K. Morokuma, V.G. Zakrzewski, G.A. Voth, P. Salvador, J.J. Dannenberg, S. Dapprich, A.D. Daniels, Ö. Farkas, J.B. Foresman, J.V. Ortiz, J. Cioslowski, D.J. Fox, Gaussian, Inc., Wallingford, CT, USA, 2009.
[58] R. Dovesi, V.R. Saunders, C. Roetti, R. Orlando, C.M. Zicovich-Wilson, F. Pascale, B. Civalleri, K. Doll, N.M. Harrison, I.J. Bush, P. D'Arco, M. Llunell, CRYSTAL09 User's Manual, Torino, Italy, 2009.
[59] A. Schäfer, H. Horn, R. Ahlrichs, The Journal of Chemical Physics 97/4 (1992) 2571.
[60] F. Weigend, R. Ahlrichs, Physical Chemistry Chemical Physics 7/18 (2005) 3297.
[61] J. Scaranto, S. Giorgianni, Journal of Molecular Structure: THEOCHEM 858/1-3 (2008) 72.
[62] B. Metz, H. Stoll, M. Dolg, The Journal of Chemical Physics 113/7 (2000) 2563.
[63] P. Chen, J.H. Yum, F.D. Angelis, E. Mosconi, S. Fantacci, S.-J. Moon, R.H. Baker, J. Ko, M.K. Nazeeruddin, M. Grätzel, Nano Letters 9/6 (2009) 2487.
[64] P. Persson, R. Bergström, S. Lunell, The Journal of Physical Chemistry B 104/44 (2000) 10348.
[65] M.K. Nazeeruddin, R. Humphry-Baker, P. Liska, M. Grätzel, The Journal of Physical Chemistry B 107/34 (2003) 8981.

[66] S.-R. Jang, K. Zhu, M.J. Ko, K. Kim, C. Kim, N.-G. Park, A.J. Frank, ACS Nano 5/10 (2011) 8267.
[67] G. Schlichthörl, S.Y. Huang, J. Sprague, A.J. Frank, The Journal of Physical Chemistry B 101/41 (1997) 8141.
[68] A.C. Fisher, L.M. Peter, E.A. Ponomarev, A.B. Walker, K.G.U. Wijayantha, The Journal of Physical Chemistry B 104/5 (2000) 949.
[69] P. Salvador, M.G. Hidalgo, A. Zaban, J. Bisquert, The Journal of Physical Chemistry B 109/33 (2005) 15915.
[70] H.J. Snaith, L. Schmidt-Mende, M. Grätzel, M. Chiesa, Physical Review B 74/4 (2006) 045306.

Chapter 5. Efficiency Enhancement of Solid-State PbS Quantum Dot-Sensitized Solar Cells with Al_2O_3 Barrier Layer

Atomic layer deposition (ALD) was used to grow both PbS quantum dots and Al_2O_3 barrier layers in a solid-state quantum dot-sensitized solar cell (QDSSC). Barrier layers grown prior to quantum dots resulted in a near-doubling of device efficiency (0.30% to 0.57%) whereas barrier layers grown after quantum dots did not improve efficiency, indicating the importance of quantum dots in recombination processes.

5.1. Introduction

The dye-sensitized solar cell (DSSC) pioneered by Grätzel and O'Regan has served as a template for a variety of modular solar cell designs given the ease of modifying critical cell components like the photoanode, the absorbing material, and the hole-transport material (HTM) [1]. Research into increasing dye absorption has yielded large improvements in device performance—12.3% efficiency in the latest record device [2]—but alternatives to molecular dyes have also been studied, such as recently-reported perovskite absorbers [3, 4]. In addition to perovskites, another promising alternative to dye absorbers are chalcogenide semiconductors such as Sb_2S_3 [5-9], In_2S_3 [10], CdS [11-18], CdSe [19-22], and PbS [23-31]. These chalcogenide absorbers can be grown or deposited on the photoanode surface to form either a continuous film—an "extremely thin absorber" (ETA) cell—or discrete nano-scale particles, *i.e.* quantum dots (QDs) [32, 33]. In ETA solar cells, absorber dimensions are limited by the diffusion length of excited carriers, while in quantum dot solar cells, the absorber dimensions are in the quantum confined regime. While the ETA design maximizes surface area utilization and minimizes contact between the photoanode and HTM (an important recombination pathway), QD absorbers offer the ability to tune the band gap by varying the QD particle size for optimal spectrum matching and energy band offsets, the latter of which is necessary for charge transfer in materials like PbS with low bulk band gaps.

Chalcogenide absorbers can be grown and deposited via several different routes including *in situ* methods such as chemical bath deposition (CBD) [8, 11], successive ion layer absorption and reaction (SILAR) [14, 27], and atomic layer deposition (ALD) [9, 10, 15, 34], and *ex situ* methods in which QDs are grown via colloidal synthesis and then attached to the photoanode surface using linker molecules [22, 25]. The precise thickness control and conformal growth enabled by ALD have led to its widespread use in solar cells [35], and spatial ALD, a variation of the traditional process, is even well-suited to industrial-scale manufacturing [36]. Of particular relevance for QDSSCs, certain ALD systems proceed from an "island" growth mode wherein growth is initiated at highly-reactive surface sites which results in a number of small clusters rather than a continuous film during the first several ALD cycles [37]. These small clusters or islands have been shown to exhibit quantum confinement (*i.e.* to be QDs) in both CdS [15] and PbS [34] ALD systems. A further advantage to ALD with respect to QDSSCs is the facile mass transfer of the gas phase precursor molecules, which enables uniform growth throughout a nanoporous substrate. ALD may also give better insight into how absorbers grow—because ALD is performed in an inert vacuum environment it opens the door for *in situ* characterization of QDs which may, for example, improve understanding of defect formation. Our present report demonstrates, to our knowledge, the first QDSSC utilizing ALD-grown PbS QDs.

The current record efficiency DSSC [2] as well as many high performing QDSSCs employ liquid HTMs (a cobalt redox couple in the former, and polysulfide solutions in QDSSCs), but a transition to solid-state HTMs is desired to eliminate concerns over device sealing and corrosion of other cell components. One promising solid-state HTM is spiro-OMeTAD (2,2',7,7'-tetrakis-(*N*,*N*-di-*p*-methoxyphenylamine)-9,9'-spirobifluorene), which was originally developed for DSSCs [38] but has also been used with perovskite [3, 4] and chalcogenide [6, 12, 14, 15, 18, 24, 27, 29] absorbers. Spiro-OMeTAD eliminates the challenges associated with corrosive liquid HTMs but has its own disadvantages: filling nanopores with the HTM, which is crucial in devices with thick active layers, is more difficult with solid-state than liquid HTMs [39, 40], and the recombination rate between electrons in the photoanode (typically TiO_2) and holes in the

HTM is much higher with spiro-OMeTAD than with the iodide/triiodide redox couple, the archetypal electrolyte of liquid DSSCs [41].

Despite the benefits of the QD absorber materials, QDSSC device efficiencies remain low, having only recently reached efficiencies of 5.6% in QDSSCs with a liquid electrolyte [31] and 1.5% in QDSSCs with a solid-state HTM [27]. The differences in efficiency of the record efficiency liquid and solid-state QDSSCs are due to the differences in short-circuit current (J_{SC}) of the devices: 30.0 mA/cm^2 for the liquid and 4.6 mA/cm^2 for the solid-state device. Both devices employed PbS QDs, and the large disparity in J_{SC} is primarily due to differences in charge collection efficiencies. The record-efficiency solid-state QDSSC was reported by Grätzel and coworkers, in an article that focused on recent fabrication improvements for QD deposition and infiltration of the HTM [27]. Thus, the literature to date on solid-state QDSSCs is still focused on device fabrication and QD synthesis techniques, as well as interface treatments to improve charge collection efficiencies.

Two strategies for improving the performance of solid-state QDSSCs, therefore, are to reduce the recombination rate by separating the photoanode and HTM and to maximize absorption by increasing QD surface coverage in the active layer. Increasing QD surface coverage is critical as the thickness of the active layer is limited by pore-filling considerations: the optimal thickness for spiro-based DSSCs and QDSSCs is around 2 μm [42] in contrast to the 5-10 μm typical of liquid DSSCs and QDSSCs. A common method to reduce photoanode-HTM recombination in QDSSCs and DSSCs is to deposit a thin insulating layer in between the absorbing material and photoanode. Both ALD and CBD processes have been used to deposit a number of insulating metal oxides such as Al_2O_3 [18, 43-48], SiO_2 [44, 49], ZrO_2 [44, 50], and HfO_2 [51]. Al_2O_3 has also been observed in a variety of ALD applications to act as a nucleation seed; that is, depositing a small amount of Al_2O_3 (*e.g.* 1-2 ALD cycles) prior to ALD of a second material tends to enhance the nucleation and subsequent growth of the second material [52-54]. This potential two-fold benefit from ALD of Al_2O_3 prior to PbS growth therefore motivated the current investigation. The ability to deposit both the barrier layer

and QD by ALD in a single reaction chamber without breaking vacuum opens new avenues for studying the intricacies of substrate-absorber-barrier interaction.

There are two notable differences in strategies for reducing recombination in DSSCs versus QDSSCs. In DSSCs, recombination barriers are typically deposited *before* dye adsorption due to the limited stability of dye molecules in solution (CBD) or under high temperature (ALD). The higher stability of QDs enables barrier layer deposition *after* QDs are deposited. In this configuration the barrier layer separates the photoanode and HTM without blocking electron injection from the absorbing material (*i.e.* the dye or QD) into the photoanode, which has been observed when barrier layers are deposited before the absorbing material [46, 47]. Additionally, in DSSCs the majority of research on recombination suppression focuses on the photoanode-HTM pathway because, due to the rapid regeneration of dye molecules by commonly-used HTMs (both liquid and solid), recombination from the photoanode to the oxidized dye molecule is not significant. Studies of QDSSCs have shown, however, that QD regeneration by spiro-OMeTAD is slower than dye regeneration, which means that the photoanode-QD recombination pathway is relevant [27, 55]. A third difference noted by Lee *et al.* between DSSC and QDSSC recombination is restricted to QDs of materials with small bulk bandgaps, like PbS: when the QDs reach a large enough size, the QD HOMO energy level exceeds the HTM HOMO energy level and the QDs then serve as mediators of photoanode-HTM recombination [27]. In order to investigate these various recombination scenarios, QDSSCs with Al_2O_3 barrier layers grown after PbS were compared to those with barrier layers grown before PbS.

5.2. Experimental Details

5.2.1. Fabrication of Nanostructured TiO_2 Substrates

As described elsewhere [56], fluorine-doped tin oxide (FTO)-coated glass (Pilkington, 15 Ω/□) was etched using 4 M HCl and Zn powder in order to create the desired device pattern. A compact layer of TiO_2 ~50 nm thick (to prevent contact between the FTO and the hole-transport material (HTM)) was deposited on the substrates at 450 °C by spray pyrolysis of titanium diisopropoxide bis(acetylacetonate) (Aldrich) in

ethanol (1:9 v/v) using air as the carrier gas. Roughly 2 μm-thick nanoporous TiO_2 films were made by doctor-blading a 1:1 (w/w) ratio of terpineol and a commercial paste (Dyesol 18NR-T) atop the compact TiO_2 layer followed by an anneal at 450 °C. The substrates were then left overnight in a bath of aqueous 0.02 M $TiCl_4$ and subsequently annealed again at 450 °C for thirty minutes.

5.2.2. Atomic Layer Deposition of PbS and Al_2O_3

The PbS quantum dots were deposited by using a low number of ALD cycles on nanoporous TiO_2 substrates. Bis(2,2,6,6-tetramethyl-3,5-heptanedionato)lead(II) ($Pb(tmhd)_2$) (Strem Chemicals, Inc.), sublimated at 140 °C, and 3.5% H_2S in N_2 were the deposition reagents. At a temperature of 160 °C, the reactions took place in a customized ALD station that is H_2S compatible [57]. Pulse/purge times of 0.5/45 s for $Pb(tmhd)_2$ and 0.1/40 s for H_2S were used. In the same reactor and conditions, Al_2O_3 was deposited at 160 °C using trimethylaluminum (TMA) (Aldrich) and DI water as the deposition reagents. Pulse/purge times of 0.1/40 s were used for both TMA and H_2O. Promptly after deposition, the samples were stored in an inert environment awaiting further processing and characterization.

Auger electron spectroscopy (AES) was used to verify growth of the quantum dots throughout the depth of a ~5 μm thick nanoporous TiO_2 film made in the same fashion as the ~2 μm thick TiO_2 films used in devices. The results of an AES linescan of a nanoporous TiO_2 film on a silicon substrate are shown in Figure 5-1 both as the raw signal intensity and the corresponding atomic concentrations. Despite the fact that the ALD process was not optimized for films as thick as 5 μm, the data indicate growth of PbS throughout this nanoporous TiO_2 layer, which is much thicker than that used in devices. The signal intensity of sulphur is independent of depth in the substrate, although there is some dropoff in the lead signal away from the surface which could be due to superior infiltration of the smaller sulphur precursor.

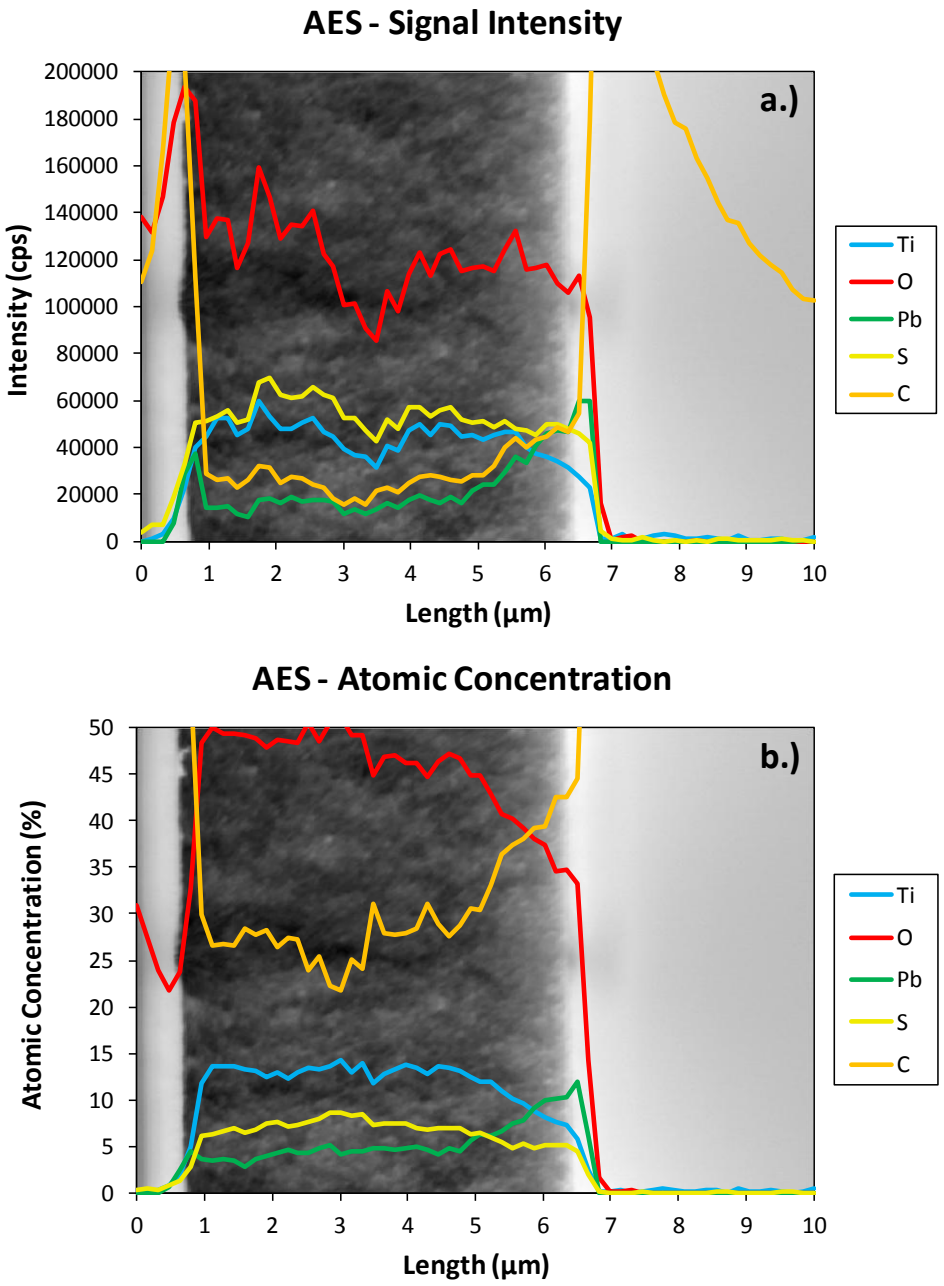


Figure 5-1: Auger electron spectroscopy linescan of 10 ALD cycles of PbS grown on a nanoporous TiO_2 substrate with data reported in terms of signal intensity, a), and atomic concentration, b). The linescan was performed at the midpoint of the SEM image, i.e. the 100000 counts per second (CPS) line in a), and the 25% line in b). The nanoporous TiO_2 layer, approximately 5 µm thick, was deposited atop a silicon substrate which is at the far left of the SEM image, meaning that the top of the nanoporous TiO_2 film is at approximately the 6 µm mark.

5.2.3. QDSSC Device Fabrication

Spiro-OMeTAD (2,2',7,7'-tetrakis-(*N*,*N*-di-*p*-methoxyphenylamine)-9,9'-spirobifluorene) (Lumtec) was dissolved in chlorobenzene at a concentration of 225 mL^{-1}. *Tert*-butylpyridine was added to the solution at the ratio of 1:10.3 µL:mg of spiro-OMeTAD, and lithium bis-(trifluoromethylsulfonyl)imide salt (170 mg mL^{-1} in acetonitrile) was added at the ratio of 1:4.8 µL:mg of spiro-OMeTAD. The resultant solution was deposited onto QD-coated TiO_2 substrates (~30 µL per 3 cm^2 substrates) and then spin-coated for 30 s at 2000 RPM. 200 nm-thick silver electrodes were then evaporated onto the substrates under vacuum at 10^{-6} torr yielding device areas ~9-10 mm^2.

5.2.4. Device Testing

Solar cell performance was measured as described elsewhere [56]. Current-voltage (*J-V*) curves were obtained using a Xe lamp AM 1.5 solar simulator calibrated to 1 sun. Devices were light-soaked until maximum efficiencies were obtained (~30 minutes). Recombination lifetimes were obtained via transient photovoltage experiments [58, 59]. Devices were biased at 1 sun using a white LED array. A Keithley 2400 SourceMeter was used to keep the device current constant at a value corresponding to a given photovoltage (the photovoltage was swept in 0.05 V increments). A white LED (~0.05 sun) was then pulsed (50 ms square-wave) at the samples, yielding a transient increase and subsequent in the device photovoltage. Recombination lifetimes were obtained by fitting the exponential decay of the photovoltage. Incident photon-to-current efficiency (IPCE; also known as external quantum efficiency, or EQE) measurements were taken at short circuit using monochromated white light from a 100 W tungsten lamp, which was focused through a monochromator. The monochromated illumination, chopped at 40 Hz, was superimposed on top of a continuous-wave white light illumination (~1 sun) from a white LED array incident on the device. The photocurrent action spectrum of the device was acquired through a lock-in amplifier and IPCE was calculated by referencing the device current to a NIST traceable calibration photodiode. While we have not performed rigorous long-term device stability studies, we note that

device performance (and behavior, for example, in recombination measurements) is reproducible over several-day time intervals.

5.2.5. Characterization via Transmission Electron Microscopy (TEM) and UV-Vis Spectroscopy

Plain-view TEM micrographs of the samples were taken using a FEI Tecnai G2 F20-X-TWIN at an accelerating voltage of 200 kV. Before TEM characterization, the PbS QD/nanoporous TiO_2 composite films were scratched off from the glass substrates using a sterile razor. Afterwards, the residue was sonicated in 1 mL of ethanol for 5 mins. A fresh ultrathin carbon on copper TEM grid (Ted Pella, Inc.) was introduced into the solution to extract PbS QD/nanoporous TiO_2 clusters.

Also in the TEM, Energy-dispersive spectroscopy (EDS) was performed on the X-rays emitted by the samples of interest. EDS helped identify the main atomic species present. Table 5-1 summarizes the average atomic concentrations of the samples with PbS QDs on nanoporous TiO_2 with and without the Al_2O_3 barrier layer. No samples with spiro-OMeTAD were analyzed using TEM-EDS. The X-ray signal is dominated by the carbon and copper peaks from the TEM grid. The comparable atomic concentrations of Pb and S strongly suggest the existence of PbS in the samples.

Table 5-1: Average atomic concentrations measured using TEM-EDS. The atomic shells used for each element are denoted inside parentheses next to the respective element.

Atomic Species (shell)	PbS x 10	Al_2O_3 x 1 + PbS x 10
C (K)	54.3	50
O (K)	15.3	24.4
Al (K)	-	0.8
S (K)	1.9	0.3
Ti (K)	8.1	10.9
Cu (K)	17.8	13
Pb (L)	2.6	0.6

UV-Vis measurements were taken using two different methods. Transmission spectra were obtained using a PerkinElmer Lambda 1050 UV/VIS/NIR Spectrometer. The samples were measured as deposited after the ALD step (*i.e.* lacking both spiro-

OMeTAD and silver electrodes). The second set of UV-Vis measurements were collected from completed devices. These measurements, reported in terms of spectral absorptance, were collected using the same tungsten lamp and monochromator as the IPCE measurements and were measured using an integrating sphere with an attached silicon photodiode.

5.3. Results & Discussion

PbS quantum dots grown by ALD on nanoporous anatase TiO_2 were studied using transmission electron microscopy (TEM). Figure 5-2 shows the conformal and dispersed PbS QD coverage with (a) and without (b, c) an ALD cycle of Al_2O_3 between the PbS QDs and the TiO_2 nanoparticles. This TEM study strongly suggests that the PbS QD coverage is not affected by the Al_2O_3 surface treatment. It is important to note that it is difficult to capture the as-deposited shape of the PbS QDs since they are sensitive to electron-beam annealing in the TEM. Annealing of the PbS QDs usually results in the dome-shaped clusters observed in Figure 5-2, which may not be the morphology of the PbS QDs in a working solar cell. Nevertheless, the TEM images provide key insight on the surface coverage and dimensions of the PbS QDs. Most of the PbS QDs are between 2.8 nm and 4.8 nm in diameter, similar in size to those employed elsewhere in TiO_2-based QDSSCs [25, 29]. As shown in Figure 5-2b, the lattice spacing of a PbS QD captured by TEM has a measured lattice constant of 5.9 Å, which agrees with the known bulk lattice constant of PbS. TEM-EDAX analysis of the samples (Table 5-1) verifies the presence of O, S, Ti, and Pb atoms.

a)

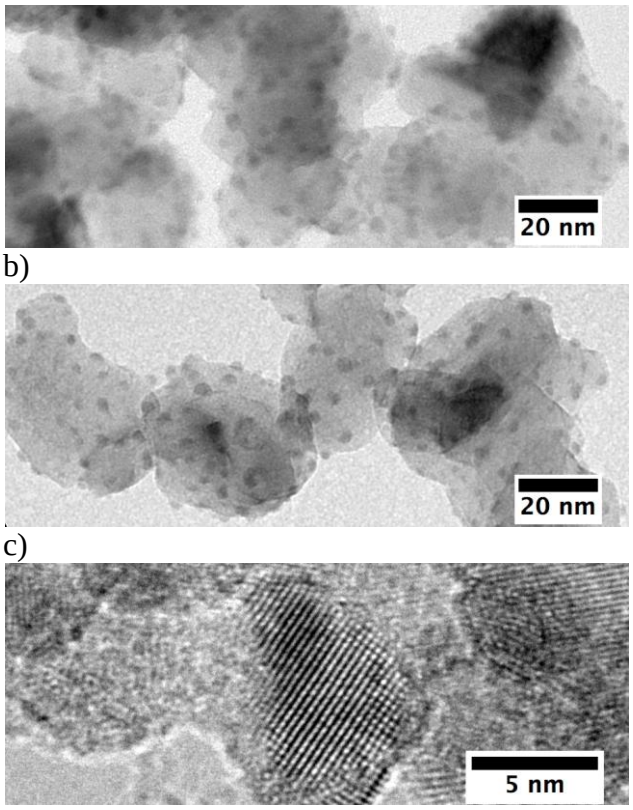


Figure 5-2: Transmission electron micrographs of PbS QDs on nanoporous TiO_2 with (a) and without (b, c) an intermediate Al_2O_3 cycle. As seen in (a) and (b), the coverage of the QDs is not affected by Al_2O_3. (c) Lattice diffraction of the rock salt PbS QDs is captured with a measured lattice constant of 5.9 Å.

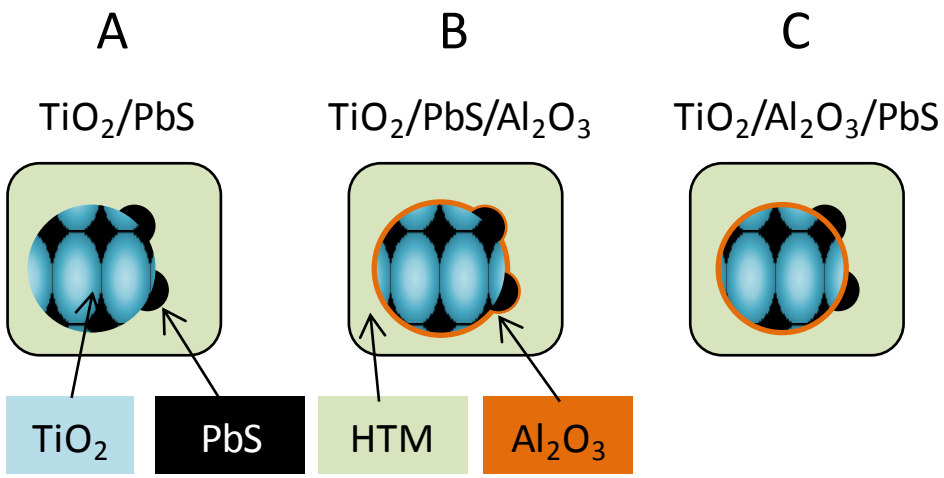


Figure 5-3: Schematics of the three configurations studied (not to scale). A: control devices with PbS quantum dots grown on TiO_2 nanoparticles, surrounded by the spiro-OMeTAD hole transport material (HTM). B: Al_2O_3 deposited after growth of quantum dots. In this configuration the Al_2O_3 barrier layer is expected to slow recombination involving electrons in TiO_2 and holes in the HTM. C: Al_2O_3 deposited prior to quantum dot growth. In this configuration the Al_2O_3 barrier layer is expected to slow recombination involving electrons in TiO_2 and holes in both the HTM and oxidized quantum dots. Configuration C yielded the highest device efficiencies.

Starting from $TiCl_4$-treated nanoporous TiO_2 substrates, three different sample types were created in order to study light absorption and device performance: 10 cycles of PbS ALD (TiO_2/PbS) (the control sample); 1 cycle of Al_2O_3 ALD followed by 10 cycles of PbS ALD (TiO_2/Al_2O_3/PbS); 10 cycles of PbS ALD followed by 1 cycle of Al_2O_3 ALD (TiO_2/PbS/Al_2O_3). Schematics are shown in Figure 5-3. We note that a single ALD cycle of Al_2O_3 covers approximately 50-75% of the TiO_2 surface with a single Al_2O_3 layer [46]. UV-Vis spectroscopy, which was used to measure the PbS absorption, indicates that Al_2O_3 deposited prior to PbS ALD does not increase PbS nucleation: absorption levels are unchanged and there is no qualitative change in the shape of the absorption spectrum that would indicate Al_2O_3 alters the size distribution of subsequent PbS QDs (Figure 5-4). In all configurations, the onset of PbS absorption occurs near 800 nm, which suggests the larger PbS QDs have optical band gaps around 1.6 eV and significant deviation from the blank TiO_2 substrates begins after 650 nm (Figure 5-4a). Such large band gaps are needed for favorable energetic alignment of the PbS and TiO_2 conduction bands. The deviation of the absorption onset energy from the bulk PbS band gap of 0.37 eV clearly indicate that 10 ALD cycles of PbS result in the deposition of quantum-confined structures on the TiO_2 surface with favorable absorption properties.

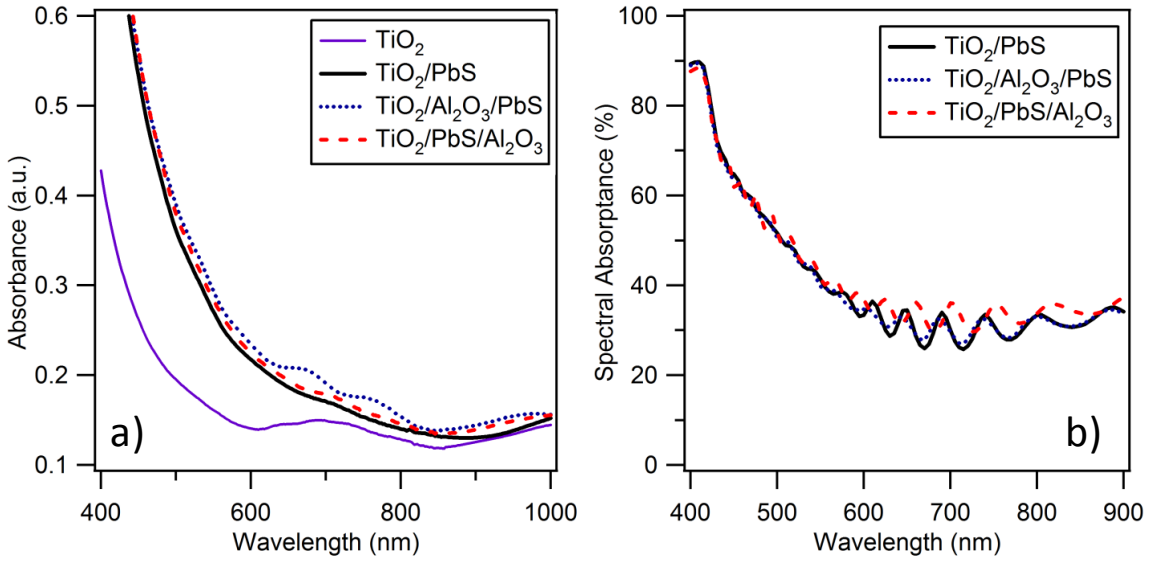


Figure 5-4: a) UV-Vis absorbance spectra taken in transmission mode of nanoporous TiO_2 substrates on FTO coated with PbS QDs in the three different configurations studied. A TiO_2 control is also shown. No significant changes were observed when a single ALD cycle of Al_2O_3 preceded PbS deposition, indicating that it did not lead to enhanced PbS nucleation. In all three configurations containing PbS QDs, the absorption onset occurs near 800 nm indicating a band gap for the largest QDs ~1.6 eV. b) UV-Vis spectra of full devices, measured in terms of spectral absorptance (percent of incident light absorbed), collected in an integrating sphere. As in a), no significant changes in light absorption were observed when a single ALD cycle of Al_2O_3 preceded PbS deposition indicating that it did not lead to enhanced PbS nucleation. All three spectra exhibit interference fringes common in thin films.

In contrast to the absorption data, device performance was dramatically different for the TiO_2/Al_2O_3/PbS configuration versus the other two: a single cycle of Al_2O_3 ALD improved device efficiency by nearly a factor of two (from 0.30% to 0.57%) whereas no appreciable change was observed for the TiO_2/PbS/Al_2O_3 configuration (Table 5-2 and Figure 5-5). The improved performance in the TiO_2/Al_2O_3/PbS configuration arises from a much higher J_{SC} and a modestly-improved V_{OC}. We note that the 0.57% efficiency for the TiO_2/Al_2O_3/PbS configuration is on par with that reported by Lee *et al.* (0.72%) in a device otherwise identical but for the fact that SILAR was used to grow the PbS QDs [27]. Lee *et al.* also observed that using larger TiO_2 nanoparticles for the active layer (which results in larger pores, and hence, more facile HTM pore-filling) doubled device efficiency, a strategy that may also prove fruitful with ALD-grown PbS [27].

Table 5-2: Average device parameters for the three configurations tested. A substantial improvement in efficiency was achieved by performing a single ALD cycle of Al_2O_3 prior to PbS growth whereas no improvement was observed with a single Al_2O_3 ALD cycle after PbS growth. The efficiency improvement is driven by a large increase in J_{SC} and a smaller increase in V_{OC}. Values were obtained by taking the average of the top two of four devices (~10 mm^2 in area) on a given substrate and then averaging over the four substrates tested with each configuration.

	J_{SC} (mA/cm^2)	V_{OC} (V)	Fill Factor	Efficiency (%)
TiO_2/PbS	0.89	0.51	0.69	0.30
TiO_2/Al_2O_3/PbS	1.73	0.58	0.58	0.57
TiO_2/PbS/Al_2O_3	0.93	0.49	0.57	0.26

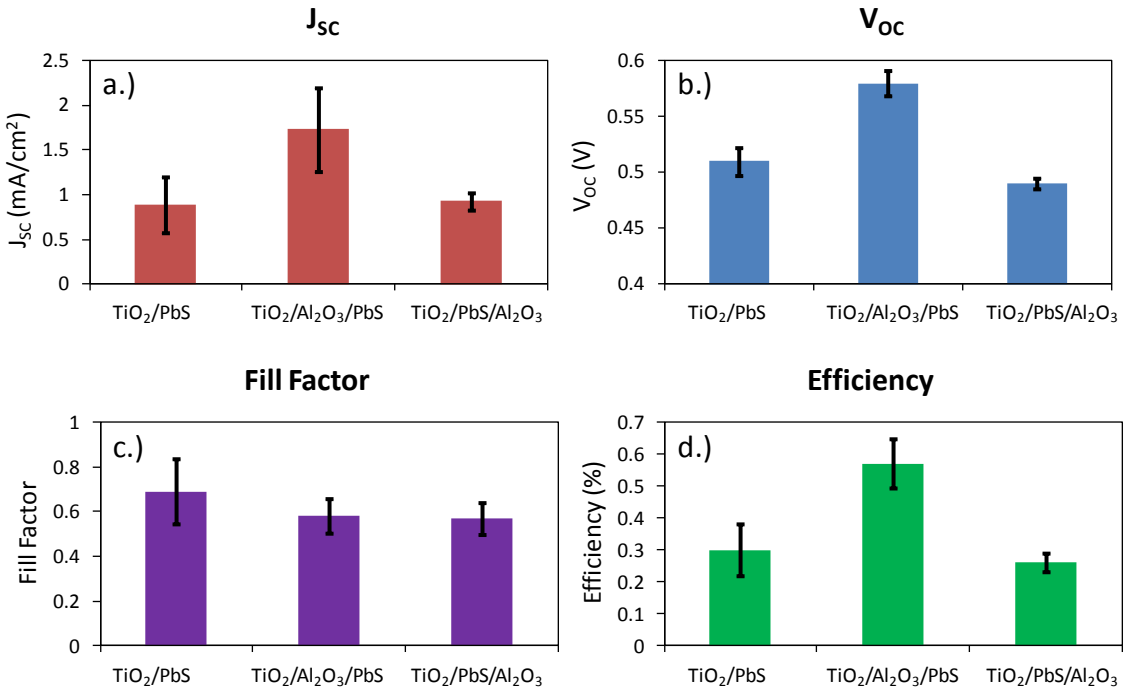


Figure 5-5: Average device data for the PbS QDSSCs with and without Al_2O_3 barrier layers. Values were calculated by averaging the top two (of four) devices on each of four separate substrates for each configuration; therefore the values represent the average of eight different devices. Error bars indicate standard deviation of device parameters.

The fact that J_{SC} improved dramatically with a pre-PbS ALD cycle of Al_2O_3 despite the absence of changes to the QDs in quantity or size suggests that the barrier layer aspect of Al_2O_3 is significant. In order to understand the effect of Al_2O_3 on recombination we collected dark current-voltage (*J-V*) curves and incident photon-to-current efficiency (IPCE) data and performed transient photovoltage analysis [60], which is particularly well-suited for measuring recombination with the spiro-OMeTAD HTM. IPCE results (Figure 5-6) indicate that the superior performance of the TiO_2/Al_2O_3/PbS

configuration is due to enhanced efficiency across a wide spectral range, which, coupled with the lack of change in light absorption observed in the UV-Vis data (Figure 5-4), suggests an improvement in internal quantum efficiency (IQE) in the $TiO_2/Al_2O_3/PbS$ configuration. A decrease relative to control devices larger than that observed in the *J-V* measurements is apparent in the IPCE data for the $TiO_2/PbS/Al_2O_3$ configuration; we attribute this unusually low IPCE to the fact that the bias light source used in IPCE measurements may alter the effects of light-soaking, as compared to the AM1.5G light spectrum used in *J-V* measurements.

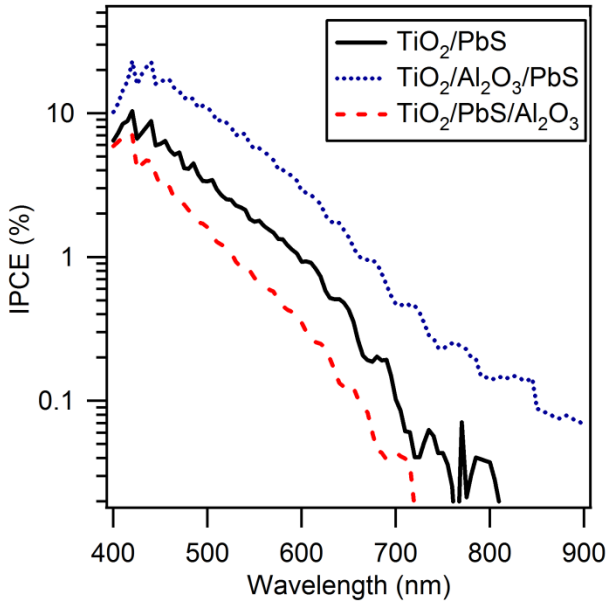


Figure 5-6: Incident photon-to-current efficiency (IPCE) averaged from multiple devices in each of the three configurations collected at zero bias. When Al_2O_3 precedes PbS QD growth, a substantial improvement in IPCE is observed.

Dark *J-V* curves (Figure 5-7a) indicate that the single ALD cycle of Al_2O_3 reduces dark current whether it is deposited before or after the PbS. The transient photovoltage studies show that in both instances Al_2O_3 increases recombination lifetime relative to control cells (Figure 5-8), but the enhancement is most apparent at higher photovoltages in the $TiO_2/Al_2O_3/PbS$ configuration and at lower photovoltages in the $TiO_2/PbS/Al_2O_3$ configuration. We attribute the lifetime enhancement in the $TiO_2/Al_2O_3/PbS$ configuration to suppression of recombination with (or mediated by) oxidized PbS QDs. The recombination suppression in the $TiO_2/PbS/Al_2O_3$ configuration is attributed to blocking of recombination with holes in spiro-OMeTAD (we note that the

recombination pathway from the PbS excited state to spiro-OMeTAD, which should also be blocked in this configuration, is not detectable via transient photovoltage measurements). We speculate that the reason recombination to oxidized QDs appears to dominate at higher photovoltages and recombination to spiro-OMeTAD dominates at lower photovoltages is due to the different routes and energetics for each process (the model described by Hod *et al*. wherein TiO_2-QD interface states mediate recombination is particularly illustrative here [61]).

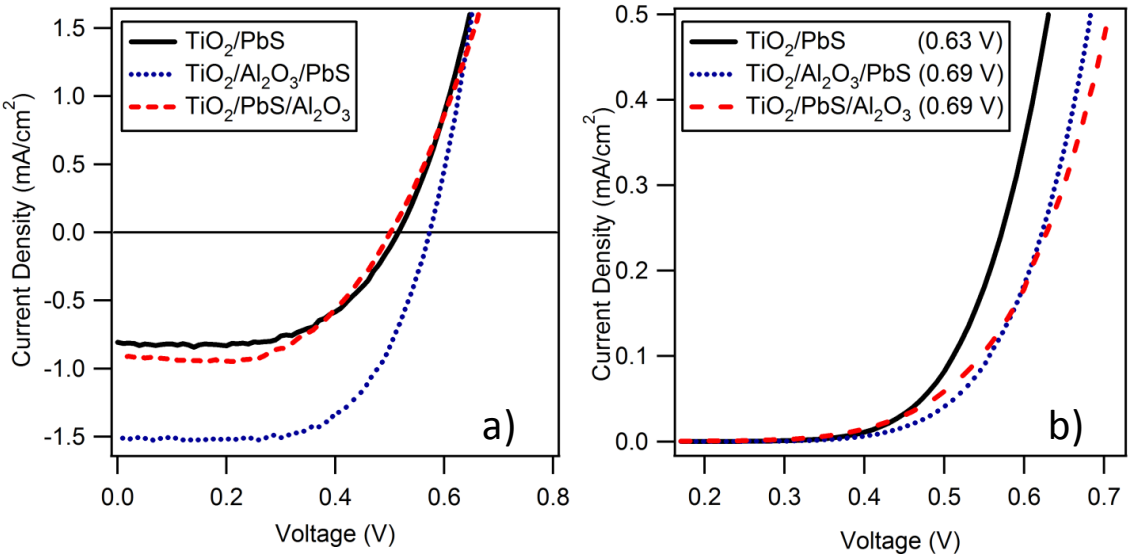


Figure 5-7: Light, a), and dark, b), current-voltage (*J-V*) curves for typical devices of the three configurations studied. Whether deposited before or after the PbS quantum dots, a single cycle of Al_2O_3 suppressed the onset of dark current to a similar degree. The value in parentheses corresponds to a current-threshold voltage, that is, the voltage at which the dark current in the devices exceeded an arbitrary value (here, 0.4 mA/cm^2). These current threshold values are averaged over all the devices for that particular configuration.

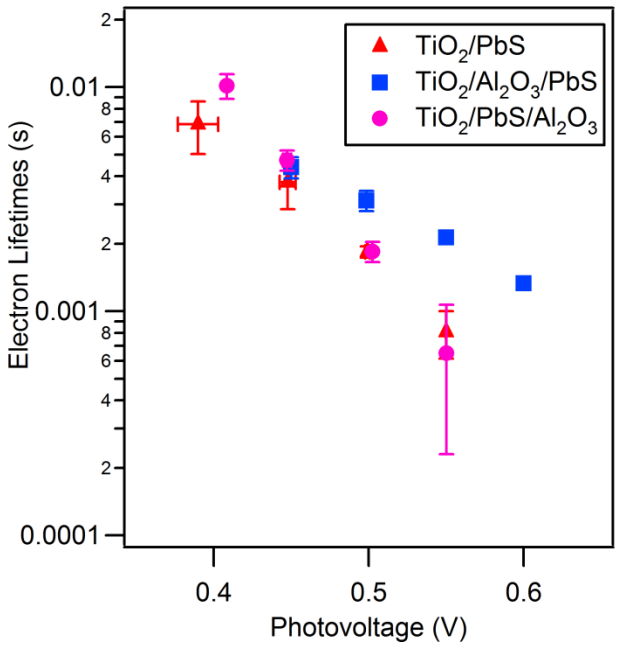


Figure 5-8: Electron lifetimes for the three different device configurations as determined by fitting the photovoltage decay obtained from transient photovoltage experiments. At higher photovoltages the recombination suppression from depositing Al_2O_3 prior to PbS growth is readily apparent and is superior to Al_2O_3 deposited after PbS, although recombination is also reduced in that configuration, particularly at lower photovoltages. Error bars indicate standard deviations of the several devices tested.

Given the lifetime enhancement observed in the TiO_2/PbS/Al_2O_3 configuration, it is therefore surprising that J_{SC} and IPCE did not increase as in the TiO_2/Al_2O_3/PbS configuration: this could be due to the Al_2O_3 on PbS blocking regeneration of the PbS QDs, which has been observed previously with CdS QDs and Al_2O_3 [18]. While this hypothesis is consistent with the observed increase in J_{SC} in the TiO_2/Al_2O_3/PbS configuration, it is also possible that Al_2O_3 increases J_{SC} in this cell configuration by improving charge injection efficiency by lowering the TiO_2 conduction band (away from vacuum), raising the PbS conduction band (towards vacuum), or reducing surface states at the PbS-TiO_2 interface that participate in trap-mediated recombination. Further investigation is needed to probe this mechanism, which is an intriguing contrast to the detrimental effects of Al_2O_3 on injection efficiency observed in DSSCs [46, 47].

5.4. Conclusion

In summary, we have demonstrated the application of ALD to grow lead sulfide QD absorbers for use in a solid-state QDSSC. Metal oxide barrier layers were deposited

in the same reactor without a vacuum break, allowing for rigorous control over device interfaces. A single ALD cycle of Al_2O_3 prior to PbS growth improved efficiency nearly twofold and the resultant devices were on par with spiro-based cells in the literature utilizing the SILAR growth method. The improvement in device efficiency observed in the $TiO_2/Al_2O_3/PbS$ configuration as compared to the $TiO_2/PbS/Al_2O_3$ configuration was attributed to the greater importance of blocking recombination at the TiO_2-PbS interface than the TiO_2-HTM interface, as indicated by the large improvement in IPCE observed in the $TiO_2/Al_2O_3/PbS$ configuration. This result highlights the importance of recombination with oxidized QDs and not just with the hole-transport material. The growth scheme employed in this work is highly modular and further work is underway to optimize performance by adjusting the number of ALD cycles and material choices for absorber, barrier, and passivation layers. We believe that fundamental interfacial studies enabled by this single-chamber deposition method will further understanding and guide future progress in QDSSCs.

5.5. Collaborations & Copyrights

This chapter is adopted from work originally published in the *Journal of Materials Chemistry A* [62] and is reproduced by permission of The Royal Society of Chemistry. This work was a collaboration with Orlando Trejo, Katherine Roelofs, and John Xu. Orlando and John performed the ALD in the lab of Fritz Prinz and Orlando collected and analyzed the UV-Vis and TEM data. The device fabrication and testing was performed in the lab of Michael McGehee and the transient photovoltage experimental setup was originally developed by Colin Bailie, Eric Hoke, and George Margulis.

5.6. References

[1] B. O'Regan, M. Grätzel, Nature 353/6346 (1991) 737.
[2] A. Yella, H.-W. Lee, H.N. Tsao, C. Yi, A.K. Chandiran, M.K. Nazeeruddin, E.W.-G. Diau, C.-Y. Yeh, S.M. Zakeeruddin, M. Grätzel, Science 334/6056 (2011) 629.
[3] H.-S. Kim, C.-R. Lee, J.-H. Im, K.-B. Lee, T. Moehl, A. Marchioro, S.-J. Moon, R. Humphry-Baker, J.-H. Yum, J.E. Moser, M. Grätzel, N.-G. Park, Sci. Rep. 2 (2012) 1.
[4] M.M. Lee, J. Teuscher, T. Miyasaka, T.N. Murakami, H.J. Snaith, Science 338/6107 (2012) 643.

[5] J.A. Chang, J.H. Rhee, S.H. Im, Y.H. Lee, H.-j. Kim, S.I. Seok, M.K. Nazeeruddin, M. Grätzel, Nano Letters 10/7 (2010) 2609.
[6] S.-J. Moon, Y. Itzhaik, J.-H. Yum, S.M. Zakeeruddin, G. Hodes, M. Grätzel, The Journal of Physical Chemistry Letters 1/10 (2010) 1524.
[7] S.H. Im, C.-S. Lim, J.A. Chang, Y.H. Lee, N. Maiti, H.-J. Kim, M.K. Nazeeruddin, M. Grätzel, S.I. Seok, Nano Letters 11/11 (2011) 4789.
[8] J.A. Chang, S.H. Im, Y.H. Lee, H.-j. Kim, C.-S. Lim, J.H. Heo, S.I. Seok, Nano Letters 12/4 (2012) 1863.
[9] H. Wedemeyer, J. Michels, R. Chmielowski, S. Bourdais, T. Muto, M. Sugiura, G. Dennler, J. Bachmann, Energy & Environmental Science (2013) 67.
[10] S.K. Sarkar, J.Y. Kim, D.N. Goldstein, N.R. Neale, K. Zhu, C.M. Elliott, A.J. Frank, S.M. George, The Journal of Physical Chemistry C 114/17 (2010) 8032.
[11] M. Shalom, S. Dor, S. Rühle, L. Grinis, A. Zaban, The Journal of Physical Chemistry C 113/9 (2009) 3895.
[12] C.-F. Chi, P. Chen, Y.-L. Lee, I.P. Liu, S.-C. Chou, X.-L. Zhang, U. Bach, Journal of Materials Chemistry 21/43 (2011) 17534.
[13] H. Choi, R. Nicolaescu, S. Paek, J. Ko, P.V. Kamat, ACS Nano 5/11 (2011) 9238.
[14] P. Ardalan, T.P. Brennan, H.-B.-R. Lee, J.R. Bakke, I.K. Ding, M.D. McGehee, S.F. Bent, ACS Nano 5/2 (2011) 1495.
[15] T.P. Brennan, P. Ardalan, H.-B.-R. Lee, J.R. Bakke, I.K. Ding, M.D. McGehee, S.F. Bent, Advanced Energy Materials 1/6 (2011) 1169.
[16] Q. Zhang, X. Guo, X. Huang, S. Huang, D. Li, Y. Luo, Q. Shen, T. Toyoda, Q. Meng, Physical Chemistry Chemical Physics 13/10 (2011) 4659.
[17] Z. Yang, C.-Y. Chen, C.-W. Liu, C.-L. Li, H.-T. Chang, Advanced Energy Materials 1/2 (2011) 259.
[18] K.E. Roelofs, T.P. Brennan, J.C. Dominguez, C.D. Bailie, G.Y. Margulis, E.T. Hoke, M.D. McGehee, S.F. Bent, The Journal of Physical Chemistry C 117/11 (2013) 5584.
[19] S.-Q. Fan, D. Kim, J.-J. Kim, D.W. Jung, S.O. Kang, J. Ko, Electrochemistry Communications 11/6 (2009) 1337.
[20] S.-Q. Fan, B. Fang, J.H. Kim, B. Jeong, C. Kim, J.-S. Yu, J. Ko, Langmuir 26/16 (2010) 13644.
[21] H.J. Lee, D.W. Chang, S.-M. Park, S.M. Zakeeruddin, M. Grätzel, M.K. Nazeeruddin, Chemical Communications 46/46 (2010) 8788.
[22] X.-Y. Yu, B.-X. Lei, D.-B. Kuang, C.-Y. Su, Journal of Materials Chemistry 22/24 (2012) 12058.
[23] S.-m. Yang, C.-h. Huang, J. Zhai, Z.-s. Wang, L. Jiang, Journal of Materials Chemistry 12/5 (2002) 1459.
[24] R. Plass, S. Pelet, J. Krueger, M. Grätzel, U. Bach, The Journal of Physical Chemistry B 106/31 (2002) 7578.
[25] B.-R. Hyun, Y.-W. Zhong, A.C. Bartnik, L. Sun, H.D. Abruña, F.W. Wise, J.D. Goodreau, J.R. Matthews, T.M. Leslie, N.F. Borrelli, ACS Nano 2/11 (2008) 2206.
[26] H.J. Lee, P. Chen, S.-J. Moon, F.d.r. Sauvage, K. Sivula, T. Bessho, D.R. Gamelin, P. Comte, S.M. Zakeeruddin, S.I. Seok, M. Grätzel, M.K. Nazeeruddin, Langmuir 25/13 (2009) 7602.

[27] H. Lee, H.C. Leventis, S.-J. Moon, P. Chen, S. Ito, S.A. Haque, T. Torres, F. Nüesch, T. Geiger, S.M. Zakeeruddin, M. Grätzel, M.K. Nazeeruddin, Advanced Functional Materials 19/17 (2009) 2735.
[28] A. Braga, S. Giménez, I. Concina, A. Vomiero, I.n. Mora-Seró • , The Journal of Physical Chemistry Letters 2/5 (2011) 454.
[29] H.J. Snaith, A. Stavrinadis, P. Docampo, A.A.R. Watt, Solar Energy 85/6 (2011) 1283.
[30] L. Etgar, T. Moehl, S. Gabriel, S.G. Hickey, A. Eychmüller, M. Grätzel, ACS Nano 6/4 (2012) 3092.
[31] J.-W. Lee, D.-Y. Son, T.K. Ahn, H.-W. Shin, I.Y. Kim, S.-J. Hwang, M.J. Ko, S. Sul, H. Han, N.-G. Park, Sci. Rep. 3 (2013) 1.
[32] G. Hodes, D. Cahen, Accounts of Chemical Research 45/5 (2012) 705.
[33] P.V. Kamat, Accounts of Chemical Research (2012) 1906.
[34] N.P. Dasgupta, H.J. Jung, O. Trejo, M.T. McDowell, A. Hryciw, M. Brongersma, R. Sinclair, F.B. Prinz, Nano Letters 11/3 (2011) 934.
[35] J.R. Bakke, K.L. Pickrahn, T.P. Brennan, S.F. Bent, Nanoscale 3/9 (2011) 3482.
[36] P. Poodt, D.C. Cameron, E. Dickey, S.M. George, V. Kuznetsov, G.N. Parsons, F. Roozeboom, G. Sundaram, A. Vermeer, Journal of Vacuum Science & Technology A: Vacuum, Surfaces, and Films 30/1 (2012) 010802.
[37] R.L. Puurunen, W. Vandervorst, Journal of Applied Physics 96/12 (2004) 7686.
[38] U. Bach, D. Lupo, P. Comte, J.E. Moser, F. Weissortel, J. Salbeck, H. Spreitzer, M. Grätzel, Nature 395/6702 (1998) 583.
[39] I.K. Ding, N. Tétreault, J. Brillet, B.E. Hardin, E.H. Smith, S.J. Rosenthal, F. Sauvage, M. Grätzel, M.D. McGehee, Advanced Functional Materials 19/15 (2009) 2431.
[40] J. Melas-Kyriazi, I.K. Ding, A. Marchioro, A. Punzi, B.E. Hardin, G.F. Burkhard, N. Tétreault, M. Grätzel, J.-E. Moser, M.D. McGehee, Advanced Energy Materials 1/3 (2011) 407.
[41] H.J. Snaith, L. Schmidt-Mende, Advanced Materials 19/20 (2007) 3187.
[42] L. Schmidt-Mende, S.M. Zakeeruddin, M. Grätzel, Applied Physics Letters 86/1 (2005) 3504.
[43] E. Palomares, J.N. Clifford, S.A. Haque, T. Lutz, J.R. Durrant, Chemical Communications/14 (2002) 1464.
[44] E. Palomares, J.N. Clifford, S.A. Haque, T. Lutz, J.R. Durrant, Journal of the American Chemical Society 125/2 (2003) 475.
[45] C. Lin, F.-Y. Tsai, M.-H. Lee, C.-H. Lee, T.-C. Tien, L.-P. Wang, S.-Y. Tsai, Journal of Materials Chemistry 19/19 (2009) 2999.
[46] L.J. Antila, M.J. Heikkilä, V. Mäkinen, N. Humalamäki, M. Laitinen, V. Linko, P. Jalkanen, J. Toppari, V. Aumanen, M. Kemell, P. Myllyperkiö, K. Honkala, H. Häkkinen, M. Leskelä, J.E.I. Korppi-Tommola, The Journal of Physical Chemistry C 115/33 (2011) 16720.
[47] T.P. Brennan, J.R. Bakke, I.K. Ding, B.E. Hardin, W.H. Nguyen, R. Mondal, C.D. Bailie, G.Y. Margulis, E.T. Hoke, A. Sellinger, M.D. McGehee, S.F. Bent, Physical Chemistry Chemical Physics 14/35 (2012) 12130.
[48] S.-Q. Fan, Y. Geng, C. Kim, S. Paik, J. Ko, Materials Chemistry and Physics 132/2-3 (2012) 943.

[49] M. Shanmugam, B. Bills, M.F. Baroughi, Materials Research Society Symposium Proceedings 1260/T10 (2010) 1.
[50] T.C. Li, M.S. Goes, F. Fabregat-Santiago, J. Bisquert, P.R. Bueno, C. Prasittichai, J.T. Hupp, T.J. Marks, Journal of Physical Chemistry C 113/42 (2009) 18385.
[51] M. Shanmugam, M.F. Baroughi, D. Galipeau, Thin Solid Films 518/10 (2010) 2678.
[52] C.A. Wilson, R.K. Grubbs, S.M. George, Chemistry of Materials 17/23 (2005) 5625.
[53] J.W. Elam, J.A. Libera, M.J. Pellin, A.V. Zinovev, J.P. Greene, J.A. Nolen, Applied Physics Letters 89/5 (2006) 053124.
[54] S.D. Standridge, G.C. Schatz, J.T. Hupp, Langmuir 25/5 (2009) 2596.
[55] H.C. Leventis, F. O'Mahony, J. Akhtar, M. Afzaal, P. O'Brien, S.A. Haque, Journal of the American Chemical Society 132/8 (2010) 2743.
[56] T. Leijtens, I.K. Ding, T. Giovenzana, J.T. Bloking, M.D. McGehee, A. Sellinger, ACS Nano 6/2 (2012) 1455.
[57] N.P. Dasgupta, J.F. Mack, M.C. Langston, A. Bousetta, F.B. Prinz, Review of Scientific Instruments 81/4 (2010) 044102.
[58] B.C. O'Regan, F. Lenzmann, The Journal of Physical Chemistry B 108/14 (2004) 4342.
[59] B.C. O'Regan, J.R. Durrant, P.M. Sommeling, N.J. Bakker, The Journal of Physical Chemistry C 111/37 (2007) 14001.
[60] P.R.F. Barnes, K. Miettunen, X. Li, A.Y. Anderson, T. Bessho, M. Grätzel, B.C. O'Regan, Advanced Materials 25/13 (2013) 1881.
[61] I. Hod, V. González-Pedro, Z. Tachan, F. Fabregat-Santiago, I. Mora-Seró, J. Bisquert, A. Zaban, The Journal of Physical Chemistry Letters 2/24 (2011) 3032.
[62] T.P. Brennan, O. Trejo, K.E. Roelofs, J. Xu, F.B. Prinz, S.F. Bent, Journal of Materials Chemistry A (2013).

Chapter 6. The Dynamical Orientation of Large Molecules on Oxide Surfaces and its Implications for Dye-Sensitized Solar Cells

A dual experimental-computational approach utilizing near-edge X-ray absorption fine structure (NEXAFS) spectroscopy and density functional theory-molecular dynamics (DFT-MD) is presented for determining the orientation of a large adsorbate on an oxide substrate. A system of interest in the field of dye-sensitized solar cells is studied: an organic cyanoacrylic acid-based donor-π-acceptor dye (WN1) bound to anatase TiO_2. Assessment of nitrogen K-edge NEXAFS spectra is supported by calculations of the electronic structure that indicate energetically discrete transitions associated with the two π systems of the C-N triple bond in the cyanoacrylic acid portion of the dye. Angle-resolved NEXAFS spectra are fitted to determine the orientation of these two orbital systems and the results indicate an upright orientation of the adsorbed dye, 63° from the TiO_2 surface plane. These experimental results are then compared to computational studies of the WN1 dye on an anatase (101) TiO_2 slab. The ground state structure obtained from standard DFT optimization is less upright (45° from the surface) than the NEXAFS results but DFT-MD simulations, which provide a more realistic depiction of the dye at room temperature, exhibit excellent agreement—within 2° on average—with the angles determined via NEXAFS, demonstrating the importance of accounting for the dynamic nature of adsorbate-substrate interactions DFT-MD's powerful predictive abilities.

6.1. Introduction

Adsorbate-substrate interactions underpin a variety of important applications including catalysis, electronics, chemical sensing, and photovoltaics [1-4]. In these systems, adsorbates can be used to functionalize the surface (*e.g.* in electronics, to form a dielectric layer [2]) or the adsorbate-substrate interactions can constitute the primary process of interest (*e.g.* in catalysis). A critical element in understanding these interactions is determining how adsorbates orient on the surface, which can properties such as surface coverage and charge transfer and can dictate interactions with the external

environment. A wide array of experimental and computational methods is available for probing these interactions but interpretation can become complicated or even unfeasible when the adsorbates are large in size. A further consideration is that large adsorbates are dynamic, not static, and their orientations—and consequently their interactions with the substrate, with each other, and with the external environment—are also dynamic. One system that particularly illustrates the importance of adsorbate-substrate interactions is the attachment of photoactive molecules to oxide surfaces in dye-sensitized solar cells (DSSCs).

Efficient DSSCs were developed by Grätzel and coworkers in the 1990s [4-6] and have reached efficiencies in excess of 12% [7], narrowing the performance gap between DSSCs and thin-film solar technologies. The archetypal DSSC consists of a high surface area nanoporous anatase TiO_2 substrate that serves as a photoanode and a scaffold for the adsorption of a monolayer of dye molecules. A dye molecule, after absorbing a photon which generates an electron-hole pair, injects the excited electron into the TiO_2 conduction band where it then diffuses to the front contact, typically the transparent conductor fluorine-doped tin oxide (FTO). The oxidized dye is regenerated by a hole-transport material (HTM) which then conveys the hole to a back electrode (typically a metal). In the original DSSC design [5], the HTM was an acetonitrile-based iodide/triiodide redox couple, but it can also be a cobalt redox complex (as in the efficiency record device [7]) or a solid-state conductor (organic or inorganic) [8, 9], which has practical benefits over liquid-based HTMs. A primary advantage of DSSCs is their highly modular design: departures from the archetypal cell have been the subject of considerable research over the past two decades including modifications of the photoanode (in both material and structure), HTM, and, most frequently, the dye itself. The original class of high-performing DSSC dyes were ruthenium-based organometallic compounds [4] but recently, all-organic "donor-π-acceptor" (D-π-A) dyes have become popular due to their greater design flexibility, ease of synthesis, low-toxicity, low-cost, and high molar extinction coefficients [4]. For example, D-π-A dyes were used to obtain the current device efficiency records in both liquid (co-adsorbed with a porphyrin dye) [7] and organic solid-state [10] devices.

In addition to the energy of a dye's highest occupied molecular orbital (HOMO) and lowest unoccupied molecular orbital (LUMO) levels, which dictate light absorption onset and the ability both to inject electrons into the photoanode (LUMO) and to be regenerated by the HTM (HOMO), an important determinant of DSSC performance is the dye's molecular structure and orientation when adsorbed on the TiO_2 surface. Dye molecules are designed to have HOMO and LUMO states that are spatially separated such that in an adsorbed dye the LUMO is localized near the TiO_2 surface (for rapid electron injection) and the HOMO is localized away from the surface (to minimize recombination and facilitate regeneration). The separation of the HOMO (or "donor") and LUMO (or "acceptor") by a conjugated backbone is the origin of the "D-π-A" name for the class of dyes studied here. This D-π-A design consideration typically results in a strong molecular dipole with negative charge localized near the acceptor region. When this dipole, bookended by the acceptor and donor regions of the dye, is directed outward from the surface (such as when the dye is adsorbed in an upright configuration), it has the effect of raising the TiO_2 conduction band (relative to the vacuum level), which in turn increases the open-circuit voltage (V_{OC}) of the device [11-14]. In addition to dipole contributions, the orientation of the dye molecule affects the availability of TiO_2 surface sites (for dye binding) and dye packing, both of which are important determinants of dye surface coverage (which in turn affects short-circuit current, J_{SC}). Dye orientation and coverage also dictate how much TiO_2 surface may be exposed and accessible to the HTM; close contact between the HTM and TiO_2 can accelerate back-recombination, reducing V_{OC} [15]. Back-recombination (in this case to the oxidized dye) can also be accelerated through proximity of the TiO_2 to the dye HOMO (donor) which again is a function of dye orientation [16].

Starting with ruthenium-based dyes, there have been numerous efforts to understand dye geometry and binding coordination [17, 18]. Typical ruthenium dyes bind to TiO_2 through 1-2 bi-isonicotinic acid ligands (each with two carboxylic groups) involving anywhere from 1-4 carboxylic acid groups in direct bonds to the surface. Infrared spectroscopy has proven useful in determining both the number of carboxylic acid groups involved in dye attachment as well as the bonding coordination [18]. Density functional theory (DFT) studies have complemented these experimental results, enabling

calculation of the energies of various proposed structures, examining possible dye geometries given different binding modes, and linking experimental results to observed differences in device performance [19-21]. Analogous studies linking computational and device results using D-π-A dyes (and other dye varieties) have also been reported [11-13]. The experimental assessments of dye binding using infrared spectroscopy and device performance metrics, however, do not explicitly measure dye orientation itself, necessitating more specialized techniques to truly link computational and experimental results with respect to orientation.

One technique particularly well-suited for studying the orientation of adsorbed molecules is angle-resolved near-edge X-ray absorption fine structure (NEXAFS) spectroscopy [22, 23]. NEXAFS, a subset of X-ray absorption spectroscopy (XAS) that examines energies near the ionization edge of core electrons in light elements, probes transitions between core levels and unoccupied molecular orbitals. The signal intensity in NEXAFS is a function of the overlap of the electric field component of the polarized, incident radiation and the spatial orientation of the empty orbitals. Performing the NEXAFS measurement at various incident X-ray angles therefore enables the determination of the orientation of different unoccupied orbitals and, in some cases, the molecule itself [22]. While the octahedral coordination and lack of linear symmetry in ruthenium-based dyes prevents easy analysis using NEXAFS, many studies have been reported on bi-isonicotinic acid, the pyridine-based ligand which plays a critical role in ruthenium dye attachment [24-27]. These studies have examined both the orientation of adsorbed bi-isonicotinic acid as well as its charge-transfer states supported by theoretical simulations. Porphyrins, another promising class of dye molecules, exhibit a planar backbone with a well-defined π* and σ* geometry that renders straightforward NEXAFS angular alignment analysis possible, as Rangan *et al.* and González-Moreno *et al.* recently reported [28, 29].

D-π-A dyes, typically containing a single carboxylic group and a conjugated backbone that results in a mostly-planar structure, are also attractive targets for orientation studies using NEXAFS. Yu *et al.* employed NEXAFS to study a simple 2-cyanoacrylic acid (CAA)-based D-π-A dye adsorbed under ultrahigh vacuum onto rutile

TiO_2 (110) and observed that the dye had a mostly-upright orientation on the substrate [30]. The features of the nitrogen K-edge X-ray absorption spectra that they observed were consistent with work on CAA-based D-π-A dyes by Rensmo and coworkers, which while employing NEXAFS, did not use this technique for dye orientation analysis as the dyes were adsorbed onto a nanocrystalline TiO_2 film [31-33]. They did, however, compare intensity differences in X-ray photoelectron spectroscopy (XPS) data of the CAA nitrogen atom and a nitrogen atom located in the dyes' donor regions to deduce, based on different escape depths, that the dyes were oriented in an upright manner, consistent with the results of Yu *et al.*

While combined experimental and theoretical studies of model compounds such as bi-isonicotinic acid are abundant in the literature [24, 27], there is a lack of studies that bridge the experimental and theoretical results for complete dye molecules. In the current study, we have used angle-resolved nitrogen K-edge NEXAFS to experimentally measure the orientation of WN1 [34, 35], a CAA-based D-π-A dye, adsorbed on TiO_2. The WN1 dye was chosen as a model dye for this study due to its relatively high power conversion efficiency in solid-state DSSCs (4.9%) [35] and the fact that its structure (depicted in Figure 6-1a) is similar to most of the D-π-A dyes studied with NEXAFS [30-32] and several other high-performing dyes (*e.g.* Y123 [10], C218 [36]), in that it has a CAA-based acceptor group which binds to the TiO_2 surface and a triphenylamine (TPA)-based donor group. In order to closely mimic the preparation and structure of the TiO_2-dye system in a working DSSC, atomic layer deposition (ALD) was used to grow a polycrystalline anatase film upon which the dye was adsorbed from solution. The NEXAFS results were compared to DFT simulations, including DFT molecular dynamics (DFT-MD), of an anatase (101) TiO_2-dye slab. Assignment of transitions observed in the NEXAFS spectra was aided by DFT-based calculations [37] which identified energetically discrete transitions associated with the two different π systems of the C-N triple bond in CAA, enabling determination of the dye's tilt angle as well as the angle made by the C-N bond relative to the surface normal. The tilt angle of the dye was measured to be 63.0° from the surface—in excellent agreement with the 61.4° angle reported by Yu *et al.* for a similar, but smaller dye [30]—and the C-N bond 45.1° from the surface. Whereas a static geometry optimization of the TiO_2-dye system indicated a

less upright orientation of the dye—45.4° from the surface (with 51.2° for the C-N bond)—DFT-MD simulations at room temperature demonstrated remarkable agreement with the NEXAFS results—60.8° (tilt) and 44.6° (C-N)—indicating both the relevance of dynamics when evaluating computational results and the ability of DFT-MD to accurately predict dye behavior on TiO_2.

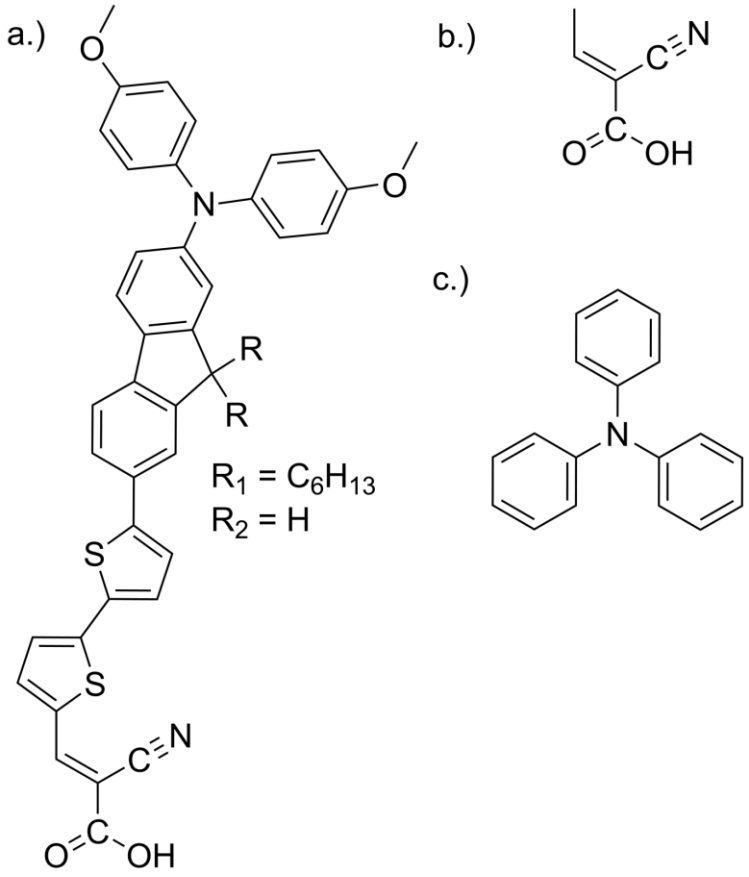


Figure 6-1: Structures of the relevant molecules in this study. a) WN1 dye molecule (R_1) and the reduced system used for DFT calculations (R_2). b) 2-Cyanoacrylic Acid (CAA) and c) Triphenylamine (TPA) reduced systems used to simulate X-ray absorption spectra.

6.2. Results & Discussion

6.2.1. Experimental and Simulated X-Ray Absorption Spectrum of WN1 Dye and Measured Orientation

In WN1, the CAA and the TPA group each contribute a single N atom, making nitrogen K-edge NEXAFS an attractive choice for WN1. The NEXAFS spectrum of the WN1 dye powder is shown in Figure 6-2. The powder spectrum had significant charging which can induce non-linear total electron yield (TEY) response across resonances with varying intensities and over an extended energy range—*e.g.* the π* to σ* relative intensities can be sensitive to background treatment. Here we show a short energy range, 397-412 eV, over which we have applied a simple linear background subtraction. We observed three narrow peaks in the low energy π* region (at approximately 398.2, 399.4, and 400.5 eV, in general agreement with those previously reported [30-32]) and a single broad peak in the σ* region. In order to better understand the origin of these observed peaks, we performed theoretical X-ray absorption simulations of N1s excitations in CAA (Figure 6-1b) and TPA (Figure 6-1c) models using the cluster-based DFT code StoBe [37], generating *Kohn-Sham* orbitals and associated transition amplitudes [37]. The theoretical spectrum for each structure is compared to the dye spectrum in Figure 6-2.

We note in particular the close correspondence in the relative energies and intensities of the first two π* peaks which arise solely from the CAA group, while the third π* is shifted approximately 0.3 eV relative to the experimental spectrum. Investigation of the orbitals corresponding to these first two peaks yields an interesting result, also observed by Hahlin *et al.* [32], that the lower energy peak (π_1^*) corresponds to a transition to an orbital that is perpendicular to the plane of the CAA group (Figure 6-3b) whereas the second peak (π_2^*) involves a transition to the π* orbital located in the CAA plane. The fact that these two π* systems have energetically distinct transitions means that the orientation of each orbital can be independently determined with angle-resolved NEXAFS, a unique aspect of this experimental approach.

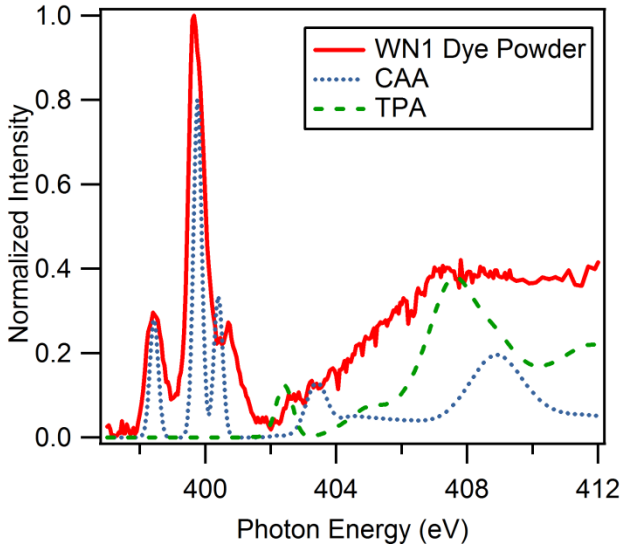


Figure 6-2: Experimental NEXAFS spectrum of the WN1 dye powder compared to the theoretical X-ray absorption spectra for the 2-cyanoacrylic acid (CAA) and triphenylamine (TPA) substructures. The WN1 powder spectrum was normalized to 1.0 and the theoretical spectra to 0.8 for clarity. The theoretical spectra were shifted 0.3 eV to higher energy to match the first transition in the experimental spectrum. The first two peaks of the WN1 and CAA spectra, which show excellent agreement in relative energy and intensity, correspond to transitions into π* orbitals.

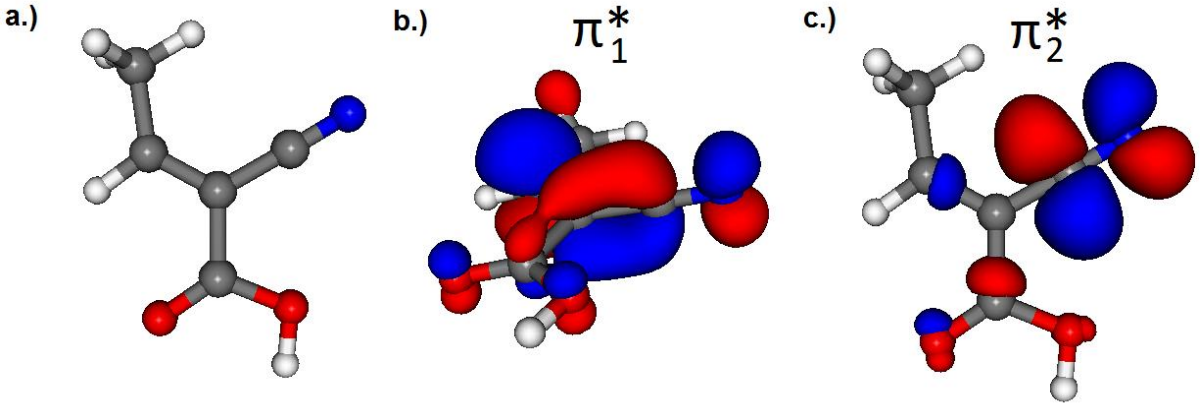


Figure 6-3: a) 3-D structure of the highly-planar 2-cyanoacrylic acid (CAA). b) π^*_1 orbital corresponding to the lowest energy peak of Figure 6-2. This orbital is located out of the plane of CAA, which is rotated here relative to a) for clarity. c) π^*_2 orbital corresponding to the second lowest energy peak in Figure 6-2. This orbital is located in the plane of CAA. An optimized geometry for CAA was obtained using a B3LYP hybrid functional and the orbitals, drawn using an isovalue of 0.05 in the Molekel software program [38], were calculated using the StoBe software [37] with BP86 functional.

For the angle-resolved NEXAFS, spectra were collected at five different incident X-ray angles (relative to the substrate plane) and different angle dependencies were clearly apparent for the π_1^* and π_2^* peaks (Figure 6-4a). Following Stohr and Outka [22], we use the equations describing transitions to an orbital defined by a vector on an isotropic surface (as in the case of the polycrystalline TiO_2 used here), where intensity is defined as follows [23]:

$$Intensity\ \alpha\ \frac{P}{3}\left\{1+\frac{1}{2}(3\cos^2\theta-1)(3\cos^2\Psi-1)\right\}+\frac{1-P}{2}\sin^2\Psi \qquad (6.1)$$

The measured intensity is a function of the polarization of the X-ray source, *P*, the incident X-ray angle relative to the surface plane, θ, and the angle of the orbital's characteristic vector relative to the surface normal, Ψ. The spectra for each angle were fit to the sum of five Gaussian peaks and an arc-tangent function describing the ionization step edge (Figure 6-4b) [23]. The peak intensities for π_1^* and π_2^* (the two lowest energy peaks in Figure 6-4b) at the five different incident X-ray angles were then fit to Eq. (6.1 (Figure 6-4c), indicating orbital angles of 63.0° and 45.1° relative to the surface normal for π_1^* and π_2^*, respectively. The definition of these orbital angles, denoted Ψ_1 and Ψ_2 (in correspondence to π_1^* and π_2^*), are visualized in Figure 6-5. Since the planar CAA group effectively dictates the orientation of the conjugated backbone and donor region of the dye, Ψ_1 can be thought of as the tilt angle of the molecule. Because the π_1^* orbital is perpendicular to the dye and is defined relative to the surface normal, Ψ_1 indicates the angle between the surface and the dye backbone. A value of 63.0° for Ψ_1 therefore implies a mostly-upright orientation of the dye, in excellent agreement with the 61.4° tilt angle reported by Yu *et al.* for a TPA- and CAA-based D-π-A dye [30]. Ψ_2 indicates the angle between the surface normal and the line perpendicular to the C-N bond, in the plane of the CAA group; the 45.1° value for Ψ_2 is also therefore the angle between the surface and the C-N bond.

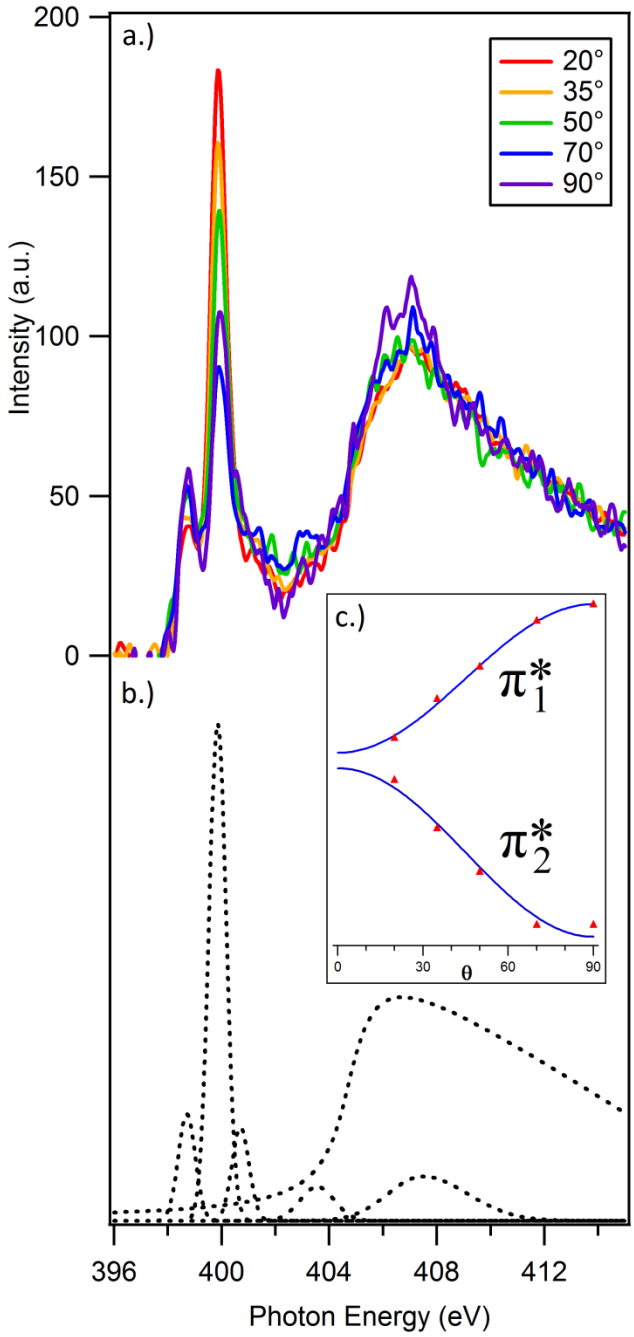


Figure 6-4: a) Nitrogen K-edge NEXAFS spectra for a representative sample of the WN1 dye adsorbed on TiO_2 at five different incident X-ray angles (relative to the substrate surface plane). The lowest energy peak, π_1^*, increases in intensity as the incident angle is increased whereas the opposite trend is observed for the next lowest energy peak, π_2^*. b) Peaks used to fit the angle-resolved NEXAFS spectra (in this instance, the 20° spectrum), including five Gaussians and an arctangent function used for the ionization step-edge. c) Intensities from the Gaussian fitting of the raw data (red) versus the fitted NEXAFS equation result (Eq. (3.3))) for the π_1^* and π_2^* peaks, which yielded angles of 63.0° and 45.1°, respectively.

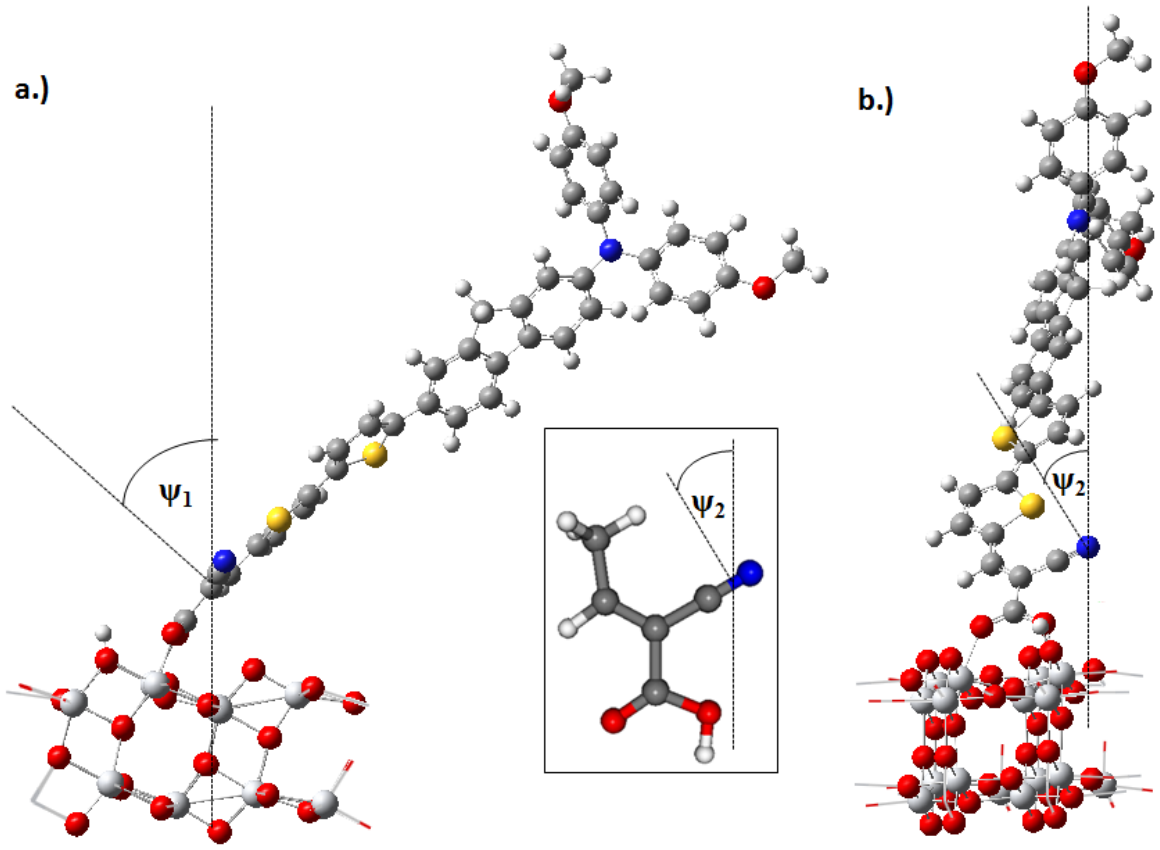


Figure 6-5: Two views of the DFT-optimized ground state of the reduced WN1 system. In a), the angle associated with the π_1^* orbital (Ψ_1) is shown. Ψ_1 dictates the tilt angle of the dye molecule and is calculated at 45.4° in the ground state DFT. b) shows an approximate view of the angle associated with the π_2^* orbital (Ψ_2) which defines the angle of the C-N bond relative to the surface normal. Ψ_2 is found to be 51.2° from the DFT. For clarity, the inset shows the Ψ_2 angle in the simpler case where the cyanoacrylic acid group is completely upright (*i.e.* Ψ_1 = 90°); a low value for the Ψ_2 angle therefore would indicate the C-N bond is roughly parallel to the surface. Computational Analysis of WN1 Dye Orientation

To confirm the dye orientation determined by NEXAFS, we performed DFT calculations on TiO_2-WN1 surface systems by focusing on two bonding configurations where the COOH hydrogen has been transferred from the dye to the surface, since this surface protonation is preferred for dyes with carboxylic acid functional groups [39], such as WN1. The configurations are identified in Figure 6-6a. Namely, we focused on a binding configuration **1** where the dye is bound to the surface via two Ti-O bonds, leaving a cyano (CN) group available for hydrogen bonding with a surface OH species.

In binding configuration **2** the dye is bound to the surface via Ti-O and Ti-N bonds leaving a CO group available for hydrogen bonding (see Figure 6-6b). Note that the configuration **1** is the "bridging bidentate" coordination described in several experimental and computational studies with bi-isonicotinic acid (in ruthenium dyes) [17, 27, 40] and CAA (in D-π-A dyes) [11, 30, 41, 42], whereas configuration 2 corresponds to a "tridentate" coordination that has been recently reported to be energetically favored over bridging bidentate configurations [43].

Computational models for the DFT calculations were generated by placing the WN1 dye on the TiO_2 surface with a density of 1.33 molecules/nm^2, in the range of typical dye densities of 1-2 molecules/nm^2 (see for instance Ref. [44] and references therein) and with a tilt angle similar to the one suggested by NEXAFS. This was followed by allowing both the unit cell and the atomic positions to fully relax by PBE0 optimizations, giving access to relative energies for the two configurations. We determined the relative energies also for a WN1 model truncated after the thiophene rings (Table 6-1) to estimate the effect of dye model size on the energetics.

The two binding configurations for the non-truncated dyes are calculated to be nearly equal energetically, with binding configuration **1** favored by only 0.9 kcal/mol at 0 K. In contrast, configuration **2** is calculated to be energetically favored over **1** by 5.6 kcal/mol for the truncated dye models. This finding is in agreement with the study by Jiao *et al*. [43] where binding configuration **2** was shown to be energetically favored over **1** by using a truncated dye model. Hence, our calculations demonstrate that the energetics are a function of the size of the dye modeled and highlight the importance of adopting sufficiently large dye models in the computational investigation of dye binding on TiO_2.

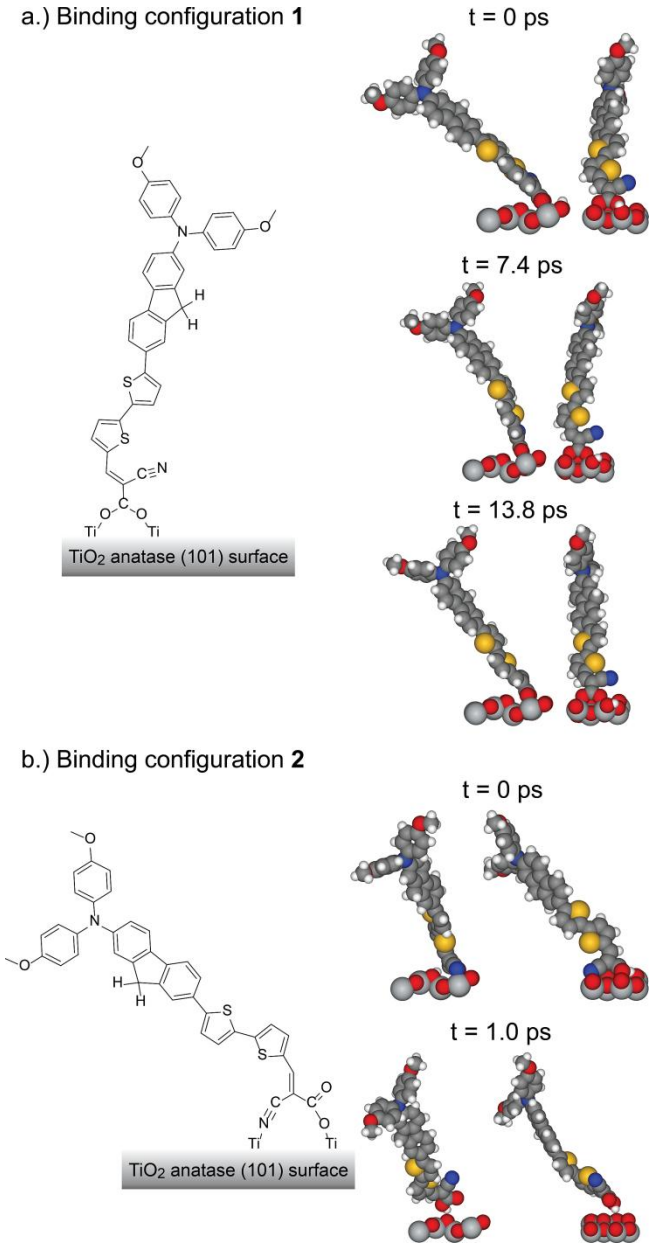
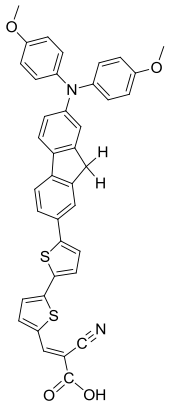
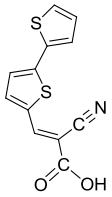


Figure 6-6: Schematic structures and snapshots from the DFT-MD simulations (T = 300 K, side and front views at indicated times) for the binding configurations a) 1 with the dye bonding to the surface via two Ti-O bonds and b) 2 with the dye bonding to the surface via both Ti-O and Ti-N bonds. No periodic images of the unit cell and only the outermost atomic layers of the TiO_2 surface are shown in the snapshots for clarity. A video of the full DFT-MD simulation of binding configuration 1, is available as a digital supplementary file to this thesis.

Table 6-1: Energies of the investigated TiO_2-WN1systems in binding configurations 1 and 2 for the WN1 without the C_6H_{13} alkyl chains and the WN1 truncated after the thiophene rings. The energies in kcal/mol are given relative to the binding configuration 2 structures.

WN1 Dye structure	Binding configuration 1	Binding configuration 2
WN1 without alkyl chains 	- 0.9	0.0
Truncated WN1 	5.6	0.0

In addition to the PBE0 optimizations, DFT-MD simulations, which are becoming feasible for systems of considerable size, were performed on both binding configurations to estimate their dynamic stability at room temperature. The DFT-MD simulation results demonstrate binding configuration **1** to be stable at room temperature, whereas system **2** is unstable and undergoes significant distortion by becoming bound to the surface only via hydrogen bonding (see snapshots of the simulations in **Error! Reference source not found.**; a video of the entire simulation trajectory is available as a digital supplementary file). System **1** remains stable for the simulation time of 15 ps, whereas the system **2** undergoes distortion into the hydrogen bonded orientation in less than 1 ps. These results can be explained by structural and steric factors originating from the orientation of the WN1 backbone relative to the reactive group of the molecule: in binding configuration **1** the dye adopts an orientation close to its ground state structure and covers the TiO_2 surface efficiently due to the close to linear alignment of the reactive carboxylic group

and the backbone of the dye (see Figure 6-6a). This is not feasible for the binding configuration **2** due to non-linear alignment between the reactive group and the backbone of the dye, resulting in stronger steric repulsion between the dye molecules as compared to configuration **1**. The repulsion causes the dye to adopt a distorted structure on the surface and destabilizes configuration **2** as compared to configuration **1** at the investigated dye surface coverage of 1.33 molecules/nm^2. Thus, the DFT-MD simulations demonstrate the importance of taking dynamics into account in the investigation of TiO_2-dye systems, and suggest the bridging bidentate configuration **1** to be relevant for the WN1 dye.

For direct comparison between the DFT-MD and the NEXAFS results on the dye orientation, we analyzed the evolution of Ψ_1 and Ψ_2 over time from the trajectory of the 15 ps DFT-MD simulation on the TiO_2-WN1 system in binding configuration **1** (see Materials & Methods section for details), and the results, together with the convergence of the Ψ_1 and Ψ_2 angles as a function of simulation length, are illustrated in Figure 6-7b. The evolution of the angles demonstrates the extent of structural fluctuation the dye undergoes at room temperature, with the Ψ_1 angle varying between nearly 30° and 90° (see also Figure 6-6), and Ψ_2 between about 20° and 70°. Whereas the PBE0 optimized ground-state geometry of TiO_2-WN1 indicates a lower tilt angle with Ψ_1 and Ψ_2 values of 45.4° and 51.2°, respectively, averaging the data shown in Figure 6-7a gives Ψ_1 and Ψ_2 values of 60.8° and 44.6°, respectively, in remarkable agreement with the NEXAFS angles of 63.0° and 45.1°, providing strong support for this orientation of the WN1 dye on TiO_2. For further verification, we simulated the angular intensity variation that would be apparent in NEXAFS by applying Eq. (6.1) to all dye orientations produced by the 15 ps DFT-MD simulation. Fitting this time-averaged intensity variation yielded only slightly different angles of Ψ_1 = 59.0° and Ψ_2 = 44.8°. Overall, our DFT-MD results corroborate the NEXAFS results on the dye surface orientation and highlight the importance of taking dynamics into account in the computational investigation of dye behavior and behavior of other large molecules on TiO_2 surfaces. The relevant computational and experimental values for Ψ_1 and Ψ_2 are tabulated in Table 6-2.

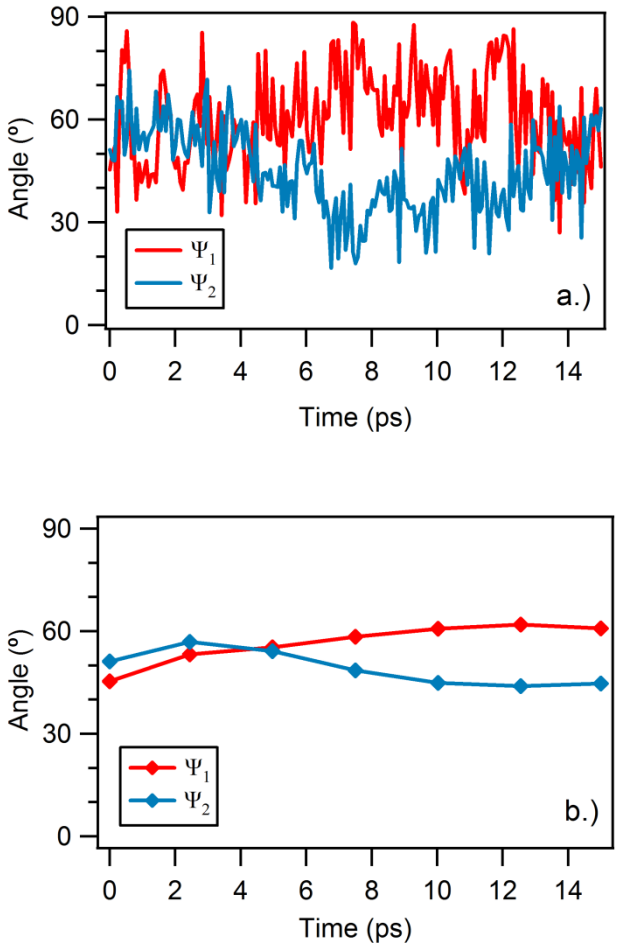


Figure 6-7: a) Ψ_1 and Ψ_2 angles over time determined from atomic coordinates for all dye orientations produced by the 15 ps DFT-MD simulation (T = 300 K) on the TiO_2-WN1 system in binding configuration *1* with the dye binding to the surface via two Ti-O bonds. b) Cumulative average Ψ_1 and Ψ_2 angles from the DFT-MD simulation (*i.e.* averaged from time 0 to time *t*) as a function of simulation length.

6.2.2. Implications for DFT Simulations as a Predictive Tool for Device Performance

The close correspondence between the orientation of WN1 measured by NEXAFS and the time-averaged orientation in the DFT-MD demonstrates the enormous potential of DFT-MD as a predictive tool for alignment of dyes on TiO_2 in particular, and alignment of large molecular systems on oxide surfaces in general. While the ground-state orientation predicted by DFT is not irreconcilably different than the NEXAFS and DFT-MD results, the tilt angle (Ψ_1) difference of approximately 15° does have important implications for understanding the effect of the dye's orientation on device properties.

The change in the dye's effective dipole offers perhaps the clearest illustration of why these orientation differences are relevant. The dipole in a D-π-A dye points in the general direction of acceptor-to-donor and it is the component of this dipole normal to the surface that can raise the TiO_2 conduction band and increase the device V_{OC}. The normal component is a function of the total dipole moment times *cos* ω, where ω is the angle between the total dipole moment and the surface normal [11]. Using the dye tilt angle to approximate the dipole moment directionality—*i.e.* $\omega = 90° - \Psi_1$—we estimate that the higher tilt angles calculated from NEXAFS and DFT-MD result in a normal dipole component 19-25% larger than that predicted from the ground-state DFT orientation. For verification, we determined the dipoles for the optimized structure (initial structure in the DFT-MD simulation), and for a structure corresponding to a high tilt angle in the DFT-MD simulation at a simulation time of about 7.4 ps by PBE0 calculations (see Figures 6 and 7). Resulting dipoles of 3.5 D for the optimized structure and 4.3 D for the high tilt angle structure indicate an increase of 23%, in agreement with the 19-25% change estimated when approximating dipole strength using Ψ_1. As differences in dye dipoles can lead to V_{OC} variations on the order of hundreds of mVs, a 20% change in dipole strength is a significant deviation when comparing dyes and understanding changes in V_{OC} [11, 15]. Heretofore, the use of DFT-MD to study TiO_2-dye systems has been limited due to computational costs [20, 43], but we anticipate that the ability of DFT-MD, as demonstrated in this work, to accurately describe dye orientation warrants further investigations and will lead to improved understanding of device performance and screening of potential dye chemistries. Furthermore, with increasing computational power and advances in both theoretical methods and computational codes, *ab initio* simulation of surface-adsorbent systems of increasing complexity will become feasible. Utilization of advanced DFT functionals or higher level methods that avoid some of the well-known DFT limitations [45, 46] will enable more accurate simulations to be performed.

Table 6-2: Compilation of the two angles calculated from NEXAFS, DFT optimization, and DFT-MD.

Angle	NEXAFS	DFT	DFT-MD[a]	DFT-MD[b]
Ψ_1	63.0°	45.4°	60.8°	59.0°
Ψ_2	45.1°	51.2°	44.6°	44.8°

[a]: value determined by averaging the angle at each time step in the DFT-MD simulation. [b]: value determined by using the NEXAFS equation (Eq. (3.3)) to calculate an intensity at each time point for the five different incident X-ray angles scanned in the NEXAFS experiments, averaging these intensities, and fitting them using the Eq. (3.3). This is the angle that NEXAFS would "see" given the dye fluctuations shown in Figure 6-7.

6.3. Conclusions

Angle-resolved NEXAFS was performed to measure the orientation of a triphenylamine and cyanoacrylic acid-based D-π-A dye, WN1, adsorbed onto anatase TiO_2. NEXAFS indicated that the C-N bond is oriented approximately 45° from the surface and the tilt angle of the dye is approximately 63° from the surface plane, consistent with the upright orientation observed elsewhere for similar dyes. DFT calculations have been performed to confirm the NEXAFS results on dye orientation on TiO_2. DFT-MD simulations demonstrate the importance of taking dynamics into account in the investigation of dye-TiO_2 binding and provide evidence for the WN1 dye to bond to the surface in a bidentate bridging coordination at typical dye surface densities of about 1.3 molecules/nm^2. Furthermore, the dye orientation predicted by DFT-MD is in excellent agreement with NEXAFS results, providing strong support for the dye orientation reported herein. The less-upright orientation indicated by standard DFT optimization demonstrates an important advantage offered by DFT-MD to better predict and understand dye behavior in a device context. More generally, the coupled NEXAFS/DFT-MD approach described here demonstrates a powerful tool set for understanding the dynamics of adsorbate/substrate alignment with a broad applicability in many scientific fields.

6.4. Materials & Methods

6.4.1. Fabrication of TiO_2-Dye Substrates

Atomic layer deposition (ALD) was used to deposit TiO_2 on a piranha-cleaned Si substrate. Films were grown at 100 °C using titanium (IV) tetrachloride and H_2O as

precursors, and then annealed at 600 °C for ten hours under N_2 in order to yield polycrystalline anatase films with a preferred [101] orientation [47]. No effect of varying the film thickness between 5 and 10 nm was observed. Dye adsorption was performed in the same fashion as in typical DSSCs: after heating the TiO_2 substrates for 30 min at 500 °C in order to remove any H_2O, the substrates were left to cool to 80 °C and then immersed in a 0.1 mM solution of WN1, synthesized as described elsewhere [35], in 1:1 *tert*-butanol:acetonitrile. A short dip time of 3 hours was used to prevent dye aggregation after which the substrates were removed from the dye solutions and rinsed in acetonitrile and dried before promptly being loaded into the NEXAFS chamber.

6.4.2. NEXAFS Measurements and Spectra-Fitting

In NEXAFS, incident polarized, monochromated X-rays (from a synchrotron radiation source) generate transitions of electrons from core atomic orbitals into unoccupied molecular orbitals; the transition is detected when the excited electron decays via Auger or radiative process. The transition probability is determined by the overlap integral of the core atomic orbital and the unoccupied orbital via the dipole operator (determined by the electric-field component of the polarized X-rays). For orbitals with simple symmetries, such as a 1s core orbital and a 2p-derived unoccupied orbital (π and σ), the overlap integral greatly simplifies to a function of the electric field vector orientation relative to the high symmetry axis of the unoccupied π (or σ) orbitals [23], where a strong signal is detected when the X-ray's electric field vector is closely aligned with the axis having the largest amplitude of a given empty σ or π bonding (or antibonding) orbital.

Nitrogen K-edge NEXAFS was measured at Stanford Synchrotron Radiation Lightsource (SSRL) bending magnet beamline 8-2 [48], equipped with a spherical grating monochromator operated at a photon energy resolution of about 0.2 eV and a beam spot size of about 1x1 mm at the sample position. The incoming photon flux was recorded from a freshly evaporated gold mesh upstream of the analysis chamber. The degree of linear p-polarization was assumed to be around 0.85. All samples were mounted onto an aluminum stick, isolated from ground, attached with carbon tape. The powder samples were applied directly to the carbon tape prior to loading. Total electron yield (TEY) was

measured as the sample drain current, where background levels from scattered ions and electrons from the analysis chamber ion pump was subtracted prior to normalization. All measurements were performed at better than 10^{-8} torr at room temperature. The energy scale is referenced to the reported π^* resonance of bi-isonicotinic acid [24] that was measured in the same run. No beam-damage was observed for consecutive scans at the same sample position. A linear background was subtracted from the spectra and aligned at 415 eV (this shorter energy range was selected to reduce the effect of uncertainties in the background variation). The powder spectrum in Fig 2 was recorded at BL 10-1 using the same type of detection (TEY and gold grid normalization), energy alignment (bi-isonicotinic acid) and photon energy resolution (~0.2 eV).

Spectra were collected at five different incident X-ray angles (20°, 35°, 50°, 70°, 90°, relative to the substrate surface plane) at three sample spots. Each spectrum was fit [49] using four symmetric Gaussian peaks (centered at 398.7, 399.85, 400.7, and 403.55 eV, with full-width half maxima (FWHM) of 0.75, 0.75, 0.75, and 1.5 eV, respectively), one asymmetric Gaussian peak (at 407.45 eV and FWHMs of 3 and 4 eV), and one arctangent function with a step-edge at 404.8 eV, FWHM of 2.5 eV [23]. The normalized, fitted intensities for the two low-energy peaks (π_1^* and π_2^*) at each incident angle were then averaged across all three sample spots and fitted to Eq. (3.2)) with a value of 0.85 for *P*, the light source polarization, using a least-squares method to calculate the orbital angles Ψ_1 and Ψ_2. These values, 63.0° (Ψ_1) and 45.1° (Ψ_2), were virtually identical to those determined by averaging the fits to Eq. (3.2)) for each sample spot, 63.0°±2.4° and 45.0°±2.5°, respectively, indicating little variance across the samples.

6.4.3. Computational Details

Gaussian 09 [50] was used to obtain optimized geometries of the 2-cyanoacrylic acid (CAA) and triphenylamine (TPA) dye substructures at the B3LYP/6-31G* level of theory. The StoBe software [37] was then used to calculate a discrete nitrogen K-edge X-ray absorption spectrum using a similar method to Rensmo and coworkers [31, 32]. A half-core-hole (on the N atom) method [51] was used with an IGLO-III basis set [52] for N atoms, (311/1) for H, (521/41) for C, and (631/31/1) for O along with the auxiliary

basis sets (5,2;5,2) for N, C and O, and (3,1;3,1) for H. The energy values of the generated spectra were then adjusted using a ΔKohn-Sham correction, setting the first transition energy to the energy difference between the lowest core-hole excited state and the ground state of the molecule, and then adding 0.3 eV to account for relativistic effects [53]. After the relativistic correction, a small discrepancy of 0.3 eV in absolute energy of the first π* peak (at 398.7 eV in the experimental spectrum) was found between the theory and the experiment, which is well within the expected errors in energy from functional dependence, incompleteness in basis sets, as well as experimental energy calibration [53]. The theoretical spectrum was manually shifted to higher energy by this remaining 0.3 eV absolute energy discrepancy in Figure 6-2 to align the first resonance. The spectra shown in Figure 6-2 were generated by using the corresponding discrete spectra to construct Gaussian peaks with FWHM of 0.3 eV at energies below 400 eV with the FWHM linearly increasing from 0.3 eV to 4.5 eV as the energy increased from 400 to 430 eV [54]. The images of the excited states shown in Figure 6-3 were generated using the Molekel software based on the StoBe Kohn-Sham orbital output [38].

Periodic density functional (DFT) calculations of WN1 dye bound on anatase TiO_2 (101) slab were carried out by CRYSTAL09 [55] and Vienna Ab initio Simulation Program (VASP) [56, 57] codes. Full structural optimizations of the TiO_2-dye slabs were performed by CRYSTAL09 using PBE0 [58, 59] hybrid functional and all-electron def2-SVP basis [60, 61] for H, C, N, O, and S. A modified basis set was necessary for Ti to avoid diffuse functions that are not desirable in periodic calculations and often give rise to numerical difficulties and degradations of performance. Accordingly, a 86-51G* basis, which has previously been utilized for TiO_2 (110) and (101) surfaces [62], was adopted for Ti. To investigate the dynamic stability of the TiO_2-WN1 slabs at room temperature, DFT molecular dynamics (DFT-MD) simulations on the TiO_2-dye slabs were performed by VASP. A PBE [58] functional coupled with standard versions of the projector augmented wave (PAW) pseudopotentials for all atoms [63], as implemented in VASP, was used in the simulations. The DFT-MD was performed using Γ point k-sampling, an energy cutoff value of 350 eV, Nosé thermostat, and default accuracy parameters for fast Fourier transform (FFT) grid and real space projectors (PREC=NORMAL in VASP input). This computational approach, together with a

simulation time step of 1.5 fs, enabled well-behaved simulations 15 ps in length to be performed, and a control simulation of 5 ps in length with a time step of 1 fs provided angles and total energies in agreement with those from the simulation with a time step of 1.5 fs (Figure 6-8). The DFT-MD was performed on workstations with 2.66 GHz Intel Xeon X5650 12-CPU core processors and 72 GB RAM per node, and the runtime for the 15 ps simulation using 12 CPUs was about 17 days. In the determination of the Ψ_1 and Ψ_2 angles from the 15 ps simulation trajectory, the convergence of the angles was verified by restarting the simulation from the last structure in the trajectory and simulating it for an additional 15 ps. Averaging the Ψ_1 and Ψ_2 angles over the structures produced by both 15 ps simulations provided angles that deviated at most only 1.8^{o} from the ones produced by the first 15 ps simulation, demonstrating the angle convergence. The anatase (101) surface was simulated by a periodic 2x2 slab model having a thickness of 12 atomic layers and a unit cell stoichiometry of $Ti_{16}O_{32}$. Notably, structurally analogous surface models have been utilized in a number of works focusing on the interaction between TiO_2 and dye molecule (see for instance References [12], [43], and [64]). A slightly simplified model of the WN1 dye molecule, with only the two C_6H_{13} alkyl chains (see Figure 6-1) replaced by two hydrogen atoms, was utilized in the calculations for computational efficiency.

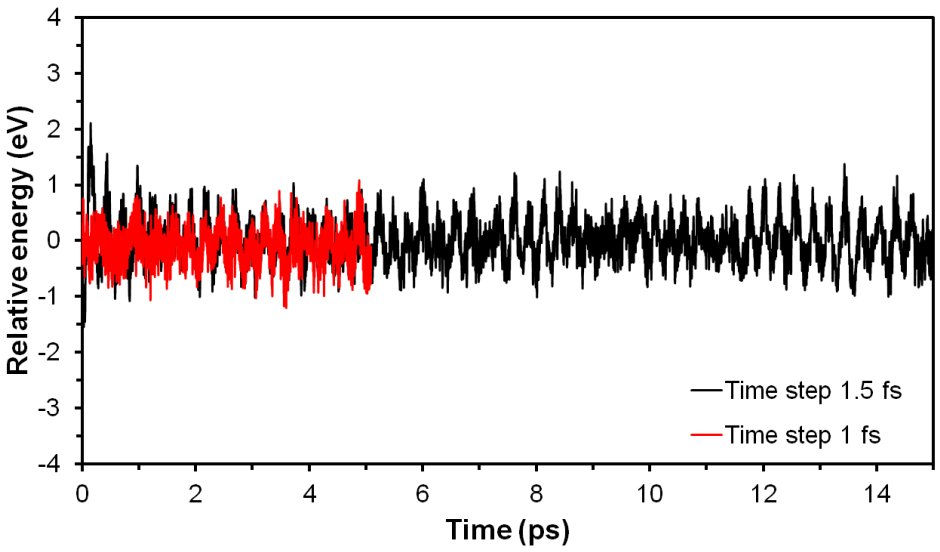


Figure 6-8: Total energies during the 15 ps DFT-MD simulation with a time step of 1.5 fs and during the 5 ps control simulation with a time step of 1 fs of the TiO_2-WN1 system in binding configuration 1. The total energies are given relative to the averaged total energy from the 15 ps simulation.

6.5. Collaborations & Copyrights

This chapter is adapted from a manuscript currently under peer review. Jukka Tanskanen performed the DFT and DFT-MD analysis, with the exception of the StoBe analysis, provided in this chapter. This work was part of a close collaboration with Jonathan Bakke. Michael Toney and Dennis Nordlund at SSRL helped develop this project and Dennis Nordlund assisted greatly with NEXAFS data collection and normalization. The beamtime was granted at SSRL under proposal #3338. The WN1 dye was synthesized by William Nguyen in the lab of Alan Sellinger and Michael McGehee. Han Bo-Ram Lee performed the TiO_2 ALD.

6.6. References

[1] A. Kolmakov, M. Moskovits, Annual Review of Materials Research 34/1 (2004) 151.
[2] O. Yildirim, P.J. de Veen, M.G. Maas, M.D. Nguyen, D.N. Reinhoudt, D.H.A. Blank, G. Rijnders, J. Huskens, Journal of Materials Chemistry 22/6 (2012) 2405.
[3] S. Onclin, B.J. Ravoo, D.N. Reinhoudt, Angewandte Chemie International Edition 44/39 (2005) 6282.
[4] A. Hagfeldt, G. Boschloo, L. Sun, L. Kloo, H. Pettersson, Chemical Reviews 110/11 (2010) 6595.
[5] B. O'Regan, M. Grätzel, Nature 353/6346 (1991) 737.
[6] B.E. Hardin, H.J. Snaith, M.D. McGehee, Nat Photon 6/3 (2012) 162.
[7] A. Yella, H.-W. Lee, H.N. Tsao, C. Yi, A.K. Chandiran, M.K. Nazeeruddin, E.W.-G. Diau, C.-Y. Yeh, S.M. Zakeeruddin, M. Grätzel, Science 334/6056 (2011) 629.
[8] U. Bach, D. Lupo, P. Comte, J.E. Moser, F. Weissortel, J. Salbeck, H. Spreitzer, M. Grätzel, Nature 395/6702 (1998) 583.
[9] K. Tennakone, G.R.R.A. Kumara, A.R. Kumarasinghe, K.G.U. Wijayantha, P.M. Sirimanne, Semiconductor Science and Technology 10/12 (1995) 1689.
[10] J. Burschka, A. Dualeh, F. Kessler, E. Baranoff, N.-L. Cevey-Ha, C. Yi, M.K. Nazeeruddin, M. Grätzel, Journal of the American Chemical Society 133/45 (2011) 18042.
[11] W.H. Howie, F. Claeyssens, H. Miura, L.M. Peter, Journal of the American Chemical Society 130/4 (2008) 1367.
[12] P. Chen, J.H. Yum, F.D. Angelis, E. Mosconi, S. Fantacci, S.-J. Moon, R.H. Baker, J. Ko, M.K. Nazeeruddin, M. Grätzel, Nano Letters 9/6 (2009) 2487.
[13] A. Dualeh, F. De Angelis, S. Fantacci, T. Moehl, C. Yi, F. Kessler, E. Baranoff, M.K. Nazeeruddin, M. Grätzel, The Journal of Physical Chemistry C 116/1 (2012) 1572.
[14] E. Ronca, M. Pastore, L. Belpassi, F. Tarantelli, F. De Angelis, Energy & Environmental Science 6/1 (2013) 183.
[15] T. Marinado, K. Nonomura, J. Nissfolk, M.K. Karlsson, D.P. Hagberg, L. Sun, S. Mori, A. Hagfeldt, Langmuir 26/4 (2009) 2592.

[16] M. Pastore, F. De Angelis, Physical Chemistry Chemical Physics 14/2 (2012) 920.
[17] K.S. Finnie, J.R. Bartlett, J.L. Woolfrey, Langmuir 14/10 (1998) 2744.
[18] M.K. Nazeeruddin, R. Humphry-Baker, P. Liska, M. Grätzel, The Journal of Physical Chemistry B 107/34 (2003) 8981.
[19] F. De Angelis, S. Fantacci, A. Selloni, M. Grätzel, M.K. Nazeeruddin, Nano Letters 7/10 (2007) 3189.
[20] F. De Angelis, S. Fantacci, A. Selloni, M.K. Nazeeruddin, M. Grätzel, The Journal of Physical Chemistry C 114/13 (2010) 6054.
[21] C. Anselmi, E. Mosconi, M. Pastore, E. Ronca, F. De Angelis, Physical Chemistry Chemical Physics 14/46 (2012) 15963.
[22] J. Stöhr, D.A. Outka, Physical Review B 36/15 (1987) 7891.
[23] J. Stöhr, NEXAFS Spectroscopy, Springer-Verlag, Berlin, 1992.
[24] L. Patthey, H. Rensmo, P. Persson, K. Westermark, L. Vayssieres, A. Stashans, A. Petersson, P.A. Bruhwiler, H. Siegbahn, S. Lunell, N. Martensson, The Journal of Chemical Physics 110/12 (1999) 5913.
[25] P. Persson, S. Lunell, P.A. Bruhwiler, J. Schnadt, S. Sodergren, J.N. O'Shea, O. Karis, H. Siegbahn, N. Martensson, M. Bassler, L. Patthey, The Journal of Chemical Physics 112/9 (2000) 3945.
[26] J. Schnadt, J. Schiessling, J.N. O'Shea, S.M. Gray, L. Patthey, M.K.J. Johansson, M. Shi, J. Krempaský, J. Åhlund, P.G. Karlsson, P. Persson, N. Mårtensson, P.A. Brühwiler, Surface Science 540/1 (2003) 39.
[27] A.G. Thomas, W.R. Flavell, C. Chatwin, S. Rayner, D. Tsoutsou, A.R. Kumarasinghe, D. Brete, T.K. Johal, S. Patel, J. Purton, Surface Science 592/1-3 (2005) 159.
[28] R.n. González-Moreno, P.L. Cook, I. Zegkinoglou, X. Liu, P.S. Johnson, W. Yang, R.E. Ruther, R.J. Hamers, R.n. Tena-Zaera, F.J. Himpsel, J.E. Ortega, C. Rogero, The Journal of Physical Chemistry C 115/37 (2011) 18195.
[29] S. Rangan, S. Coh, R.A. Bartynski, K.P. Chitre, E. Galoppini, C. Jaye, D. Fischer, The Journal of Physical Chemistry C 116/45 (2012) 23921.
[30] S. Yu, S. Ahmadi, M. Zuleta, H. Tian, K. Schulte, A. Pietzsch, F. Hennies, J. Weissenrieder, X. Yang, M. Göthelid, The Journal of Chemical Physics 133/22 (2010) 224704.
[31] E.M.J. Johansson, T. Edvinsson, M. Odelius, D.P. Hagberg, L. Sun, A. Hagfeldt, H. Siegbahn, H. Rensmo, The Journal of Physical Chemistry C 111/24 (2007) 8580.
[32] M. Hahlin, M. Odelius, M. Magnuson, E.M.J. Johansson, S. Plogmaker, D.P. Hagberg, L. Sun, H. Siegbahn, H. Rensmo, Physical Chemistry Chemical Physics 13/8 (2011) 3534.
[33] K.M. Karlsson, X. Jiang, S.K. Eriksson, E. Gabrielsson, H. Rensmo, A. Hagfeldt, L. Sun, Chemistry – A European Journal 17/23 (2011) 6415.
[34] T.P. Brennan, J.R. Bakke, I.K. Ding, B.E. Hardin, W.H. Nguyen, R. Mondal, C.D. Bailie, G.Y. Margulis, E.T. Hoke, A. Sellinger, M.D. McGehee, S.F. Bent, Physical Chemistry Chemical Physics 14/35 (2012) 12130.
[35] W.H. Nguyen, C.D. Bailie, J. Burschka, T. Moehl, M. Grätzel, M.D. McGehee, A. Sellinger, Chemistry of Materials 25/9 (2013) 1519.

[36] R. Li, J. Liu, N. Cai, M. Zhang, P. Wang, The Journal of Physical Chemistry B 114/13 (2010) 4461.
[37] K. Hermann, L.G.M. Pettersson, M.E. Casida, C. Daul, A. Goursot, A. Koester, E. Proynov, A. St-Amant, D.R. Salahub, V. Carravetta, H. Duarte, C. Friedrich, N. Godbout, J. Guan, C. Jamorski, M. Leboeuf, M. Leetmaa, M. Nyberg, S. Patchkovskii, L. Pedocchi, F. Sim, L. Triguero, A. Vela, 2011.
[38] U. Varetto, Swiss National Supercomputing Centre, Lugano, Switzerland, 2009.
[39] M. Pastore, S. Fantacci, F. De Angelis, The Journal of Physical Chemistry C 117/8 (2013) 3685.
[40] P. Persson, S. Lunell, Solar Energy Materials and Solar Cells 63/2 (2000) 139.
[41] K. Hara, T. Sato, R. Katoh, A. Furube, T. Yoshihara, M. Murai, M. Kurashige, S. Ito, A. Shinpo, S. Suga, H. Arakawa, Advanced Functional Materials 15/2 (2005) 246.
[42] C.-Y. Chen, M. Wang, J.-Y. Li, N. Pootrakulchote, L. Alibabaei, C.-h. Ngoc-le, J.-D. Decoppet, J.-H. Tsai, C. Grätzel, C.-G. Wu, S.M. Zakeeruddin, M. Grätzel, ACS Nano 3/10 (2009) 3103.
[43] Y. Jiao, F. Zhang, M. Grätzel, S. Meng, Advanced Functional Materials 23/4 (2013) 424.
[44] H.A. Harms, N. Tetreault, V. Gusak, B. Kasemo, M. Grätzel, Physical Chemistry Chemical Physics 14/25 (2012) 9037.
[45] S.N. Steinmann, C. Piemontesi, A. Delachat, C. Corminboeuf, Journal of Chemical Theory and Computation 8/5 (2012) 1629.
[46] K. Burke, L.O. Wagner, International Journal of Quantum Chemistry 113/2 (2013) 96.
[47] Q. Xie, J. Musschoot, D. Deduytsche, R.L. Van Meirhaeghe, C. Detavernier, S. Van den Berghe, Y.-L. Jiang, G.-P. Ru, B.-Z. Li, X.-P. Qu, Journal of The Electrochemical Society 155/9 (2008) H688.
[48] K.G. Tirsell, V.P. Karpenko, Nuclear Instruments and Methods in Physics Research Section A: Accelerators, Spectrometers, Detectors and Associated Equipment 291/1-2 (1990) 511.
[49] T. Ressler, Journal of Synchrotron Radiation 5/2 (1998) 118.
[50] M.J. Frisch, G.W. Trucks, H.B. Schlegel, G.E. Scuseria, M.A. Robb, J.R. Cheeseman, G. Scalmani, V. Barone, B. Mennucci, G.A. Petersson, H. Nakatsuji, M. Caricato, X. Li, H.P. Hratchian, A.F. Izmaylov, J. Bloino, G. Zheng, J.L. Sonnenberg, M. Hada, M. Ehara, K. Toyota, R. Fukuda, J. Hasegawa, M. Ishida, T. Nakajima, Y. Honda, O. Kitao, H. Nakai, T. Vreven, J. Montgomery, J. A., J.E. Peralta, F. Ogliaro, M. Bearpark, J.J. Heyd, E. Brothers, K.N. Kudin, V.N. Staroverov, R. Kobayashi, J. Normand, K. Raghavachari, A. Rendell, J.C. Burant, S.S. Iyengar, J. Tomasi, M. Cossi, N. Rega, J.M. Millam, M. Klene, J.E. Knox, J.B. Cross, V. Bakken, C. Adamo, J. Jaramillo, R. Gomperts, R.E. Stratmann, O. Yazyev, A.J. Austin, R. Cammi, C. Pomelli, J.W. Ochterski, R.L. Martin, K. Morokuma, V.G. Zakrzewski, G.A. Voth, P. Salvador, J.J. Dannenberg, S. Dapprich, A.D. Daniels, Ö. Farkas, J.B. Foresman, J.V. Ortiz, J. Cioslowski, D.J. Fox, Gaussian, Inc., Wallingford, CT, USA, 2009.
[51] L. Triguero, L.G.M. Pettersson, H. Ågren, Physical Review B 58/12 (1998) 8097.
[52] W. Kutzelnigg, U. Fleischer, M. Schindler, NMR-Basic Principles and Progress, Springer-Verlag, Heidelberg, 1990.

[53] L. Triguero, O. Plashkevych, L.G.M. Pettersson, H. Ågren, Journal of Electron Spectroscopy and Related Phenomena 104/1 (1999) 195.
[54] C. Kolczewski, R. Püttner, O. Plashkevych, H. Ågren, V. Staemmler, M. Martins, G. Snell, A.S. Schlachter, M. Sant'Anna, G. Kaindl, L.G.M. Pettersson, The Journal of Chemical Physics 115/14 (2001) 6426.
[55] R. Dovesi, V.R. Saunders, C. Roetti, R. Orlando, C.M. Zicovich-Wilson, F. Pascale, B. Civalleri, K. Doll, N.M. Harrison, I.J. Bush, P. D'Arco, M. Llunell, CRYSTAL09 User's Manual, Torino, Italy, 2009.
[56] G. Kresse, J. Furthmüller, Physical Review B 54/16 (1996) 11169.
[57] G. Kresse, J. Furthmüller, Computational Materials Science 6/1 (1996) 15.
[58] J.P. Perdew, K. Burke, M. Ernzerhof, Physical Review Letters 77/18 (1996) 3865.
[59] C. Adamo, V. Barone, The Journal of Chemical Physics 110/13 (1999) 6158.
[60] A. Schäfer, H. Horn, R. Ahlrichs, The Journal of Chemical Physics 97/4 (1992) 2571.
[61] F. Weigend, R. Ahlrichs, Physical Chemistry Chemical Physics 7/18 (2005) 3297.
[62] J. Scaranto, S. Giorgianni, Journal of Molecular Structure: THEOCHEM 858/1-3 (2008) 72.
[63] G. Kresse, D. Joubert, Physical Review B 59/3 (1999) 1758.
[64] H. Kusama, H. Orita, H. Sugihara, Langmuir 24/8 (2008) 4411.

Chapter 7. Conclusions & Outlook

7.1. Summary of Dissertation

Dye- and quantum dot-sensitized solar cells (SSCs) represent a promising pathway to a variety of inexpensive photovoltaic technologies. Their modular nature allows for near-limitless modification and research direction. The disadvantage to this modularity, however, is that highly systematic studies are required in order to achieve transferable insight that will lead to the production of record efficiency devices. An essential part of SSCs is their high interfacial surface area. In this thesis we describe two approaches to further understanding of SSC interfaces: engineering the TiO_2 photoanode to reduce charge recombination via thin, insulating metal oxide layers, and characterization of dye molecules adsorbed on TiO_2 from both an experimental and computational perspective.

Our engineering work began in Chapter 3 with a comprehensive study of Al_2O_3 recombination barrier layers grown by atomic layer deposition (ALD) in solid-state DSSCs. Because Al_2O_3 is easily grown and highly insulating, much work has previously examined its role as a recombination barrier. However, no studies had examined its use with the most popular solid-state hole transport material (HTM) spiro-OMeTAD. The purpose of our study was to examine the behavior of Al_2O_3 barrier layers as a function of thickness as well as device parameters such as dye chemistry, the $TiCl_4$ surface treatment, and the device active layer thickness. Our results highlighted the importance of the dye molecule paired with the barrier layer, as the excited state energy level of the dye plays an important role in dictating whether electron injection can proceed through an insulating layer. We observed that performance improvements were only achievable in our devices when the $TiCl_4$ treatment was left out. This observation helps explain some of the variable results previously reported with Al_2O_3 barrier layers in the literature and also motivates Al_2O_3 barrier layers as an alternative when the $TiCl_4$ treatment is not feasible. The effect of Al_2O_3 on device performance was not observed to vary with the thickness of the TiO_2 photoanode, suggesting that the charge collection efficiency in

spiro-based DSSCs is actually quite high. Overall, our results highlighted the need for fine control over the thickness and simulating properties of barrier layers.

Using the lessons learned with Al_2O_3 we proceeded to study In_2O_3 barrier layers in similar spiro-based solid-state DSSCs, as described in Chapter 4. We utilized a recently-reported ALD process to deposit In_2O_3 at a very low growth rate to minimize the sensitivity of device performance to the number of ALD cycles. We were able to achieve small increases in overall efficiency and large improvements in device open-circuit voltage (V_{OC}) as In_2O_3 barrier layers were observed to both suppress recombination and exert a favorable dipole that lifts up the TiO_2 conduction band. An unexpected phenomenon emerged when the In_2O_3 layers grew past a certain critical thickness. Large decreases in V_{OC} occurred and we used a combination of device measurements and computational studies to conclude that this was due to both a reversal in direction of the In_2O_3-induced dipole (thereby lowering the TiO_2 conduction band) and an acceleration, rather than suppression, of recombination that we attribute to the formation of In_2O_3 states in the TiO_2 band gap. This dramatic reversal in behavior highlights the stark changes that can occur as sub-monolayer surface treatments approach bulk scale.

In Chapter 5 we again studied Al_2O_3 recombination barrier layers, but this time in PbS-based solid-state QDSSCs. In comparison to DSSCs, recombination in QDSSCs tends to be more severe due to a lower surface coverage of the quantum dots in comparison to dye molecules—which leads to closer proximity of the photoanode and HTM—as well as non-negligible recombination to oxidized quantum dots (in contrast to oxidized dye molecules). In this study, Al_2O_3 proved highly effective at improving device performance, nearly doubling the efficiency due to a large enhancement in device current. We also demonstrated in this study how a single ALD reactor could be used to deposit both a recombination barrier layer and an absorbing material in a single process without breaking vacuum. This method enables the design of exciting new research avenues to examine interfaces *in situ* in QDSSCs.

Following the presentation of our interface engineering studies, we discuss the use of the synchrotron radiation technique near-edge X-ray absorption fine structure (NEXAFS) spectroscopy in Chapter 6. Here we use NEXAFS as an experimental means

of determining the molecular configuration of a dye molecule adsorbed on TiO_2 by measuring the orientation of individual molecular orbitals. We are able to determine an upright configuration of the dye molecule which is then compared to density functional theory (DFT) calculations of the same dye/TiO_2 system. Using an advanced method, DFT-molecular dynamics (DFT-MD) simulations, we demonstrate remarkable agreement between the NEXAFS results and the computational studies. At a basic level, this work demonstrates the orientation of a molecule belonging to perhaps the most widely-used class of dyes. More broadly, we demonstrate the importance of including "real-world" conditions and dynamics when interpreting computational studies and we provide a paradigm for the study of adsorbate/substrate systems outside the realm of DSSCs.

Finally, in the three appendices that follow this chapter, we describe experiments related to the engineering and characterization studies described above. In Appendix A: we detail an organic route to recombination barrier layers through the pre-deposition of a phosphonic acid self-assembled monolayer (SAM) and subsequent linkage of dye molecules. In Appendix B: we briefly detail published work that combines elements of Chapter 5 and Appendix A: in CdS QDSSCs. Finally, in Appendix C: we present the results of NEXAFS experiments on the adsorption of ruthenium-based dye molecules (in contrast to the organic dye described in Chapter 6) and their constituent ligands.

7.2. Outlook on the Future of Sensitized Solar Cells

The impressive improvements in the cost and performance of competing photovoltaic technologies means that SSCs must hit a moving target in order to realize successful commercialization and wide-scale adoption. The massive scale of the solar energy resource coupled with rapid growth in PV installations over the past decade presage a bright future for solar as developed nations transition to carbon-free energy sources and developing nations seek easily distributed generation technologies to drive progress. Several companies are currently working to ensure that SSCs secure a share of the solar market, ranging from large corporations such as Sony to smaller, specialized companies such as G24i, 3GSolar, and Dyesol. The modular nature of SSCs, the ease with which they can be made translucent, and the ability to tailor their color and opacity opens up several niche application areas for SSCs such as in building-integrated PV and

in consumer products. Furthermore, the ability to tune the opacity and absorption spectrum of SSCs makes them potential candidates for use in a tandem device structure atop a thin-film cell [1]. This combination may yield a device that will bring SSCs from windows and interiors to rooftops around the world.

Successfully entering these application areas, however, requires further engineering advances to make SSCs more efficient, more stable, and more practical. The interface-engineering component of this dissertation, for example, was specifically geared towards developing further understanding of the recombination process in solid-state devices. Solid-state SSCs have yet to reach the efficiencies demonstrated in liquid SSCs but they offer substantial practical benefits with regards to commercialization. The barrier layer studies demonstrate that achieving performance enhancements is much more difficult in already high-performing devices than in less-optimized structures. This remains, however, primarily an engineering obstacle rather than a theoretical boundary—designing a barrier layer that significantly reduces recombination without significantly reducing electron injection is a function of materials choice and fabrication method. While SSCs are highly modular, the behavior of each component is context-specific, such as the Al_2O_3 barrier layer used in dye and quantum dot devices. SSCs cannot simply be designed on the basis of favorable component energy levels; numerous studies have indicated that the interaction of these materials, both structurally and electronically, is critical [2]. The design of future SSCs should be guided by a systems-level rather than a plug-and-play approach.

The workhorse of the SSC is the absorbing material and that is where a large portion of SSC research is focused. The 12% record DSSC, for example, employed a class of dyes—porphyrins—that had not previously demonstrated strong performance [3]. This result motivates research into molecules that had previously been largely-neglected for use in SSCs. Another intriguing concept in SSCs is the use of perovskite absorbers. Three recent reports demonstrated remarkably high efficiencies for solid-state SSCs using a lead iodide perovskite absorber that coats the photoanode much like a chalcogenide material in an extremely-thin absorber SSC device [4-6]. The charge transfer kinetics of this new material are quite different than those in dye molecules and chalcogenide

semiconductors, yet these perovskite-sensitized devices will still require interface understanding and engineering in order to improve further. Surface treatments, such as the deposition of thin metal oxide layers or the adsorption of small molecules may prove beneficial in reducing charge recombination at the perovskite/photoanode interface or improving the uniformity of the perovskite surface coverage. As the absorbing material composition, in addition to determining light absorption properties, can influence the energy levels of the photoanode and HTM, prudent engineering of the perovskite (or chalcogenide or dye) absorbers can yield improvements in both device current and voltage.

The use of ALD was an important part of this thesis. ALD is an ideal deposition method for barrier layers because its self-limiting nature allows for conformal coverage of high aspect ratio photoanodes at a low growth rate. This is particularly well-suited for performing comprehensive investigations into the thickness-dependence of barrier layer behavior, but the high vacuum required for traditional ALD may present an obstacle to the use of barrier layers in SSCs at production-scale. New developments in ALD technology, however, seek to make high pressure ALD feasible [7]. Technical advances such as high pressure ALD may in the end be more conducive to inexpensive device production than the $TiCl_4$ chemical bath treatment that it is often compared against. In a similar vein, the chapter of this dissertation on dye orientation utilized synchrotron radiation. While such experiments are not, due to the scarcity of synchrotrons in the world, easily scalable, an important lesson from this study was that sophisticated computational methods can well-approximate real world experimental conditions. With increasing computational capabilities, high throughput screening of potential dye molecules becomes feasible, whereby promising dyes can be isolated before they have even been synthesized, let alone tested in a device.

The ability to bridge the lab-scale SSC research described in this dissertation and throughout the literature to production scale will dictate the eventual commercial success of SSCs. While SSCs are attractive due to their modularity and their use of inexpensive and relatively low-purity materials, as the work described here indicates, improving these devices requires atomic level understanding. Directing this understanding towards

concrete milestones in SSC performance is likely to yield a host of high efficiency, practical devices utilizing a variety of architectures.

7.3. References

[1] Z.M. Beiley, M.D. McGehee, Energy & Environmental Science 5/11 (2012) 9173.
[2] S.H. Im, C.-S. Lim, J.A. Chang, Y.H. Lee, N. Maiti, H.-J. Kim, M.K. Nazeeruddin, M. Grätzel, S.I. Seok, Nano Letters 11/11 (2011) 4789.
[3] A. Yella, H.-W. Lee, H.N. Tsao, C. Yi, A.K. Chandiran, M.K. Nazeeruddin, E.W.-G. Diau, C.-Y. Yeh, S.M. Zakeeruddin, M. Grätzel, Science 334/6056 (2011) 629.
[4] H.-S. Kim, C.-R. Lee, J.-H. Im, K.-B. Lee, T. Moehl, A. Marchioro, S.-J. Moon, R. Humphry-Baker, J.-H. Yum, J.E. Moser, M. Grätzel, N.-G. Park, Sci. Rep. 2 (2012) 1.
[5] M.M. Lee, J. Teuscher, T. Miyasaka, T.N. Murakami, H.J. Snaith, Science 338/6107 (2012) 643.
[6] J.H. Noh, S.H. Im, J.H. Heo, T.N. Mandal, S.I. Seok, Nano Letters 13/4 (2013) 1764.
[7] P. Poodt, D.C. Cameron, E. Dickey, S.M. George, V. Kuznetsov, G.N. Parsons, F. Roozeboom, G. Sundaram, A. Vermeer, Journal of Vacuum Science & Technology A: Vacuum, Surfaces, and Films 30/1 (2012) 010802.

Appendix A: Phosphonic Acid SAM Recombination Barrier Layers

A.1. Introduction

The recombination barrier studies discussed in Chapter 3, Chapter 4, and Chapter 5 focused on the use of inorganic metal oxides deposited prior to dye adsorption. The work described in this appendix focuses on an organic route to the same end through the deposition of an organic self-assembled monolayer (SAM) of phosphonic acids with functional tail groups. The goal is to chemically link the tail group of the phosphonic acid SAM to the carboxylic acid group of the dye molecules so that the there is little-to-no reduction in dye surface coverage. The phosphonic acid SAM would serve to reduce the concentration of pinholes in dye coverage (which can be up to 20% of the TiO_2 surface [1]) and to prevent the hole-transport material (HTM) from accessing the TiO_2 surface in between dye molecules.

Adsorbing an additional molecule or molecules either before or during the dye adsorption step is a widely-explored area due to the many possible benefits such molecules may impart. Such molecules may have a dipole that raises the TiO_2 (or other photoanode material) conduction band and increase device open-circuit voltage (V_{OC}) [2, 3] (see also: Chapter 4 and Chapter 6). Other molecules can reduce recombination by screening the HTM or excluding it from the TiO_2 surface [3, 4] or reduce the formation of dye aggregates in solution, such as the commonly-used chenodeoxycholic acid [5]. The disadvantage to these pre- and co-adsorbents is that they can reduce the coverage of dye molecules thereby reducing light absorption, particularly when the device thickness is already limited by HTM pore-filling or fast recombination, as in solid state-DSSCs. This motivates the development of systems wherein dye molecules can be attached to the pre- or co-adsorbent, in principle offering the benefits of such molecules without the associated drop in dye uptake. The attachment of dye molecules to SAMs is rather less explored than the use of co-adsorbents, although some routes have been reported, including: click-chemistry attachment to surface-grafted alkanes [6]; formation of dative bonds from the nitrogen atoms of carboxylic acid-attached pyridine rings to porphyrin

metal centers [7]; and the linkage of a second layer of dye molecules to already-adsorbed dye molecules via conjugated linkers [8]. The goal of the work described below is the attachment of dye molecules to an amine-terminated phosphonic acid SAM via the formation of an amide bond.

A.2. Selection of Phosphonic Acids

SAM molecules are typically described as having "head" and "tail" groups connected by a linker; the head is designed to form a strong bond to the surface while the tail and linker are designed with the desired surface functionalization in mind. The adsorption of molecules on metal oxide surfaces through the formation of Metal-Oxygen-X bonds is a well-studied field, with perhaps the most obvious example in the context of this dissertation being the attachment of dye molecules via carboxylic acid head groups (a Ti-O-C bond). The strength of the M-O-X attachment is a function of both the metal and "X" atom; for example, on SiO_2 surfaces, silanes are typically used to functionalize the surface in order to utilize strong Si-O-Si bonds. On TiO_2, Ti-O-P bonds have been shown to be very strong, motivating the use of phosphonic acids for surface functionalization [9, 10] (indeed, phosphonic acids have also been used as the attachment group for DSSC dyes and demonstrated improved thermal stability, although carboxylic acid still represents the standard [11]).

With the head group chosen, it is important to choose a tail group that can form some sort of strong chemical bond with the dye molecules. Constrained by the availability of only COOH-based dye molecules, the tail group options are limited, but amine ($-NH_2$) groups were chosen here due to their ability to form strong amide linkages. The linker group is also very important in the context of this experiment due to the need to maintain charge injection from the dye molecules into TiO_2; it is expected that long unconjugated alkyl chains, for instance, would inhibit electron injection (akin to the same phenomenon observed with metal oxide barrier layers in Chapter 3 and Chapter 4) [12]. In order to study this effect a variety of conjugated and unconjugated linker groups were selected. Given these various criteria and the desire to use non-functionalized methyl tail groups as experimental controls, the following commercially-available phosphonic acids, shown in Figure A-1, were chosen: aminomethyl phosphonic acid (AMPA), 3-

aminopropyl phosphonic acid (APPA), *p*-aminobenzyl phosphonic acid (ABPA) [13], 3-phosphopropionic acid (PPA) [14, 15], butyl phosphonic acid (BPA), and octadecyl phosphonic acid (ODPA) [10]; (AMPA, PPA, BPA and ODPA were purchased from Alfa-Aesar; APPA and ABPA were purchased from Sigma-Aldrich).

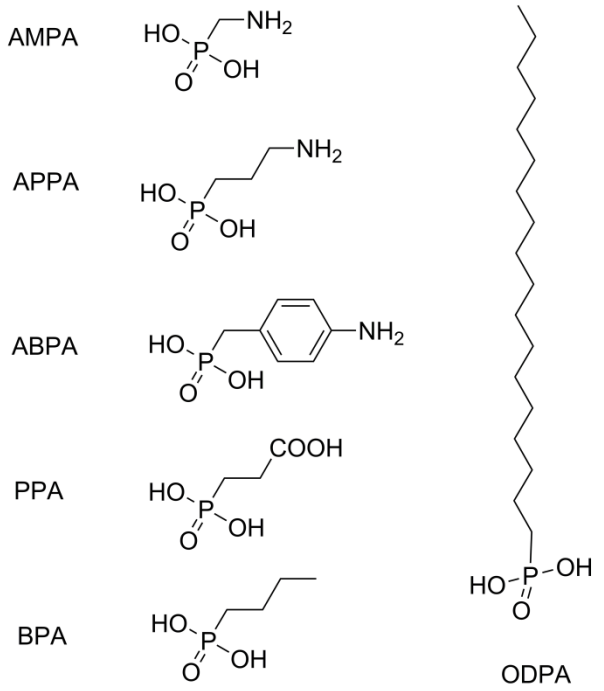


Figure A-1: Phosphonic acids studied: aminomethyl phosphonic acid (AMPA), 3-aminopropyl phosphonic acid (APPA), *p*-aminobenzyl phosphonic acid (ABPA), 3-phosphopropionic acid (PPA), butyl phosphonic acid (BPA), and octadecyl phosphonic acid (ODPA).

Solution deposition methods were developed for each phosphonic acid. It was observed that the methyl-terminated acids, BPA and ODPA, are highly soluble in ethanol, and the acid-terminated PPA is soluble in water, methanol and acetone (note that PPA was not studied to the same degree as the other SAMs due to its –COOH tail group that is expected to form an unstable anhydride link to a dye –COOH group). Dissolving the amine-terminated acids, particularly ABPA, proved more difficult. ABPA requires the addition of either acid or base to dissolve in both water and methanol (as was suggested in Ref. [13]), but AMPA and APPA dissolve (albeit slowly) in neutral pH water and only require the addition of acid or base to dissolve in methanol. Unlike in dye adsorption processes wherein water precludes the stable bonding of -COOH groups to the TiO_2 surface, phosphonic acid SAMs were observed to form as readily from

aqueous solutions as from organic solutions. In both instances, the solution concentrations were on the order of 1 - 10 mM and the deposition times were approximately 48 hours. The adsorption of these molecules was studied first on planar TiO_2 substrates (grown on the oxide surface of silicon substrates via atomic layer deposition) with techniques such as ellipsometry, water contact angle (WCA) measurements, and X-ray photoelectron spectroscopy (XPS). XPS was able to detect the presence of P and N (in the instance of the amine-terminated SAMs) atoms following the SAM deposition process. Due to the small size of the molecules, with the exception of ODPA, ellipsometry did not prove particularly informative. Changes in WCA before and after the solution deposition processes were detectable, but determining the meaning of the measured angles with regards to the nature of the SAM layers formed was difficult. As with ellipsometry, analysis of the ODPA WCA results was made easier by the large changes in WCA observed and the body of literature on SAMs of similar 18-carbon chain silane molecules. WCAs of over 100° were observed with ODPA, consistent with a hydrophobic SAM.

On the whole, analyzing the phosphonic acid SAMs on planar TiO_2 did not prove particularly elucidating. Using nanoporous TiO_2 substrates, in addition to more closely simulating the ultimate usage of the phosphonic acid SAMs in a device, provided a high surface-area substrate (and therefore higher signal) on which to perform Fourier transform infrared spectroscopy (FTIR) experiments. FTIR is adept at identifying chemical signatures particular to certain molecular structures, which are identified in the spectra shown in Figure A-2. Peaks of interest include those corresponding to C-H stretches in alkyl chains at around 2900 cm^{-1} (as in ODPA) which can indicate the extent of SAM ordering, the "ring mode" at 1515 cm^{-1} in ABPA, and the N-H bending modes around 1600 cm^{-1} in the amine-terminated SAMs; the disappearance or movement of these peaks, for example, could indicate the attachment of dye molecules via an amide linkage.

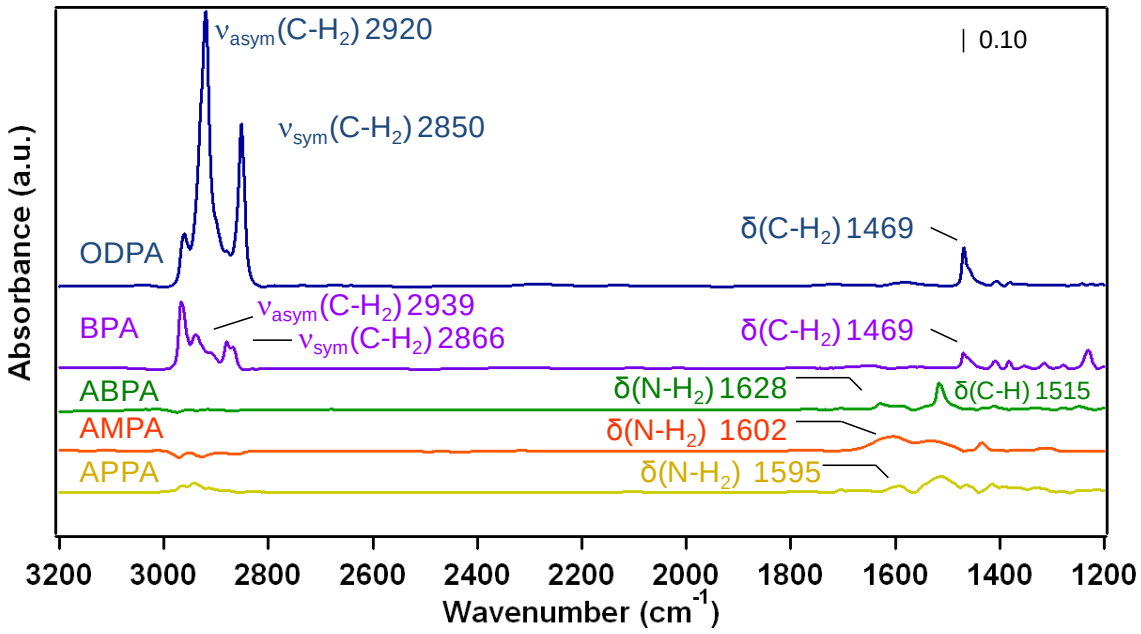


Figure A-2: FTIR spectra of phosphonic acid SAMs adsorbed on nanoporous TiO_2, normalized to bare TiO_2. Various important and characteristic peaks are indicated.

A.3. Dye Adsorption on SAM-Coated TiO_2

After the formation of the phosphonic acid SAM layers, the coated nanoporous TiO_2 substrates were immersed in a Z907 dye (Figure A-3a) solution (0.3 mM, 1:1 (v/v) *tert*-butanol:acetonitrile, as in device fabrication). Unfortunately, the presence of SAMs significantly reduced the uptake of dye molecules as was visible by eye and is clear in the FTIR spectra (Figure A-4). Note that in the spectra of BPA and ODPA that there are negative peaks in the C-H stretch region, suggesting that some dye was adsorbed at the expense of desorbing phosphonic acid molecules. The lack of a similar negative peak in, for example, the characteristic ring mode of ABPA may indicate that the SAM desorption is a function of the respective phosphonic acid's solubility in the dye solution (as noted previously, BPA and ODPA were generally more soluble than ABPA). The large peak ~2100 cm^{-1} characteristic of the isothiocyanate (N=C=S) ligand of the Z907 dye provides the clearest signal of dye uptake and suggests that BPA and ODPA block dye adsorption the most. However, this is not necessarily indicative of amide formation: the amine-terminated SAMs also block dye uptake appreciably and the greater blocking by APPA as compared to AMPA suggests that this blocking is more a function of the quality of the SAM layer than the tail groups. Furthermore, in comparing the spectra with and without

amine-terminated SAMs, there is no indication that an amide bond is forming. In sum, amide formation does not appear to follow from the standard deposition of Z907 on SAM-coated TiO_2, motivating the development of a chemical process to catalyze this reaction.

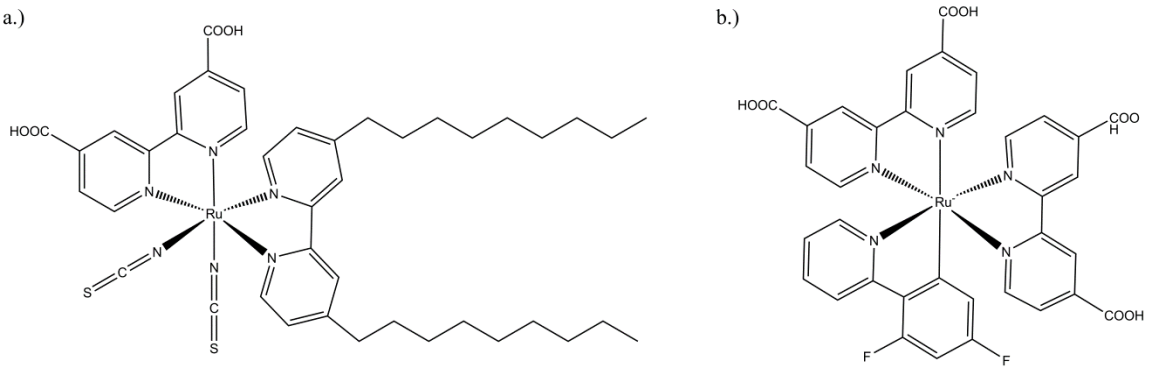


Figure A-3: The ruthenium-based dyes Z907, a.), and YE05, b.), used in the phosphonic acid SAM studies.

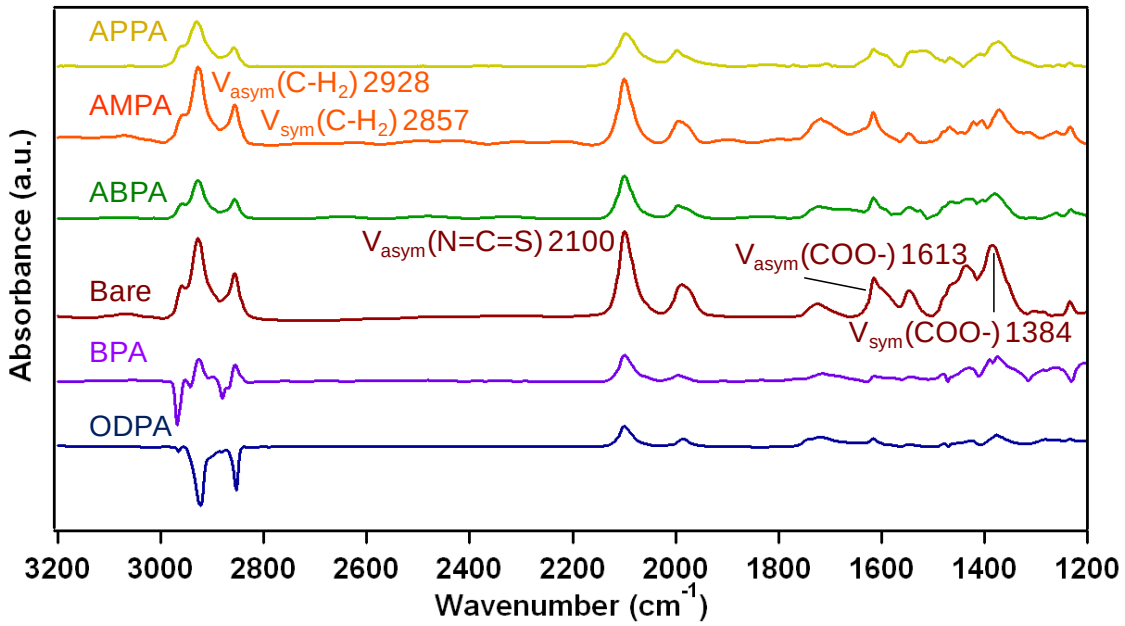


Figure A-4: FTIR spectra of the Z907 dye adsorbed on phosphonic acid SAM-covered nanoporous TiO_2, normalized to spectra taken after the SAM deposition, prior to dye adsorption. "Bare" indicates that the TiO_2 was not coated with a SAM prior to dye adsorption. Various important and characteristic peaks are indicated.

A.4. Activation of Carboxylic Acid Groups

A.4.1. DCC/NHS Activation

Given the lack of amide formation, routes to promote this bond's formation were sought. The importance of amide bonds in polypeptides and proteins has motivated much research into promoting this reaction with the general strategy being to convert the –OH of the –COOH group into a better leaving group. One such route is to use N,N'-dicyclohexylcarbodiimide (DCC) which reacts with the hydroxyl group of the carboxylic acid and turns it into a better leaving group. N-hydroxysuccinimide (NHS) is typically added to make a more stable and isolable intermediate [16]. NHS replaces the DCC-carboxylic acid compound yielding an activated acid and insoluble byproduct, N,N'-dicyclohexylurea (DHCU); this activation reaction is shown in Figure A-5.

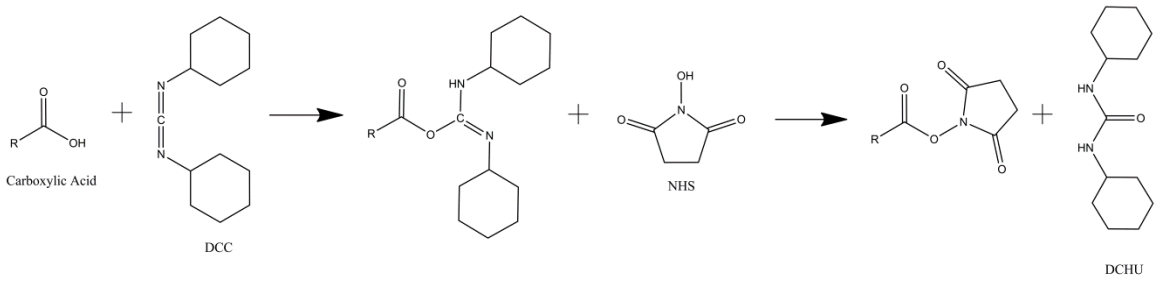


Figure A-5: Activation of a carboxylic acid using N,N'-dicyclohexylcarbodiimide (DCC) and N-hydroxysuccinimide (NHS). The reaction yields an activated acid and the insoluble byproduct N,N'-dicyclohexylurea (DHCU).

This reaction process was first tested using a model carboxylic acid, $CH_3(CH_2)_6COOH$ (octanoic, or caprylic, acid), dissolved in dichloromethane at a concentration of 20 mM. To this solution, NHS powder was added and then DCC, dissolved in the same volume of dichloromethane, was added dropwise (1.1 molar equivalents, relative to octanoic acid, were used for both NHS and DCC). After 24 hours stirring at room temperature in a sealed flask, a precipitate was filtered out. FTIR yielded a spectrum for the precipitate consistent with DCHU. The resultant activated octanoic acid in dichloromethane was then added to an APPA SAM-coated nanoporous TiO_2 substrate along with triethylamine (as base) for 24 hours. FTIR was used to characterize the resulting substrates, and while indicating high uptake of octanoic acid on APPA-

coated TiO_2, did not indicate clear evidence of an amide bond formation or preferential adsorption relative to unactivated octanoic acid (Figure A-6).

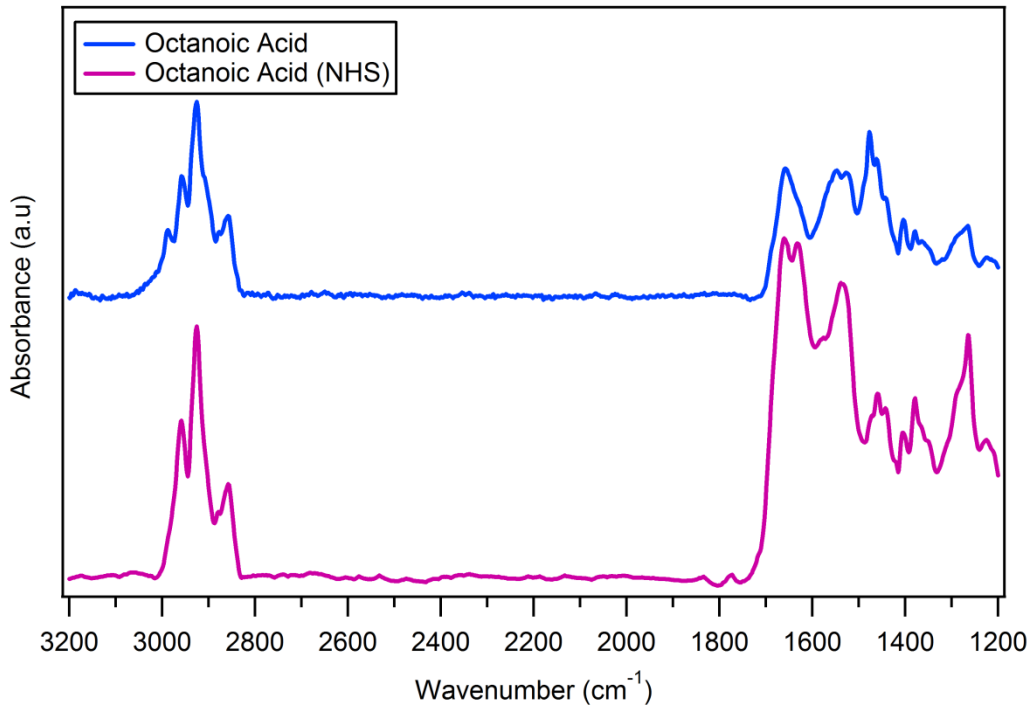


Figure A-6: FTIR spectra of octanoic acid and NHS-activated octanoic acid adsorbed on APPA-coated nanoporous TiO_2. Spectra normalized to corresponding spectrum of APPA SAM on TiO_2.

The DCC-NHS activation reaction was then attempted with the Z907 dye. Because Z907 has minimal solubility in dicholormethane, dimethylformamide (DMF) was chosen as the solvent. When the resultant activated dye was adsorbed onto bare nanoporous TiO_2, however, two observations were noted: the substrates were significantly less red than as in a typical dye adsorption step, and the isothiocyanate peak at 2100 cm^{-1} was diminished relative to the C-H stretch peaks characteristic of the Z907's alkyl chains. The lack of uptake was attributed to DMF molecules adsorbing to TiO_2 and therefore blocking dye uptake. The reduced isothiocyanate mode was attributed to an undesirable reaction wherein the electrophilic isothiocyanate ligands are attacked by the nucleophilic NHS.

Given this result, an activation reaction scheme using only DCC (*i.e.* no longer adding in NHS) was pursued using a new solvent, methanol, to avoid the problems with DMF. This route, however, was unsuccessful: very little dye uptake on APPA-coated

TiO_2 was observed in comparison to a significant uptake on bare TiO_2. Given the lack of success using DCC-activation schemes, a new carbodiimide compound was chosen which required a new solvent, and therefore new dye.

A.4.2. EDC/NHS Activation

As an alternative to DCC, 1-ethyl-3-(3-dimethylaminopropyl) carbodiimide (EDC) hydrochloride is commonly used for amide formation, particularly in aqueous solutions [17]. The lessons described above regarding the importance of solvent choice and the susceptibility of isothiocyanate groups to nucleophilic attack motivate using a dye that is soluble in a number of solvents and is more chemically robust. The development of the YE05 dye (Figure A-3b) in 2009 presented one particularly promising alternative [18]. YE05 is the first high-performing ruthenium dye that lacks isothiocyanate ligands, which are regarded as the "chemical weak point" of the dye in terms of stability [18]. Furthermore, the lack of long alkyl chains such as those present in Z907 increase YE05's solubility in polar solvents like water (note: other common ruthenium dyes such as N3 (Figure 1-7a) also lack these alkyl chains). These two characteristics—stability and water solubility—motivated the EDC/NHS carboxylic acid activation scheme shown in Figure A-7.

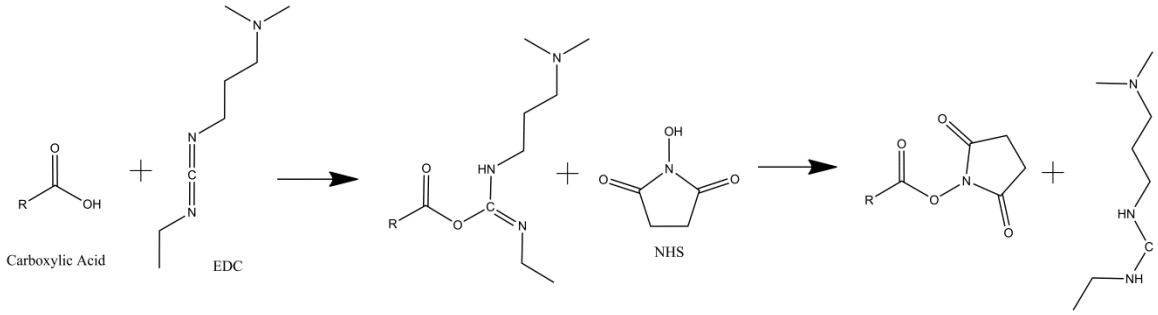


Figure A-7: Activation of a carboxylic acid using 1-ethyl-3-(3-dimethylaminopropyl) carbodiimide (EDC) and N-hydroxysuccinimide (NHS).

After synthesizing the YE05 dye as described by Bessho *et al*. [18], it was dissolved in water in a round-bottom flask at a concentration of 0.3 mM and then 4.1 molar equivalents (to account for the four carboxylic acid groups per YE05 dye molecule) of EDC (the hydrochloride salt form) and NHS were added. After activation, the water was evaporated off and the activated YE05 dye was redissolved in ethanol before adding it to ABPA SAM-coated TiO_2 substrates in the presence of triethylamine.

An increase in dye uptake following activation (as compared to uptake of unactivated dye on ABPA) was apparent by sight and suggested by FTIR. The ring mode FTIR peak of ABPA indicated that this increase in dye uptake was not due to an enhancement of ABPA desorption, as in fact the FTIR spectra suggested that less ABPA desorption occurs in the presence of the activated YE05. Furthermore, the clear visual difference in dye uptake on ABPA-coated versus bare TiO_2 when using unactivated dye was no longer present. Unfortunately, however, the lack of isothiocyanate ligands and the alkyl chains in YE05 makes quantitative comparison much more difficult than with Z907. Furthermore, FTIR did not show any clear indication of the appearance of an amide bond.

Given the promising if inconclusive results of the FTIR experiments with ABPA, devices were fabricated using this same YE05 activation scheme. While activation was not observed to affect device performance (when compared to device results with unactivated YE05 dye), the presence of any of the three amine-terminated SAMs (AMPA, APPA, ABPA) resulted in significant efficiency drops of over 50% when compared to devices without any phosphonic acid SAMs.

A.5. Conclusion

In this appendix, phosphonic acid SAMs were studied for the purpose of recombination blocking. The adsorption of these molecules from aqueous and organic solutions was observed via FTIR. Both functionalized (*i.e.* amine-terminated) and non-functionalized phosphonic acids were observed to significantly reduce the uptake of dye molecules on nanoporous TiO_2 substrates. This motivated the activation of the dye carboxylic acid groups in order to promote amide bond formation. The first route, using DCC and NHS was shown to deleteriously react with the isothiocyanate ligands of the Z907 dye. Using the isothiocyanate-lacking dye YE05, activation was pursued using EDC and NHS in water and this activation scheme was observed to increase dye uptake on a TiO_2 substrate coated with an amine-terminated SAM. Unfortunately, this same process was shown to significantly reduce the performance of devices in comparison to those without phosphonic acid SAMs.

A.6. Outlook

While the recombination barrier strategy described here did not yield positive results, the general methodology proposed remains sound. Phosphonic acids bind strongly to TiO_2 under a wide range of pH values and their tail groups can be functionalized. The amide connection to dye molecules has the advantage of both being chemically strong and enables the use of vast number of COOH-based dye molecules that have already been developed. One of the primary challenges encountered in the work described in this appendix was the difficulty of characterizing the activation and surface attachment of dye molecules. Both Z907 and YE05 contain multiple -COOH groups, not all of which are necessary for dye attachment. Furthermore, different orientations of these dye molecules can yield a variety of –COOH binding mechanisms that result in a number of associated FTIR peaks. Moving to organic D-π-A dyes, for example may be one means of developing better insight. These dyes typically attach via one carboxylic acid group and their structure can be better tailored for chemical stability and solubility. While we were unable to improve the performance of DSSCs using these phosphonic acids, as described in Appendix B:, we did in fact achieve large performance gains using these same molecules [19].

A.7. Collaborations

This project was first proposed by Craig Peters and he provided much valuable insight and encouragement. The activation chemical routes using DCC, EDC, and NHS were developed in large part by a lab rotation student, Stephen Fried, who also proved to be an invaluable chemistry teacher to me. The YE05 dye was synthesized (and recommended) by Rajib Mondal.

A.8. References

[1] S. Handa, H. Wietasch, M. Thelakkat, J.R. Durrant, S.A. Haque, Chemical Communications 0/17 (2007) 1725.
[2] C. Goh, S.R. Scully, M.D. McGehee, Journal of Applied Physics 101/11 (2007) 114503.
[3] A. Allegrucci, N.A. Lewcenko, A.J. Mozer, L. Dennany, P. Wagner, D.L. Officer, K. Sunahara, S. Mori, L. Spiccia, Energy & Environmental Science 2/10 (2009) 1069.
[4] P. Wang, S.M. Zakeeruddin, P. Comte, R. Charvet, R. Humphry-Baker, M. Grätzel, The Journal of Physical Chemistry B 107/51 (2003) 14336.

[5] N.R. Neale, N. Kopidakis, J. van de Lagemaat, M. Grätzel, A.J. Frank, The Journal of Physical Chemistry B 109/49 (2005) 23183.
[6] M.C. Benson, R.E. Ruther, J.B. Gerken, M.L. Rigsby, L.M. Bishop, Y. Tan, S.S. Stahl, R.J. Hamers, ACS Applied Materials & Interfaces 3/8 (2011) 3110.
[7] N.K. Subbaiyan, C.A. Wijesinghe, F. D'Souza, Journal of the American Chemical Society 131/41 (2009) 14646.
[8] S.-R. Jang, R. Vittal, J. Lee, N. Jeong, K.-J. Kim, Chemical Communications 0/1 (2006) 103.
[9] J.P. Folkers, C.B. Gorman, P.E. Laibinis, S. Buchholz, G.M. Whitesides, R.G. Nuzzo, Langmuir 11/3 (1995) 813.
[10] S. Marcinko, A.Y. Fadeev, Langmuir 20/6 (2004) 2270.
[11] P. Wang, C. Klein, J.-E. Moser, R. Humphry-Baker, N.-L. Cevey-Ha, R. Charvet, P. Comte, S.M. Zakeeruddin, M. Grätzel, The Journal of Physical Chemistry B 108/45 (2004) 17553.
[12] J.B. Asbury, E. Hao, Y. Wang, T. Lian, The Journal of Physical Chemistry B 104/50 (2000) 11957.
[13] G.M. Kosolapoff, Journal of the American Chemical Society 69/9 (1947) 2112.
[14] P.-H. Heubel, A. Popov, Journal of Solution Chemistry 8/9 (1979) 615.
[15] S. Pawsey, K. Yach, L. Reven, Langmuir 18/13 (2002) 5205.
[16] J. Telser, K.A. Cruickshank, K.S. Schanze, T.L. Netzel, Journal of the American Chemical Society 111/18 (1989) 7221.
[17] Z. Grabarek, J. Gergely, Analytical Biochemistry 185/1 (1990) 131.
[18] T. Bessho, E. Yoneda, J.-H. Yum, M. Guglielmi, I. Tavernelli, H. Imai, U. Rothlisberger, M.K. Nazeeruddin, M. Grätzel, Journal of the American Chemical Society 131/16 (2009) 5930.
[19] P. Ardalan, T.P. Brennan, H.-B.-R. Lee, J.R. Bakke, I.K. Ding, M.D. McGehee, S.F. Bent, ACS Nano 5/2 (2011) 1495.

Appendix B: CdS QDSSC Interface Engineering

B.1. Introduction

The chalcogenide semiconductor CdS is a popular choice for the absorbing material in quantum dot-sensitized solar cells (QDSSCs) as it can be readily grown using chemical bath deposition (CBD) [20-23], successive ion layer adsorption and reaction (SILAR) [19, 24-30], electrodeposition [31], and colloidal [32] methods. While the high bandgap of CdS is not ideally-matched to the solar spectrum, CdS-based QDSSCs provide an excellent model system for demonstrating new strategies for improving QDSSC performance. This Appendix summarizes three separate, published studies that include interface engineering themes previously discussed in the chapters of this dissertation but applied to CdS QDSSCs utilizing the same basic device architecture as those DSSCs and PbS QDSSCs: spiro-OMeTAD was the hole-transport material, and the devices used ~2 μm-thick nanoporous TiO_2 photoanodes. In Section B.2, the same phosphonic acid molecules described in Appendix A: are used to significantly improve current and efficiency. In Section B.3, Al_2O_3 barrier layers are used, just as in Chapter 3 and Chapter 5, to reduce recombination and improve the performance of a CdS QDSSC. In Section B.4 CdS quantum dots are for the first time grown via atomic layer deposition (ALD), adding to the long list of CdS QD growth methods listed above; ALD was also used to grow the PbS QDs in Chapter 5.

B.2. CdS QDSSCs with Phosphonic Acid SAMs

In this study, published in *ACS Nano* in 2011 [19], the phosphonic acids shown in Figure A-1—aminomethyl phosphonic acid (AMPA), 3-aminopropyl phosphonic acid (APPA), 4-aminobenzyl phosphonic acid (ABPA), 3-phospopropionic acid (PPA), butyl phosphonic acid (BPA), and octadecyl phosphonic acid (ODPA)—were deposited on the TiO_2 photoanode prior to the growth of CdS QDs via the SILAR process. Three of the phosphonic acids—APPA, BPA, and PPA—were demonstrated to improve the device performance versus devices without SAMs by a factor of 3 (from 0.14% to 0.43 - 0.44%) due to large increases in J_{SC}. Interestingly, these three SAMs had very different tail groups—an amine (APPA), a methyl (BPA), and a carboxylic acid (PPA)—but they were

all approximately the same length. The performance improvements relative to control cells were attributed to the blocking of recombination and potentially beneficial changes in the nucleation behavior of CdS during the SILAR process.

B.3. CdS QDSSCs with Al_2O_3 Barrier Layers

In this study, published in the *Journal of Physical Chemistry C* in 2013 [30], Al_2O_3 was used as a recombination barrier and was applied, using 1, 3, and 5 ALD cycles, both before and after the deposition of CdS QDs via the SILAR process (Figure B-1). One Al_2O_3 ALD cycle was observed to improve efficiency when deposited either before or after CdS deposition, but three and five cycles both reduced efficiency due to a drop in J_{SC}. In the instance of Al_2O_3 deposited prior to the QDs, this was consistent with the observations of Al_2O_3 and In_2O_3 barrier layers in DSSCs (Chapter 3 and Chapter 4)—a too-thick Al_2O_3 layer impedes injection of electrons into the TiO_2 photoanode. The current drop observed when Al_2O_3 was deposited after the CdS was attributed to a blocking of the regeneration of oxidized CdS QDs by spiro-OMeTAD.

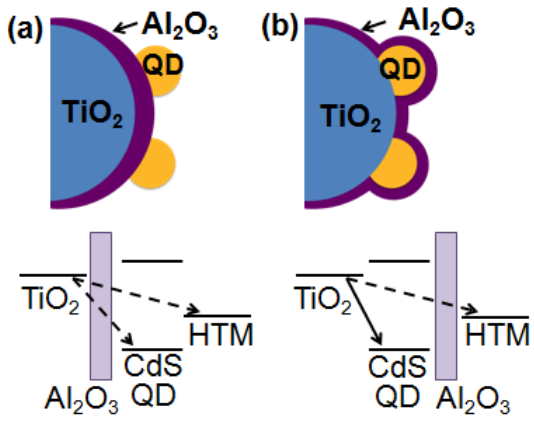


Figure B-1: Schematic of the two different device configurations studied in Ref. [30] based on the placement of the Al_2O_3 barrier layer and the recombination processes that each placement is expected to impede. Figure reprinted with permission from Ref. [30]. Copyright 2013 American Chemical Society. (Image courtesy of Katherine Roelofs).

Recombination lifetime measurements (via transient photovoltage experiments) indicated an interesting trend with regards to Al_2O_3 barrier layers deposited before as opposed to after CdS growth. Barrier layers deposited prior to CdS growth were shown to reduce recombination more than those deposited after CdS growth; this was attributed to the importance of blocking recombination to the CdS QDs, which is only achieved in

the former configuration. Despite the disparity in effects on recombination lifetime, the changes in device performance were similar, with one Al_2O_3 ALD cycle improving efficiency by ~30% whether deposited before or after CdS growth.

B.4. Growth of CdS QDs via Atomic Layer Deposition

In this study, published as the cover article in the *Advanced Energy Materials* in 2011 [33], ALD—as opposed to SILAR—was used to grow the CdS QDs. This study relied upon the nature of growth initiation in ALD, wherein nucleation occurs at certain surface sites (*e.g.* defects) that grow in an island-fashion before coalescing; prior to this coalescing, quantum confinement behavior can be observed (this is what was also observed by the Prinz group with PbS [34] and served as the basis for the PbS QDSSCs in Chapter 5). A transmission electron micrograph (TEM) of CdS QDs grown via ALD on nanoporous TiO_2 is shown in Figure B-2. A variety of CdS ALD cycle numbers were tested—3, 5, 10, 15, and 20—and a maximum efficiency of 0.25% was achieved after 5 cycles. This efficiency was less than (but comparable to) that observed via the SILAR process, as described in Section B.2 (note that the phosphonic acid SAM APPA was also used in these ALD-grown CdS QDSSCs). The growth of QDs via ALD as opposed to solution methods has potential advantages including better control over growth rate, more uniform growth throughout a nanoporous substrate, being less corrosive to certain surface treatments or substrates.

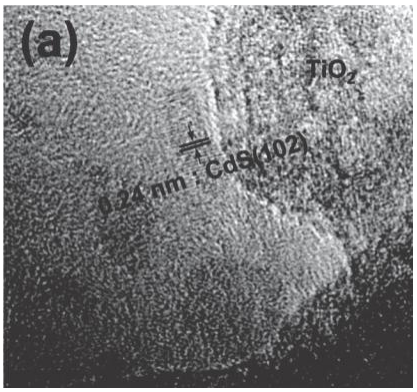


Figure B-2: TEM image of a CdS quantum dot grown on nanoporous TiO_2. Reprinted from Ref. [33] with permission from John Wiley & Sons, Ltd. (Image courtesy of Han Bo-Ram Lee).

B.5. Collaborations & Copyrights

The work described in Sections B.2 and B.4 was part of a collaboration with Pendar Ardalan and was featured in his thesis [35]. Jonathan Bakke developed the ALD platform for this work, Han Bo-Ram Lee performed the TEM analysis, and I-Kang Ding assisted with device fabrication in the lab of Michael McGehee. The work described in Section B.3 was led by Katherine Roelofs. Juan Dominguez assisted with transient photovoltage measurements which utilized the same setup described in Chapter 3 and Chapter 5 developed by Colin Bailie, George Margulis, and Eric Hoke in the lab of Michael McGehee.

B.6. References

[1] L. Xiu, Y. Kehan, L. Ganhua, C. Junhong, Y. Chris, Journal of Physics D: Applied Physics 46/2 (2013) 024004.
[2] Q. Zhang, X. Guo, X. Huang, S. Huang, D. Li, Y. Luo, Q. Shen, T. Toyoda, Q. Meng, Physical Chemistry Chemical Physics 13/10 (2011) 4659.
[3] M. Shalom, J. Albero, Z. Tachan, E. Martínez-Ferrero, A. Zaban, E. Palomares, The Journal of Physical Chemistry Letters 1/7 (2010) 1134.
[4] K. Yu, X. Lin, G. Lu, Z. Wen, C. Yuan, J. Chen, RSC Advances 2/20 (2012) 7843.
[5] C.-F. Chi, P. Chen, Y.-L. Lee, I.P. Liu, S.-C. Chou, X.-L. Zhang, U. Bach, Journal of Materials Chemistry 21/43 (2011) 17534.
[6] R. Vogel, P. Hoyer, H. Weller, The Journal of Physical Chemistry 98/12 (1994) 3183.
[7] Y.-L. Lee, Y.-S. Lo, Advanced Functional Materials 19/4 (2009) 604.
[8] Z. Yang, C.-Y. Chen, C.-W. Liu, C.-L. Li, H.-T. Chang, Advanced Energy Materials 1/2 (2011) 259.
[9] H.J. Lee, P. Chen, S.-J. Moon, F.d.r. Sauvage, K. Sivula, T. Bessho, D.R. Gamelin, P. Comte, S.M. Zakeeruddin, S.I. Seok, M. Grätzel, M.K. Nazeeruddin, Langmuir 25/13 (2009) 7602.
[10] H. Lee, H.C. Leventis, S.-J. Moon, P. Chen, S. Ito, S.A. Haque, T. Torres, F. Nüesch, T. Geiger, S.M. Zakeeruddin, M. Grätzel, M.K. Nazeeruddin, Advanced Functional Materials 19/17 (2009) 2735.
[11] P. Ardalan, T.P. Brennan, H.-B.-R. Lee, J.R. Bakke, I.K. Ding, M.D. McGehee, S.F. Bent, ACS Nano 5/2 (2011) 1495.
[12] K.E. Roelofs, T.P. Brennan, J.C. Dominguez, C.D. Bailie, G.Y. Margulis, E.T. Hoke, M.D. McGehee, S.F. Bent, The Journal of Physical Chemistry C 117/11 (2013) 5584.
[13] X.-Y. Yu, J.-Y. Liao, K.-Q. Qiu, D.-B. Kuang, C.-Y. Su, ACS Nano 5/12 (2011) 9494.
[14] Z. Ning, H. Tian, C. Yuan, Y. Fu, H. Qin, L. Sun, H. Agren, Chemical Communications 47/5 (2011) 1536.

[15] T.P. Brennan, P. Ardalan, H.-B.-R. Lee, J.R. Bakke, I.K. Ding, M.D. McGehee, S.F. Bent, Advanced Energy Materials 1/6 (2011) 1169.
[16] N.P. Dasgupta, H.J. Jung, O. Trejo, M.T. McDowell, A. Hryciw, M. Brongersma, R. Sinclair, F.B. Prinz, Nano Letters 11/3 (2011) 934.
[17] P. Ardalan, Organic and inorganic surface modification of semiconductors for electronic and energy conversion devices, Stanford University, Stanford, 2010.

Appendix C: NEXAFS Studies on Ruthenium Dyes

C.1. Introduction

The work described in this appendix is related to the study on dye orientation described in Chapter 6 using near-edge X-ray absorption spectroscopy (NEXAFS) (Section 2.6) [36]. Before switching focus to the organic D-π-A dye WN1, we studied the ruthenium dyes Z907 and YE05 and the ligands that they are composed of. The ultimate goal was to observe relevant orientation changes when coupled with recombination barrier layers—organic or inorganic—to provide further insight into how the barrier layers may affect device performance. As a result, the data in this chapter includes the phosphonic acid *p*-aminobenzyl phosphonic acid (ABPA), described in Appendix A:, as well as several metal oxide materials including Al_2O_3, ZrO_2, HfO_2, MgO, and ZnO. The reason for the transition to the organic D-π-A dye is that determining the orientation of ruthenium-based dyes is extremely difficult: the octahedral coordination, multiple carboxylic acid attachment groups, and symmetry (*i.e.* the large number of pyridine rings) mean that even given the orientation of various bonds within the dye molecule, there still exists several possible dye configurations.

Previous studies have utilized X-ray absorption spectroscopy to study the bi-isonicotinic acid (BINA) ligand, shown in Figure C-1c, common to the ruthenium dyes as it is through the carboxylic acids on this ligand that such dyes bond to metal oxide surfaces. Given the simple, mostly-planar structure of BINA, angle-resolved NEXAFS studies are able to deduce the tilt angle of the adsorbed molecule. Patthey *et al*. found a tilt angle for BINA of 25° from the surface normal on a single crystal rutile (110) TiO_2 substrate and a twist in the plane of BINA (*i.e.* the two pyridine rings are not co-planar but are both twisted an equal amount from the surface normal) [37]. Thomas *et al*. used an anatase (101) TiO_2 substrate and found a BINA tilt angle of 20° from the surface normal [38], comparable to that seen on a rutile surface. In both of these studies, BINA was adsorbed from the vapor phase; in contrast, the experiments with BINA, ABPA, and dye molecules described in this appendix use solution deposition methods similar to those used in the course of device fabrication. While not the focus of the work in this

appendix, X-ray absorption spectroscopy has also been used to study the electronic structure of both BINA and dye molecules in order to better understand important processes such as electron injection [39-42].

Although we were not able to make firm conclusions about the orientation of dye molecules (unlike our work with the WN1 dye), the work presented here provides an excellent example of the "building-block" nature of NEXAFS (that is, the fact that the spectra of large molecules can be often be approximated as superpositions of their constituent moieties) and changes in absorption characteristics of dye molecules on different metal oxide surfaces.

C.2. Experimental Details

C.2.1. Metal Oxide Fabrication

The metal oxide films used in this study were grown on the native oxide of piranha-cleaned silicon (100) wafers using atomic layer deposition (ALD) to thicknesses of ~5 nm. TiO_2 films were grown at 100 °C with titanium tetrachloride and water as precursors. To achieve anatase TiO_2 films, these substrates were annealed at 600 °C for ten hours [43]; we have observed that growing under amorphous conditions (*i.e.* low temperatures) and then annealing yields smoother anatase films than growing TiO_2 under anatase conditions (*i.e.* high temperatures) [44]. Al_2O_3 was grown at 175 °C using trimethylaluminum and water as precursors; ZrO_2 was grown at 200 °C using tetrakis(dimethylamido) zirconium and water as precursors; HfO_2 was grown at 225 °C using tetrakis(dimethylamido) hafnium and water as precursors; ZnO was grown at 150 °C using diethyl zinc and water as precursors; MgO was grown at 150 °C using bis-cyclopentadienyl magnesium and water as precursors.

C.2.2. Adsorbate Deposition

As in Appendix A:, *p*-aminobenzyl phosphonic acid (ABPA) (95%, Sigma-Aldrich; Figure C-1a) self-assembled monolayers (SAMs) were deposited over 48 hours from an acidic aqueous solution of 10 mM concentration (the acidity is achieved by adding concentrated HCl dropwise until a pH ~2-3 reached). Bi-isonicotinic acid (BINA), also known as 2,2'-bipyridine-4,4'-dicarboxylic acid (Dyesol; Figure C-1c), was

deposited from a 0.8 mM dimethylformamide solution with a dip time of 20 hours (note: this is the first, to our knowledge, solution deposition of BINA reported). Dye deposition of both Z907 (Dyesol; Figure C-1e) and YE05 (synthesized as described by Bessho *et al*. [18]; Figure C-1f) followed the same method used in device fabrication: 18-24 hour immersion in a 0.3 mM solution using either ethanol (for YE05) or 1:1 v/v *tert*-butanol:acetonitrile (for Z907) as the solvent. The dip time was shortened to 3 hours on ZnO because ZnO is susceptible to acid etching. Chenodeoxycholic acid (98%, Sigma-Aldrich; Figure C-1b), which is commonly used as a co-adsorbent in dye cells [5], was deposited using a three hour immersion in a 1 mM 1:1 v/v *tert*-butanol:acetonitrile solution.

Three non-adsorbing compounds were also studied. Two metal-thiocyanate compounds were studied in powder form to better understand the NCS ligands of the Z907 dye: copper (I) thiocyanate (Cu(NCS); 99%, Sigma-Aldrich) and cobalt (II) thiocyanate ($Co(NCS)_2$; 99.95%, Sigma-Aldrich). The molecule 2-(2,4-Difluorophenyl) pyridine (97%, Sigma-Aldrich; Figure C-1d), which in YE05 replaces the two NCS ligands present in ruthenium dyes like N3 and Z907, is a liquid at room temperature and was therefore pulsed into the NEXAFS chamber and analyzed in the vapor phase.

C.2.3. NEXAFS Experiments

The NEXAFS measurements reported here, with the exception of chenodeoxycholic acid, were conducted in Beamline 10-1 at the Stanford Synchrotron and Radiation Laboratory (SSRL) under ultrahigh vacuum (chenodeoxycholic acid was studied in Beamline 8-2 at SSRL). These measurements were conducted over the course of several beam times and as a result, there is some variation in the energy scale calibration (on the order of tenths of an eV) across different studies. To the extent that this can be accounted for, using either literature standards or the same samples across multiple beam times, is explained in the text.

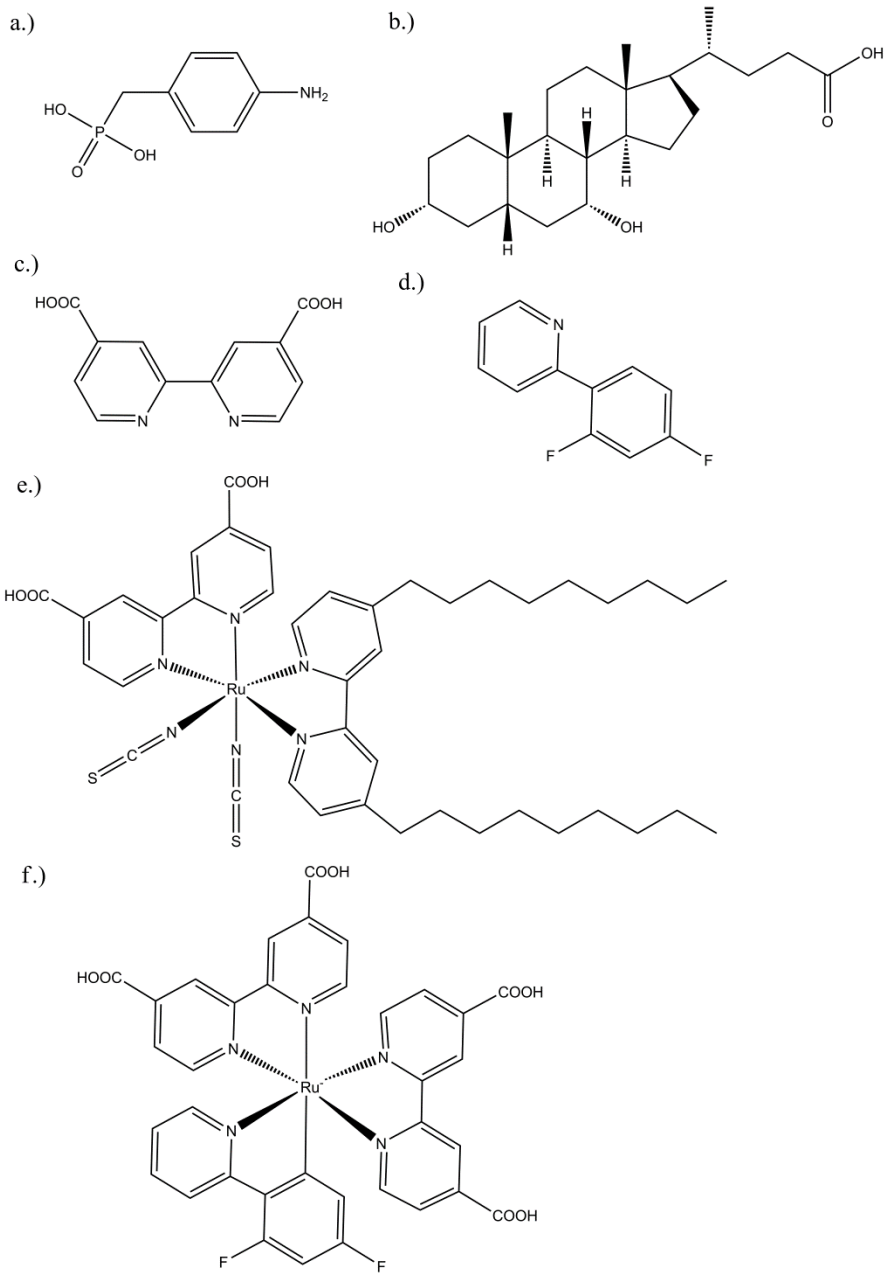


Figure C-1: Molecules studied in this appendix include: a.) *p*-aminobenzyl phosphonic acid (ABPA); b.) chenodeoxycholic acid; c.) bi-isonicotinic acid (BINA); d.) 2-(2,4-difluorophenyl) pyridine; e.) Z907 dye; f.) YE05 dye.

C.3. Results & Discussion

C.3.1. *p*-Aminobenzyl Phosphonic Acid (ABPA)

The ABPA (Figure C-1a) carbon K-edge spectrum, shown in Figure A-2, is characterized by two strong C=C π^* modes at ~258.6 and 286.0 eV (note, these transitions in full would be written as C1s $\rightarrow$ π^* (C=C), but for simplicity the K-shell

origin of the electrons is assumed). The defined peak at 289.0 eV is attributed to C-H σ* modes [45], but the origin of the shoulder at ~288 eV is unclear. This shoulder is a common feature of the carbon K-edge spectra in this appendix. Note that because these two features are also strongly exhibited by unconjugated molecules like chenodeoxycholic acid (*vide infra*) and octadecyl phosphonic acid (not shown), they are not attributed to additional C=C π* modes [38, 45], although in the instance of ABPA (and any of the other molecules presented here), such modes could also be contributing. The similar angular dependence of the shoulder (288 eV) mode and the π* modes at ~286 eV, for example, could be indicative of a strong π* contribution to the 288 eV mode. The strong angular dependence visible in the two π* modes ~286 eV indicates that the benzene rings in adsorbed ABPA have a consistent tilt angle. Fitting these modes using Gaussian peaks in WinXAS [46], and then fitting the angle-intensity data to the NEXAFS vector equation [36] yielded an orientation of 46° relative to the surface normal for the benzene ring of ABPA (see also Section 2.6 and Chapter 6 for details on the NEXAFS equation).

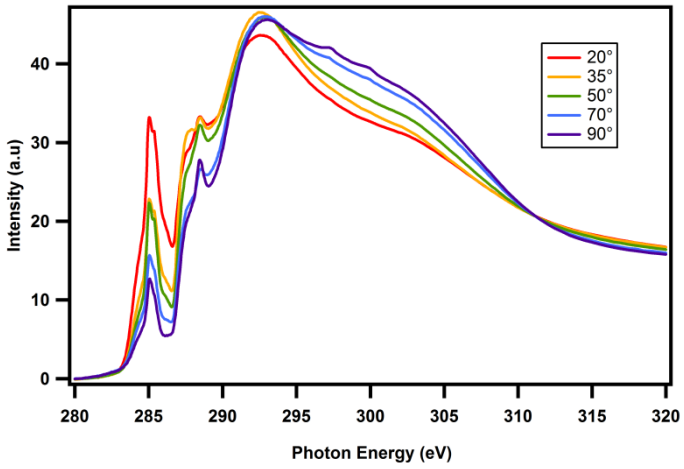


Figure C-2: Angle-resolved NEXAFS carbon K-edge spectra for ABPA.

C.3.2. Bi-isonicotinic Acid (BINA)

As discussed above, given the importance of BINA (Figure C-1c) in the adsorption and electron injection of ruthenium dyes, BINA has been previously studied using X-ray absorption spectroscopy. In comparing the carbon K-edge spectra for BINA powder (Figure C-3a) and BINA adsorbed on TiO_2 (Figure C-3c), there are some clear

differences. The two C=C π* modes visible in the powder at 284.8 eV and 285.6 eV are no longer individually distinguishable upon adsorption. At the same time, the peak at 286.4 eV that is only very faintly visible in the powder, becomes more pronounced upon adsorption. A sharp peak, similar to that seen in ABPA, is visible at 288.5 eV in both the powder and adsorbed BINA. The small shoulder to the right of the large 288.5 eV peak is visible in both the powder and adsorbed BINA, but the peak at 290.5 eV is only visible in the powder. Thomas *et al*., who observed peaks at very similar energies, attribute this 290.5 eV peak to a transition involving the carboxylic acid groups [38]; the disappearance of this peak could be due to these carboxylic groups adsorbing to the TiO_2 surface. This is consistent with the variable intensity of these peaks in the YE05 dye when adsorbed on different metal oxide surfaces (*vide infra*). The C=C σ* mode located at approximately 293 eV exhibits the opposite angular dependence of the π* modes. There are two peaks of unknown origin in the adsorbed BINA spectra at ~297 and 300 eV. These peaks are visible in many of the spectra collected from ALD-grown oxide substrates. The energies appear to be consistent with potassium, but the source of this potassium is unknown.

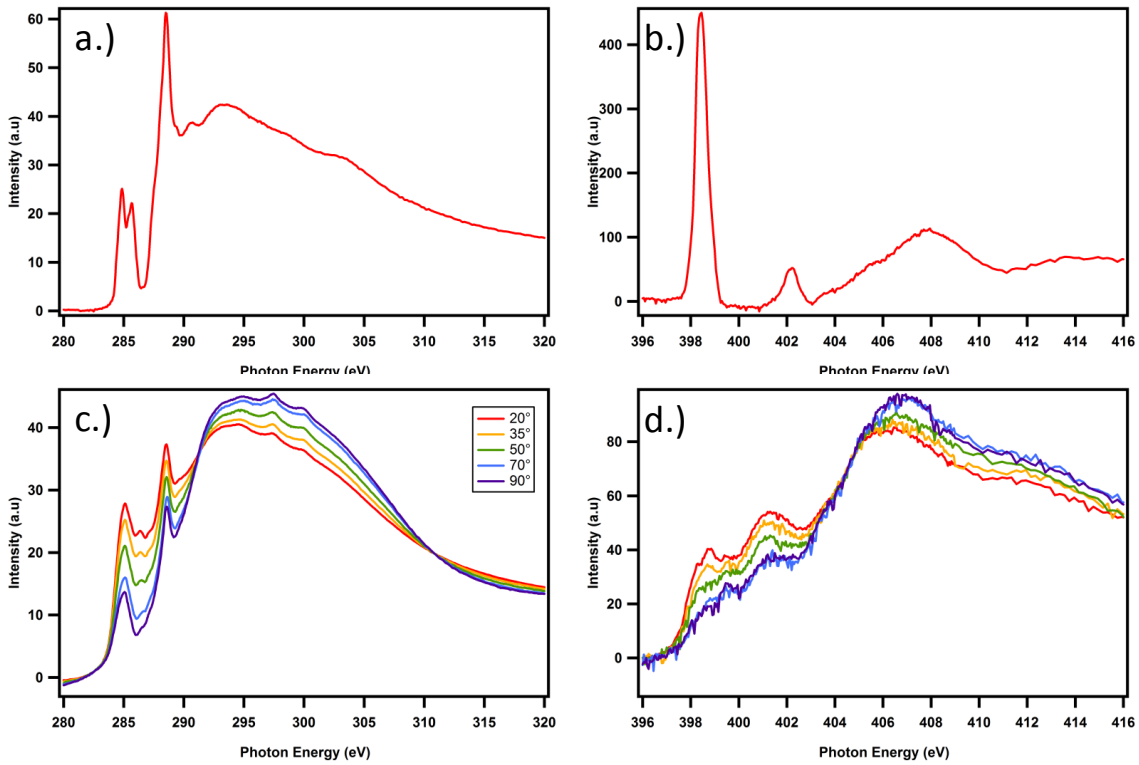


Figure C-3: NEXAFS K-edge spectra for BINA powder and BINA adsorbed from solution onto anatase TiO_2. Spectra for the BINA powder are shown in a.) for carbon and b.) for nitrogen. Angle-resolved NEXAFS spectra of BINA adsorbed on TiO_2 are shown in c.) for carbon and d.) for nitrogen (which uses the same color scheme for angles as c.). In both of the angle-resolved plots a clear angular-dependence is visible. Note that the nitrogen spectra were shifted 1.05 eV to lower energy based on literature references and subsequent beam time experiments of the same materials.

The nitrogen K-edge spectra of BINA powder (Figure C-3b) and adsorbed BINA (Figure C-3d) are more straightforward. In the powder, two sharp π* peaks are visible at 398.4 eV and 402.2 eV and there are two broad σ* modes centered around 408 eV and 415 eV, consistent with previous studies [37, 39, 47]. These π* peaks are significantly broadened upon adsorption, and the second π* mode is shifted to 401.3 eV. Due to the low concentration of N atoms in the film (as compared to C atoms), there is much more noise in the nitrogen spectra than in the carbon spectra for adsorbed BINA. However, it is clear that in both there is a strong and consistent angular dependence of the π* and σ* modes. A Gaussian fit for these spectra was approximated by taking the area under the spectra in the energy range of 284.0 – 285.0 eV for carbon and 397.95 – 399.95 eV for nitrogen. Fitting the angular dependencies for both the carbon and nitrogen spectra using the vector NEXAFS equation yielded very similar tilt angles of the BINA rings of 48.4° and 46.6° relative to the surface normal for carbon and nitrogen, respectively. In

comparison to the 25° and 20° reported previously [37, 38], our results suggest that the BINA rings are oriented relatively less upright from the surface when deposited via solution on ALD-grown anatase TiO_2.

C.3.3. $Co(NCS)_2$ and Cu(NCS)

The isothiocyanate ligand, N=C=S, is a feature of nearly all high-performing ruthenium-based dyes including N3, Z907, and N719. In order to examine how these ligands may contribute to the NEXAFS spectra of the full Z907 dye we examined two small metal-NCS compounds in powder form. The two compounds exhibit very similar X-ray absorption properties at both the carbon (Figure C-4a) and nitrogen (Figure C-4a) K-edge. The carbon spectra include a very strong peak located near 287.4 eV in $Co(NCS)_2$ and 287.3 eV in Cu(NCS) and two weaker peaks located at 288.6 eV and 289.4 eV in $Co(NCS)_2$ and 288.8 eV and 289.8 eV in Cu(NCS). The nitrogen spectra include one very strong peak at 399.5 eV and 399.6 eV in $Co(NCS)_2$ and Cu(NCS), respectively. The strong peak in the carbon spectra is not readily apparent in the Z907 spectrum whereas the strong nitrogen peak is (*vide infra*). Given that the close similarity of these two spectra suggests that X-ray absorption modes are not very sensitive to the choice of metal atom, we believe that this discrepancy is related to the concentration of these atoms with the full dye molecule: in Z907, NCS ligands account for two of the six nitrogen atoms in the full dye whereas NCS ligands only account for two of the forty two carbon atoms in Z907.

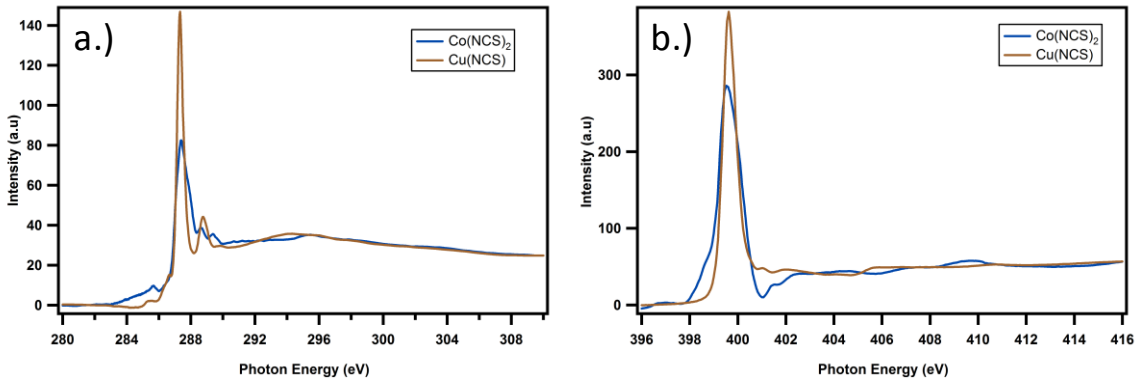


Figure C-4: NEXAFS carbon, a.), and nitrogen, b.), K-edge spectra of $Co(NCS)_2$ and Cu(NCS) powders.

C.3.4. 2-(2,4-difluorophenyl) Pyridine

In the YE05 dye the isothiocyanate ligands have been replaced by 2-(2,4-difluorophenyl) pyridine. As described in Appendix A:, this has advantages for dye stability. Carbon K-edge NEXAFS was used to study this ligand in the gas phase and the resultant spectrum is shown in Figure C-5. In addition to the π* modes located at 285.2 and 285.7 eV, there is a small peak located at 287.0 eV, a split peak centered around 288.1 eV and a peak at 289.4 eV. There also appears to be a shoulder located around 290.7 eV in the broad σ* peak. Previous reports [48] and computational simulations (data not shown) indicate a large shift to higher energy, on the order of 2.0 eV, for the C=C π* mode of fluorine-bonded carbon atoms in comparison to hydrogen-bonded carbon atoms. This likely accounts for one of the peaks located near 287-288 eV. A C-F σ* mode is also anticipated in the 289 - 290 eV range (Ref. [48] and simulation data), as well as the second C=C π* and C-H modes common to the BINA spectrum.

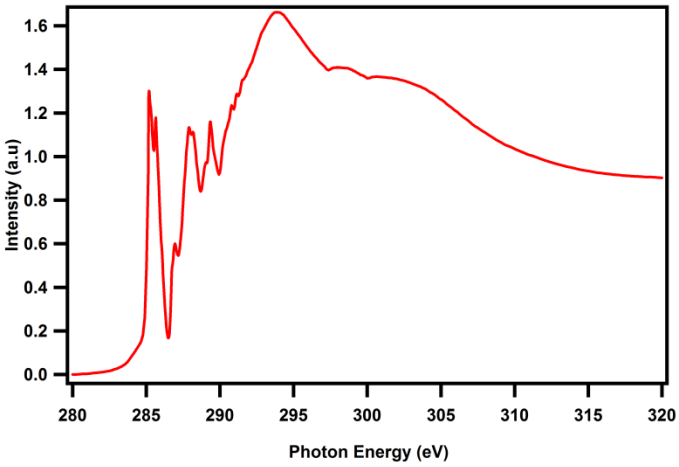


Figure C-5: Carbon K-edge NEXAFS spectrum of 2-(2,4-difluorophenyl) pyridine. Molecule was studied in the gas phase.

C.3.5. Z907 and YE05 Dye Powder

On the whole, the carbon K-edge NEXAFS spectra of the Z907 and YE05 dye powders are quite similar (Figure C-6a). Both have identically-placed C=C π* peaks; the lower energy mode is in fact split into two small, but distinguishable peaks at 284.8 and 285.0 eV with the higher energy C=C π* mode at 285.6 eV. These energies are highly consistent with the same C=C π* modes seen in BINA (Figure C-3a). Both dyes have the strong shoulder at lower energy to the sharp peak located at 288.4 eV and 288.5 eV in

YE05 and Z907, respectively. The only prominent difference between the two dyes' carbon spectrum is the definition of the peak at 290.4 eV—the peak is much sharper in YE05. Given the analysis of the BINA spectrum above, this difference can be attributed to the greater number of carboxylic acid groups in YE05 than Z907 (two versus four). Note that there is no clear difference in the YE05 carbon spectrum that could be due to the 2-(2,4-difluorophenyl) pyridine ligand; this is probably due to the fact that the unique features of this ligand—two fluorine-bonded carbon atoms—constitute a small percentage of the carbon atoms in the full dye molecule.

The nitrogen spectrum for each dye, shown in Figure C-6b, is marked by a single strong π* mode at 400.0 eV. Note that this mode is much broader in the Z907 dye which is understandable given the nitrogen spectra for BINA and the NCS compounds shown above: the strong π* mode in the NCS compounds is located at approximately 1 eV higher energy than that in BINA and this likely causes the high energy broadening of the Z907 π* peak. There are also smaller, less well-defined peaks present in the dye spectra, including one peak at 403.0 eV in each dye that may be due to ether a π* or σ* mode.

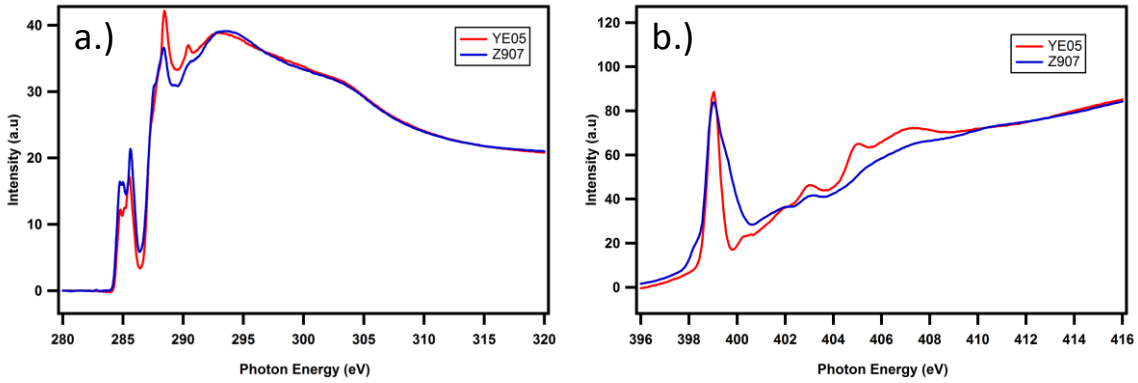


Figure C-6: NEXAFS carbon, a.), and nitrogen, b.), K-edge spectra of Z907 and YE05 dye powders.

C.3.6. Dyes Adsorbed on Metal Oxide Substrates

The adsorption behavior of both Z907 and YE05 appears to be surface-dependent. Angle-resolved NEXAFS experiments indicate different behavior of the dyes on TiO_2 in comparison to other metal oxides. Figure C-7 shows carbon K-edge NEXAFS spectra of Z907 adsorbed on TiO_2 (Figure C-7a), ZrO_2 (Figure C-7b), and Al_2O_3 (Figure C-7c). In the TiO_2 spectra, a clear angular-dependence of the π* mode near 285 eV is apparent. The higher intensity of this mode at lower angles suggest that the pyridine rings are

oriented closer to the surface plane than the surface normal plane; the σ* mode indicates the opposite angular-dependence, as would be expected. In the ZrO_2 and Al_2O_3 samples, however, there is no angular-dependence, suggesting that there is no consistent adsorption orientation. Further, the 290.4 eV mode attributed to unbound carboxylic acid groups is much stronger in the ZrO_2 and Al_2O_3 samples than in the TiO_2 sample. This could indicate that Z907 is much more likely to bind via both carboxylic acid groups on TiO_2, that a different carboxylic acid binding mode occurs on ZrO_2 and Al_2O_3, or that the ZrO_2 and Al_2O_3 substrates lead to aggregation of unbound dye molecules. In contrast, the peak at 288.5 eV is much sharper in the TiO_2 spectra than in the ZrO_2 and Al_2O_3 spectra. Because the origin of this peak is not known, however, it is difficult to understand the implications of this observation.

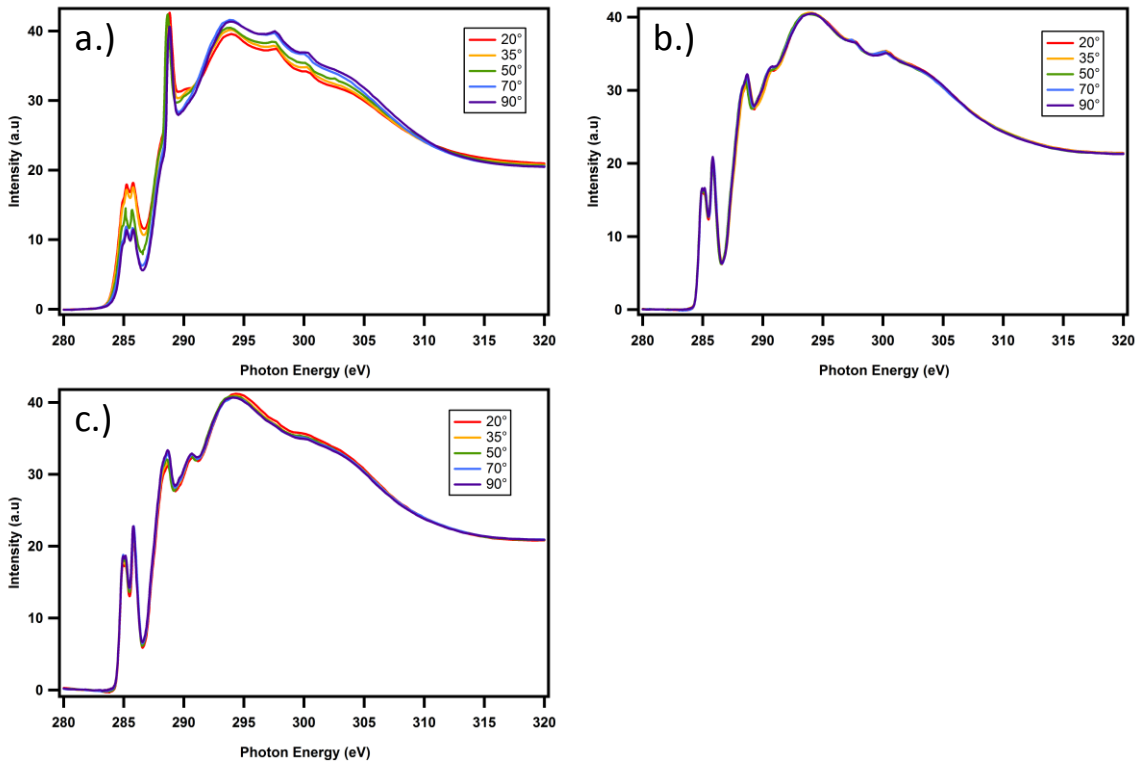


Figure C-7: Angle-resolved carbon K-edge NEXAFS spectra of Z907 adsorbed on anatase TiO_2, a.), ZrO_2, b.), and Al_2O_3, c.).

Analogous work with the YE05 dye yielded very similar results, shown in Figure C-8. Notable angular-dependence is visible in YE05 adsorbed on anatase TiO_2 (Figure C-8a), with the same trend as in Z907. In comparison, four other substrates indicate very little angular dependence: ZrO_2 (Figure C-8c) and Al_2O_3 (Figure C-8d)—as with Z907—

as well as amorphous TiO_2 (Figure C-8b) and ZnO (Figure C-8e). Furthermore, as with Z907, all of these substrates have much stronger carboxylic acid peaks (at 290.4 eV) indicating that fewer carboxylic acid groups per molecule are binding to the surface or that dye aggregation is occurring. The difference between annealed (anatase) and unannealed TiO_2 (amorphous) is particularly interesting and suggests that both the structure and chemistry of the surface is relevant in dye attachment. MgO appears to demonstrate some angular dependence and has a smaller carboxylic acid peak. The fact that dye adsorption on MgO appears most similar to anatase TiO_2 may help explain the beneficial effects of MgO barrier layers seen in the literature (particularly on SnO_2 photoanodes) [49].

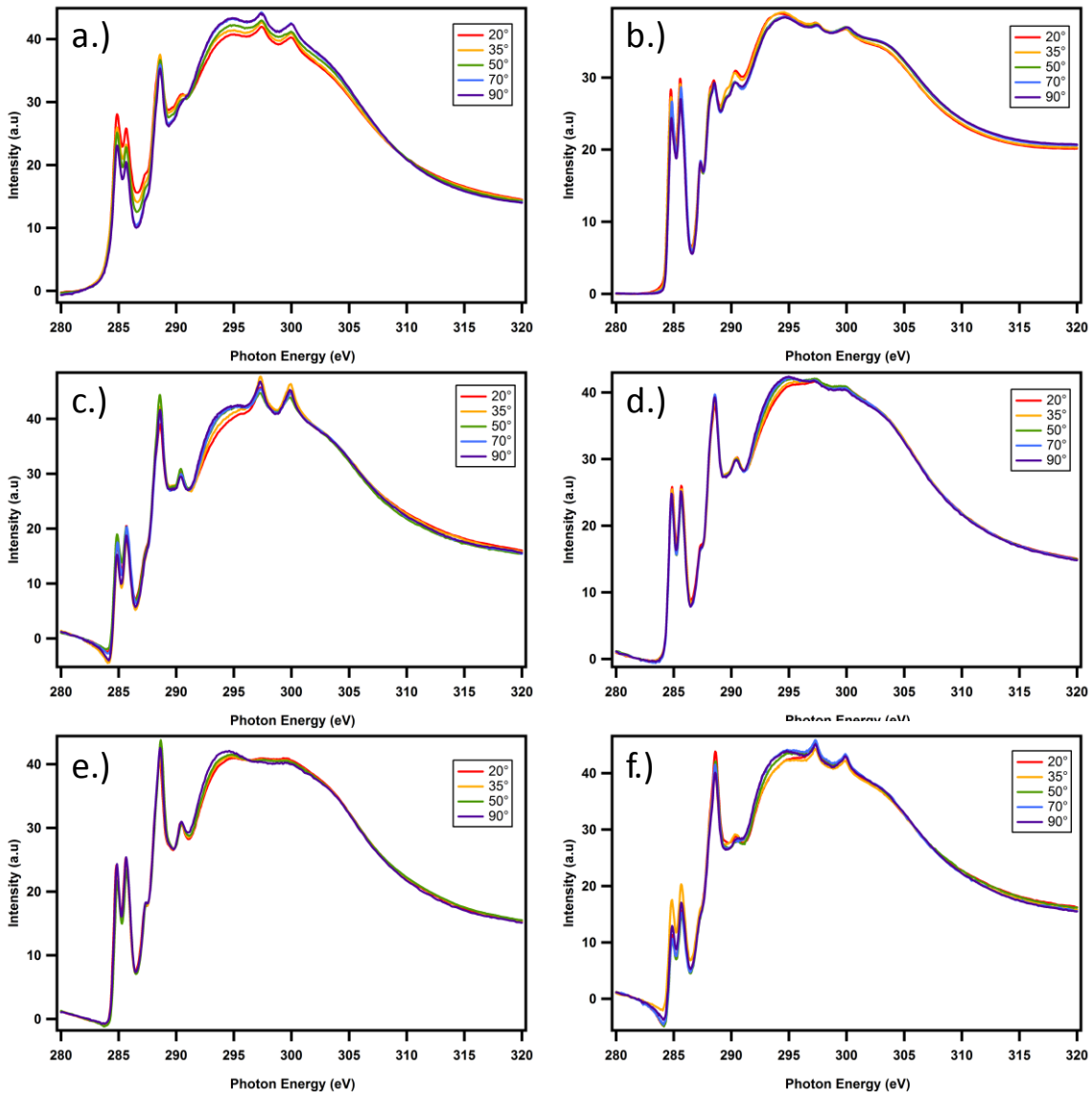


Figure C-8: Angle-resolved carbon K-edge NEXAFS spectra of YE05 adsorbed on anatase TiO_2, a.), amorphous TiO_2, b.), ZrO_2, c.), and Al_2O_3, d.), ZnO, e.), and MgO, f.).

C.3.7. Chenodeoxycholic Acid

Chenodeoxycholic acid (Figure C-1b) is frequently used as a co-adsorbent with dye molecules that are susceptible to aggregation [5]. "Cheno" as it is sometimes called, adsorbs to metal oxide surface via a carboxylic acid group (just as in dye molecules) which means that it can compete with dye molecules for surface sites, leading to reduced device current; the benefits of reduced aggregation must be weighed against this reduction in surface coverage. Cheno was studied using carbon K-edge NEXAFS in both the powder form (Figure C-9a) and adsorbed, in the absence of dye molecules, on anatase

TiO_2 (Figure C-9b). No difference is apparent in comparing the cheno powder with the adsorbed spectra. Both contain a strong, sharp peak at 288.7 eV with a lower-energy shoulder and a broad C-C σ* mode near 293 eV. Additionally, there is a small π* mode visible near 285.2 eV; as there are no C=C bonds in cheno, the origin of this peak is unclear. As described above, the close correspondence of the 288.7 eV peak (and its shoulder) with similar peaks in the conjugated dye molecules and dye components suggest that C-H modes may strongly contribute. No angular dependence is observed in the spectra of the adsorbed cheno.

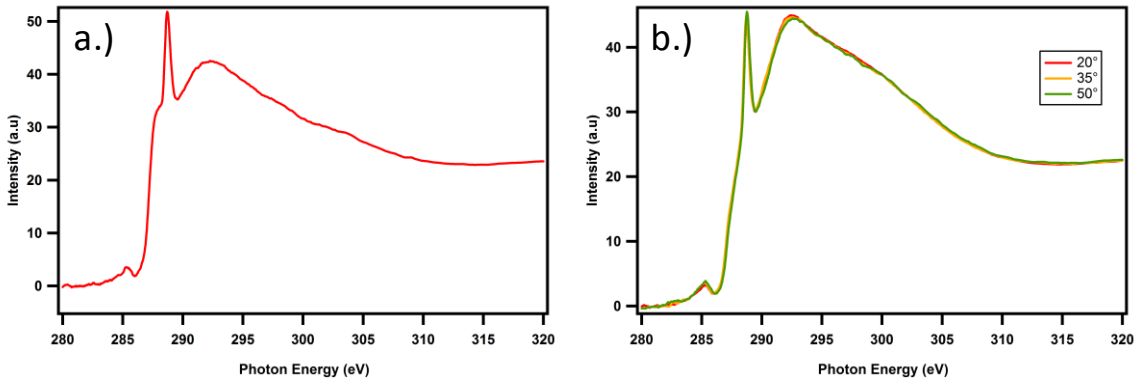


Figure C-9: Carbon K-edge NEXAFS spectrum of chenodeoxycholic acid powder, a.), and adsorbed on anatase TiO_2, b.).

C.4. Conclusions and Outlook

Although the structure of ruthenium-based dyes precludes easy analysis of dye orientation, the data presented in this appendix indicates significant differences between dyes adsorbed on TiO_2 in comparison to other metal oxides. Further, this information provides insight into the electronic structure of these dye molecules and their associated ligands. The shift away from ruthenium dyes towards organic and porphyrin dyes motivates research into the orientation of these classes of dyes, such as that presented in Chapter 6. The design of these dyes, which typically includes fewer carboxylic acid binding groups, and, more importantly a mostly-planar (as opposed to octahedral) structure, makes orientation analysis using NEXAFS feasible.

C.5. Collaborations

The sample fabrication and NEXAFS data collection were performed in close collaboration with Jonathan Bakke. Rajib Mondal synthesized the YE05 dye studied

here. Michael Toney and Dennis Nordlund at SSRL helped develop this project and Dennis Nordlund assisted greatly with NEXAFS data collection and normalization. The beamtime was granted at SSRL under proposal #3338.

C.6. References

[1] S. Handa, H. Wietasch, M. Thelakkat, J.R. Durrant, S.A. Haque, Chemical Communications 0/17 (2007) 1725.
[2] C. Goh, S.R. Scully, M.D. McGehee, Journal of Applied Physics 101/11 (2007) 114503.
[3] A. Allegrucci, N.A. Lewcenko, A.J. Mozer, L. Dennany, P. Wagner, D.L. Officer, K. Sunahara, S. Mori, L. Spiccia, Energy & Environmental Science 2/10 (2009) 1069.
[4] P. Wang, S.M. Zakeeruddin, P. Comte, R. Charvet, R. Humphry-Baker, M. Grätzel, The Journal of Physical Chemistry B 107/51 (2003) 14336.
[5] N.R. Neale, N. Kopidakis, J. van de Lagemaat, M. Grätzel, A.J. Frank, The Journal of Physical Chemistry B 109/49 (2005) 23183.
[6] M.C. Benson, R.E. Ruther, J.B. Gerken, M.L. Rigsby, L.M. Bishop, Y. Tan, S.S. Stahl, R.J. Hamers, ACS Applied Materials & Interfaces 3/8 (2011) 3110.
[7] N.K. Subbaiyan, C.A. Wijesinghe, F. D'Souza, Journal of the American Chemical Society 131/41 (2009) 14646.
[8] S.-R. Jang, R. Vittal, J. Lee, N. Jeong, K.-J. Kim, Chemical Communications 0/1 (2006) 103.
[9] J.P. Folkers, C.B. Gorman, P.E. Laibinis, S. Buchholz, G.M. Whitesides, R.G. Nuzzo, Langmuir 11/3 (1995) 813.
[10] S. Marcinko, A.Y. Fadeev, Langmuir 20/6 (2004) 2270.
[11] P. Wang, C. Klein, J.-E. Moser, R. Humphry-Baker, N.-L. Cevey-Ha, R. Charvet, P. Comte, S.M. Zakeeruddin, M. Grätzel, The Journal of Physical Chemistry B 108/45 (2004) 17553.
[12] J.B. Asbury, E. Hao, Y. Wang, T. Lian, The Journal of Physical Chemistry B 104/50 (2000) 11957.
[13] G.M. Kosolapoff, Journal of the American Chemical Society 69/9 (1947) 2112.
[14] P.-H. Heubel, A. Popov, Journal of Solution Chemistry 8/9 (1979) 615.
[15] S. Pawsey, K. Yach, L. Reven, Langmuir 18/13 (2002) 5205.
[16] J. Telser, K.A. Cruickshank, K.S. Schanze, T.L. Netzel, Journal of the American Chemical Society 111/18 (1989) 7221.
[17] Z. Grabarek, J. Gergely, Analytical Biochemistry 185/1 (1990) 131.
[18] T. Bessho, E. Yoneda, J.-H. Yum, M. Guglielmi, I. Tavernelli, H. Imai, U. Rothlisberger, M.K. Nazeeruddin, M. Grätzel, Journal of the American Chemical Society 131/16 (2009) 5930.
[19] P. Ardalan, T.P. Brennan, H.-B.-R. Lee, J.R. Bakke, I.K. Ding, M.D. McGehee, S.F. Bent, ACS Nano 5/2 (2011) 1495.
[20] L. Xiu, Y. Kehan, L. Ganhua, C. Junhong, Y. Chris, Journal of Physics D: Applied Physics 46/2 (2013) 024004.
[21] Q. Zhang, X. Guo, X. Huang, S. Huang, D. Li, Y. Luo, Q. Shen, T. Toyoda, Q. Meng, Physical Chemistry Chemical Physics 13/10 (2011) 4659.

[22] M. Shalom, J. Albero, Z. Tachan, E. Martínez-Ferrero, A. Zaban, E. Palomares, The Journal of Physical Chemistry Letters 1/7 (2010) 1134.
[23] K. Yu, X. Lin, G. Lu, Z. Wen, C. Yuan, J. Chen, RSC Advances 2/20 (2012) 7843.
[24] C.-F. Chi, P. Chen, Y.-L. Lee, I.P. Liu, S.-C. Chou, X.-L. Zhang, U. Bach, Journal of Materials Chemistry 21/43 (2011) 17534.
[25] R. Vogel, P. Hoyer, H. Weller, The Journal of Physical Chemistry 98/12 (1994) 3183.
[26] Y.-L. Lee, Y.-S. Lo, Advanced Functional Materials 19/4 (2009) 604.
[27] Z. Yang, C.-Y. Chen, C.-W. Liu, C.-L. Li, H.-T. Chang, Advanced Energy Materials 1/2 (2011) 259.
[28] H.J. Lee, P. Chen, S.-J. Moon, F.d.r. Sauvage, K. Sivula, T. Bessho, D.R. Gamelin, P. Comte, S.M. Zakeeruddin, S.I. Seok, M. Grätzel, M.K. Nazeeruddin, Langmuir 25/13 (2009) 7602.
[29] H. Lee, H.C. Leventis, S.-J. Moon, P. Chen, S. Ito, S.A. Haque, T. Torres, F. Nüesch, T. Geiger, S.M. Zakeeruddin, M. Grätzel, M.K. Nazeeruddin, Advanced Functional Materials 19/17 (2009) 2735.
[30] K.E. Roelofs, T.P. Brennan, J.C. Dominguez, C.D. Bailie, G.Y. Margulis, E.T. Hoke, M.D. McGehee, S.F. Bent, The Journal of Physical Chemistry C 117/11 (2013) 5584.
[31] X.-Y. Yu, J.-Y. Liao, K.-Q. Qiu, D.-B. Kuang, C.-Y. Su, ACS Nano 5/12 (2011) 9494.
[32] Z. Ning, H. Tian, C. Yuan, Y. Fu, H. Qin, L. Sun, H. Agren, Chemical Communications 47/5 (2011) 1536.
[33] T.P. Brennan, P. Ardalan, H.-B.-R. Lee, J.R. Bakke, I.K. Ding, M.D. McGehee, S.F. Bent, Advanced Energy Materials 1/6 (2011) 1169.
[34] N.P. Dasgupta, H.J. Jung, O. Trejo, M.T. McDowell, A. Hryciw, M. Brongersma, R. Sinclair, F.B. Prinz, Nano Letters 11/3 (2011) 934.
[35] P. Ardalan, Organic and inorganic surface modification of semiconductors for electronic and energy conversion devices, Stanford University, Stanford, 2010.
[36] J. Stöhr, NEXAFS Spectroscopy, Springer-Verlag, Berlin, 1992.
[37] L. Patthey, H. Rensmo, P. Persson, K. Westermark, L. Vayssieres, A. Stashans, A. Petersson, P.A. Bruhwiler, H. Siegbahn, S. Lunell, N. Martensson, The Journal of Chemical Physics 110/12 (1999) 5913.
[38] A.G. Thomas, W.R. Flavell, C. Chatwin, S. Rayner, D. Tsoutsou, A.R. Kumarasinghe, D. Brete, T.K. Johal, S. Patel, J. Purton, Surface Science 592/1-3 (2005) 159.
[39] P. Persson, S. Lunell, P.A. Bruhwiler, J. Schnadt, S. Sodergren, J.N. O'Shea, O. Karis, H. Siegbahn, N. Martensson, M. Bassler, L. Patthey, The Journal of Chemical Physics 112/9 (2000) 3945.
[40] K. Westermark, H. Rensmo, J. Schnadt, P. Persson, S. Södergren, P.A. Brühwiler, S. Lunell, H. Siegbahn, Chemical Physics 285/1 (2002) 167.
[41] L.C. Mayor, J.B. Taylor, G. Magnano, A. Rienzo, C.J. Satterley, J.N. O'Shea, J. Schnadt, The Journal of Chemical Physics 129/11 (2008) 114701.
[42] K.E. Lee, M.A. Gomez, T. Regier, Y. Hu, G.P. Demopoulos, The Journal of Physical Chemistry C 115/13 (2011) 5692.

[43] Q. Xie, J. Musschoot, D. Deduytsche, R.L. Van Meirhaeghe, C. Detavernier, S. Van den Berghe, Y.-L. Jiang, G.-P. Ru, B.-Z. Li, X.-P. Qu, Journal of The Electrochemical Society 155/9 (2008) H688.
[44] J.R. Bakke, Atomic Layer Deposition of Materials for Applications to Photovoltaics, Stanford University, Stanford, 2011.
[45] N. Graf, E. Yegen, T. Gross, A. Lippitz, W. Weigel, S. Krakert, A. Terfort, W.E.S. Unger, Surface Science 603/18 (2009) 2849.
[46] T. Ressler, Journal of Synchrotron Radiation 5/2 (1998) 118.
[47] J. Schnadt, A. Henningsson, M.P. Andersson, P.G. Karlsson, P. Uvdal, H. Siegbahn, P.A. Brühwiler, A. Sandell, The Journal of Physical Chemistry B 108/10 (2004) 3114.
[48] O. Plashkevych, L. Yang, O. Vahtras, H. Ågren, L.G.M. Petterson, Chemical Physics 222/2-3 (1997) 125.
[49] P. Docampo, P. Tiwana, N. Sakai, H. Miura, L. Herz, T. Murakami, H.J. Snaith, The Journal of Physical Chemistry C 116/43 (2012) 22840.